FERMILAB-THESIS-2020-30
DOI: 10.6082/uchicago.2230

THE UNIVERSITY OF CHICAGO

A MEASUREMENT OF THE TOTAL HADRONIC π^- ON ARGON CROSS SECTION IN THE KINETIC ENERGY RANGE FROM 0.2–1 GIGA-ELECTRON VOLTS IN A LIQUID ARGON TIME PROJECTION CHAMBER

A DISSERTATION SUBMITTED TO
THE FACULTY OF THE DIVISION OF THE PHYSICAL SCIENCES
IN CANDIDACY FOR THE DEGREE OF
DOCTOR OF PHILOSOPHY

DEPARTMENT OF PHYSICS

BY
JOHNNY HO

CHICAGO, ILLINOIS
JUNE 2020

To my mom and my sister

The road to wisdom?—Well, it's plain
and simple to express:

Err
and err
and err again,
but less
and less
and less.

—Piet Hein, *Grooks*

Table of Contents

List of Figures viii

List of Tables xxiii

Acknowledgments xxiv

Abstract xxvi

1 Introduction 1

2 Detecting Neutrinos in Liquid Argon 4

2.1 The Liquid Argon Time Projection Chamber 4

2.1.1 Working principle 5

2.1.2 The case for liquid argon 8

2.2 Neutrino Interactions in Liquid Argon 10

2.3 Charged Pion Interactions in Liquid Argon 16

3 The LArIAT Experiment 23

3.1 Scientific Goals 25

3.2 Beamline Instrumentation 27

3.2.1 Tertiary beam spectrometer and particle identification system 29

3.3 The LArIAT Detector 33

3.3.1 Cryogenic system 33

3.3.2 Time projection chamber 35

3.4 Data Acquisition 41

3.5 Trigger System 42

3.6 Monitoring 45

3.6.1 DAQ monitoring . . . 45
3.6.2 Data quality monitoring . . . 46
3.7 TPC Event Reconstruction . . . 47

4 Data-Driven Monte Carlo Simulation . . . 50
4.1 Tertiary Beam . . . 50
4.2 Halo Pile-Up . . . 51

5 Total Hadronic π^- on Argon Cross Section . . . 58
5.1 Event Selection . . . 59
5.1.1 Beamline-based selection . . . 59
5.1.2 Data-constrained re-weighting of fractional particle content in MC . . . 65
5.1.3 Mitigation of electron background events . . . 73
5.2 Cross Section . . . 75
5.2.1 Thin-target approximation . . . 75
5.2.2 Thin-slab method . . . 80
5.2.3 Corrections to the cross section . . . 87
5.3 Uncertainties . . . 108
5.3.1 Statistical uncertainties . . . 108
5.3.2 Systematic uncertainties . . . 108
5.4 Result . . . 110

6 Conclusion . . . 113

A Estimation of Halo Pile-Up Rate . . . 115

B Monte Carlo Simulations for Propagation of Statistical Uncertainties . . . 120

C Monte Carlo Simulations for Propagation of Systematic Uncertainties . . . 133

D Pion Single-Charge Exchange 141

References 149

List of Figures

2.1 The working principle of a LArTPC. (a) A muon passes through the liquid argon detector medium and produces an ionization track of Ar^+ and e^- pairs, and induces the emission of VUV scintillation light. (b) A fraction of the Ar^+ and e^- pairs recombine to emit additional scintillation light; the remaining pairs are separated by the electric field. (c) The Ar^+ ions drift towards the high voltage cathode, and the electrons drift towards the anode wire planes; drifting electrons may attach to electronegative impurities, diminishing signal integrity. (d) The drifting electrons produce signals at the anode wire planes, which are amplified and read out. 6

2.2 Illustration of charged particles emerging from a neutrino interaction vertex and producing ionization tracks. Waveforms of signals read out from the wires are processed through a chain of algorithms to reconstruct the 3D trajectories of the charged particles and the energy that they deposited. Figure taken from Ref. [14]. 7

2.3 Event displays of neutrino interactions with electromagnetic activity in the MicroBooNE LArTPC detector. Time is plotted along the vertical axis, and wire number is plotted along the horizontal axis. The neutrino beam is incident from the left. The top shows a ν_e candidate event with an electron-induced eletromagnetic shower, while the bottom shows a ν_μ candidate event with gamma-induced electromagnetic showers. 9

2.4 Example Feynman diagrams of several neutrino–nucleon interaction modes. . . . 11

2.5 Total neutrino (top) and anti-neutrino (bottom) charged-current cross sections (for an isoscalar target) divided by neutrino energy plotted as a function of energy [36]. Predictions for the quasi-elastic (QE), resonant (RES), and deep inelastic scattering (DIS) processes are provided by the NUANCE neutrino simulation software. Updated from Ref. [36] by A. Schukraft and G. Zeller. 14

2.6 Illustration of a ν_μ CCQE interaction (top) and a ν_μ CC1π^+ interaction (bottom). The panels on the left show details of possible final-state interactions that may occur within a target nucleus; the panels on the right show that the final observables in the detector may be the same. The trajectories of ionizing particles are depicted with solid lines; the trajectories of non-ionizing particles are depicted with broken lines. In this example of a CC1π^+ interaction, the final-state π^+ is absorbed through a two-body pion absorption process, producing a p and a n. . 15

2.7 Various pion–argon interaction candidate events from the LArIAT experiment, with ionization tracks incident from the left. Time is plotted along the vertical axis, and wire number is plotted along the horizontal axis. The density of ionization charge is indicated by the color, with red being the most dense. . . . 19

2.8 Simulated neutrino event in MicroBooNE. 19

2.9 Historical data of pion scattering on different light and heavy nuclei. Taken from Ref. [42]. 21

2.10 π^+–Ar cross section (top) and π^-–Ar cross section (bottom) as functions of kinetic energy as predicted by the GEANT4 Bertini intranuclear cascade model. The elastic, reactive, and total hadronic cross sections are plotted with dotted, dashed, and dash-dot lines, respectively. 22

3.1 Various candidate events from data, with ionization tracks incident from the left. Time is plotted along the vertical axis, and wire number is plotted along the horizontal axis. The density of ionization charge is indicated by the color, with red being the most dense. 24

3.2 Top-down schematic of the tertiary beamline. Beam is incident from the left. . . 28

3.3 Momentum spectra and compositions of the tertiary beam downstream of the spectrometer for different magnet polarities and energy tunes. 30

3.4 One of the multi-wire proportional chambers (WC4) in the tertiary beamline. . 32

3.5 Reconstructed momentum vs. time of flight of particles in the tertiary beam for data collected with the positive polarity configuration. The colored lines are the expectations for different species of particles. 32

3.6 The LArIAT cryostat opened with the TPC inside the inner vessel (left), and the cryostat fully sealed (right). 33

3.7 A screenshot of the LArIAT cryostat monitoring page displaying the argon levels within the cryostat and supply dewar (top). Position of the liquid valve that allows liquid argon to flow into the cryostat and corresponding pressure within the cryostat (bottom). 36

3.8 The three wire layers in the LArIAT TPC as viewed from inside the TPC volume (beam is incident from the right). 37

3.9 One of the wire planes during the wire plane assembly process. 38

3.10 Schematic diagram of the LArIAT TPC. The induction plane and collection plane wires are oriented at $\pm 60^{\circ}$ relative to the z axis in the y–z plane, respectively; the wire pitch and interplanar spacing are both 4 mm. Figure modified from Ref. [67]. 39

3.11 Schematic diagram of the three drift regions within the LArIAT TPC. 40

3.12 An induction wire signal (left) and a collection wire signal (right) of an event from the Run-II dataset. The first pulse comes from a proton candidate and the second pulse comes from a gamma-induced electromagnetic shower candidate. . 41

3.13 Block diagram of the LArIAT DAQ system and data flow. 43

3.14 The LArIAT DAQ timeline during a super cycle. The BEAMON and COSMICON gates are inputs to the trigger system. 43

3.15 Schematic diagram of the LArIAT digitizer timing and clock configuration. . . . 44

3.16 The LArIAT run status page. 47

3.17 DQM monitoring page displaying a set of time series plots of the number of data fragments collected per super cycle over the previous 16 hours of operation. . . . 48

3.18 DQM monitoring page displaying a set of time series plots of the RMS on each TPC wire over the previous 16 hours of operation. 48

4.1 Reconstructed quantities from WC tracks in the Run-II -100 A dataset. 52

4.2 Momentum spectrum of the DDMC simulation for the Run-II -100 A dataset. . 53

4.3 Projected x and y positions of the WC track onto the front face of the TPC. . . 53

4.4 Various events with pile-up from the LArIAT Run-II dataset. 54

4.5 Angular and energy distributions of muons from decays of charged pions at 64 GeV/c. 54

4.6 Distributions of (x, y) of upstream-most point of halo pile-up tracks (top) and angle of halo pile-up tracks (bottom) for the Run-II -100 A dataset. The distributions in the left-hand column are from data; the distributions in the right-hand column are from the DDMC simulation. 56

4.7 Distribution of the number of halo pile-up tracks per event for the Run-II -100 A dataset. 57

5.1 Illustration of the true trajectory of a particle scattering off the downstream collimator in the tertiary beamline, and the reconstructed trajectory of the particle. In this example, the WC3–WC4 track does not pass through the second aperture of the downstream collimator, thus the event is rejected. 60

5.2 Reconstructed WC track momentum and time of flight in the Run-II -100 A dataset. 61

5.3 Squared mass computed from the reconstructed WC track momentum and measured time of flight in the Run-II -100 A dataset. Events that satisfy the $m^2 < 350^2$ MeV$^2/c^4$ criterion lie within the green-shaded region. 62

5.4 Illustration of the WC-to-TPC track matching procedure. The WC track is projected into the TPC; the angle between the projected WC track and a primary TPC track candidate is defined to be α. The differences between the x and y positions of the WC track projected onto the front face of the TPC and the upstream-most point of a primary TPC track candidate are defined to be Δx and Δy. The upsteam-most point of the TPC track must satisfy the $z < 4$ cm criterion in order to be considered. 63

5.5 2D histogram of Δx vs. Δy from the WC-to-TPC track matching procedure in the Run-II -100 A dataset. TPC tracks that satisfy the $\Delta r < 5$ cm criterion lie within the black circle. The background is due to beam halo pile-up. 64

5.6 Distributions of Δr and α from the WC-to-TPC track matching procedure in the Run-II -100 A dataset. 64

5.7 Momentum spectra of tertiary beam particles at WC4 for events that satisfy the WC/TPC match requirement. Data plotted with markers accompanied with statistical error bars, and data-driven Monte Carlo plotted with colored stacked histograms showing the MC predicted particle content. 67

5.8 Momentum spectra of tertiary beam particles at WC4 for events that satisfy the WC/TPC match requirement. The π^- category is subcategorized: μ^- (a), if the WC track is matched to a TPC track of a μ^- from a π^- decaying upstream of WC4; μ^- (b), if the WC track is matched to a TPC track of a halo pile-up μ^- from the secondary beam; and π^-, if the π^- penetrates into the TPC volume and has a proper WC/TPC track match. 67

5.9 The interacting length is defined to be the length of a reconstructed track within the fiducial region up to the interaction point of an interacting event. The non-interacting length is defined to be the length of a reconstructed track within the fiducial region of a non-interacting event. 68

5.10 Interacting and non-interacting length of the Run-II −60 A and −100 A datasets. 69

5.11 Interacting and non-interacting length of the Run-II −60 A and −100 A datasets after re-weighting. 71

5.12 Momentum spectra of tertiary beam particles at WC4 (for events that satisfy the WC/TPC match requirement) after re-weighting. The π^- category is subcategorized: μ^- (a), if the WC track is matched to a TPC track of a μ^- from a π^- decaying upstream of WC4; μ^- (b), if the WC track is matched to a TPC track of a halo pile-up μ^- from the secondary beam; and π^-, if the π^- penetrates into the TPC volume and has a proper WC/TPC track match. 72

5.13 Diagrams illustrating Molière regions of two different events. 74

5.14 Number of non-primary tracks that lie entirely within Molière region per event. To mitigate the electron background, we reject events with more than 4 non-primary tracks that lie entirely within the Molière region. 74

5.15 Schematic diagram of the LArIAT TPC showing the 4 mm wire pitch and 4.6 mm track pitch in the collection plane. The beam axis is oriented at −3° from the z axis in the x–z plane. 81

5.16 Distribution of energy loss in the uninstrumented material between WC4 and the front face of TPC as estimated from the −100 A DDMC simulation. The mode (most probable value) of the distribution is 50 MeV. The horizontal black line at the bottom of the distribution indicates the 68.3% highest density interval. . . . 82

5.17 Distribution of energy deposited in a slab of argon, $E_i^{\text{deposited}}$, from the Run-II −100 A dataset and DDMC simulation. The data and Monte Carlo distributions are fit to a convolution of a Landau distribution and a Gaussian distribution. The width of the Landau ⊗ Gaussian fit is 0.0808 MeV for data and 0.0658 MeV for Monte Carlo. 82

5.18 LArIAT TPC divided into thin slabs with thicknesses determined by the collection plane wires and reconstructed track pitches. 84

5.19 Example of non-interacting and interacting histograms for the illustrated $\pi^{\pm}$ interaction event. 85

5.20 Example of non-interacting and interacting histograms over an ensemble of events. 86

5.21 Demonstrations of estimating the π^{-}–Ar cross section with a toy Monte Carlo simulation by (a) minimizing the negative log-likelihood function and (b) by taking the ratio of the unweighted interacting and weighted non-interacting histograms. 87

5.22 3D distance between true position of π^{-} interaction point and closest reconstructed hit. We require that the reconstructed hit be within 2 cm of the true position of the interacting point to be considered a possible "signal" hit. 91

5.23 Hit index difference between reconstructed hit selected as an interacting hit and reconstructed hit closest to the true position of the π^- interaction point. We require that the reconstructed hit be within 3 hits of the closest-to-true hit to be a reconstructed π^- to be considered a possible "signal" hit. 92

5.24 Reconstructed kinetic energy of selected interacting and non-interacting hits from a -100 A π^- Monte Carlo sample categorized into signal and background hits. . 94

5.25 True kinetic energy of interacting and non-interacting signal points from a -100 A π^- Monte Carlo sample categorized into selected and non-selected MC truth points. 95

5.26 Response matrix and inverted response matrix for interacting hits. 98

5.27 Response matrix and inverted response matrix for non-interacting hits. 99

5.28 Covariance and correlation matrices for interacting hits from the Run-II -100 A dataset. 100

5.29 Covariance and correlation matrices for non-interacting hits from the Run-II -100 A dataset. 101

5.30 Background-subtracted of distributions of kinetic energy of hits in the Run-II -100 A dataset. The reconstructed distributions are plotted with dotted lines, and the background-subtracted distributions are plotted with markers accompanied with statistical error bars. 103

5.31 Unfolding of distributions of kinetic energy of hits using matrix inversion on the Run-II -100 A dataset. The background-subtracted distributions are plotted with dashed lines, and the unfolded distributions are plotted with markers accompanied with statistical error bars. Non-selected MC truth points are excluded from the Monte Carlo distribution. 104

5.32 Efficiency-corrected distributions of kinetic energy of hits in the Run-II −100 A dataset. The background-subtracted distributions are plotted with dashed lines, and the unfolded distributions are plotted with dotted lines, and the efficiency-corrected distributions are plotted with markers accompanied with statistical error bars. 104

5.33 Total hadronic π^-–Ar cross section estimate using the Run-II −100 A dataset. The darker error bars indicate statistical errors on the number of selected hits; the lighter error bars indicate statistical errors on the Monte Carlo correction factors in addition to the statistical errors on the number of selected hits. 105

5.34 Total hadronic π^-–Ar cross section estimate using the Run-II −60 A and −100 A datasets. The darker error bars indicate statistical errors on the number of selected hits; the lighter error bars indicate statistical errors on the Monte Carlo correction factors in addition to the statistical errors on the number of selected hits. 106

5.35 Monte Carlo closure test. Total hadronic π^-–Ar cross section estimate using a −100 A Monte Carlo sample. The darker error bars indicate statistical errors on the number of selected hits; the lighter error bars indicate statistical errors on the Monte Carlo correction factors in addition to the statistical errors on the number of selected hits. 107

5.36 Total hadronic π^-–Ar cross section estimate using the Run-II −100 A dataset. The darker error bars indicate statistical uncertainties; the lighter error bars indicate the combined statistical and systematic uncertainties. 111

A.1 Number of reconstructed halo pile-up tracks per event measured from the −100 A dataset. 117

A.2 Tracking efficiencies of halo pile-up particles estimated from Monte Carlo. 117

A.3 Estimated probability mass of reconstructing k pile-up tracks in an event, $f(k)$, taken from data, and estimated probability of n pile-up particles in an event, $g(n)$, from deconvolution. 119

B.1 Distributions of $p_{\text{int}}^{\text{MC}}$ generated from Monte Carlo simulations for kinetic energy bins between 100 MeV and 550 MeV. The horizontal black line at the bottom of each distribution indicates the 68.3% highest density interval (numerical labels are rounded to 3 significant figures). The nominal value of $p_{\text{int}}^{\text{MC}}$ is the mode (most probable value) of the distribution. 121

B.2 Distributions of $p_{\text{int}}^{\text{MC}}$ generated from Monte Carlo simulations for kinetic energy bins between 550 MeV and 1000 MeV. The horizontal black line at the bottom of each distribution indicates the 68.3% highest density interval (numerical labels are rounded to 3 significant figures). The nominal value of $p_{\text{int}}^{\text{MC}}$ is the mode (most probable value) of the distribution. 122

B.3 Distributions of $p_{\text{non-int}}^{\text{MC}}$ generated from Monte Carlo simulations for kinetic energy bins between 100 MeV and 550 MeV. The horizontal black line at the bottom of each distribution indicates the 68.3% highest density interval (numerical labels are rounded to 3 significant figures). The nominal value of $p_{\text{non-int}}^{\text{MC}}$ is the mode (most probable value) of the distribution. 123

B.4 Distributions of $p_{\text{non-int}}^{\text{MC}}$ generated from Monte Carlo simulations for kinetic energy bins between 550 MeV and 1000 MeV. The horizontal black line at the bottom of each distribution indicates the 68.3% highest density interval (numerical labels are rounded to 3 significant figures). The nominal value of $p_{\text{non-int}}^{\text{MC}}$ is the mode (most probable value) of the distribution. 124

B.5 Distributions of $\epsilon_{\text{int}}^{\text{MC}}$ generated from Monte Carlo simulations for kinetic energy bins between 100 MeV and 550 MeV. The horizontal black line at the bottom of each distribution indicates the 68.3% highest density interval (numerical labels are rounded to 3 significant figures). The nominal value of $\epsilon_{\text{int}}^{\text{MC}}$ is the mode (most probable value) of the distribution. 125

B.6 Distributions of $\epsilon_{\text{int}}^{\text{MC}}$ generated from Monte Carlo simulations for kinetic energy bins between 550 MeV and 1000 MeV. The horizontal black line at the bottom of each distribution indicates the 68.3% highest density interval (numerical labels are rounded to 3 significant figures). The nominal value of $\epsilon_{\text{int}}^{\text{MC}}$ is the mode (most probable value) of the distribution. 126

B.7 Distributions of $\epsilon_{\text{non-int}}^{\text{MC}}$ generated from Monte Carlo simulations for kinetic energy bins between 100 MeV and 550 MeV. The horizontal black line at the bottom of each distribution indicates the 68.3% highest density interval (numerical labels are rounded to 3 significant figures). The nominal value of $\epsilon_{\text{non-int}}^{\text{MC}}$ is the mode (most probable value) of the distribution. 127

B.8 Distributions of $\epsilon_{\text{non-int}}^{\text{MC}}$ generated from Monte Carlo simulations for kinetic energy bins between 550 MeV and 1000 MeV. The horizontal black line at the bottom of each distribution indicates the 68.3% highest density interval (numerical labels are rounded to 3 significant figures). The nominal value of $\epsilon_{\text{non-int}}^{\text{MC}}$ is the mode (most probable value) of the distribution. 128

B.9 Distributions of $\sigma_{\text{total}}^{\text{data}}$ generated from Monte Carlo simulations for kinetic energy bins between 100 MeV and 550 MeV. The horizontal black line at the bottom of each distribution indicates the 68.3% highest density interval (numerical labels are rounded to 3 significant figures). 129

B.10 Distributions of $\sigma_{\text{total}}^{\text{data}}$ generated from Monte Carlo simulations for kinetic energy bins between 550 MeV and 1000 MeV. The horizontal black line at the bottom of each distribution indicates the 68.3% highest density interval (numerical labels are rounded to 3 significant figures). 130

B.11 Distributions of $\sigma_{\text{total}}^{\text{data+MC}}$ generated from Monte Carlo simulations for kinetic energy bins between 100 MeV and 550 MeV. The horizontal black line at the bottom of each distribution indicates the 68.3% highest density interval (numerical labels are rounded to 3 significant figures). 131

B.12 Distributions of $\sigma_{\text{total}}^{\text{data+MC}}$ generated from Monte Carlo simulations for kinetic energy bins between 550 MeV and 1000 MeV. The horizontal black line at the bottom of each distribution indicates the 68.3% highest density interval (numerical labels are rounded to 3 significant figures). 132

C.1 Distributions of C_π, C_μ, and C_e. C_μ and C_e are simulated from a beta distribution with parameters $a = 1.65$ and $b = 1.0$. 134

C.2 Distributions of C_π, C_μ, and C_e simulated from a Dirichlet distribution. 134

C.3 Distributions of $\sigma_{\text{total}}^{\mu/e}$ generated from Monte Carlo simulations for kinetic energy bins between 100 MeV and 550 MeV. The horizontal black line at the bottom of each distribution indicates the 68.3% highest density interval (numerical labels are rounded to 3 significant figures). 135

C.4 Distributions of $\sigma_{\text{total}}^{\mu/e}$ generated from Monte Carlo simulations for kinetic energy bins between 550 MeV and 1000 MeV. The horizontal black line at the bottom of each distribution indicates the 68.3% highest density interval (numerical labels are rounded to 3 significant figures). 136

C.5 Distributions of $\sigma_{\text{total}}^{\pi/e}$ generated from Monte Carlo simulations for kinetic energy bins between 100 MeV and 550 MeV. The horizontal black line at the bottom of each distribution indicates the 68.3% highest density interval (numerical labels are rounded to 3 significant figures). 137

C.6 Distributions of $\sigma_{\text{total}}^{\pi/e}$ generated from Monte Carlo simulations for kinetic energy bins between 550 MeV and 1000 MeV. The horizontal black line at the bottom of each distribution indicates the 68.3% highest density interval (numerical labels are rounded to 3 significant figures). 138

C.7 Distributions of $\sigma_{\text{total}}^{\text{energy}}$ generated from Monte Carlo simulations for kinetic energy bins between 100 MeV and 550 MeV. The horizontal black line at the bottom of each distribution indicates the 68.3% highest density interval (numerical labels are rounded to 3 significant figures). 139

C.8 Distributions of $\sigma_{\text{total}}^{\text{energy}}$ generated from Monte Carlo simulations for kinetic energy bins between 550 MeV and 1000 MeV. The horizontal black line at the bottom of each distribution indicates the 68.3% highest density interval (numerical labels are rounded to 3 significant figures). 140

D.1 Illustration of a pion single-charge-exchange event within the LArIAT TPC. The nucleon from the pion charge-exchange reaction can knock other nucleons out of the target nucleus via final-state interactions. 142

D.2 Pion SCX candidate event. Raw event display is shown at the top; event display with reconstructed hits is shown at the bottom. Reconstructed hits with the same color belong in the same cluster (black excluded). 143

D.3 Pion SCX candidate event with a pile-up particle. Raw event display is shown at the top; event display with reconstructed hits is shown at the bottom. Reconstructed hits with the same color belong in the same cluster (black excluded). . 144

D.4 Examples of the overlap coefficient. ADC is plotted along the vertical axis, and time is plotted along the horizontal axis. 145

D.5 Illustration of the distance of closest approach to vertex. 146

D.6 Distributions of the distance of closest approach to vertex (top), cosine w.r.t. the z axis (bottom left), and $\mathrm{d}E/\mathrm{d}x$ (bottom right). 147

D.7 Distributions of EM shower cosine w.r.t. the z axis (bottom left) and $\frac{\mathrm{d}E}{\mathrm{d}x}$ (bottom right) after a cut is applied to reject EM showers with DCA > 5 cm (top). . . . 148

List of Tables

2.1 Select properties of liquid argon (LAr) and liquid xenon (LXe). Values taken from [29–35]. 10

3.1 Select list of trigger inputs to the CAEN V1495. 45

5.1 Event selection table for the Run-II −100 A dataset. 59

5.2 Parameters from the template fit. 70

5.3 Fractional content of WC/TPC-matched particles in the −60 A and −100 A data-driven Monte Carlo samples before and after re-weighting. Muons are subcategorized based on their source. 70

5.4 Fractional content of WC/TPC-matched particles in the −60 A and −100 A data-driven Monte Carlo samples before and after re-weighting. All muons are combined into a single fraction regardless of their source. 72

5.5 Physical constants for computing $n\langle\Delta x\rangle$. Values taken from [29, 79–81]. 77

5.6 Value of σ_{total} for each kinetic energy bin. 112

Acknowledgments

First and foremost, I would like to thank my thesis advisor, David Schmitz. Thank you for giving me the creative freedom I needed, for supporting my ideas no matter how bizarre they were, and for believing in me even when I didn't believe in myself. Your guidance and support over the years have been resounding. I cannot express my gratitude enough for the opportunities and confidence you have given me to succeed as a physicist. I would also like to extend my gratitude to my thesis committee—David Miller, Luca Grandi, and David Kutasov—for serving on my committee, and for making themselves available, especially during these trying times.

To Jen Raaf, Jonathan Asaadi, and Flavio Cavanna, you have all made the LArIAT collaboration a supportive and welcoming place. Thank you for allowing me to fiddle with nearly every part of the experiment, and for trusting me to not destroy all of it. Andrzej Szelc, thank you for getting me involved in the hardware and DAQ projects in LArIAT. I'll never forget the time you jump-started the Chicago car, minutes after reading about how to do it on Yahoo! Answers. Jason St. John, it was a pleasure working with you on basically everything in this wonderful experiment. You never faltered as Run Coordinator even when things were continually breaking, *and* you put up with my constant barrage of jokes—this is what great leadership is. To Bill Badgett, Roberto Acciarri, Raquel Castillo Fernández, Paweł Kryczyński, Elena Gramellini, Irene Nutini, Greg Pulliam, and the rest of the LArIAT collaborators, you have all made this a unique and fulfilling experience.

I've been fortunate to work with some of the most amazing people at Chicago. William Foreman, you've been a great friend and labmate ever since we started graduate school together. Our conversations during the commute to and from Fermilab were always wonderful. To the postdocs, Joseph Zennamo and Andy Mastbaum, thank you for being so supportive. To

Anthony LaTorre, thank you for always indulging my half-baked ideas. You've been a great colleague and an even greater friend. It was always fun when we got together with Albert Ryou, Mengfei He, Pavel Motloch, and Kevin Labe for our weekly dinners and occasional board game nights.

To my roommates over the years: Albert, I enjoyed political banter with you and seeing how you react to my jokes; Ntompizani Sunga, I enjoyed talking about music and watching terrible films with you—thank you for being critical of my jokes and puns, and for giving me feedback on the simplest grammar, even for this thesis; Kevin Sun, it was fun discussing politics and class blindness with you; Rodrigo Valdés Ortiz, it was amusing listening to your attempts to apply pseudo-statistical models to the most mundane things; and Carol Medina, it was great talking with you about pop culture.

Finally, I want to thank my mom and my sister for their unconditional love, and unwavering support and encouragement.

Abstract

The liquid argon time projection chamber (LArTPC) technology offers fine-grained tracking along with excellent calorimetric and particle identification capabilities, making it a powerful tool for experimental neutrino physics. Thus, the LArTPC has become the technology of choice for studying neutrino oscillations over short (< 1 km) and long (> 1000 km) baselines by experiments such as MicroBooNE, SBND, ICARUS, and DUNE. The LArIAT (Liquid Argon in a Test-beam) experiment exposes a LArTPC to a controlled beam of charged particles at the Fermilab Test Beam Facility to perform calibration studies and measurements of charged hadron–argon cross sections, with the goal of helping to reduce systematic uncertainties in LArTPC-based neutrino experiments. This work presents a measurement of the total hadronic π^-–Ar cross section in the kinetic energy range from 0.2 GeV to 1 GeV, using data from the LArIAT experiment.

Chapter 1

Introduction

> "Begin at the beginning," the King said gravely, "and go on till you come to the end: then stop."
>
> Lewis Carroll
>
> *Alice in Wonderland*

The neutrino is a marvelous particle. From its inception as the solution to the apparent energy non-conservation in nuclear beta decay to its ultra-high-energy signature of extra-galactic origin, the neutrino has been the thread tying together nuclear physics, particle physics, astrophysics, and cosmology. Substantial progress has been made over the past few decades in understanding the neutrino. It has been observed through measurements of solar, atmospheric, accelerator, and reactor neutrinos that neutrinos oscillate [1–8], and therefore mix and have mass. The discovery of the oscillation, mixing, and non-zero masses of neutrinos brought forth an extension of the Standard Model and numerous precision measurements of the properties of the neutrino. Additionally, neutrinos from extra-solar sources have been observed; in particular, experiments have detected low-energy neutrinos from SN 1987A [9, 10], a Type II supernova, and high-energy neutrinos from TXS 0506+056 [11, 12], a very high energy blazar.

Despite all that has been discovered about neutrinos, many open questions still remain. What is the absolute mass scale of the neutrinos? Could CP violation in neutrino oscillations and leptogenesis help to explain the baryon asymmetry of the universe? Is the neutrino its own

anti-particle? Are there sterile neutrino states beyond the three active neutrinos? The comprehensive accelerator-based neutrino program at Fermilab seeks to address many of these questions through the use of liquid argon time projection chamber (LArTPC) technology in short- and long-baseline experiments.

The LArTPC technique enables the use of liquid argon as both a nuclear target and a detection medium, and, as a relatively new detector technology, can benefit from studies and calibration that would reduce systematic uncertainties on the measurements of neutrino interactions. Hadrons are commonly produced in neutrino–nucleus interactions in the few-GeV energy region, and one significant source of systematic uncertainty in LArTPC-based neutrino experiments is the generally unknown dynamics of hadron–nucleon interactions within argon nuclei; there is also uncertainty in hadron–argon interactions that occur outside of the target nucleus as hadrons propagate through the liquid argon detection medium. Using a controlled beam of charged particles at Fermilab, the LArIAT (Liquid Argon in a Testbeam) experiment has taken data of charged-particle interactions in a LArTPC to perform measurements of charged hadron–argon cross sections. These measurements will enable data-driven improvements to nuclear models used in the simulation of neutrino–nucleon scattering in neutrino event generators and the simulation of hadron–argon scattering in the detection medium, which will help constrain systematic uncertainties in measurements of neutrino oscillations in LArTPC-based neutrino experiments.

This thesis presents a measurement of the total hadronic negative pion on argon cross section in the kinetic energy range from 0.2 GeV to 1 GeV, using data from the LArIAT experiment. Chapter 2 discusses the usage of LArTPC technology for neutrino detection. The working principle of the LArTPC is described, along with neutrino and pion interactions in liquid argon. The LArIAT experiment is described in Chapter 3. The scientific goals are outlined, and descriptions of the experiment's particle beam and sub-systems are given. Chapter 4 de-

scribes the data-driven methods used in producing Monte Carlo simulations for the analysis. The analysis methods and results of the measurement are described in detail in Chapter 5. Finally, concluding remarks are made in Chapter 6.

Chapter 2

Detecting Neutrinos in Liquid Argon

> I have done something very bad today by proposing a particle that cannot be detected; it is something no theorist should ever do.
>
> Wolfgang Pauli, 1930

The liquid argon time projection chamber (LArTPC) technology offers fine-grained tracking along with excellent calorimetric and particle identification capabilities, making it a powerful tool for experimental neutrino physics. Thus, the LArTPC has become the technology of choice for studying neutrino oscillations over short (< 1 km) and long (> 1000 km) baselines by experiments such as MicroBooNE, SBND, ICARUS, and DUNE [13–21].

In this chapter, we first describe the working principle of the LArTPC and why liquid argon is chosen over other liquid noble gases. We then discuss neutrino and pion interactions in liquid argon, and motivate the need for pion–argon scattering data to help reduce systematic uncertainties in neutrino–argon measurements.

2.1 The Liquid Argon Time Projection Chamber

The time projection chamber (TPC) was invented by David Robert Nygren at Lawrence Berkeley National Laboratory in the 1970s [22, 23]. The TPC was first used in the PEP-4

detector to study electron–positron annihilations at center-of-mass energies up to 29 GeV, as part of the Positron–Electron Project (PEP) at the Stanford Linear Accelerator Laboratory [24]. The detection volumes of TPCs were typically filled with noble gases where argon was often the primary choice [25]. The idea of using liquid argon as a detection medium in ionization chambers was first proposed in 1974 by W. J. Willis and V. Redeka [26], and, in 1977, Carlo Rubbia devised the concept of the liquid argon time projection chamber (LArTPC) [27].

2.1.1 Working principle

A LArTPC consists of two parallel conducting planes, an anode plane and a cathode plane, separated by a gap and submerged in liquid argon [28]. The anode is connected to ground or may be biased to a slightly positive voltage. The cathode is biased to a high negative voltage in order to create an electric field in the region between the two parallel planes. Field-shaping electrodes are placed between the anode and the cathode to ensure uniformity of the electric field across the active detector volume; the electrodes are equally spaced, and their voltages are properly biased with respect to one another. The anode plane is sub-divided into several planes with an interplanar spacing on the order of a few millimeters, each with parallel wires oriented at different angles, where detector signals are formed and read out. Additionally, the bias voltages for the anode wire planes are chosen such that the electric field satisfies the charge transparency condition in the drift regions near and in between the different anode wire planes—i.e., all the drifting electrons are transported through the intermediate wire planes (induction planes), and then collected on the last wire plane (collection plane).

As illustrated in Fig. 2.1, a charged particle propagating through the LArTPC ionizes argon atoms to create Ar^+ and e^- pairs. Argon atoms may also be raised to an excited state, instead of being ionized, and emit scintillation light in the vacuum ultraviolet (VUV) region

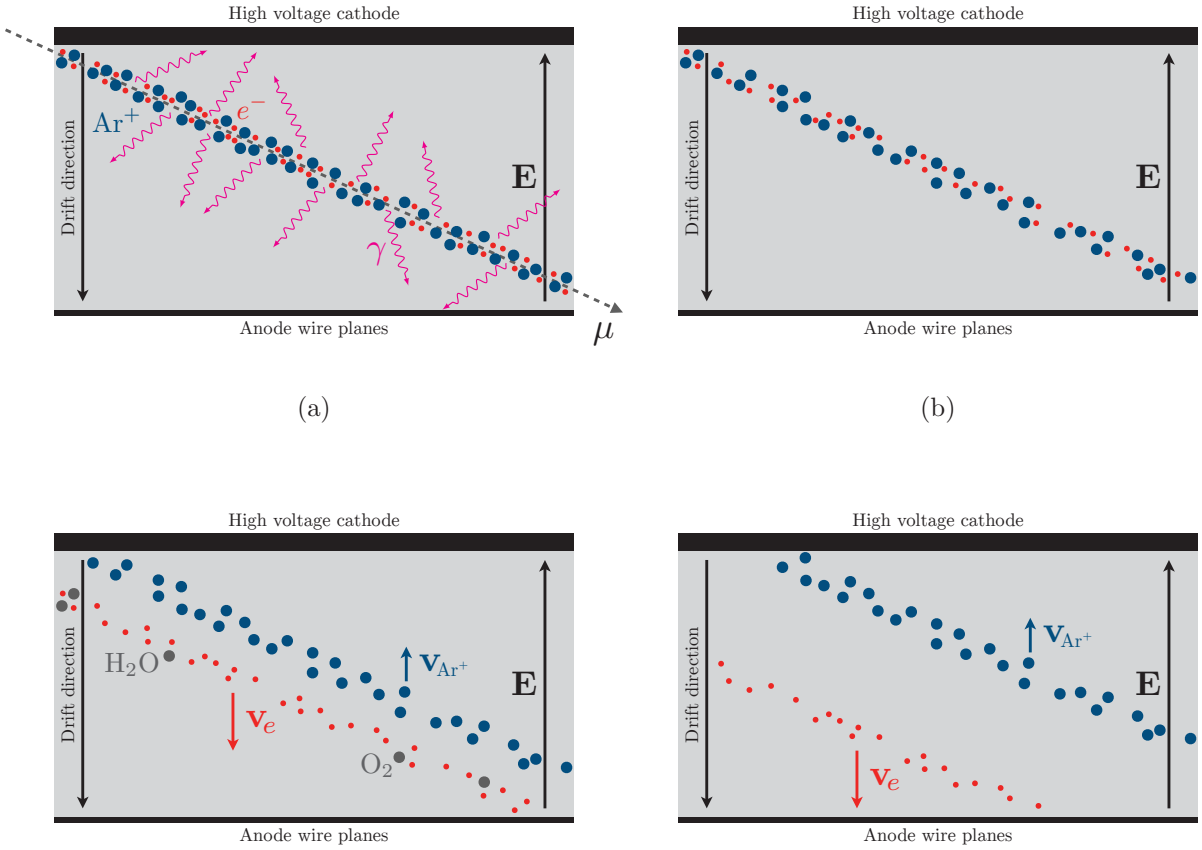

Figure 2.1: The working principle of a LArTPC. (a) A muon passes through the liquid argon detector medium and produces an ionization track of Ar^+ and e^- pairs, and induces the emission of VUV scintillation light. (b) A fraction of the Ar^+ and e^- pairs recombine to emit additional scintillation light; the remaining pairs are separated by the electric field. (c) The Ar^+ ions drift towards the high voltage cathode, and the electrons drift towards the anode wire planes; drifting electrons may attach to electronegative impurities, diminishing signal integrity. (d) The drifting electrons produce signals at the anode wire planes, which are amplified and read out.

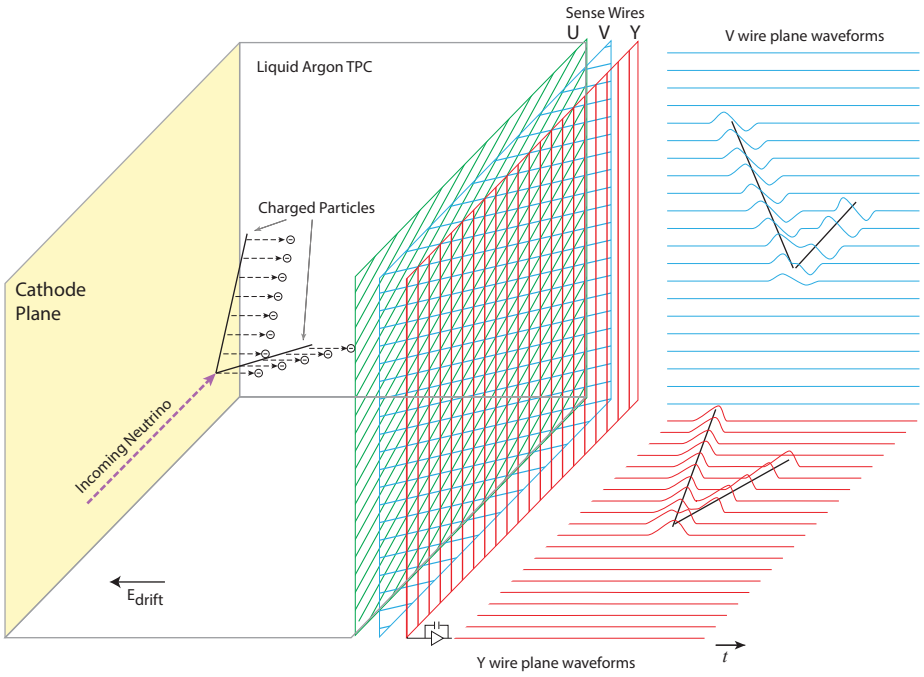

Figure 2.2: Illustration of charged particles emerging from a neutrino interaction vertex and producing ionization tracks. Waveforms of signals read out from the wires are processed through a chain of algorithms to reconstruct the 3D trajectories of the charged particles and the energy that they deposited. Figure taken from Ref. [14].

during its de-excitation. A fraction of the Ar^+ and e^- pairs recombine to emit additional scintillation light; this fraction is dependent on the magnitude of the electric field. As argon is transparent to its own VUV scintillation light, photodetectors may be used to detect this light; the detected light may be used as a trigger, to mark as the start of an event, or to augment calorimetric reconstruction. After the recombination process, the remaining Ar^+ ions and electrons are separated by the electric field and drift towards the cathode and anode, respectively. When the drifting electrons reach the anode wire planes, signals are produced, amplified electronically, and read out. During their drift, electrons may attach to electronegative impurities, such as water and oxygen molecules, dissolved in the liquid argon;

this reduces the amount of charge reaching the anode, thus diminishing the signals produced in the anode wires. The measured signals on the segmented anode wire planes combined with the measured arrival times of the drift electrons enable both calorimetric reconstruction and full 3D reconstruction of the ionization track. Fig. 2.2 illustrates the waveforms of the signals read out from the wires of different anode planes. Examples of neutrino interactions in a LArTPC are shown in Fig. 2.3.

2.1.2 The case for liquid argon

Using a liquid noble gas (LNG) as a neutrino target and a detection medium is advantageous for several reasons. First, a LNG provides a dense target to enhance the neutrino interaction rate of an already small neutrino interaction cross section. Second, because of its high density, a LNG provides a high stopping power for ionizing radiation, resulting in a high energy loss per unit distance $\left(\frac{\mathrm{d}E}{\mathrm{d}x}\right)$ within the detection medium; this enhances the calorimetric capability of the detector. In addition to its high ionization yield, a LNG also has a high scintillation light yield whilst being transparent to its own scintillation light. Select properties of liquid argon (LAr) and liquid xenon (LXe) are shown in Table 2.1. LXe would be a more desirable LNG due to its superior properties compared to LAr*, however, the relative abundance and low cost of LAr make it a far more viable option for the construction of ton- and kiloton-scale neutrino detectors, such as SBND and the DUNE far detector.

*The 14.00 cm radiation length in LAr is arguably better than the 2.872 cm radiation length in LXe—a gamma ray would travel a longer distance in LAr before inducing an electromagnetic shower. This is particularly important for distinguishing between electron- and gamma-induced electromagnetic showers.

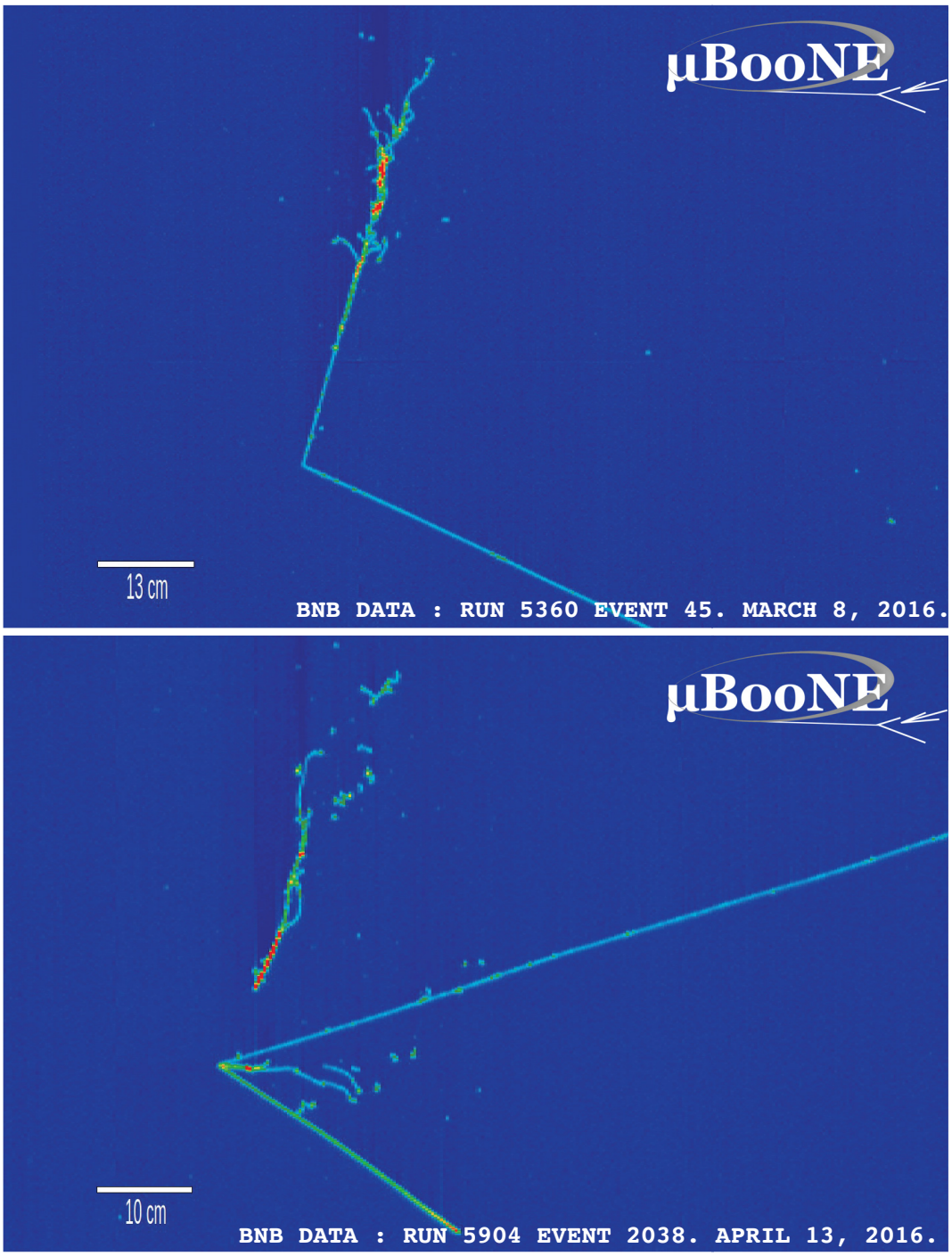

Figure 2.3: Event displays of neutrino interactions with electromagnetic activity in the MicroBooNE LArTPC detector. Time is plotted along the vertical axis, and wire number is plotted along the horizontal axis. The neutrino beam is incident from the left. The top shows a ν_e candidate event with an electron-induced eletromagnetic shower, while the bottom shows a ν_μ candidate event with gamma-induced electromagnetic showers.

Quantity	Value	
	LAr	LXe
atomic number	18	54
atomic weight	39.948(1) u	131.293(6) u
normal boiling point	87.30 K	165.1 K
density	$1.396\ \mathrm{g \cdot cm^{-3}}$	$2.953\ \mathrm{g \cdot cm^{-3}}$
nuclear collision length	54.25 cm	34.15 cm
nuclear interaction length	85.77 cm	58.29 cm
pion collision length	72.58 cm	42.31 cm
pion interaction length	106.7 cm	67.58 cm
radiation length	14.00 cm	2.872 cm
Molière radius	9.043 cm	5.224 cm
work function	23.6 eV	15.6 eV
electron mobility ($\lvert\mathbf{E}\rvert = 10^4\ \mathrm{V \cdot m^{-1}}$)	$0.047\ \mathrm{m^2 \cdot V^{-1} \cdot s^{-1}}$	$0.22\ \mathrm{m^2 \cdot V^{-1} \cdot s^{-1}}$
minimum ionization, $\langle \mathrm{d}E/\mathrm{d}x \rangle$	$2.105\ \mathrm{MeV \cdot cm^{-1}}$	$3.707\ \mathrm{MeV \cdot cm^{-1}}$
scintillation light yield	$40\,000\ \gamma \cdot \mathrm{MeV^{-1}}$	$42\,000\ \gamma \cdot \mathrm{MeV^{-1}}$
scintillation light emission peak	128 nm	178 nm
atmospheric abundance by volume (gas)	0.934%	0.000 008 7%
cost	$\approx \$0.002\ \mathrm{g^{-1}}$	$\approx \$1.5\ \mathrm{g^{-1}}$

Table 2.1: Select properties of liquid argon (LAr) and liquid xenon (LXe). Values taken from [29–35].

2.2 Neutrino Interactions in Liquid Argon

Neutrinos can interact with nucleons via the weak force, so the detection of neutrinos must consist of a dense nuclear target, such as liquid argon. Because neutrinos are electrically neutral, neutrino experiments seeking to make measurements of the neutrino must use the products of a neutrino interaction in order to (1) determine that there indeed was a neutrino, (2) determine the flavor of the neutrino and the interaction type, and (3) determine the energy of the neutrino.

Neutrino interactions within nuclei in the intermediate energy range, from about 0.1 GeV to 20 GeV, fall under three main categories, ordered by increasing neutrino energy: quasi-

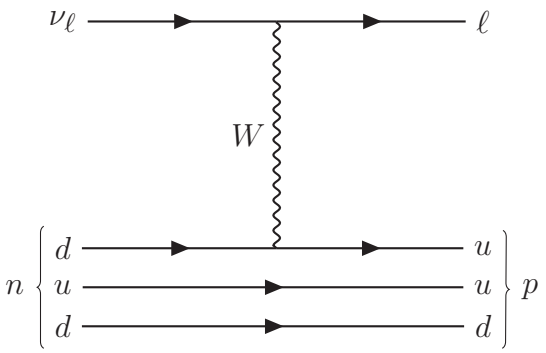

(a) Charged-current quasi-elastic (CCQE)

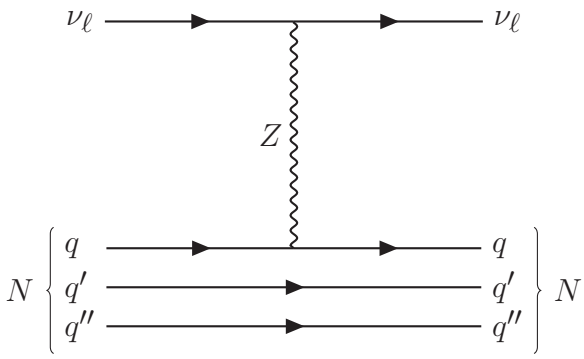

(b) Neutral-current quasi-elastic (NCQE)

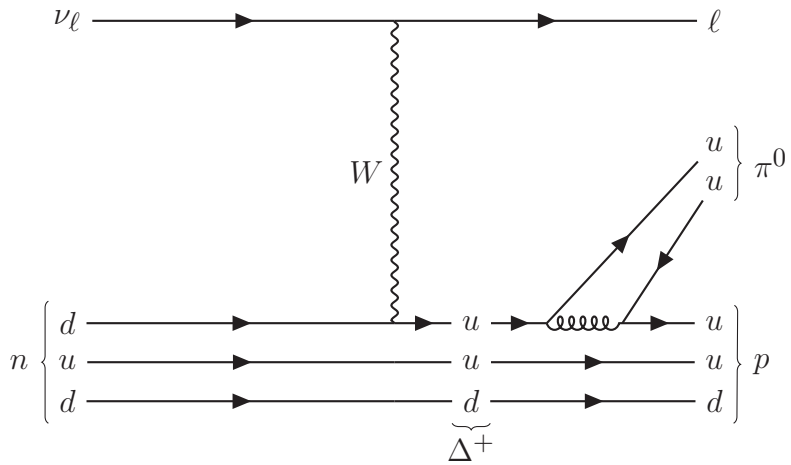

(c) Resonant (RES) pion production

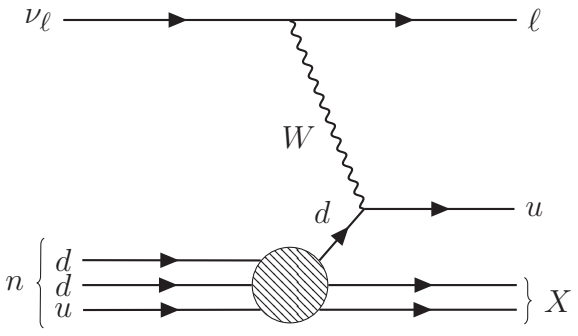

(d) Charged-current deep inelastic scattering (CCDIS)

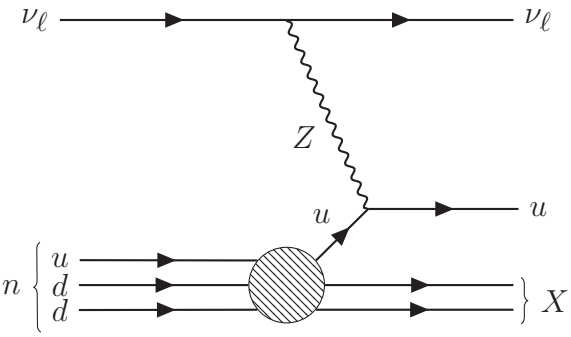

(e) Neutral-current deep inelastic scattering (NCDIS)

Figure 2.4: Example Feynman diagrams of several neutrino–nucleon interaction modes.

elastic scattering, resonance production, and deep inelastic scattering. In quasi-elastic (QE) scattering, a neutrino elastically scatters off a nucleon, resulting in one or more nucleons being ejected from the target nucleus. The QE scattering can be a charged-current quasi-elastic (CCQE) process (Fig. 2.4a)

$$\nu_\ell + n \to \ell + p, \qquad \bar{\nu}_\ell + p \to \bar{\ell} + n, \tag{2.1}$$

or a neutral-current quasi-elastic (NCQE) process (Fig. 2.4b)

$$\nu_\ell + p \to \nu_\ell + p, \qquad \bar{\nu}_\ell + p \to \bar{\nu}_\ell + p, \tag{2.2}$$

$$\nu_\ell + n \to \nu_\ell + n, \qquad \bar{\nu}_\ell + n \to \bar{\nu}_\ell + n. \tag{2.3}$$

In resonant (RES) scattering, a neutrino inelastically scatters off a nucleon and excites the nucleon into a baryonic resonance state (Δ, N^*), which subsequently decays, often into a final state of one pion and one nucleon (Fig. 2.4c)

$$\begin{aligned} \nu_\ell + N &\to \ell + \Delta \\ \Delta &\to \pi + N', \end{aligned} \tag{2.4}$$

$$\begin{aligned} \nu_\ell + N &\to \ell + N^* \\ N^* &\to \pi + N'. \end{aligned} \tag{2.5}$$

In deep inelastic scattering (DIS), a high-energy neutrino ($E_\nu \gg m_N$ in the laboratory frame) scatters off a quark in the nucleon, producing a lepton and a hadronic shower in the final state (Figs. 2.4d and 2.4e)

$$\nu_\ell + N \to \ell + X, \qquad \bar{\nu}_\ell + N \to \bar{\ell} + X, \tag{2.6}$$

$$\nu_\ell + N \to \nu_\ell + X, \qquad \bar{\nu}_\ell + N \to \bar{\nu}_\ell + X. \tag{2.7}$$

As shown in Fig. 2.5 for charged-current interactions, all three of these processes compete with one another, especially in the few-GeV energy domain.

Although theoretical frameworks of quasi-elastic scattering, resonance production, and deep inelastic scattering have been formulated, there is no unifying theory that describes the transition between these processes. And in practice, neutrinos are scattered off the nucleus of atoms, such as carbon, oxygen, or argon, thus nuclear effects can have significant impact on neutrino measurements. Final-state particles produced at the neutrino interaction vertex within a nucleus must propagate through the dense nuclear medium before observation in a detector. In particular, because final-state hadrons can interact via the strong force, there is a significant probability of final-state interactions (FSIs). FSIs affect what is observed in a detector and can conceal the true neutrino interaction that took place at the vertex. An example of this is depicted in Fig. 2.6. A ν_μ CCQE interaction where the p is ejected from the nucleus without FSI is illustrated in the top half of the figure; the final observables in the detector are a μ and a p. A ν_μ CC1π^+ interaction is illustrated in the bottom half of the figure, where the final-state π^+ is absorbed through a two-body pion absorption process, producing a n and a p which are both ejected from the nucleus; the final observables in the detector are a μ and a p, as the two n are undetected. Since the final observables in both cases are the same, the ν_μ CC1π^+ interaction may be mis-identified as a ν_μ CCQE interaction, and can contaminate a CCQE measurement.

The generally unknown dynamics of hadron–nucleon interactions within nuclei coupled with the lack of a theory to unify the quasi-elastic scattering, resonance production, and deep inelastic scattering processes present a significant source of systematic uncertainty in the measurements of neutrino–nucleus interactions in the few-GeV region. In order to reduce the systematic uncertainty, an accurate FSI model must be implemented in Monte Carlo neutrino event generators, such as GENIE [37]. Neutrino and non-neutrino data are used

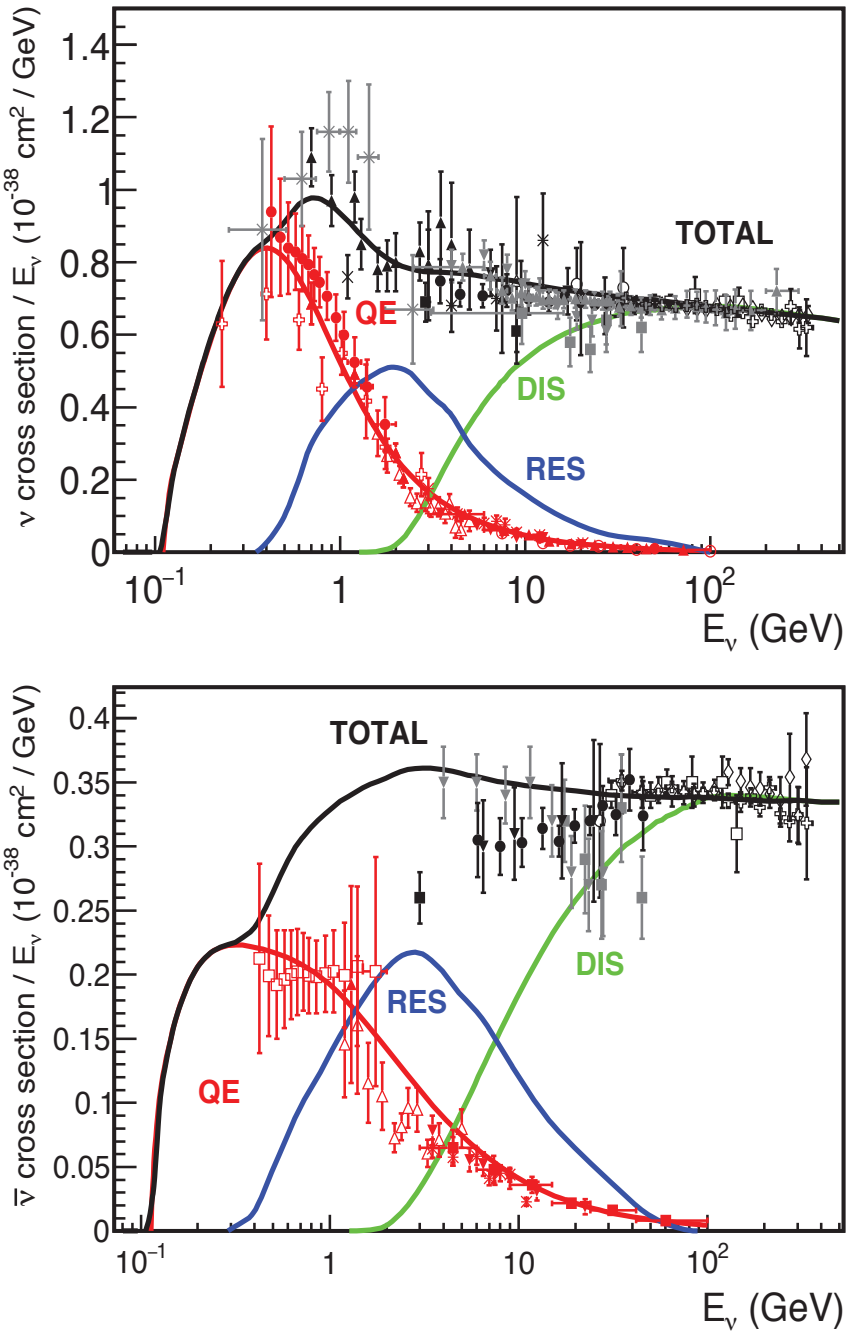

Figure 2.5: Total neutrino (top) and anti-neutrino (bottom) charged-current cross sections (for an isoscalar target) divided by neutrino energy plotted as a function of energy [36]. Predictions for the quasi-elastic (QE), resonant (RES), and deep inelastic scattering (DIS) processes are provided by the NUANCE neutrino simulation software. Updated from Ref. [36] by A. Schukraft and G. Zeller.

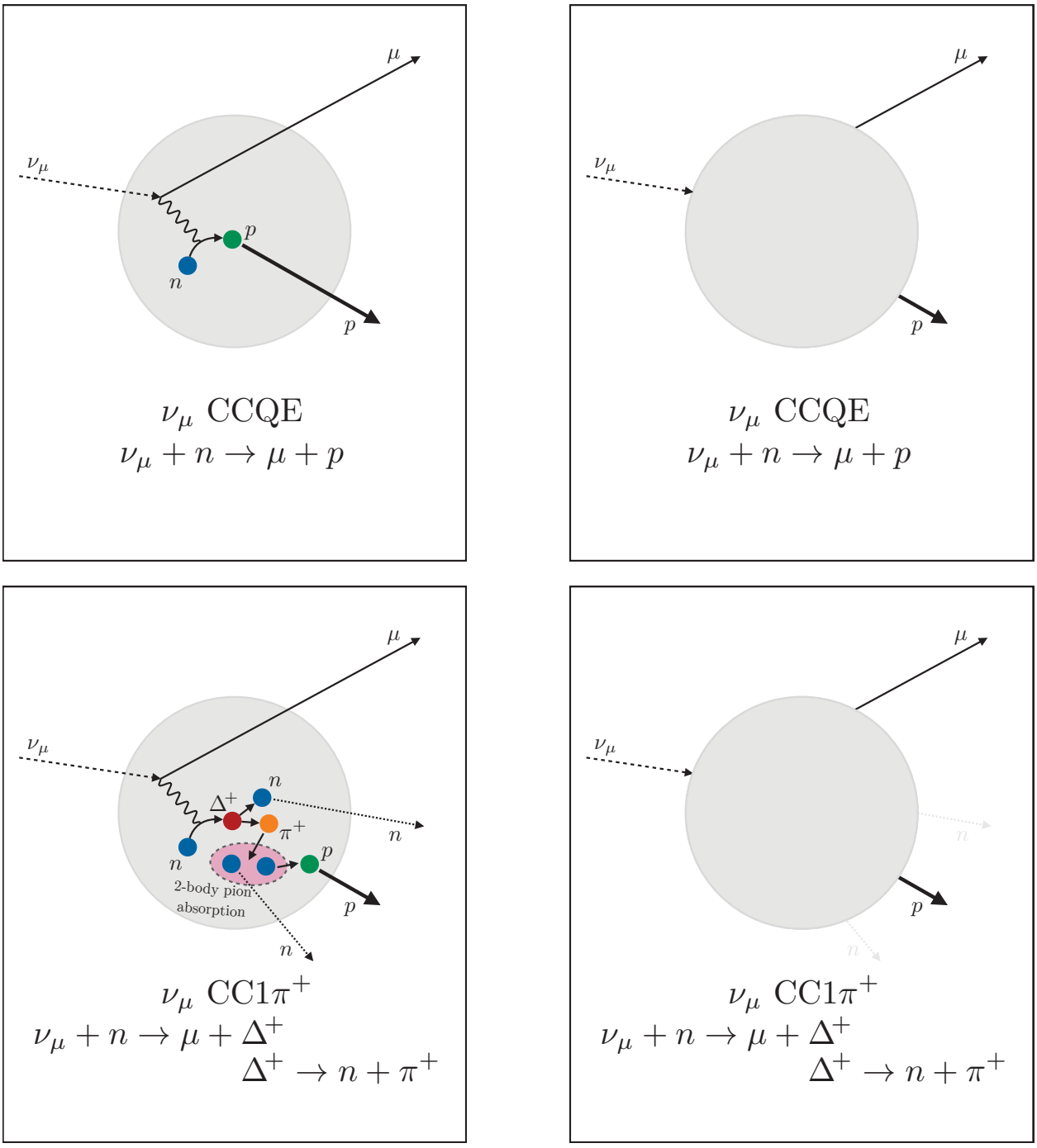

Figure 2.6: Illustration of a ν_μ CCQE interaction (top) and a ν_μ CC1π^+ interaction (bottom). The panels on the left show details of possible final-state interactions that may occur within a target nucleus; the panels on the right show that the final observables in the detector may be the same. The trajectories of ionizing particles are depicted with solid lines; the trajectories of non-ionizing particles are depicted with broken lines. In this example of a CC1π^+ interaction, the final-state π^+ is absorbed through a two-body pion absorption process, producing a p and a n.

to tune these event generators, and, given that the LArTPC is a relatively new detector technology, neutrino–argon and hadron–argon data from current and near-future LArTPC-based experiments will be invaluable. The LArIAT experiment is one of the few LArTPC-based experiments that will be able to provide hadron–argon data.

2.3 Charged Pion Interactions in Liquid Argon

Neutrino–nucleus interactions in the few-GeV energy region produce copious numbers of charged pions, especially in resonance production, deep inelastic scattering, and coherent pion production. As suggested in the previous section, the dynamics of pion–nucleon interactions within argon nuclei are generally unknown and are a significant source of systematic uncertainty in LArTPC-based neutrino experiments. There is also uncertainty in pion–argon interactions that occur outside of the target nucleus as pions propagate through the liquid argon detection medium of a LArTPC. Thus, it is important to get a good understanding of pion–argon interactions in order to model the behavior of the pion (1) inside the target nucleus, and (2) during its propagation through the detection medium.

Pions that propagate through the liquid argon detection medium can interact through one of several channels:

- **Elastic scattering** occurs when the outgoing charged pion leaves the nucleus in its ground state:

$$\pi^{\pm} + N \rightarrow \pi^{\pm} + N \tag{2.8}$$

- **Inelastic scattering** occurs when the outgoing charged pion leaves the nucleus in an

excited state:

$$\begin{aligned} \pi^- + p &\rightarrow \Delta^0 \\ \Delta^0 &\rightarrow \pi^- + p \end{aligned} \tag{2.9}$$

$$\begin{aligned} \pi^- + n &\rightarrow \Delta^- \\ \Delta^- &\rightarrow \pi^- + n \end{aligned} \tag{2.10}$$

$$\begin{aligned} \pi^+ + n &\rightarrow \Delta^+ \\ \Delta^+ &\rightarrow \pi^+ + n \end{aligned} \tag{2.11}$$

$$\begin{aligned} \pi^+ + p &\rightarrow \Delta^{++} \\ \Delta^{++} &\rightarrow \pi^+ + p \end{aligned} \tag{2.12}$$

- **Single charge exchange** occurs when a neutral pion is produced in the final state:

$$\begin{aligned} \pi^- + p &\rightarrow \Delta^0 \\ \Delta^0 &\rightarrow \pi^0 + n \end{aligned} \tag{2.13}$$

$$\begin{aligned} \pi^+ + n &\rightarrow \Delta^+ \\ \Delta^+ &\rightarrow \pi^0 + p \end{aligned} \tag{2.14}$$

- **Double charge exchange** occurs when the final state consists of the oppositely charged pion:

$$\pi^{\mp} + N \rightarrow \pi^{\pm} + X \tag{2.15}$$

- **Pion production** occurs when there are multiple pions in the final state (the kinetic energy of the initial charged pion must be greater than approximately 400 MeV):

$$\pi^{\pm} + N \rightarrow i\pi + X \tag{2.16}$$

where $i \geq 2$ and π denotes any set of final π mesons—e.g., $\pi^- + p \rightarrow \pi^- + \pi^+ + \pi^- + p$.

- **Absorption** occurs when there is no pion in the final state:

$$\pi^- + (np) \rightarrow n + n \tag{2.17}$$

$$\pi^- + (nnp) \rightarrow n + n + n \tag{2.18}$$

$$\pi^- + (npp) \rightarrow n + n + p \tag{2.19}$$

$$\pi^+ + (nn) \rightarrow n + p \tag{2.20}$$

$$\pi^+ + (nnn) \rightarrow n + n + p \tag{2.21}$$

$$\pi^+ + (nnp) \rightarrow n + p + p \tag{2.22}$$

  This process is only possible on systems of two or more nucleons—i.e., two-body pion absorption, three-body pion absorption, etc.

Various pion–argon interaction events from the LArIAT experiment are shown in Fig. 2.7.

As the pion–argon interaction cross section is relatively large, a pion emerging from a neutrino interaction vertex can interact as it propagates through the liquid argon detection medium, changing the topology of the neutrino event. Fig. 2.8 shows a simulated neutrino event in the MicroBooNE LArTPC detector from a ν_μ CC Monte Carlo sample. In this simulated event, a charged pion emerging from the neutrino interaction vertex undergoes a charge exchange with an argon nucleus, producing a neutral pion. The neutral pion subsequently decays into two gammas, each of which produces an eletron–positron pair resulting in a gamma-induced electromagnetic shower. This particular ν_μ event has the possibility of being mis-identified as a ν_e event due the similar topologies that consist of electromagnetic activity. Thus, it is important for the detector simulation to estimate the cross section of pion–argon interactions accurately.

The total hadronic pion–argon interaction cross section can be written as a sum of the elastic

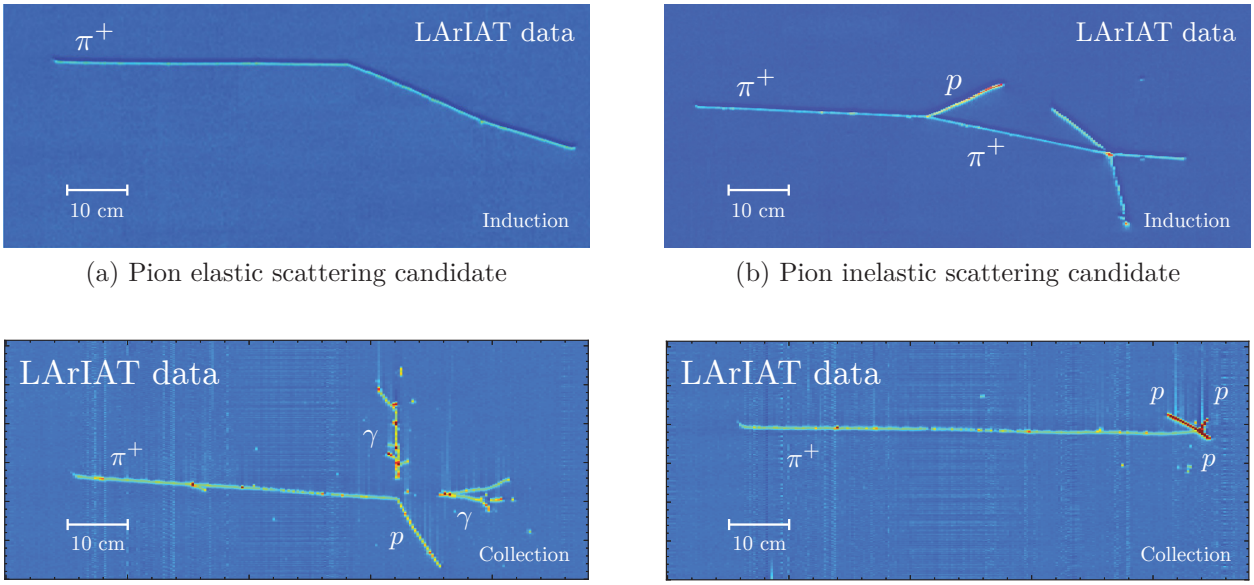

(a) Pion elastic scattering candidate

(b) Pion inelastic scattering candidate

(c) Pion single charge exchange candidate

(d) Pion absorption candidate

Figure 2.7: Various pion–argon interaction candidate events from the LArIAT experiment, with ionization tracks incident from the left. Time is plotted along the vertical axis, and wire number is plotted along the horizontal axis. The density of ionization charge is indicated by the color, with red being the most dense.

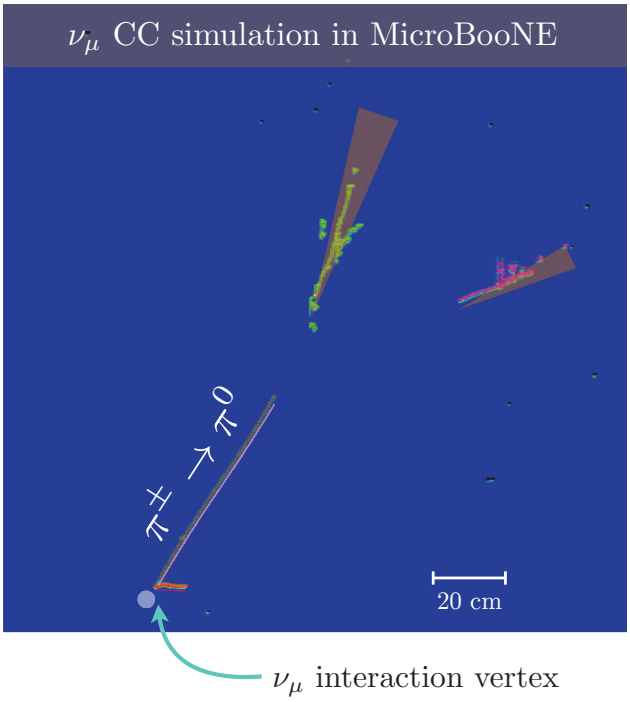

Figure 2.8: Simulated neutrino event in MicroBooNE.

and reactive cross sections

$$\sigma_{\text{total}} = \sigma_{\text{elastic}} + \sigma_{\text{reactive}} \tag{2.23}$$

where the reactive cross section includes the inelastic ($\sigma_{\text{inelastic}}$), single charge exchange (σ_{scx}), double charge exchange (σ_{dce}), pion production (σ_{prod}), and absorption (σ_{abs}) channels

$$\sigma_{\text{reactive}} = \sigma_{\text{inelastic}} + \sigma_{\text{scx}} + \sigma_{\text{dce}} + \sigma_{\text{prod}} + \sigma_{\text{abs}}. \tag{2.24}$$

Pion–nucleus scattering experiments have been performed over the past several decades and have provided detailed measurements of differential cross sections for various final-state kinematic quantities, however, the uncertainties on the total hadronic cross sections range from 10% to 30% for light nuclei and are even larger for heavy nuclei [38–45]. Historical data of pion scattering on various light and heavy nuclei are shown in Fig. 2.9. Despite the comprehensive pion scattering measurements that have been made, experimental data for pion–argon interactions are rare and Monte Carlo simulation software, such as GEANT4 [46–48], predict pion–argon cross sections by interpolating from data of lighter and heavier nuclei. The detector simulation used in LArTPC-based experiments at Fermilab utilizes the `FTFP_BERT` physics list in GEANT4, where the Bertini cascade model [49] is used to simulate the products of pion–nucleus interactions and secondary hadronic re-interactions (FSIs) within the target nucleus. Fig. 2.10 shows the elastic, reactive, and total $\pi^{\pm}$–Ar cross section as a function of $\pi^{\pm}$ kinetic energy as predicted by the GEANT4 Bertini intranuclear cascade model. The LArIAT experiment will perform measurements of various $\pi^{\pm}$–Ar interaction cross sections in order to enable data-driven improvements to the simulation of neutrino–nucleon scattering in neutrino event generators such as GENIE, and aid in the validation and tuning of nuclear models implemented in general-purpose Monte Carlo simulation software

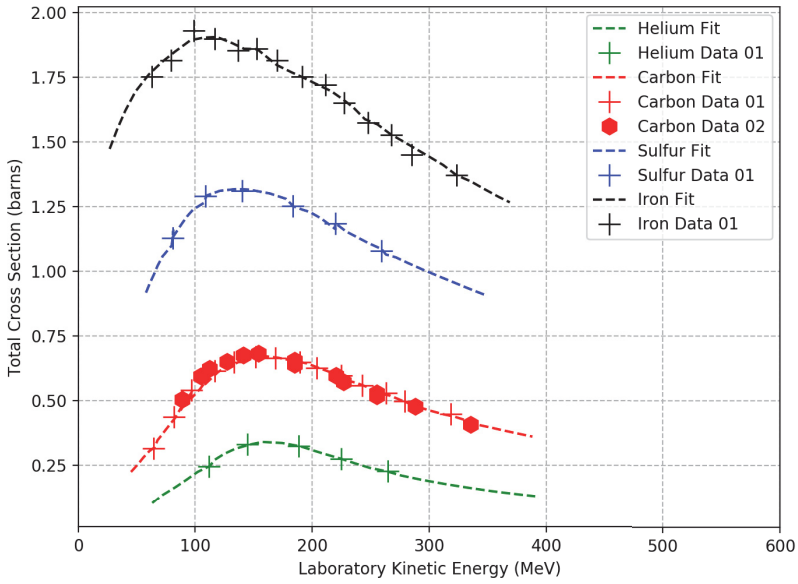

Figure 2.9: Historical data of pion scattering on different light and heavy nuclei. Taken from Ref. [42].

such as GEANT4.

This thesis presents a measurement of the total hadronic negative pion on argon cross section in the kinetic energy range from 0.2 GeV to 1 GeV, using data from the LArIAT experiment. The analysis methods described in this thesis also lay down the foundation for measurements of the exclusive channels, such as pion single-charge exchange* and pion absorption.

*A discussion of the ongoing work on the pion single-charge exchange channel is presented in Appendix D.

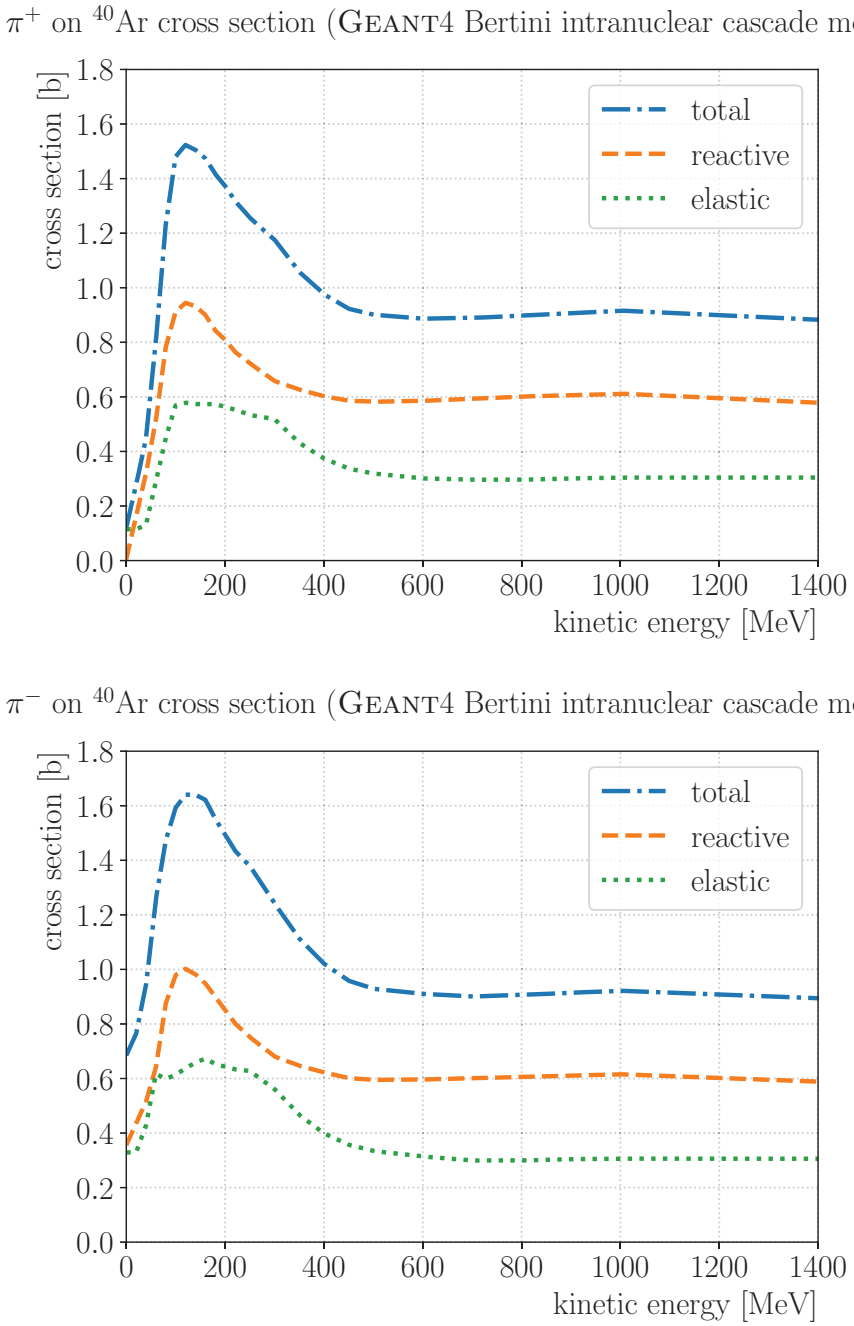

Figure 2.10: π^+–Ar cross section (top) and π^-–Ar cross section (bottom) as functions of kinetic energy as predicted by the GEANT4 Bertini intranuclear cascade model. The elastic, reactive, and total hadronic cross sections are plotted with dotted, dashed, and dash-dot lines, respectively.

Chapter 3

The LArIAT Experiment

> The word "lariat" is a contraction of the Spanish *la reata*, which literally means a "tie back." The term was originally used for a rope in picketin' horses. Some Eastern folks like to say "lariat" and "lasso" because it sounds Western, but the cowhand called his rope jes' plain "rope."
>
> Ramon Frederick Adams
> *The Old-Time Cowhand*

The LArIAT (Liquid Argon in a Test-beam) experiment [50, 51] operated at the Fermilab Test Beam Facility (FTBF) from 2015 to 2017 [52–54]. The experiment serves* a dual purpose. First, it is a research and development (R&D) tool for studying the calibration and detector response of liquid argon time projection chamber (LArTPC) technology. Second, it has the capabilities to study interactions of charged hadrons and leptons in liquid argon without additional uncertainties that emerge from nuclear effects in neutrino interactions.

The LArIAT tertiary beamline was commissioned in 2014 [55]; the beam engineering run took place from August 2014 to September 2014. Following the commissioning of the LArIAT

*Although the experiment has finished running, at the time of writing there is still ongoing work of physics analyses using the collected data.

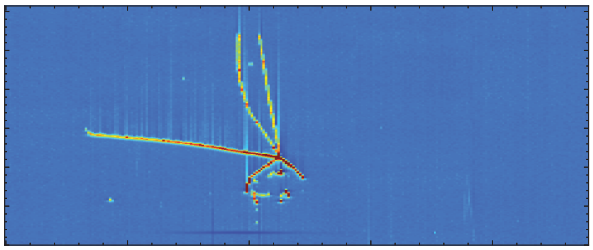

(a) Anti-proton annihilation candidate

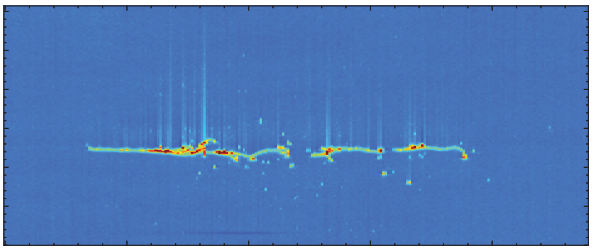

(b) Electron candidate

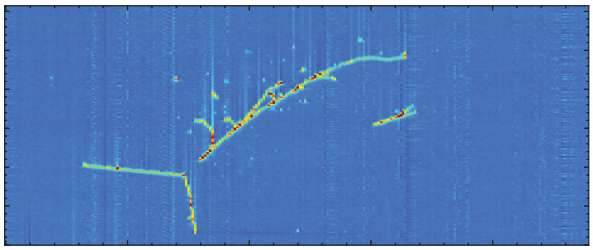

(c) Pion single-charge exchange candidate

Figure 3.1: Various candidate events from data, with ionization tracks incident from the left. Time is plotted along the vertical axis, and wire number is plotted along the horizontal axis. The density of ionization charge is indicated by the color, with red being the most dense.

cryogenic system and LArTPC in 2015, several data-taking campaigns were performed over the span of the experiment's lifetime. The first campaign, Run-I, took place from April 2015 until the annual summer shutdown of the Fermilab accelerator complex in July 2015. During the second campaign, Run-II, which started in February 2016, the experiment operated with important improvements to the wire readout and scintillation light collection systems which resulted in significant improvement to the quality of data collected. Run-II ultimately ended with the annual summer shutdown of the accelerator complex in July 2016. During Run-III in 2017, the experiment tested the use of wire planes with different wire pitches. The data from Run-II is the sole dataset that is presented in this thesis.

In this chapter, we first give a brief overview of the scientific goals of the experiment and then we describe the detector sub-systems that are relevant to the total hadronic π^-–Ar cross section analysis of this thesis.

3.1 Scientific Goals

The following is an outline of the scientific goals of the LArIAT experiment:

- **Charged pion on argon interactions**

  Neutrino–nucleus interactions in the few-GeV energy region produce copious numbers of charged pions. The dynamics of pion–nucleon interactions within argon nuclei are generally unknown and are a significant source of systematic uncertainty in LArTPC-based neutrino experiments. There is also uncertainty in pion–argon interactions that occur outside of the target nucleus as pions propagate through the liquid argon detection medium of a LArTPC. Extensive pion scattering experiments performed over the past 40 years have provided detailed measurements of differential cross sections for a number of final-state kinematic quantities, however, the uncertainties on the total hadronic cross sections range from 10% to 30% for light nuclei and are even larger for heavy nuclei [38–45]. Experimental data for pion–argon interactions, however, are sparse and Monte Carlo simulation software, such as GEANT4 [46–48], predict pion–argon cross sections by interpolating from data of lighter and heavier nuclei. LArIAT will perform measurements of various $\pi^{\pm}$–Ar interaction cross sections in order to enable data-driven improvements to the simulation of neutrino–nucleon scattering in neutrino event generators such as GENIE, and aid in the validation and tuning of nuclear models implemented in general-purpose Monte Carlo simulation software such as GEANT4.

- **Charged kaon on argon interactions**

  The identification and reconstruction of charged kaons is particularly important to proton decay searches in DUNE, especially the dominant decay mode $p \to K^{+}\bar{\nu}$ as predicted by supersymmetric grand unified theory models [56, 57]. LArIAT will utilize the small but significant fraction of charged kaons in its tertiary beam to perform

measurements of $K^{\pm}$–Ar interaction cross sections for the tuning of nuclear models in Monte Carlo simulation software packages.

- **Proton/anti-proton interactions in liquid argon**

  LArIAT collected a large sample of protons with its positive polarity beam and a small sample of anti-protons with its negative polarity beam. In addition to the measurement of p–Ar interaction cross sections, LArIAT is also well-suited to study $p\bar{p}$ annihilation in liquid argon. The results from these studies will be used to help tune and constrain the nuclear models of Monte Carlo simulation packages to be used in $n\bar{n}$ oscillation searches in DUNE. Fig. 3.1a shows an anti-proton annihilation event from the LArIAT dataset.

- **Electron-/gamma-induced electromagnetic shower discrimination**

  A charged-current (CC) ν_e neutrino interaction is identified by an electron-induced electromagnetic (EM) shower originating from the interaction vertex; the initial electron deposits its energy as it propagates away from the interaction vertex. A neutral-current (NC) neutrino interaction can produce a neutral pion which immediately decays into two gamma rays; a gamma ray can invisibly travel some distance away from the interaction vertex before converting into an electron–positron pair to induce an EM shower. The largest background to CC ν_e interactions comes from NC π^0 production in which only one EM shower is reconstructed. This can happen if both of the gamma-induced EM showers are close enough that they cannot be spatially separated, or if one of the gamma rays exits the detector before it can convert into an electron–positron pair. The fully active calorimetric volume of a LArTPC is capable of capturing the detailed information of interactions which can be used to help distinguish between electron- and gamma-induced EM showers. Gamma-induced EM showers are classified by identifying two distinct features in neutrino interaction events: (1) the spatial separation between the neutrino interaction vertex and the beginning of a gamma-induced EM

shower, and (2) the deposited ionization energy per unit length $\left(\frac{\mathrm{d}E}{\mathrm{d}x}\right)$ by an electron–positron pair at the beginning of a gamma-induced EM shower is twice that of a single electron at the beginning of an electron-induced EM shower. The ArgoNeuT collaboration has demonstrated the separation of electron- and gamma-induced EM showers in a LArTPC from a small sample of neutrino interaction events [58]. LArIAT has collected a large sample of events with electron-induced EM showers produced by the tertiary beam, and a large sample of events with gamma-induced EM showers from neutral pions produced from pion single-charge-exchange reactions. Fig. 3.1b shows an electron event from the LArIAT dataset; Pion single-charge exchange events from the LArIAT dataset are shown in Figs. 2.7c and 3.1c.

- **Scintillation light collection**

  The LArIAT collaboration implemented a scintillation light collection system adapted from designs found in LAr-based detectors for dark matter experiments [59–61]. The goal of the scintillation light collection system is to improve the calorimetric reconstruction of events by combining the use of collected scintillation light and measured ionization energy without having to rely on recombination models to account for the energy that would otherwise be lost to the production of scintillation light. The LArIAT collaboration demonstrated the calorimetric reconstruction of low-energy electrons by combining ionization charge and scintillation light using data from Run-I and Run-II [62].

3.2 Beamline Instrumentation

The goal of the Meson Center beamline systems at FTBF is to provide a well-understood, low-intensity beam of charged particles with momenta ranging from 0.3 GeV/c to 1.4 GeV/c. A primary beam of protons from the Main Injector (MI) is focused on a tungsten target,

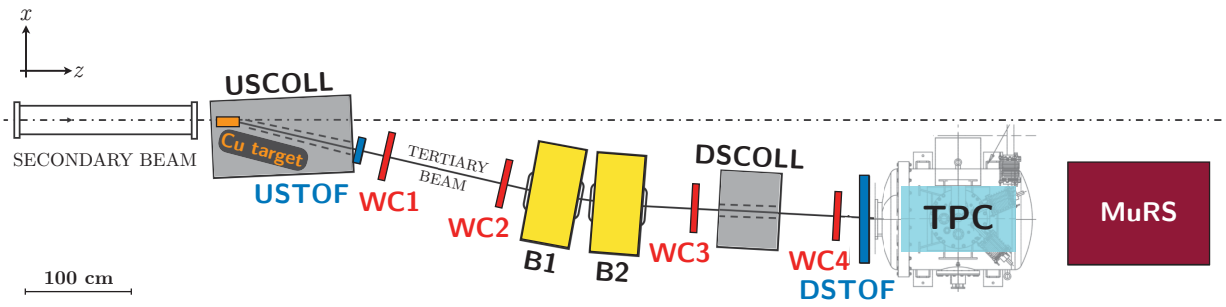

Figure 3.2: Top-down schematic of the tertiary beamline. Beam is incident from the left.

located at Meson Center 6 (MC6), producing a secondary beam of charged pions. The secondary beam is momentum-selected in the range 8 GeV/c to 80 GeV/c and transported ∼90 m downstream to the Meson Center 7 (MC7) enclosure, where it is focused on a copper target. The copper target, which is mounted and housed in a steel collimator, is the starting point of the tertiary beam and the LArIAT apparatus in the MC7 experimental hall.

In the top-down schematic of the tertiary beamline and LArIAT apparatus shown in Fig. 3.2, the secondary beam of charged pions is incident from the left. With the secondary beam focused on the copper target, a tertiary beam of charged particles is produced at the start of the upstream collimator (USCOLL). The tertiary beam exits the narrow opening of the upstream collimator at an angle of $-13°$ relative to the secondary beam, passing through the upstream time-of-flight (USTOF) detector and the magnetic spectrometer. The magnetic spectrometer consists of two multi-wire proportional chambers (WC1 and WC2), followed by two dipole bending magnets (B1 and B2), and another pair of wire chambers (WC3 and WC4); a second steel collimator (DSCOLL) sits in between WC3 and WC4. The beam then passes through the downstream time-of-flight (DSTOF) detector which sits just upstream of the TPC cryostat. Particles that pass all the way through the TPC may reach the muon range stack (MuRS) located just downstream of the cryostat. The beam is bent approximately $+10°$ by the magnetic spectrometer, resulting in a tertiary that beam enters the LArIAT

LArTPC detector at an angle of about -3° relative to the secondary beam.

The momentum of the secondary beam was fixed at 64 GeV/c for most of the data-taking campaigns. The tertiary beam was operated under the following four configurations to obtain the momentum spectra shown in Fig. 3.3:

- Positive polarity, high-energy tune with magnet current at +100 A (Fig. 3.3a)
- Negative polarity, high-energy tune with magnet current at −100 A (Fig. 3.3b)
- Positive polarity, low-energy tune with magnet current at +60 A (Fig. 3.3c)
- Negative polarity, low-energy tune with magnet current at −60 A (Fig. 3.3d)

The simulations to determine the tertiary beam composition and momentum spectra were performed using the G4Beamline [63] simulation package.

3.2.1 Tertiary beam spectrometer and particle identification system

Time-of-flight system

The time-of-flight (TOF) detector system consists of two scintillator paddles: (1) USTOF, which sits just upstream of the spectrometer, and (2) DSTOF, which sits just downstream of the spectrometer. The upstream TOF paddle is relatively small with a cross-sectional area of 10 cm × 6 cm while the downstream TOF paddle is larger with a cross-sectional area of 14 cm × 14 cm. Light guides are mounted on all four edges of each scintillator paddle and each paddle was read out by two photomultiplier tubes (PMTs). The efficiency of each TOF paddle was measured to be greater than 99%.

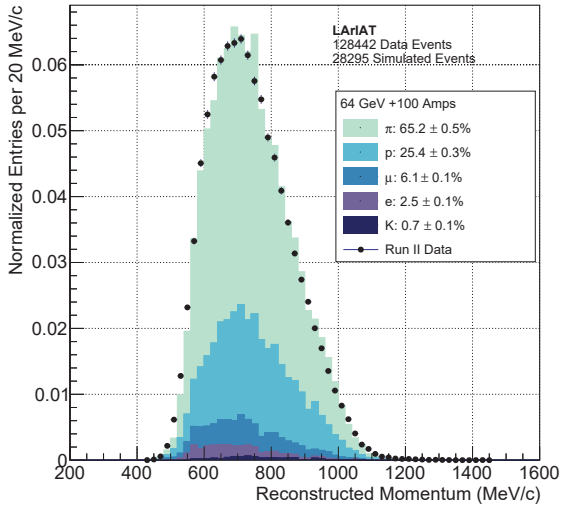

(a) Positive polarity, high-energy tune

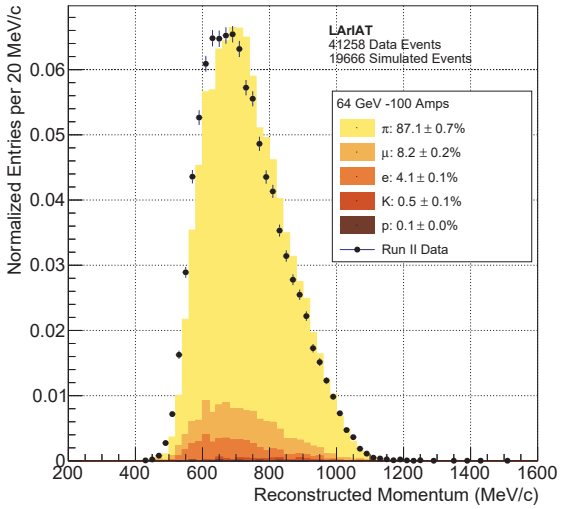

(b) Negative polarity, high-energy tune

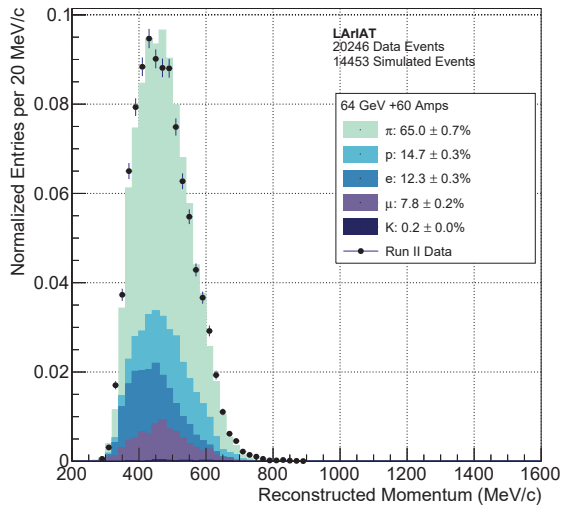

(c) Positive polarity, low-energy tune

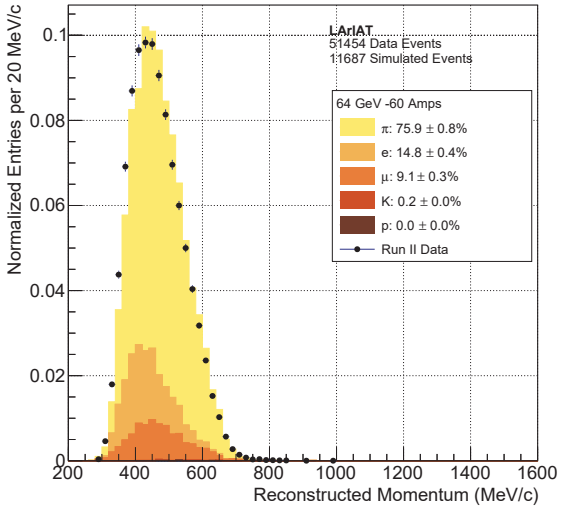

(d) Negative polarity, low-energy tune

Figure 3.3: Momentum spectra and compositions of the tertiary beam downstream of the spectrometer for different magnet polarities and energy tunes.

Magnets

The two magnets in the spectrometer of the tertiary beamline are "NDB" series dipole electromagnets that were made at Fermilab and were originally used in the anti-proton ring of Fermilab's accelerator complex. The magnets each have a gap height of 14.224 cm, a gap width of 31.75 cm, and an iron length of 46.67 cm.

Multi-wire proportional chambers

The wire chambers are based on the Fenker chambers [64] with additional grounding to improve the signal-to-noise ratio in the electronic readout. Each wire chamber has an effective square aperture of 128 mm $\times$ 128 mm. Each chamber has 128 wires along its vertical axis and 128 wires along its horizontal axis, with a wire pitch of 1 mm. The wire chambers run on a gaseous mixture of 85% argon and 15% isobutane with an operating voltage of approximately 2450 V. The efficiencies of the wire chambers were measured to be greater than 98% for cosmic ray muons. Fig. 3.4 shows one of the wire chambers in the tertiary beamline.

The combination of the momentum reconstructed via tracking through the spectrometer and the time-of-flight measurement provides the ability to distinguish between different species of particles in the tertiary beamline before they reach the TPC. This is demonstrated in Fig. 3.5 using the positive-polarity dataset from Run-II.

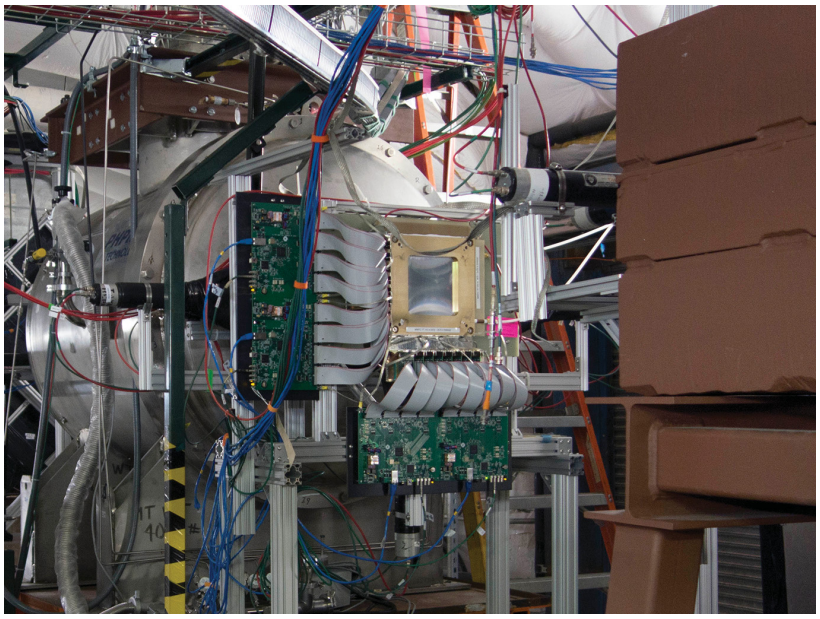

Figure 3.4: One of the multi-wire proportional chambers (WC4) in the tertiary beamline.

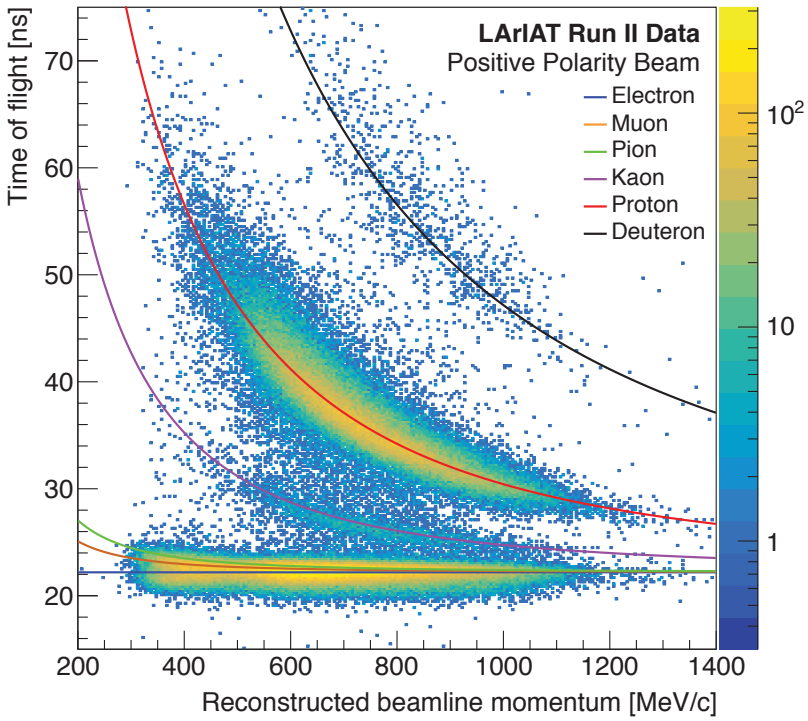

Figure 3.5: Reconstructed momentum vs. time of flight of particles in the tertiary beam for data collected with the positive polarity configuration. The colored lines are the expectations for different species of particles.

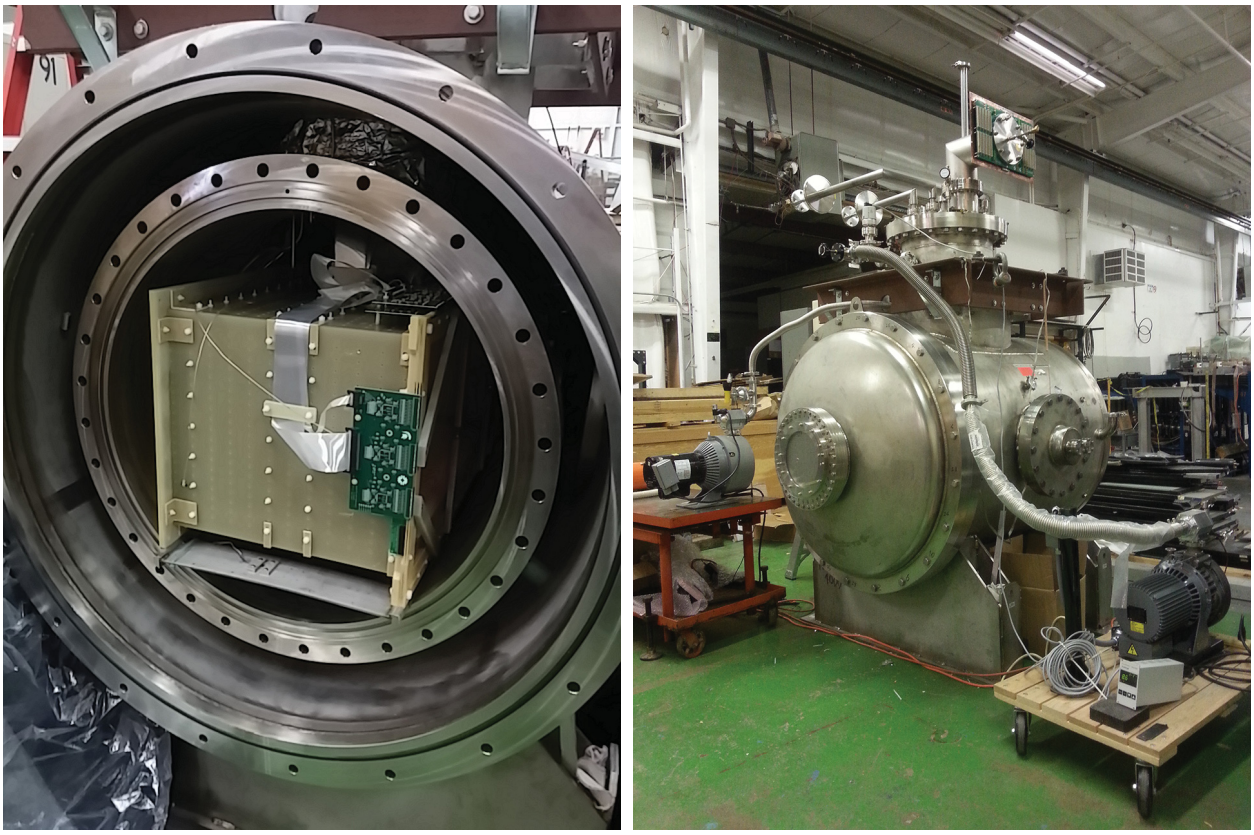

Figure 3.6: The LArIAT cryostat opened with the TPC inside the inner vessel (left), and the cryostat fully sealed (right).

3.3 The LArIAT Detector

3.3.1 Cryogenic system

Cryostat

The LArIAT cryostat, shown in Fig. 3.6, consists of an inner cylindrical vessel (76.2 cm in diameter and 130 cm in length) containing purified liquid argon and the time projection chamber (TPC), and an outer cylindrical vessel layered with aluminized mylar superinsulator which serves as a vacuum environment to provide insulation to the inner vessel. The inner vessel is capable of storing a total of 550 L (0.76 t) of liquid argon. The internal volume can

be accessed through the convex end caps of the inner and outer vessels. A wide neck (chimney) protruding from the top of the cryostat serves as an access path for signal cables from the LArTPC and its internal instrumentation and high-voltage feedthrough. The cylindrical axis of the cryostat is oriented parallel to the secondary beam.

The cryostat was inherited from the ArgoNeuT (Argon Neutrino Test) experiment [65] and modified to minimize the amount of dead material upstream of the active volume in the TPC. The steel end caps of the inner and outer vessels of the original ArgoNeuT cryostat were 4.8 mm thick. There was also a 15 cm long region of uninstrumented liquid argon upstream of the active volume in the TPC. For the LArIAT experiment, the end cap of the outer vessel was modified to include a flange that houses a thin titanium beam window that is 22.9 cm in diameter. Additionally, a hollow, concave volume (termed the *excluder*) was installed on the end cap of the inner vessel that extends toward the TPC. These modifications reduce the total thickness of the dead material from ∼1.8 radiation lengths to less than ∼0.3. In addition, CF-flanged apertures were added to the side ports of both the inner and outer vessels to accommodate the signal and high-voltage connections for the scintillation light collection system.

Liquid argon system

The liquid argon is supplied by a commercial dewar located just outside of the MC7 enclosure; argon flows from the dewar to the cryostat through a 1-inch diameter, Schedule 10 steel piping, insulated with 20 cm of polyurethane foam. The argon passes through the pipes to a purification system, modeled after the Liquid Argon Purity Demonstrator (LAPD) [66] system, which primarily removes water and oxygen (O_2), as well as small amounts of nitrogen (N_2). Ionization electrons readily attach to water and oxygen molecules, and nitrogen quenches the slow component of the argon scintillation light, so it is crucial that the con-

tamination level is at most 100 parts per trillion (ppt).

The filtered argon is piped into the inner vessel of the cryostat via a fluid feedthrough mounted on the top of the outer vessel of the cryostat. A vertical pipe, extending from the fluid feedthrough, deposits the argon at the bottom of the inner vessel of the cryostat. The liquid argon level, temperatures, and pressures within the cryostat and commercial supply dewar are continuously monitored during operation. A screenshot of the monitoring page for the cryostat and dewar are shown in Fig. 3.7.

During normal operation, liquid argon in the cryostat boils off at the surface and is released to the atmosphere. The liquid argon in the cryostat must be refilled from the supply dewar several times a day to ensure that the TPC readout electronics remain submerged.

3.3.2 Time projection chamber

The LArIAT experiment uses the refurbished ArgoNeuT TPC. The TPC is 47 cm in width, 40 cm in height, and 90 cm in length. The TPC coordinate system is oriented such that the x axis is along the width of the TPC, the y axis is along the height of the TPC, and the z axis is along the length of the TPC (parallel to the secondary beam). The LArIAT TPC consists of three wire planes (Fig. 3.8): (1) a non-instrumented shield plane with 225 wires, (2) an induction read-out plane with 240 wires, and (3) a collection read-out plane with 240 wires. Fig. 3.9 shows one of the wire planes during the wire plane assembly process. The wires on the shield, induction, and collection planes are oriented at 90°, $+60^\circ$, and -60° relative to the z axis in the y–z plane, respectively; the wire pitch and interplanar spacing are both 4 mm. A schematic diagram of the LArIAT TPC is shown in Fig. 3.10. The origin of our coordinate system in this thesis is taken to be the half-height point where the front face of the TPC and collection plane intersect, as marked by the black dot in Fig. 3.10.

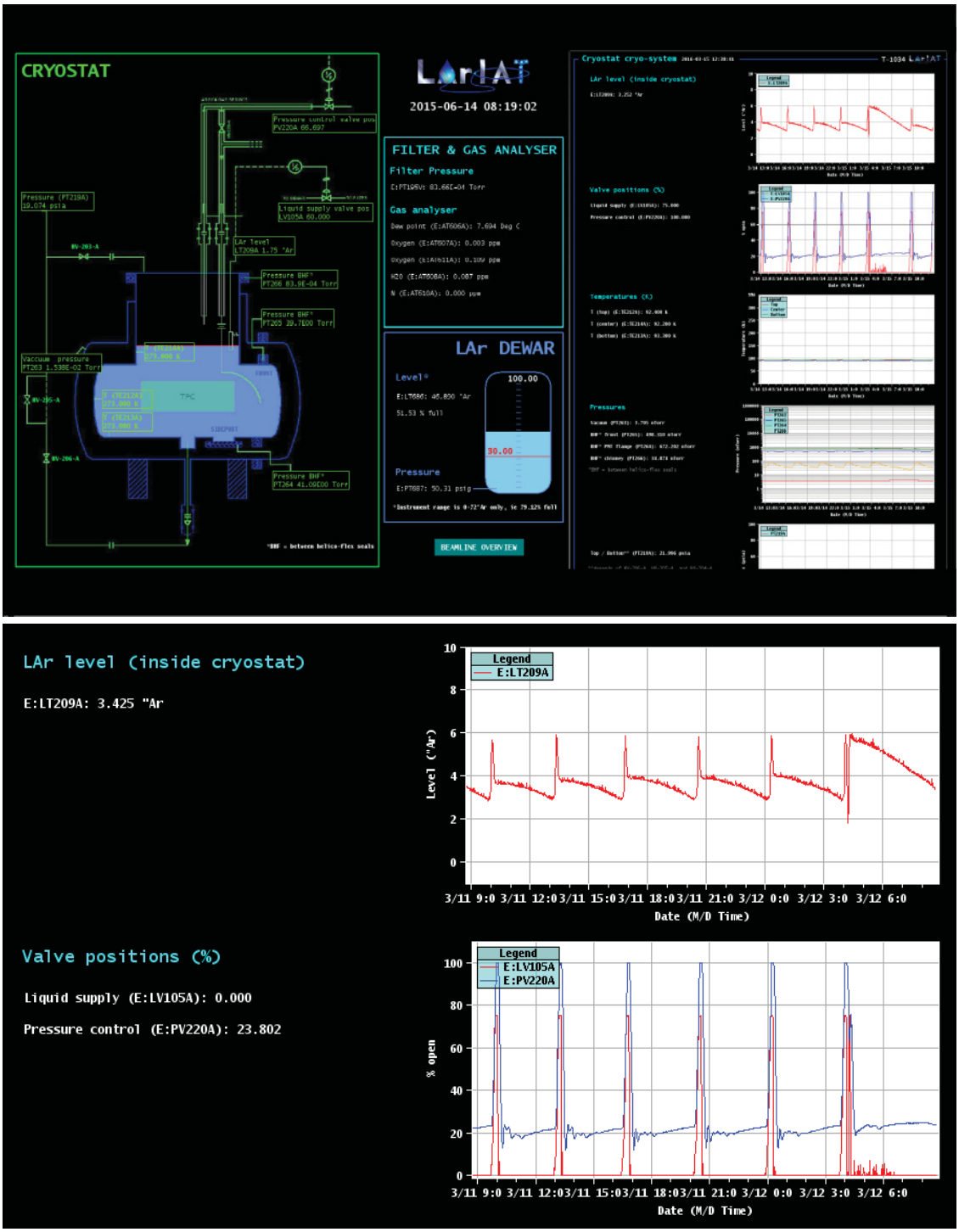

Figure 3.7: A screenshot of the LArIAT cryostat monitoring page displaying the argon levels within the cryostat and supply dewar (top). Position of the liquid valve that allows liquid argon to flow into the cryostat and corresponding pressure within the cryostat (bottom).

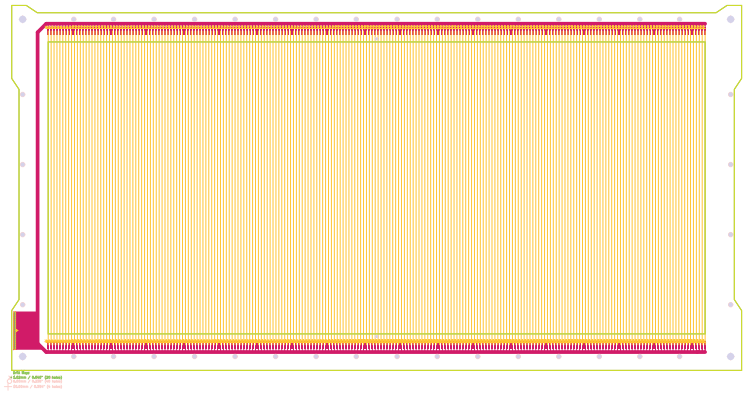

(a) Shield plane wire board

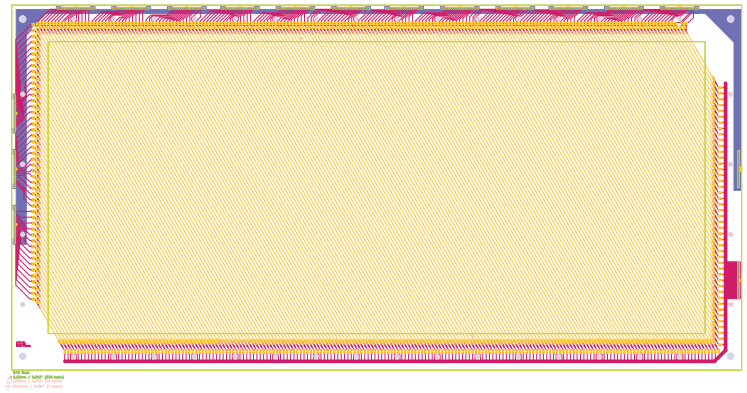

(b) Induction plane wire board

(c) Collection plane wire board

Figure 3.8: The three wire layers in the LArIAT TPC as viewed from inside the TPC volume (beam is incident from the right).

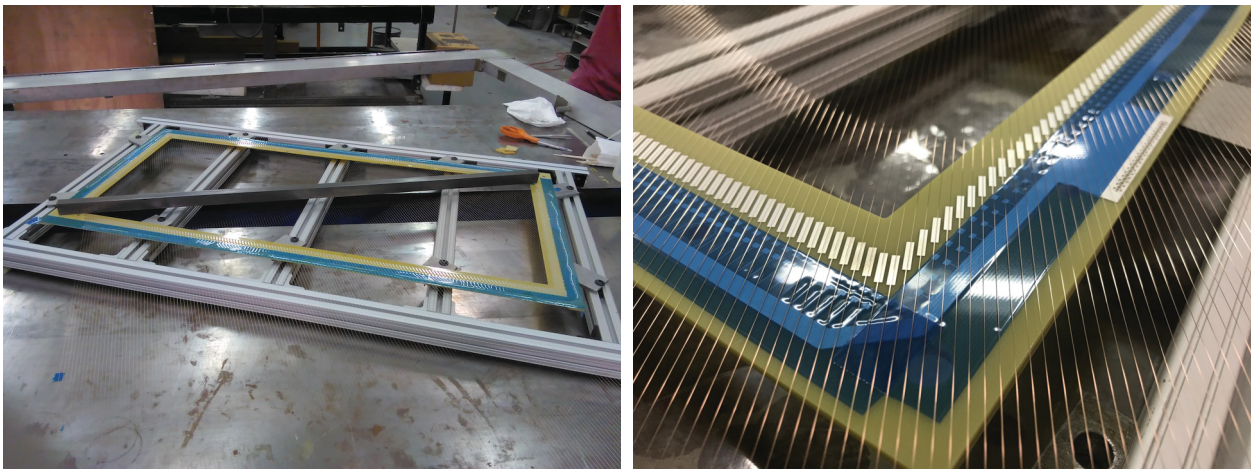

Figure 3.9: One of the wire planes during the wire plane assembly process.

The TPC contains three different drift volumes of different electric fields as depicted in Fig. 3.11. A high voltage of -23.5 kV for the TPC cathode is provided by a Glassman LX125N16 power supply. Bias voltages of -298 V, -18.5 V, and 338 V are applied to the shield, induction, and collection planes, respectively. This creates a uniform electric field of magnitude $|\mathbf{E}| = 484$ V/cm along the $+\hat{x}$ direction in the drift region between the high voltage cathode and shield plane (C–S)*. Additionally, the bias voltages for the wire planes are chosen such that the electric field satisfies the charge transparency condition in the drift regions between the shield and induction planes (S–I) and the induction to collection planes (I–C)—i.e., all the drifting electrons are transported through the shield and induction planes, and then collected on the collection plane.

Ionization electrons that are drifted to the wires produce relatively small electrical signals. In order to achieve a high signal-to-noise ratio†, the signals are amplified using low-noise, cold electronics that operate at cryogenic temperatures. All 480 analog channels from the wire planes are read out through cold amplifier motherboards hosting ASICs (LArASICs) [68],

*The electron drift velocity within the C–S region is about 1.5 mm/µs.

†The signal-to-noise ratio is calculated as the ratio of the most probable pulse amplitude for minimally-ionizing, through-going beam tracks over all collection plane wires, and pedestal RMS. The signal-to-noise ratio was ≈30 during Run-I and ≈45 during Run-II.

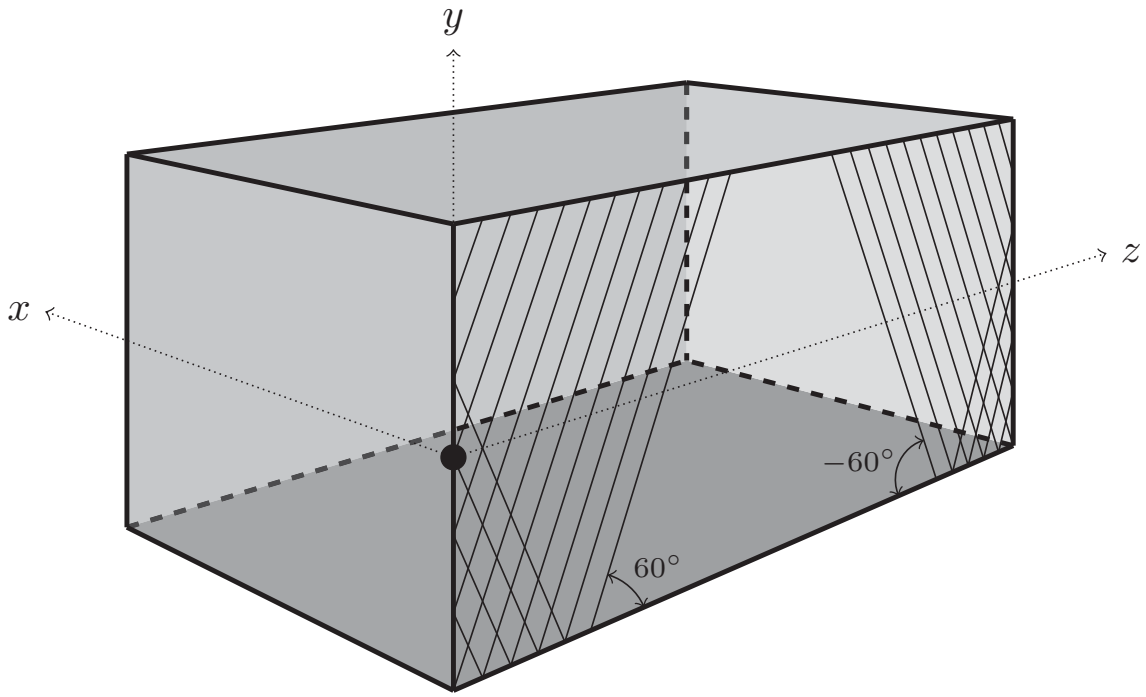

Figure 3.10: Schematic diagram of the LArIAT TPC. The induction plane and collection plane wires are oriented at $\pm 60^\circ$ relative to the z axis in the y–z plane, respectively; the wire pitch and interplanar spacing are both 4 mm. Figure modified from Ref. [67].

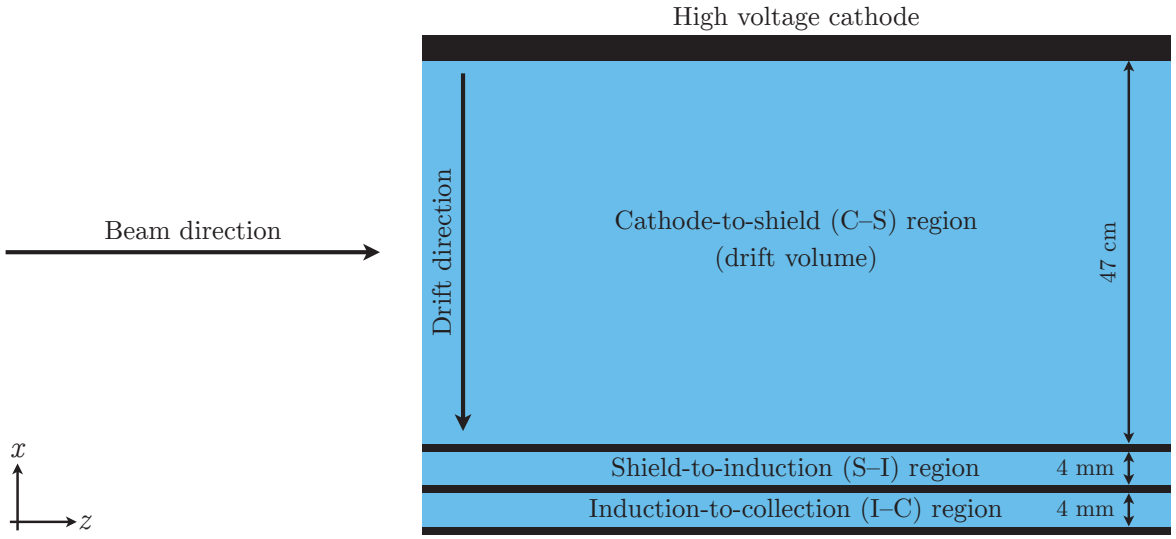

Figure 3.11: Schematic diagram of the three drift regions within the LArIAT TPC.

which are mounted directly on the outer frame of the TPC and submerged in liquid argon. For a typical gain setting of 25 mV/fC on the LArASICs, the ∼3.5 fC of ionization charge deposited on a wire from a minimum ionizing particle (MIP) will generate a ∼90 mV output.

The signals are sampled every 16 ns by CAEN V1740* digitizers. Special firmware provided by CAEN enabled us to store averages of 8 consecutive samples, leaving us with an effective sampling period of 128 ns. The maximum input range of the CAEN V1740 digitizer is 2 V. An analog offset of 0.2 V was used for the unipolar collection signals to allow for the digitization of small negative undershoots. An analog offset of 1 V was used for the bipolar induction signals to place the baseline at mid-range. The analog path from the LArASICs to the CAEN V1740 digitizers is designed to provide unity gain, thus the ∼90 mV MIP signal corresponds to an amplitude of ∼180 ADC counts. Fig. 3.12 shows an example of digitized signals from an induction wire and a collection wire.

*64-channel, 12-bit, 62.5 MS/s ADC

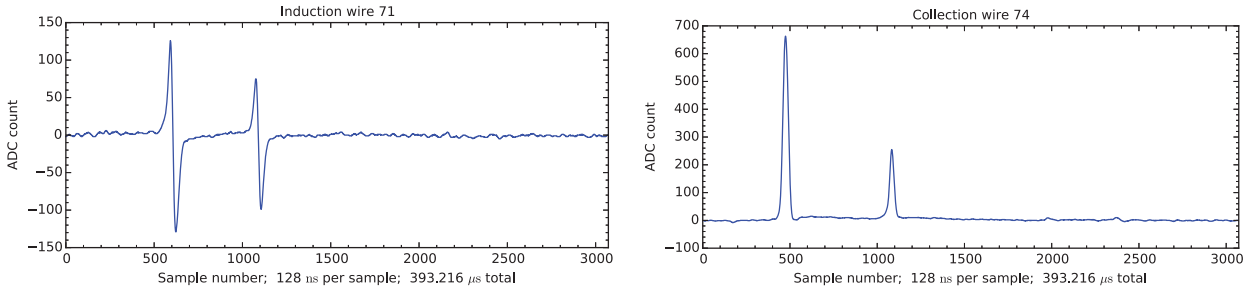

Figure 3.12: An induction wire signal (left) and a collection wire signal (right) of an event from the Run-II dataset. The first pulse comes from a proton candidate and the second pulse comes from a gamma-induced electromagnetic shower candidate.

3.4 Data Acquisition

A block diagram of the LArIAT data acquisition (DAQ) system is shown in Fig. 3.13. Every 60.5 s, as part of the Fermilab accelerator complex super cycle, beam is extracted from the Main Injector and delivered to LArIAT. At the beginning of each super cycle, indicated by the `$00` TCLK event in Fig. 3.14, all the digitizers and trigger board are reset in order to synchronize the data buffers across disparate hardware and reset local timers. Random pedestal triggers were collected at a rate of 10 Hz in between the `$30` and `$39` TCLK events. Beam data is collected during the 4.2 s between the `$39` and `$36` TCLK events and cosmic ray data is collected during the 24 s that follows.

The DAQ system was designed to collect events at rates as high as 100 Hz during the beam spill with minimal dead time. The CAEN V1740 digitizers, with a sampling period of 128 ns, were configured to store 3072 12-bit samples per channel, thus 393.216 µs of digitized waveform data were collected for each TPC wire per event. With a maximum electron drift time of approximately 320 µs in the TPC, this provides padding before and after the drift window. For a maximum trigger rate of 100 Hz, the total data rate for all 480 wires would be approximately 2 GB/s. In practice, the typical rate was 50 to 100 triggers per 4.2 s spill, or approximately 0.3 GB/s. The fast scintillation signals from the TOF and the TPC

light collection PMTs were digitized and read out by CAEN V1751* digitizers, which were configured to store 28,672 10-bit samples per channel. With a sampling period of 1 ns on the CAEN V1751, 28.672 µs of digitized waveform data were collected for each TOF and TPC light collection PMT per trigger.

The main LArIAT readout system, represented schematically in Fig. 3.15, consists of two VME crates. The first CAEN V1740 in the upper left of the figure provides the master clock that was daisy-chained to all the other CAEN digitizers. The clock synchronization procedure recommended by CAEN was applied to correct for board-to-board clock skew to the level of approximately 150 ps. The CAEN V2718 VME crate controller, shown in the bottom left of the figure, was used to configure the CAEN V1495 general-purpose logic board, which generates the experimental triggers.

The LArIAT DAQ software is built upon the *artdaq* [69] software package, which is built against the *art* [70] package. The DAQ software writes data files in *art*-readable ROOT [71] files, which are passed to nearline and offline workflows, consisting of *art*-based modules, for analysis.

3.5 Trigger System

The readout of the data buffers is triggered by a CAEN V1495 general-purpose VME board. Outputs from the TOF PMTs and spectrometer wire chambers (WC) are used to generate the main beamline trigger. Coincident activity in the TOF and WC systems suggests that a charged particle has propagated through the tertiary beamline and into the TPC. For each TOF paddle, the logical OR of discriminated pulses from the PMTs was used as a trigger input. For each WC, the logical (OR of x wires) AND (OR of y wires) was used as a trigger

*8-channel, 10-bit, 1 GS/s ADC

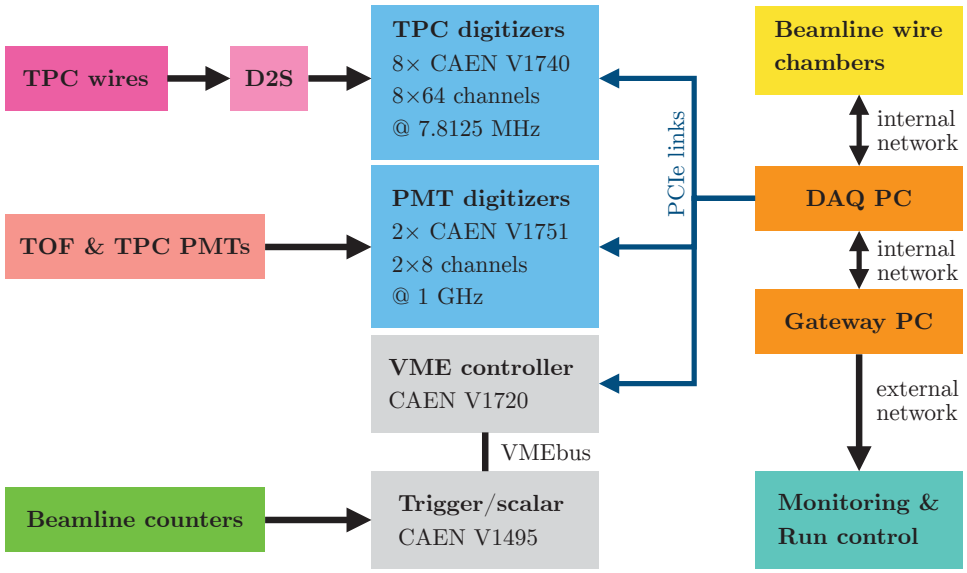

Figure 3.13: Block diagram of the LArIAT DAQ system and data flow.

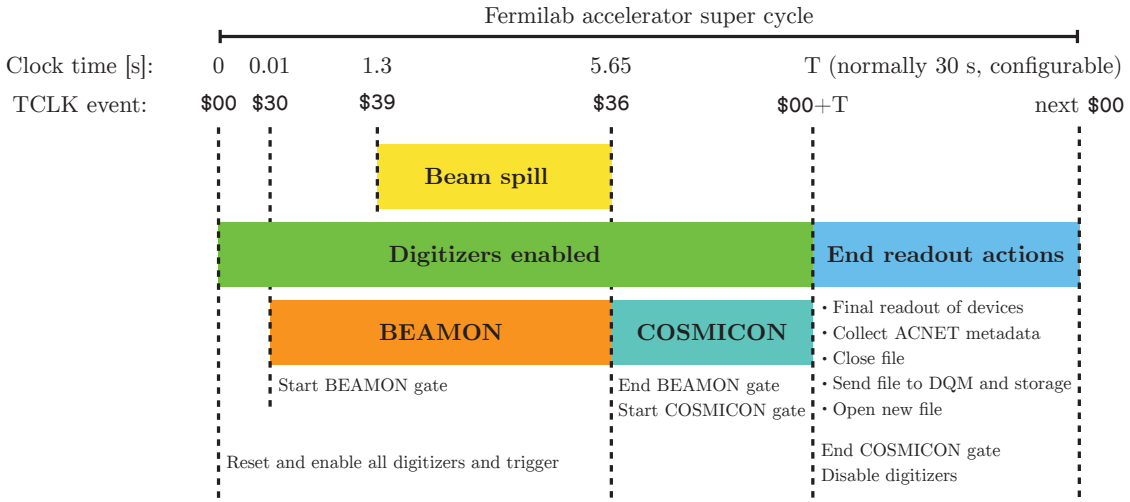

Figure 3.14: The LArIAT DAQ timeline during a super cycle. The BEAMON and COSMICON gates are inputs to the trigger system.

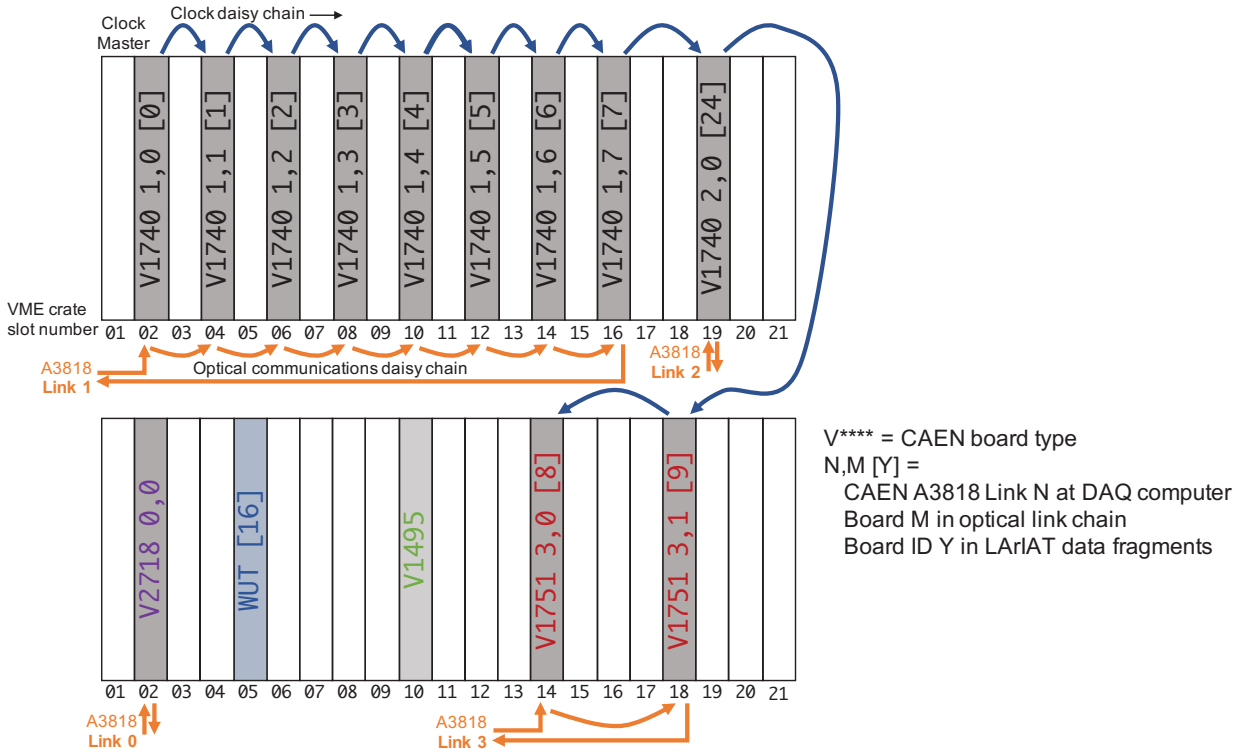

Figure 3.15: Schematic diagram of the LArIAT digitizer timing and clock configuration.

input. The BEAMON logic gate is opened by the $30 TCLK event and closed by $36, as shown in Fig. 3.14, and was used as a trigger input. A select list of trigger inputs to the CAEN V1494 and their descriptions are shown in Table 3.1. The following trigger pattern was used as our basic beamline trigger:

$$\begin{aligned} &\text{BEAMON} \\ &\quad \wedge \text{USTOF} \\ &\quad \wedge \text{DSTOF} \\ &\quad \wedge ((\text{WC1} \wedge \text{WC2} \wedge \text{WC3}) \\ &\qquad \vee (\text{WC1} \wedge \text{WC2} \wedge \text{WC4}) \\ &\qquad \vee (\text{WC1} \wedge \text{WC3} \wedge \text{WC4}) \\ &\qquad \vee (\text{WC2} \wedge \text{WC3} \wedge \text{WC4})). \end{aligned} \tag{3.1}$$

Trigger input	Description
PEDESTALON	Pedestal gate: starts on `$00`, stops on `$00`+(999 ms)
PULSER	10 Hz pulser
BEAMON	Beam spill gate: starts on `$30`, stops on `$36`
WC1	(OR of x wires) AND (OR of y wires)
WC2	(OR of x wires) AND (OR of y wires)
WC3	(OR of x wires) AND (OR of y wires)
WC4	(OR of x wires) AND (OR of y wires)
USTOF	OR of 2 PMTs
DSTOF	OR of 2 PMTs
COSMICON	Cosmic gate: starts on `$36`, stops on `$00`+T
COSMIC	Trigger signal from cosmic rack

Table 3.1: Select list of trigger inputs to the CAEN V1495.

3.6 Monitoring

3.6.1 DAQ monitoring

The DAQ keeps track of a number of low-level quantities as it is writing data to disk. All of these quantities are displayed on a simple web page (shown in Fig. 3.16) that is updated in real-time, which enables easy monitoring of the run status during data acquisition.

Some of the low-level quantities displayed include: relative time in the Fermilab accelerator complex super cycle, total number of triggers in the event per CAEN digitizer, total number of detectors triggered during a beam spill, trigger patterns and the number of times a particular trigger pattern was satisfied during a beam spill, as well as beam conditions and environmental parameters of the TPC, as seen in the figure. The web page issues an audible alarm and changes some of the page's text color to red if data-taking is not detected for a period of longer than 2 minutes.

3.6.2 Data quality monitoring

The LArIAT data-quality monitoring (DQM) system is primarily used to perform near real-time checks on low-level quantities in data. The DQM system processes the data on a spill-by-spill basis and a quick analysis is done. The results of the analysis are recorded in PostgreSQL* and Redis† databases, and displayed on an interactive web page, as shown in Figs. 3.17 and 3.18. The front-end of the DQM consists of a website running on Flask‡, with the D3.js§ library and Cubism.js¶ plugin for data visualization. The DQM webpage allows shifters and experts to view the results from the most current collection of beam spills, typically with a 2-minute delay, as well as results from past collections of beam spills.

The low-level quantities monitored by the system include:

- the number of data fragments recorded by the CAEN digitizer boards and the wire chamber controller (*data fragments* are pieced together to form an event),
- the number of recorded data fragments that are used to build a TPC event,
- the pedestal mean and pedestal RMS on the CAEN digitizer boards (this includes the readout from the TPC wires, light-collection PMTs, and PMTs of various beamline detectors), and
- the hit occupancy and hit timing plots of the multi-wire chambers.

There is also a high-level time-of-flight plot, which provides a crude monitor of the tertiary beam composition.

In addition, the DQM system has a series of alarms that are activated whenever a low-level

*PostgreSQL: `https://www.postgresql.org`

†Redis: `https://redis.io`

‡Flask: `https://palletsprojects.com/p/flask`

§D3.js: `https://d3js.org/`

¶Cubism.js: `https://square.github.io/cubism/`

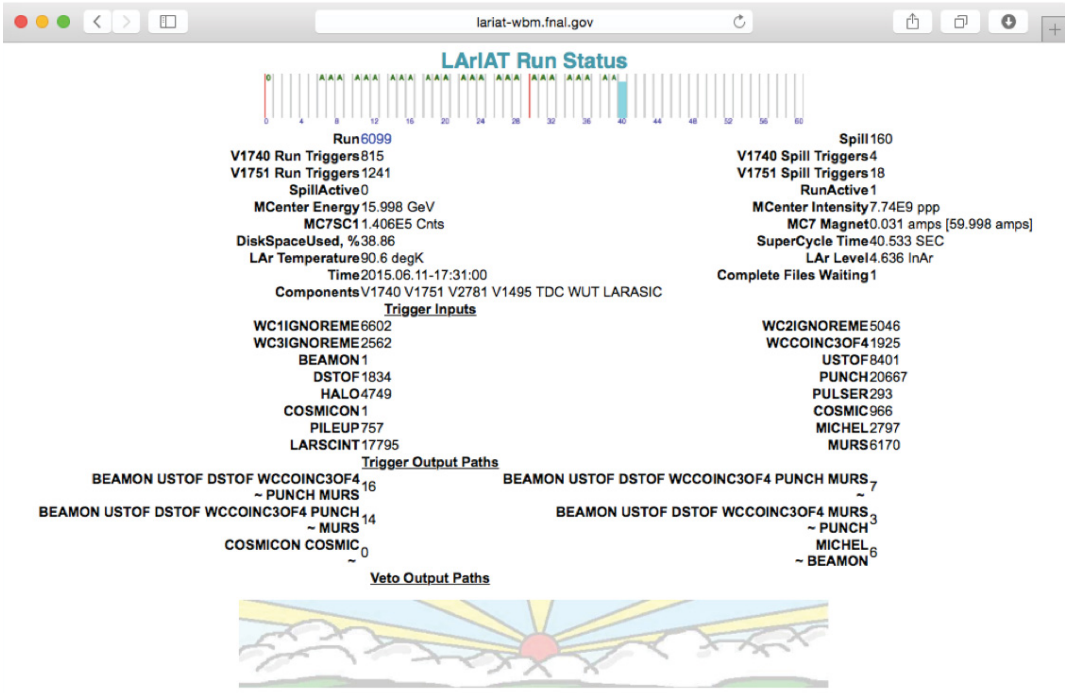

Figure 3.16: The LArIAT run status page.

quantity is found outside its tolerance during the most current beam spill. The 2-minute feedback for beam and detector conditions allows a quick response by the shifter or detector experts, minimizing beam and detector down time.

3.7 TPC Event Reconstruction

The reconstruction and analysis of events in LArIAT are performed using LArSoft [72, 73], an *art*-based software package designed to provide simulation, reconstruction, and analysis tools for LArTPC-based experiments.

Event reconstruction in a LArTPC takes ionization-induced signals on the TPC wires as input to produce three-dimensional physics objects with calorimetric quantities as output. First, deconvolution is performed on the bipolar induction-plane pulses and collection-plane pulses to transform them into unipolar, Gaussian-like pulses and mitigate the response of the

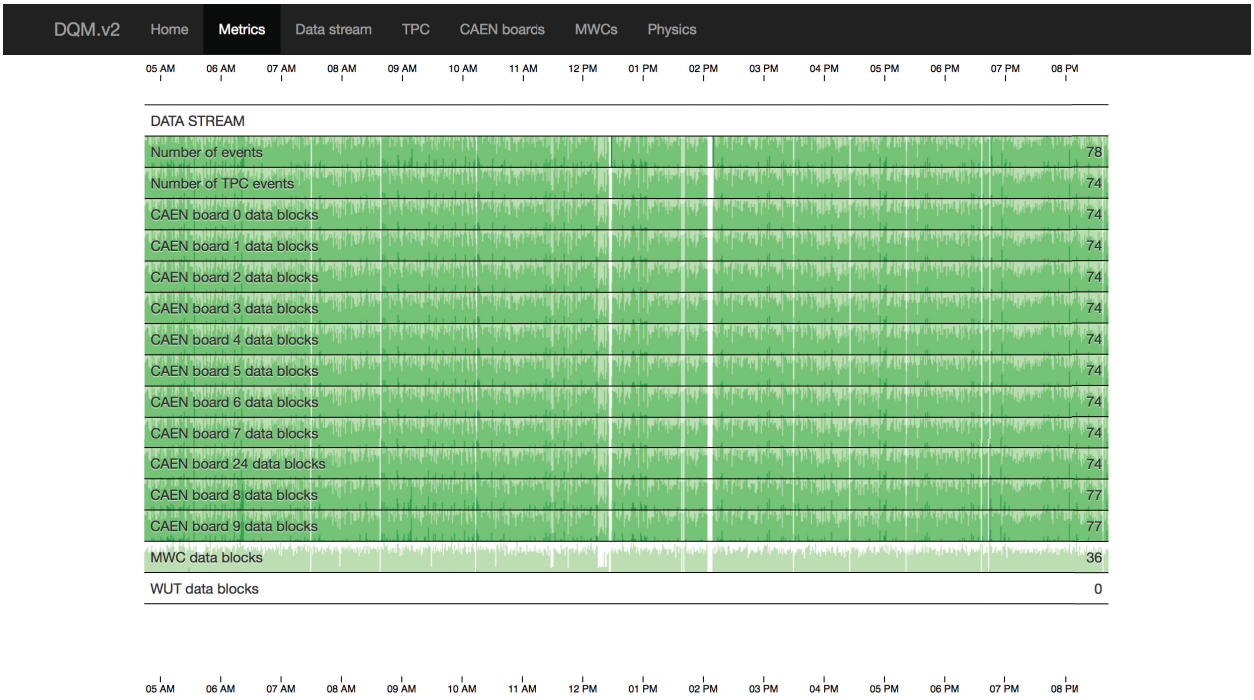

Figure 3.17: DQM monitoring page displaying a set of time series plots of the number of data fragments collected per super cycle over the previous 16 hours of operation.

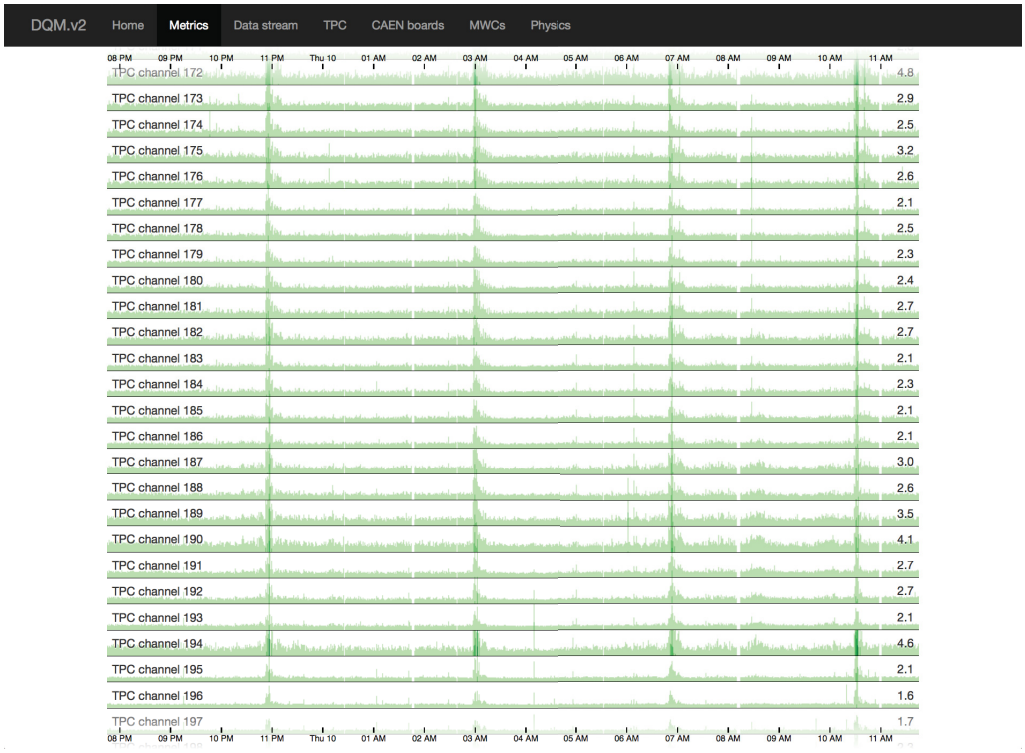

Figure 3.18: DQM monitoring page displaying a set of time series plots of the RMS on each TPC wire over the previous 16 hours of operation.

electronics [74]. Hit reconstruction is then performed on the deconvolved waveforms to look for peaks above the waveform baseline; the identified peaks are fit to a Gaussian function. The area of the fitted Gaussian is proportional to the ionization charge induced or collected on the wire, and the location parameter corresponds to the arrival time of the charge [74]. The location parameter of the fitted Gaussian is used to determine the position where the ionization occured along the drift direction.

Hits on each wire plane are topologically grouped into clusters in 2D wire–time space using a trajectory-based clustering algorithm [75]. The clustering algorithm first creates a seed trajectory from two neighboring hits, and then sequentially steps along to other hits within a close vicinity and determines if the hits will be added to the assumed trajectory. Whether a given hit is added to the trajectory primarily depends on: (1) the charge of the hit compared to the average charge and RMS of the hits in the forming trajectory, (2) how well the hit aligns with the forming trajectory, and (3) the angle between the two lines formed by the trajectory before and after the considered hit is included in the trajectory. After exhausting through the iterative steps, all the hits in the trajectory are amassed into a single cluster.

Sets of 2D clusters are matched between the two wire planes in order to form 3D tracks using a projection-matching algorithm [76]. The algorithm constructs and optimizes a 3D trajectory with iteratively increasing number of segments by minimizing the distance between the hits of 2D clusters and the projection of the 3D trajectory's points onto the 2D wire planes.

Chapter 4

Data-Driven Monte Carlo Simulation

> "Data! Data! Data!" he cried impatiently. "I can't make bricks without clay."
>
> Sir Arthur Conan Doyle
>
> *The Adventure of the Copper Beeches*

An accurate simulation is critical for evaluating the performance of our reconstruction algorithms and estimating the background contamination in our measurements. In this chapter, we discuss methods used to generate our data-driven Monte Carlo (DDMC) simulation.

4.1 Tertiary Beam

The composition of the tertiary beam is predicted using G4Beamline. In order to obtain a more realistic momentum spectrum, we use information of reconstructed wire chamber (WC) tracks from data. For each event in the data sample with a reconstructed WC track, the following reconstructed quantities are used as input into the DDMC simulation:

- the reconstructed position (x, y) at WC4 for the starting point of the particle, and
- the reconstructed momentum p_{beam} and direction $(\theta_{xz}, \theta_{yz})$ for the starting four-momentum of the particle.

The distributions of these reconstructed quantities from the Run-II -100 A dataset are

shown Fig. 4.1. In the DDMC generator, a reconstructed WC track is chosen at random and its reconstructed quantities listed above are used to generate a tertiary beam particle that starts downstream of the spectrometer at WC4 ($z = -100$ cm); the particle species is drawn at random, according to the prediction from G4Beamline, based on the particle's momentum. The momentum spectrum of the DDMC simulation for the Run-II -100 A is shown in Fig. 4.2.

4.2 Halo Pile-Up

The length of the secondary-beam transport line from MC6 to MC7 is approximately 90 m. Charged pions in the secondary beam can undergo the decay process $\pi^+ \rightarrow \mu^+\nu_\mu$ at any point along the secondary-beam transport line. Muons from these decays can penetrate the LArTPC detector located at MC7 and are a source of background contamination in our events (Fig. 4.4). The angular and energy distributions of the muons can be computed using kinematic formulae described in the appendix of Ref. [77]; distributions for muons from a 64 GeV/c secondary beam of charged pions are shown in Fig. 4.5.

Because a full simulation of the secondary beamline is not available, we take a data-driven approach in simulating halo pile-up particles. After a primary track candidate has been selected in the TPC for an event (procedure described in Section 5.1.1), we identify halo pile-up tracks in the TPC as non-primary tracks that have an upstream-most point that is within the first 4 cm of the TPC and a total track length of at least 4 cm. The reconstructed positional and directional information of halo pile-up tracks from data are then used as input into the DDMC to simulate the halo pile-up muons. The starting position of a MC halo pile-up muon is projected backwards to start in between WC4 and the front face of the TPC at $z = -40$ cm; the starting energy of the MC halo pile-up muon is drawn from a uniform distribution between $0.57E_\pi$ and E_π where E_π is the energy of the parent pion [77] (the

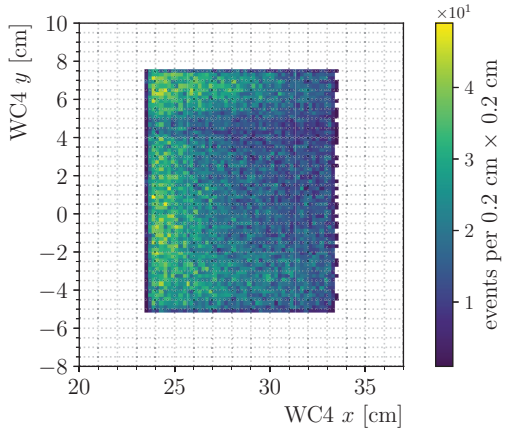

(a) Reconstructed (x, y) distribution of WC tracks downstream of the spectrometer at WC4

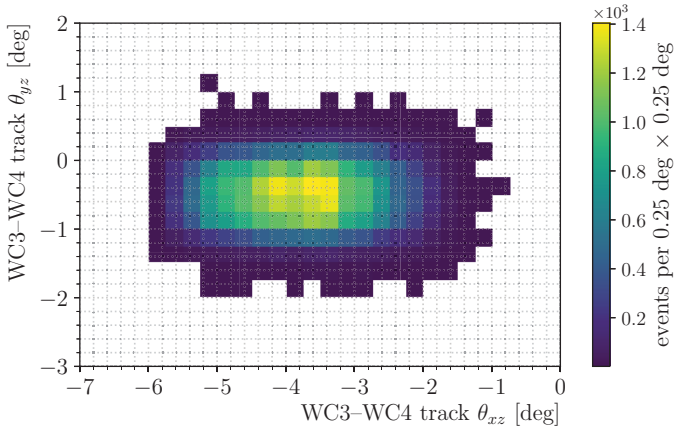

(b) Reconstructed angular distribution of WC tracks downstream of the spectrometer

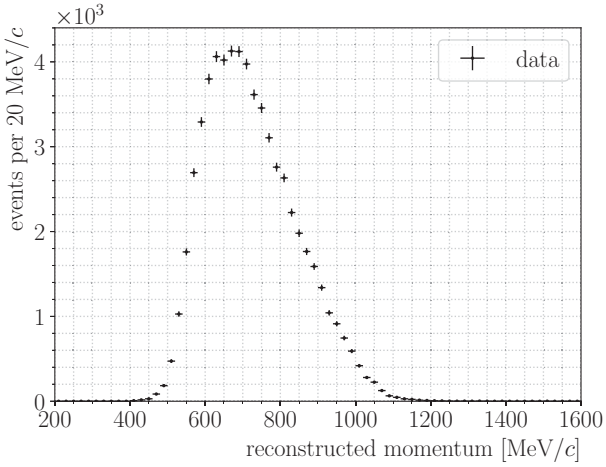

(c) Reconstructed momentum distribution of WC tracks downstream of the spectrometer

Figure 4.1: Reconstructed quantities from WC tracks in the Run-II −100 A dataset.

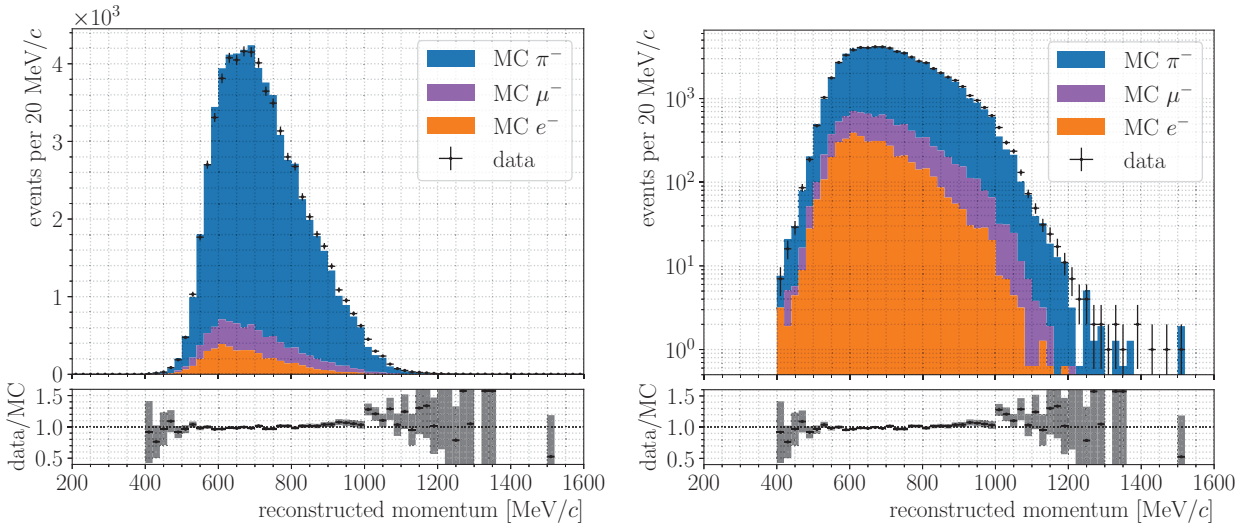

(a) Linear-linear

(b) Log-linear

Figure 4.2: Momentum spectrum of the DDMC simulation for the Run-II −100 A dataset.

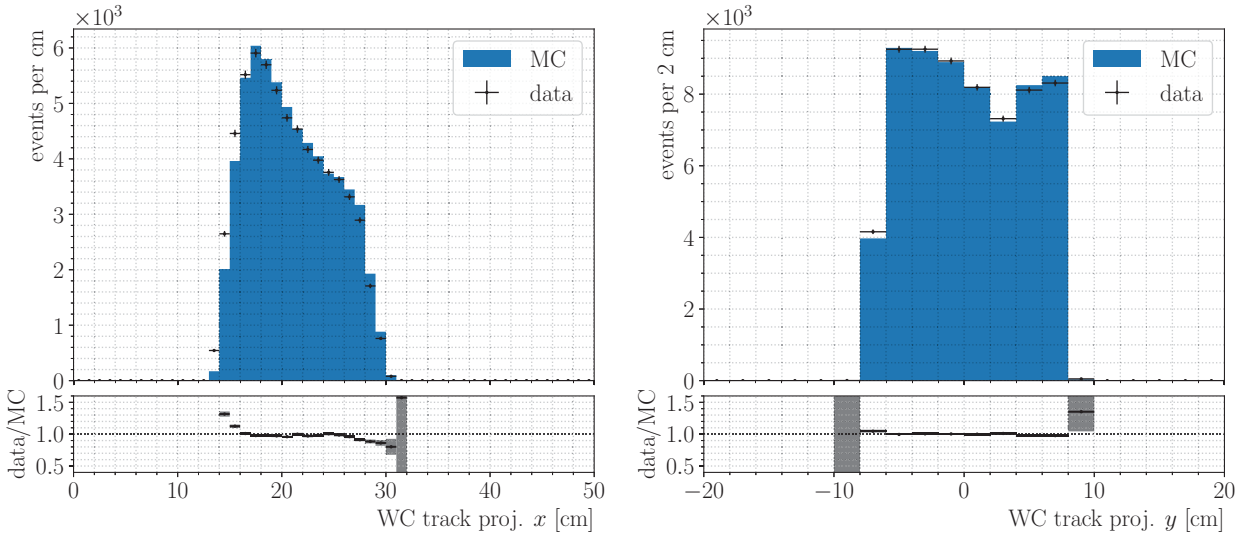

Figure 4.3: Projected x and y positions of the WC track onto the front face of the TPC.

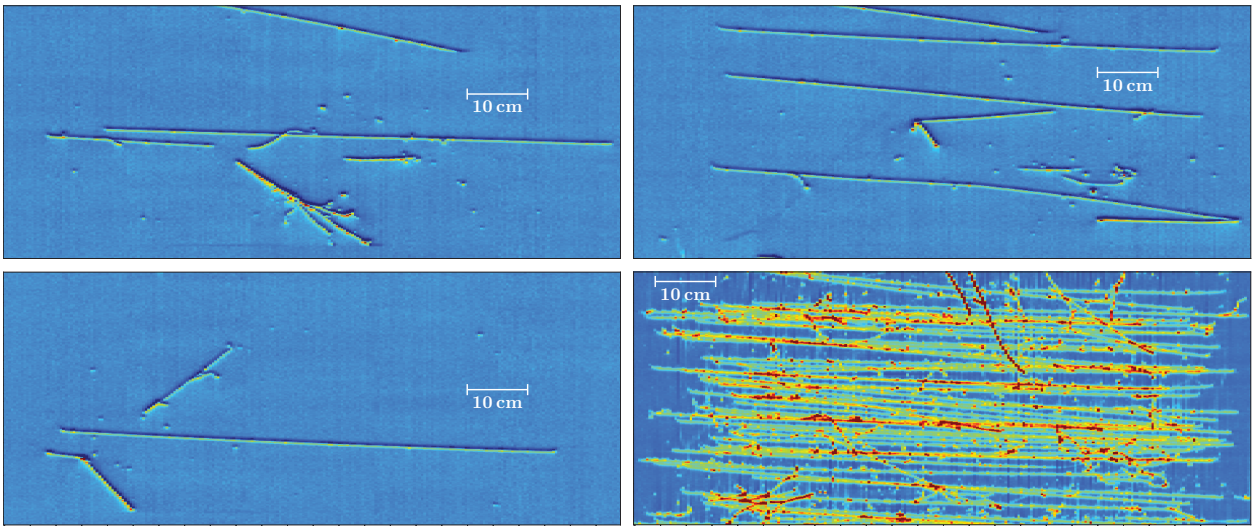

Figure 4.4: Various events with pile-up from the LArIAT Run-II dataset.

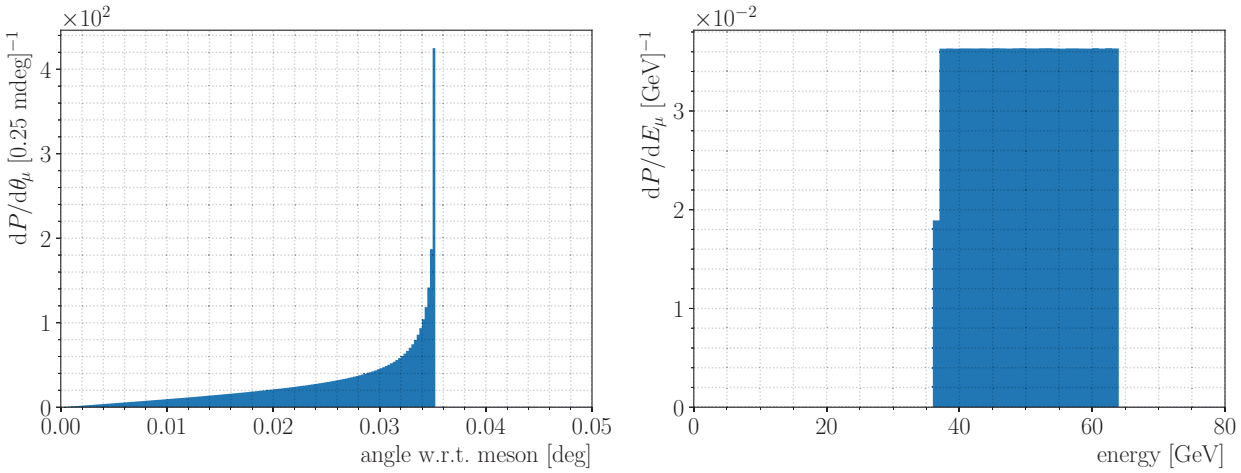

(a) Angular distribution

(b) Energy distribution

Figure 4.5: Angular and energy distributions of muons from decays of charged pions at 64 GeV/c.

energy distribution of MC halo pile-up muons from a 64 GeV/c secondary beam of charged pions is shown in Fig. 4.5b). The distributions of (x, y) of the upstream-most point of halo pile-up tracks and angle of halo pile-up tracks for data and DDMC are shown in Fig. 4.6 with fairly good agreement. The number of halo pile-up particles per event is estimated using

(a) the observed number of reconstructed halo pile-up tracks from data, and
(b) the halo pile-up tracking efficiency estimated from Monte Carlo simulations;

this method is described in detail in Appendix A. The distributions of the number of halo pile-up tracks per event for data and DDMC are shown in Fig. 4.7 with good agreement.

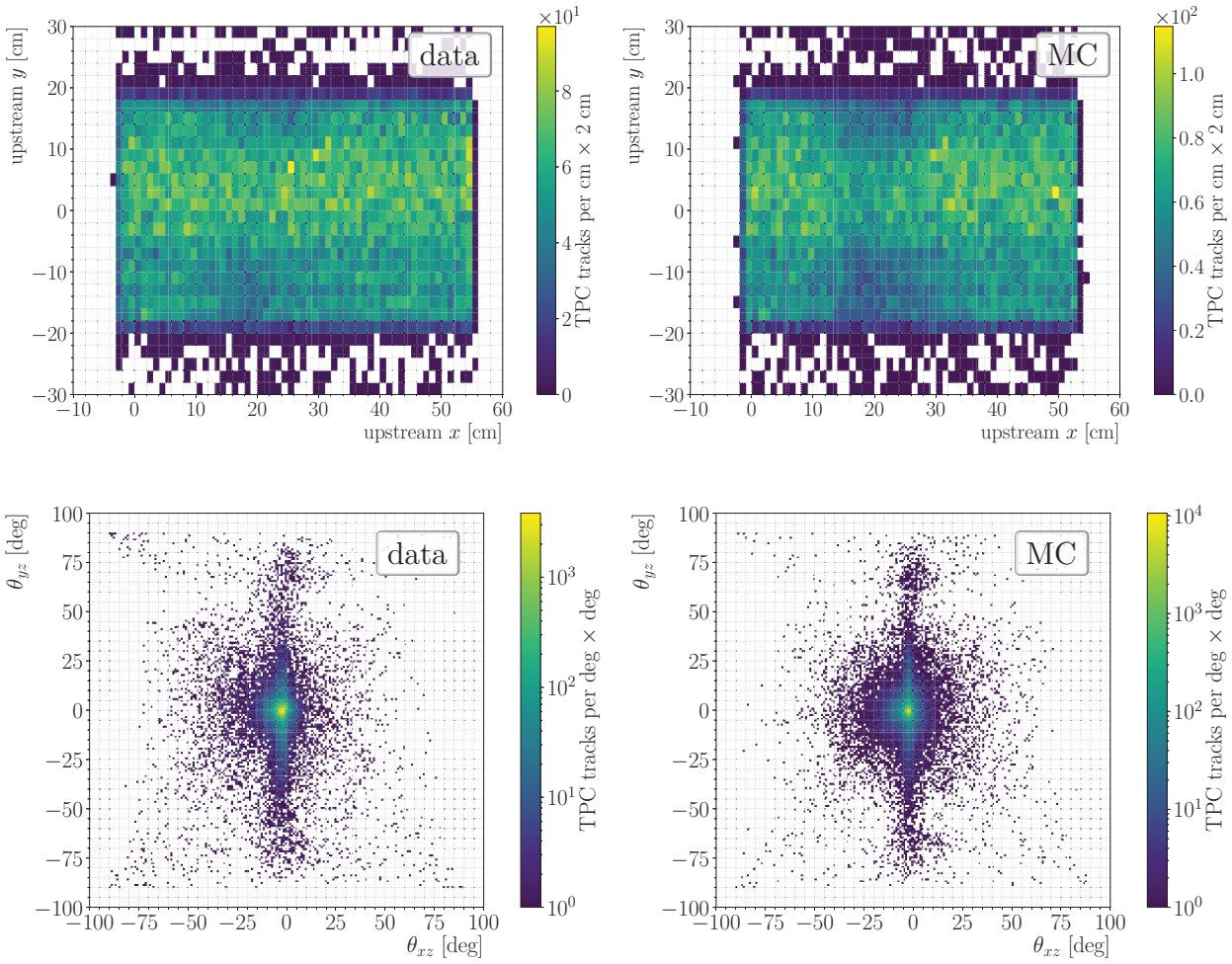

Figure 4.6: Distributions of (x, y) of upstream-most point of halo pile-up tracks (top) and angle of halo pile-up tracks (bottom) for the Run-II −100 A dataset. The distributions in the left-hand column are from data; the distributions in the right-hand column are from the DDMC simulation.

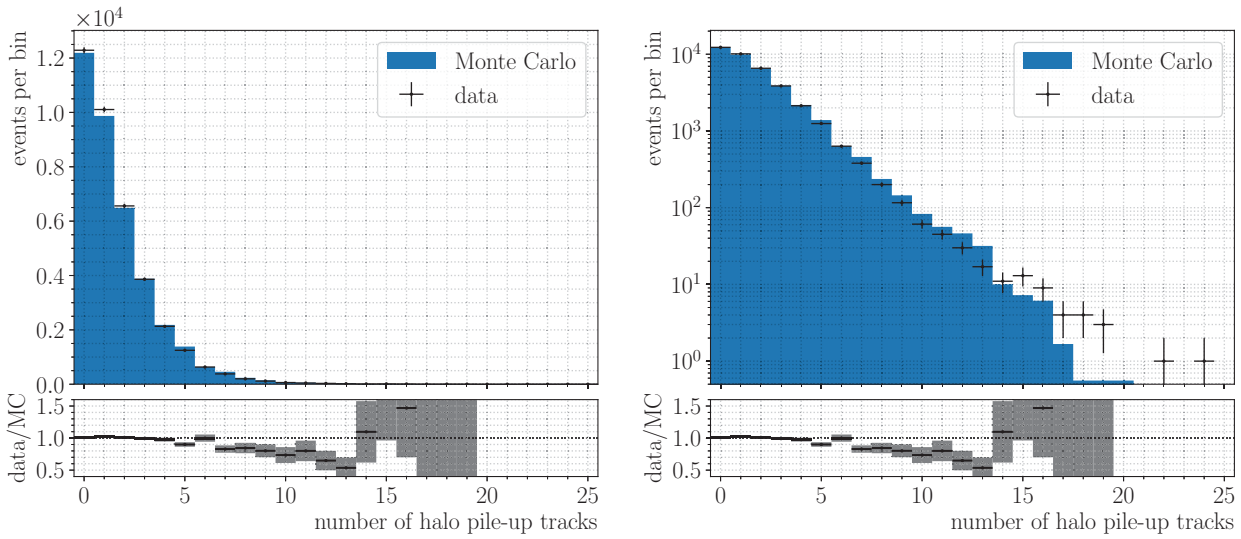

(a) Linear-linear

(b) Log-linear

Figure 4.7: Distribution of the number of halo pile-up tracks per event for the Run-II −100 A dataset.

Chapter 5

Total Hadronic π^- on Argon Cross Section

> Without experimentalists, theorists tend to drift. Without theorists, experimentalists tend to falter.
>
> Tsung-Dao Lee

This chapter describes the event selection and methods used to compute the total hadronic π^-–Ar cross section with the Run-II -100 A dataset.

We first discuss the event selection using reconstructed information from the tertiary beamline. We lay out the procedure of matching a beam wire chamber (WC) track to a track reconstructed within the TPC in order to identify π^- track candidates. We then discuss a data-constrained re-weighting of the fractional particle content in the data-driven Monte Carlo (DDMC) simulation, and mitigation of electron background events.

Next, we discuss in detail the derivation of the cross section formula from a maximum likelihood estimation. The computation of the cross section which includes background corrections, unfolding of detector resolution effects, and reconstruction efficiency corrections are described and applied to the dataset. We also discuss the Monte Carlo methods used to propagate statistical and systematic uncertainties to the cross section. Finally, we present the result of the π^-–Ar cross section measurement with the Run-II -100 A dataset.

Selection criterion	Number of events
WC track reconstructed	169 574
Require hits in all WCs	117 307
WC quality	63 658
One TOF	63 572
0 ns $<$ TOF $<$ 200 ns	63 572
$m^2 < 350^2$ MeV$^2/c^4$	62 949
$\Delta r < 5.0$ cm	45 063
$\alpha < 13^\circ$	37 391
Less than 4 halo pile-up tracks	32 534
Molière region $<$ 5 non-primary tracks	29 104

Table 5.1: Event selection table for the Run-II -100 A dataset.

5.1 Event Selection

5.1.1 Beamline-based selection

Once a WC track has been reconstructed with at least one WC hit in each of the four wire chambers, WC quality cuts are applied to the event. Particles in the tertiary beam that scatter off dense material in the beamline can produce a reconstructed WC track that is seemingly unphysical, e.g., scattering off a collimator as illustrated in Fig. 5.1. The WC quality cut rejects events if any of the following conditions exist:

- the forward projection of the WC1–WC2 track does not intersect with the aperture region of the upstream magnet,
- the backward projection of the WC3–WC4 track does not intersect with the aperture region of the downstream magnet, or
- the WC3–WC4 track does not pass through both apertures of the downstream collimator.

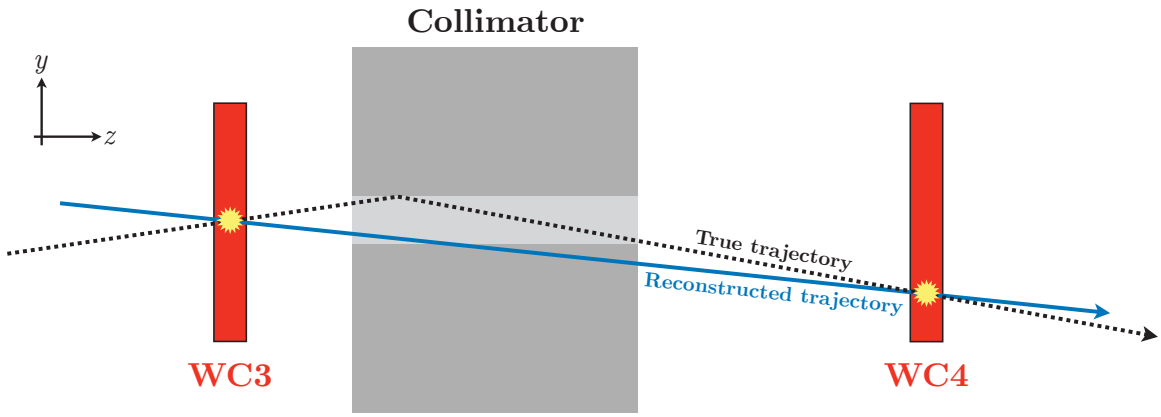

Figure 5.1: Illustration of the true trajectory of a particle scattering off the downstream collimator in the tertiary beamline, and the reconstructed trajectory of the particle. In this example, the WC3–WC4 track does not pass through the second aperture of the downstream collimator, thus the event is rejected.

Events with more than one possible time-of-flight values and a measured time of flight below 0 ns or above 200 ns are rejected. The reconstructed WC track momentum and time of flight distributions from the Run-II −100 A dataset after the above cuts have been applied are shown in Fig. 5.2.

The squared mass can be computed as

$$m^2 = \frac{p_{\text{beam}}^2}{c^2}\left[\left(\frac{c\,\Delta t}{\ell_{\text{mean}}}\right)^2 - 1\right] \tag{5.1}$$

where p_{beam} is the reconstructed WC track momentum, Δt is the measured time of flight, and $\ell_{\text{mean}} = 6.652$ m is the mean flight distance of the particle in the tertiary beamline. Due to resolution effects of the time-of-flight detectors and the use of a mean flight distance, the m^2 distribution contains values below 0 MeV$^2/c^4$ as shown in Fig. 5.3. A lighter particle (electron, muon, or pion) may have a shorter flight distance than the mean ($\ell_{\text{true}} < \ell_{\text{mean}}$), along with a short time of flight, which can lead to $\frac{c\,\Delta t}{\ell_{\text{mean}}} < 1$ and result in $m^2 < 0$ MeV$^2/c^4$.

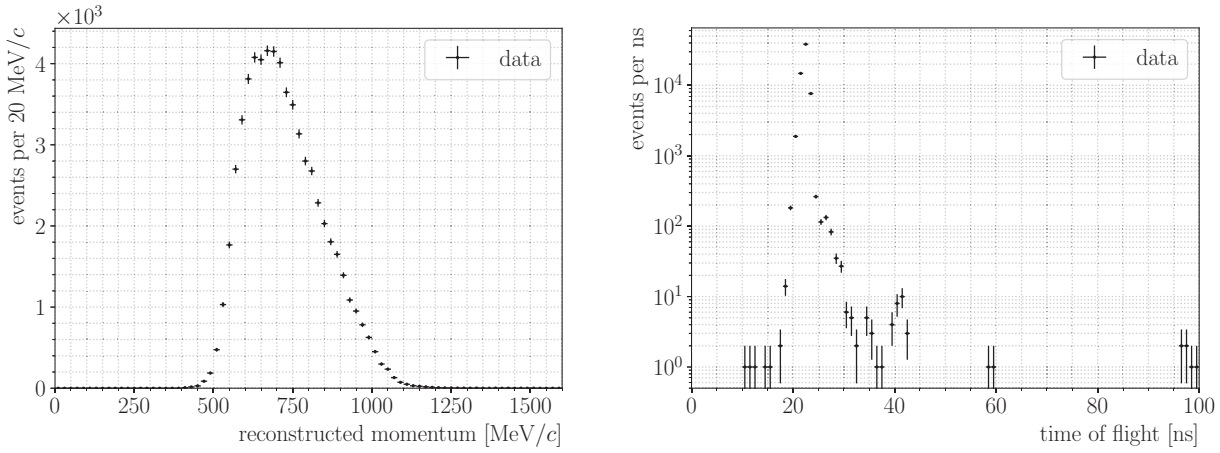

(a) Reconstructed WC track momentum in the Run-II −100 A dataset

(b) Time of flight in the Run-II −100 A dataset

Figure 5.2: Reconstructed WC track momentum and time of flight in the Run-II −100 A dataset.

Events with $m^2 > 350^2$ MeV$^2/c^4$ are rejected to reduce the number of K^- and $\bar{p}$ events in the data sample.

WC-to-TPC track matching procedure

We attempt to uniquely match a WC track to a TPC track in order to identify a primary TPC track candidate. The procedure is as follows:

(1) project the WC track into the TPC

(2) for each TPC track with an upstream-most point with $z < 4$ cm

  (2.1) compute the differences between the x and y positions of the WC track projected onto the front face of the TPC ($z = 0$ cm) and the upstream-most point of the TPC track, Δx and Δy

  (2.2) compute the angle α between the projected WC track vector and TPC track

(3) reject TPC tracks with $\Delta r \equiv \sqrt{(\Delta x)^2 + (\Delta y)^2} > 5$ cm or $\alpha > 13°$

(4) out of the remaining TPC tracks, the TPC track with the smallest Δr is selected to

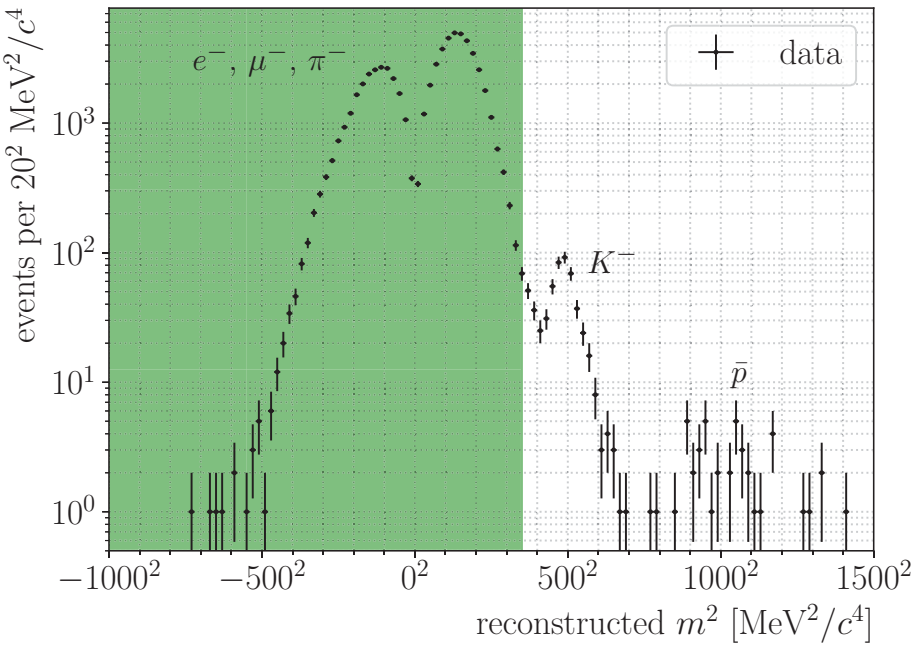

Figure 5.3: Squared mass computed from the reconstructed WC track momentum and measured time of flight in the Run-II −100 A dataset. Events that satisfy the $m^2 < 350^2$ MeV$^2/c^4$ criterion lie within the green-shaded region.

be the primary TPC track candidate.

The definitions of Δx, Δy, and α are illustrated in Fig. 5.4. A 2D histogram of Δx vs. Δy in the Run-II −100 A dataset is shown in Fig. 5.5; TPC tracks that satisfy the $\Delta r \equiv \sqrt{(\Delta x)^2 + (\Delta y)^2} < 5$ cm lie within the black circle. The distributions of Δr and α in the Run-II −100 A dataset are shown in Fig. 5.6. TPC tracks that satisfy the $\Delta r < 5$ cm criterion lie with the green-shaded region of Fig. 5.6a; TPC tracks that satisfy the $\alpha < 13°$ criterion lie within the green-shaded region of Fig. 5.6b.

The number of events satisfying each beamline-based selection in the Run-II −100 A dataset is shown in Table 5.1.

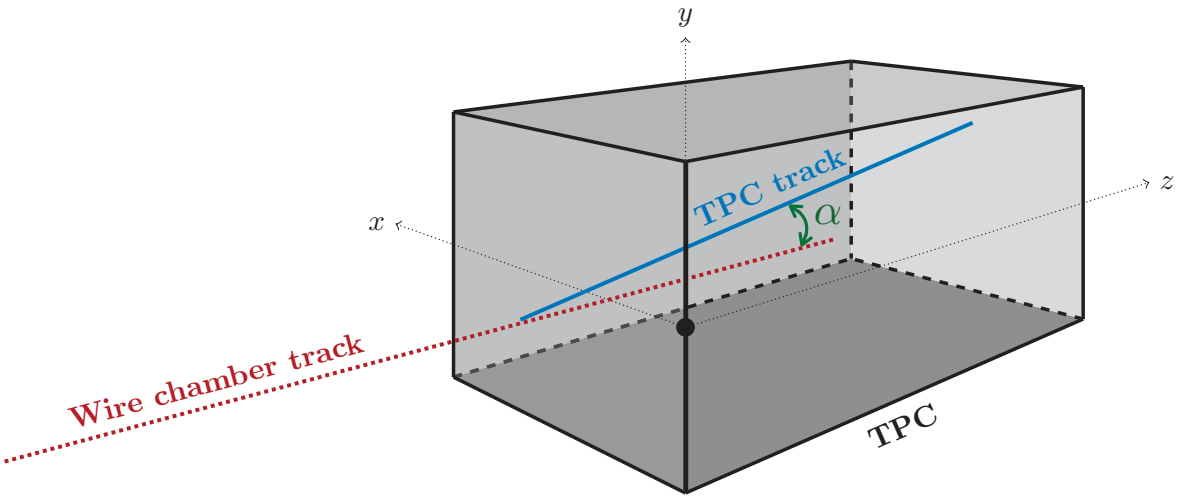

(a) Projection of the WC track into the TPC

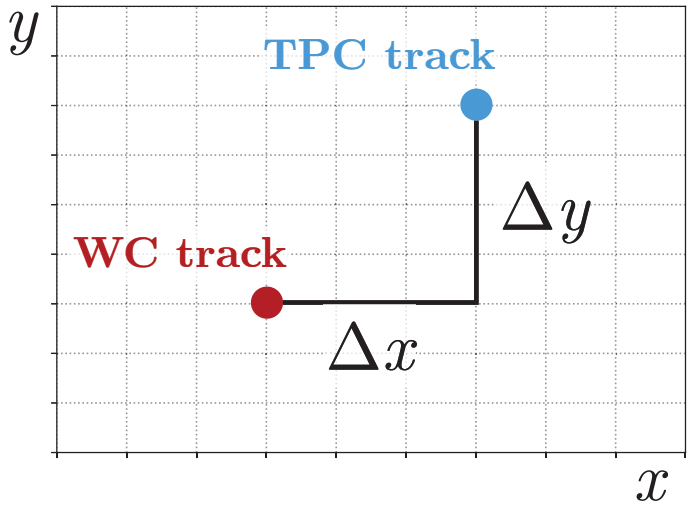

(b) Δx and Δy between the projected position of the WC track at the front face of the TPC and the upstream-most point of the TPC track

Figure 5.4: Illustration of the WC-to-TPC track matching procedure. The WC track is projected into the TPC; the angle between the projected WC track and a primary TPC track candidate is defined to be α. The differences between the x and y positions of the WC track projected onto the front face of the TPC and the upstream-most point of a primary TPC track candidate are defined to be Δx and Δy. The upsteam-most point of the TPC track must satisfy the $z < 4$ cm criterion in order to be considered.

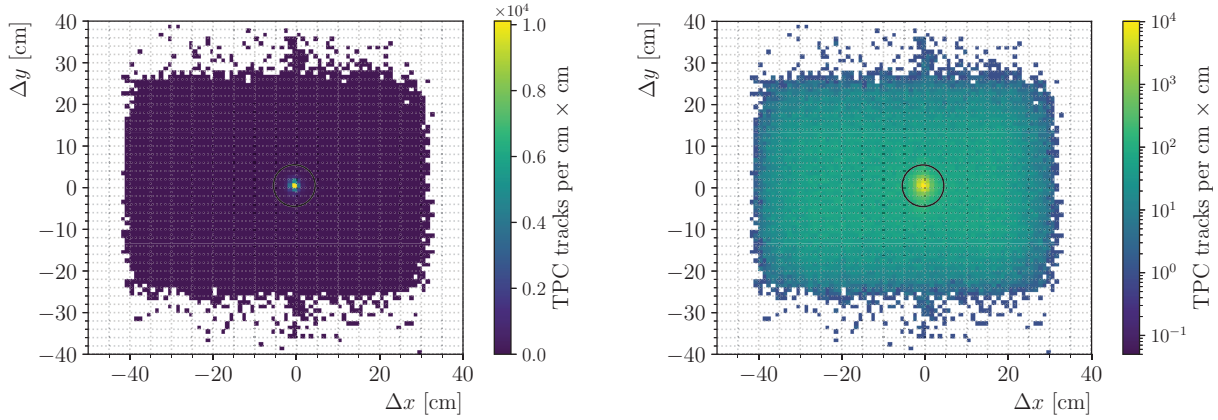

(a) Linearly scaled color bar

(b) Logarithmically scaled color bar

Figure 5.5: 2D histogram of Δx vs. Δy from the WC-to-TPC track matching procedure in the Run-II −100 A dataset. TPC tracks that satisfy the $\Delta r < 5$ cm criterion lie within the black circle. The background is due to beam halo pile-up.

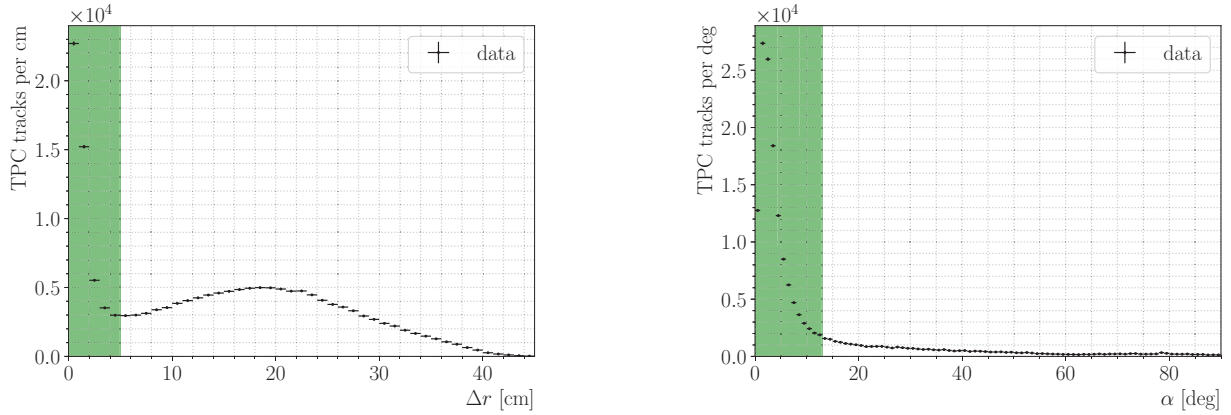

(a) TPC tracks that satisfy the $\Delta r < 5$ cm criterion lie within the green-shaded region

(b) TPC tracks that satisfy the $\alpha < 13°$ criterion lie within the green-shaded region

Figure 5.6: Distributions of Δr and α from the WC-to-TPC track matching procedure in the Run-II −100 A dataset.

5.1.2 Data-constrained re-weighting of fractional particle content in MC

The G4beamline [63] simulation can be used to estimate the particle content of the tertiary beamline. The momentum spectra of the tertiary beam are shown in Fig. 5.7 where the colored stacked histograms are categorized based on the particle species at WC4 predicted by G4beamline. As shown in Fig. 5.8, we can subcategorize the π^- category into the particle species of the reconstructed TPC track that is matched to the WC track and the source of the particle:

(a) μ^- that comes from π^- decaying in the tertiary beam upstream of WC4,

(b) halo pile-up μ^- that comes from π^- decaying in the secondary beam—i.e., π^- WC track mismatched to a halo pile-up μ^- track in the TPC, and

(c) π^- that penetrates into the TPC volume and has a proper WC/TPC track match.

This subcategorization reveals that there is a non-negligible fraction of halo pile-up μ^- TPC tracks that are matched to a WC track. It is important to note that the momenta of the actual halo pile-up muons in the μ^- (b) subcategory is not what is represented in Fig. 5.8, as the momenta of the halo pile-up muons are at much higher momenta ($\sim$32 GeV/c to $\sim$64 GeV/c)—the momenta in Fig. 5.8 represents the momenta of the original simulated particle in the tertiary beam at WC4.

Let us define the *interacting length* as the length of the reconstructed track within the fiducial region up to the interaction point of interacting events (Fig. 5.9a), and the *non-interacting length* as the length of the reconstructed track within the fiducial region of non-interacting events. (Fig. 5.9b). The interacting length and non-interacting length distributions for the Run-II -60 A and -100 A datasets are shown in Fig. 5.10 and they reveal to us that

- there may be an excess of μ^- in the MC prediction in both datasets,
- there may be a deficit of π^- in the MC prediction in the -60 A dataset, and

- there may be a deficit of e^- in the MC prediction in the -100 A dataset.

The MC distributions in Fig. 5.10 all have fairly unique shapes:

- **π^-/μ^- (a)/μ^- (b) (all three shades of blue):**

  Pions and muons in this category span both the interacting length and non-interacting length distributions.

- **μ^- (purple):**

  Muons with enough energy to penetrate the full length of the detector populate the 65 cm to 75 cm region of the non-interacting length distribution.

- **e^- (orange):**

  Electrons interact right away, so they populate the first 20 cm of the interacting length distribution.

With this in mind, we can perform a data-constrained template fit to re-weight the distributions.

Let us begin with the histograms of the interacting length and non-interacting length (Fig. 5.10). Suppose that x_k, f_k, g_k, and h_k are the values in the k^{th} bin of the data, MC π^-, MC μ^-, and MC e^- histograms, respectively, with $\Delta s_k = 1$ cm bin widths. If the histograms are area-normalized, i.e.,

$$\sum_k x_k \, \Delta s_k = 1, \qquad \sum_k f_k \, \Delta s_k = 1, \qquad \sum_k g_k \, \Delta s_k = 1, \qquad \sum_k h_k \, \Delta s_k = 1, \quad (5.2)$$

we can write down our model fit parameters as

$$\lambda_k = C_\pi \, f_k + C_\mu \, g_k + C_e \, h_k \quad (5.3)$$

where C_π, C_μ, and C_e are the fractional contents of π^-, μ^-, and e^- in the tertiary beam at

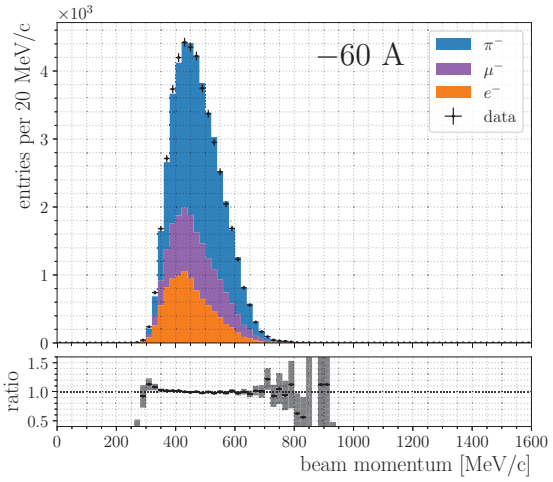

(a) Run-II −60 A dataset and data-driven Monte Carlo simulation

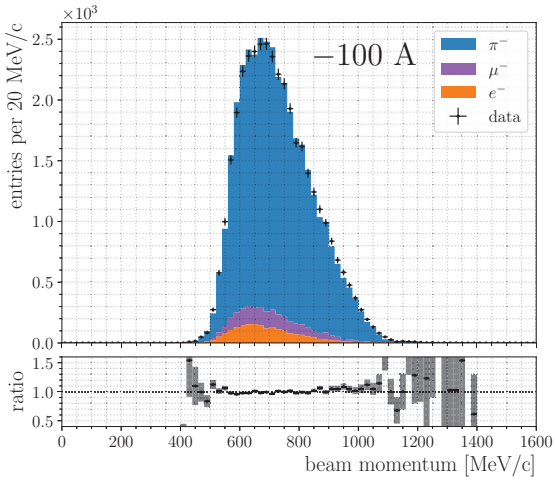

(b) Run-II −100 A dataset and data-driven Monte Carlo simulation

Figure 5.7: Momentum spectra of tertiary beam particles at WC4 for events that satisfy the WC/TPC match requirement. Data plotted with markers accompanied with statistical error bars, and data-driven Monte Carlo plotted with colored stacked histograms showing the MC predicted particle content.

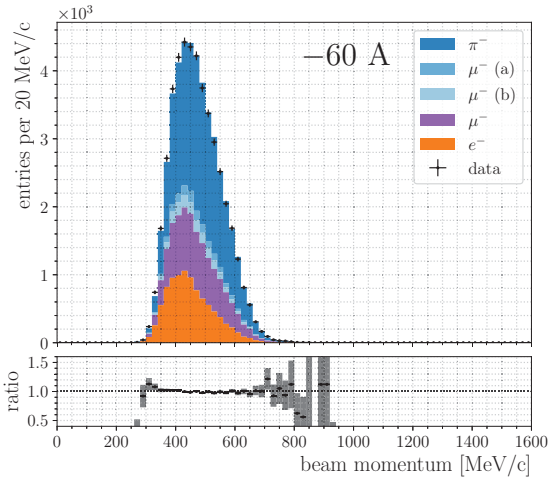

(a) Run-II −60 A dataset and data-driven Monte Carlo simulation

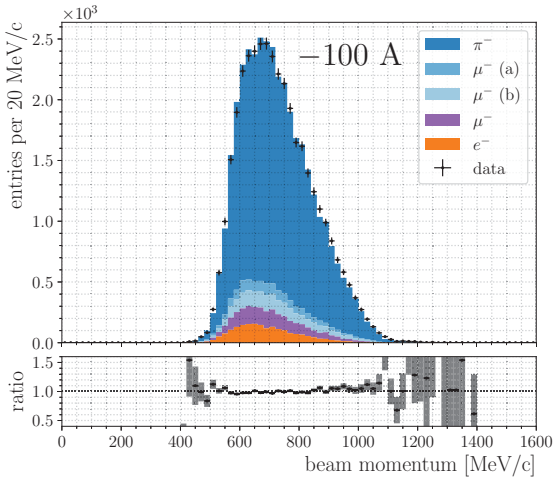

(b) Run-II −100 A dataset and data-driven Monte Carlo simulation

Figure 5.8: Momentum spectra of tertiary beam particles at WC4 for events that satisfy the WC/TPC match requirement. The π^- category is subcategorized: μ^- (a), if the WC track is matched to a TPC track of a μ^- from a π^- decaying upstream of WC4; μ^- (b), if the WC track is matched to a TPC track of a halo pile-up μ^- from the secondary beam; and π^-, if the π^- penetrates into the TPC volume and has a proper WC/TPC track match.

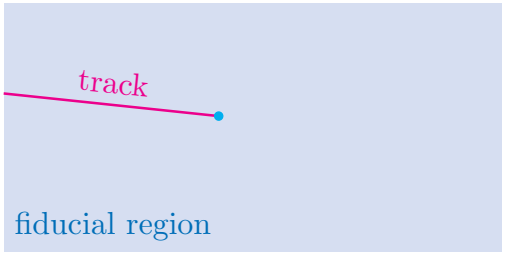

(a) Interacting event

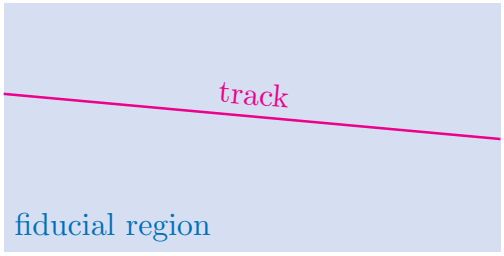

(b) Non-interacting event

Figure 5.9: The interacting length is defined to be the length of a reconstructed track within the fiducial region up to the interaction point of an interacting event. The non-interacting length is defined to be the length of a reconstructed track within the fiducial region of a non-interacting event.

WC4. Since this is a counting measurement, the probability of measuring a particular value x_k is given by the Poisson probability mass function

$$P(x_k \mid \lambda_k) = \frac{(\lambda_k)^{x_k} \exp(-\lambda_k)}{x_k!} \tag{5.4}$$

where x_k are our measurements and λ_k are parameters from our model. The likelihood (probability of the data given the model) of measuring the outcome in our experiment is

$$\mathcal{L}(\lambda \mid \text{data}) = P(\text{data} \mid \lambda) = \prod_k P(x_k \mid \lambda_k) = \prod_k \frac{(\lambda_k)^{x_k} \exp(-\lambda_k)}{x_k!}. \tag{5.5}$$

Taking the natural logarithm of the likelihood (Eq. 5.5) yields

$$\ln \mathcal{L} = \sum_k \left[x_k \ln(\lambda_k) - \lambda_k - \ln(x_k!) \right]. \tag{5.6}$$

We can fit for the parameters λ_k by maximizing the log-likelihood (Eq. 5.6). After fitting for C_π, C_μ, and C_e, we can compute the re-weighting parameters

$$w_\pi = \frac{N^{\text{MC}}_{\text{total}}}{N^{\text{MC}}_{\pi}} C_\pi, \qquad w_\mu = \frac{N^{\text{MC}}_{\text{total}}}{N^{\text{MC}}_{\mu}} C_\mu, \qquad w_e = \frac{N^{\text{MC}}_{\text{total}}}{N^{\text{MC}}_{e}} C_e, \tag{5.7}$$

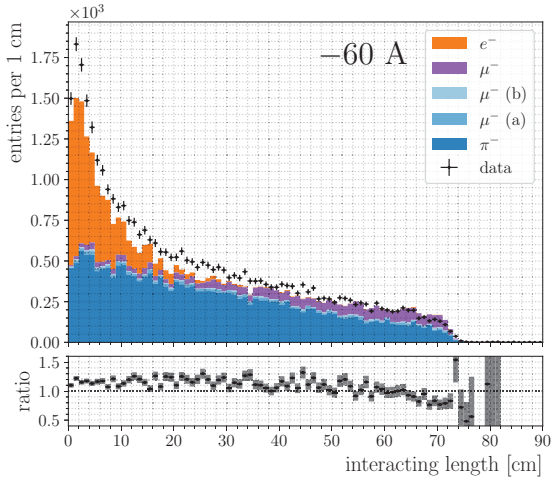

(a) Interacting length of the Run-II −60 A dataset

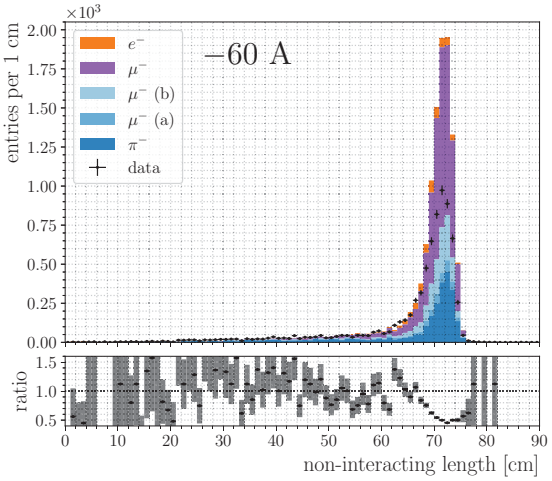

(b) Non-interacting length of the Run-II −60 A dataset

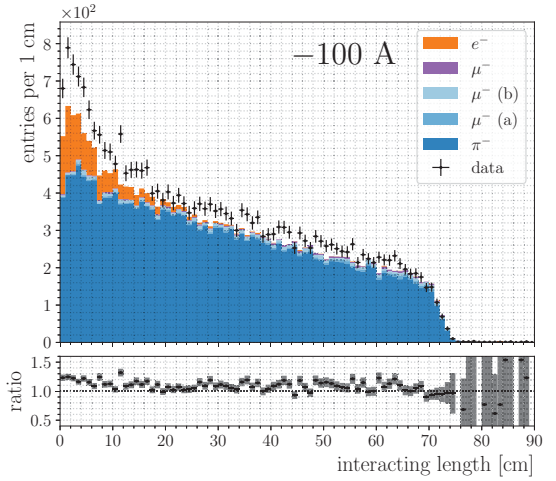

(c) Interacting length of the Run-II −100 A dataset

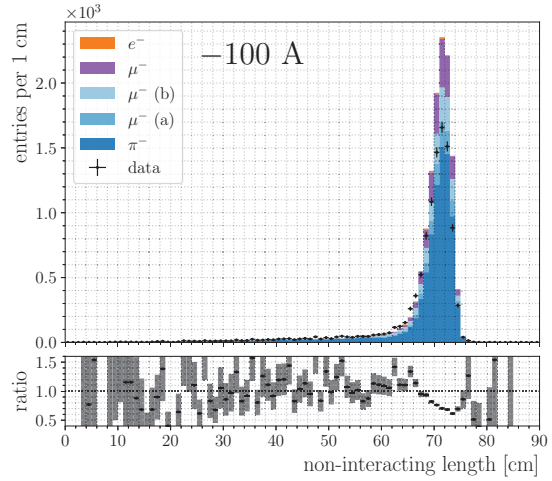

(d) Non-interacting length of the Run-II −100 A dataset

Figure 5.10: Interacting and non-interacting length of the Run-II −60 A and −100 A datasets.

Parameter	−60 A dataset	−100 A dataset
C_π	0.777	0.898
C_μ	0.004	0.000
C_e	0.219	0.102
w_π	1.327	1.005
w_μ	0.017	0.000
w_e	1.081	1.994

Table 5.2: Parameters from the template fit.

Particle species	Re-weighting parameter	−60 A dataset		−100 A dataset	
		DDMC	Re-weighted	DDMC	Re-weighted
π^-	w_π	0.507	0.673	0.804	0.807
μ^- (a)	w_π	0.031	0.041	0.037	0.037
μ^- (b)	w_π	0.047	0.063	0.053	0.054
μ^-	w_μ	0.212	0.004	0.055	0.000
e^-	w_e	0.203	0.219	0.051	0.102

Table 5.3: Fractional content of WC/TPC-matched particles in the −60 A and −100 A data-driven Monte Carlo samples before and after re-weighting. Muons are subcategorized based on their source.

where N_π^{MC}, N_μ^{MC}, and N_e^{MC} are the number of π^-, μ^-, and e^- events, respectively, and $N_{\mathrm{total}}^{\mathrm{MC}} = N_\pi^{\mathrm{MC}} + N_\mu^{\mathrm{MC}} + N_e^{\mathrm{MC}}$ is the total number of events in the Monte Carlo sample. A single template fit is done using both the interacting length and non-interacting length histograms simultaneously. Resulting parameters from the template fits are shown in Table 5.2. Adding the constraint $C_\pi + C_\mu + C_e = 1$ results in differences of less than 1% in the fit parameters.

The re-weighted interacting and non-interacting length distributions are shown in Fig. 5.11. Table 5.4 lists the fractional content of the WC/TPC-matched particles. In both data sets,

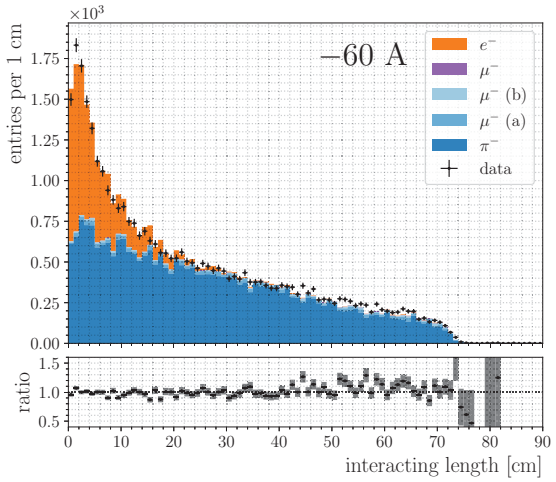

(a) Interacting length of the Run-II −60 A dataset after re-weighting

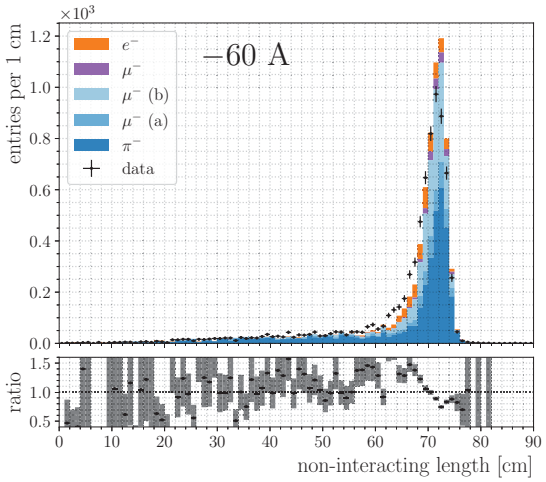

(b) Non-interacting length of the Run-II −60 A dataset after re-weighting

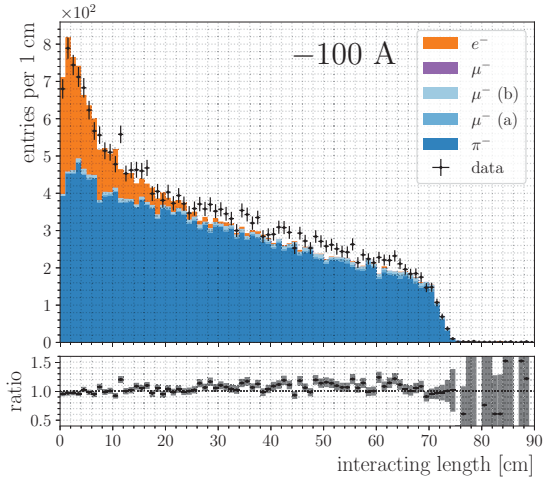

(c) Interacting length of the Run-II −100 A dataset after re-weighting

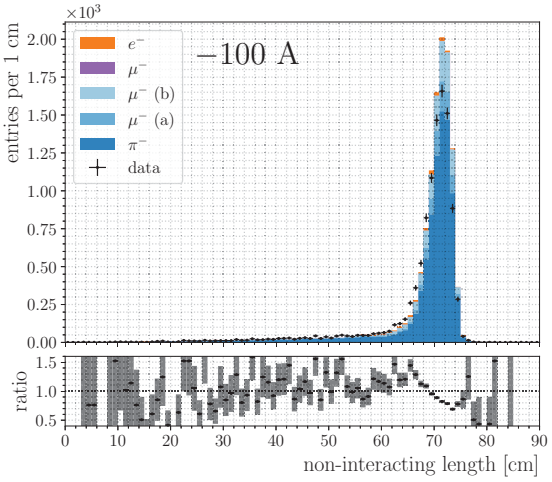

(d) Non-interacting of the Run-II −100 A dataset length after re-weighting

Figure 5.11: Interacting and non-interacting length of the Run-II −60 A and −100 A datasets after re-weighting.

Particle species	−60 A dataset		−100 A dataset	
	DDMC	Re-weighted	DDMC	Re-weighted
π^-	0.507	0.673	0.804	0.807
μ^-	0.290	0.108	0.145	0.091
e^-	0.203	0.219	0.051	0.102

Table 5.4: Fractional content of WC/TPC-matched particles in the −60 A and −100 A data-driven Monte Carlo samples before and after re-weighting. All muons are combined into a single fraction regardless of their source.

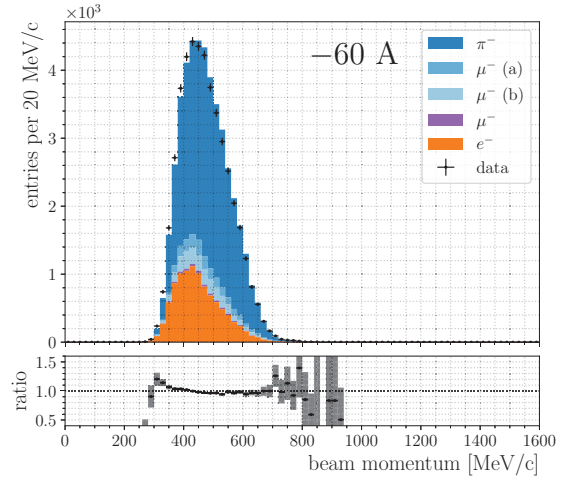

(a) Run-II −60 A dataset and data-driven Monte Carlo simulation after re-weighting

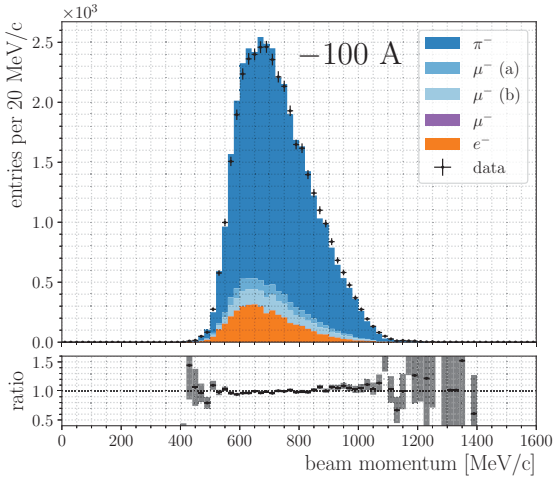

(b) Run-II −100 A dataset and data-driven Monte Carlo simulation after re-weighting

Figure 5.12: Momentum spectra of tertiary beam particles at WC4 (for events that satisfy the WC/TPC match requirement) after re-weighting. The π^- category is sub-categorized: μ^- (a), if the WC track is matched to a TPC track of a μ^- from a π^- decaying upstream of WC4; μ^- (b), if the WC track is matched to a TPC track of a halo pile-up μ^- from the secondary beam; and π^-, if the π^- penetrates into the TPC volume and has a proper WC/TPC track match.

the total μ^- content was reduced and the total e^- content was increased. In the Run-II -60 A dataset, the total μ^- fraction was reduced by 63% and the total e^- fraction was increased by 8%; in the Run-II -100 A dataset, the total μ^- fraction was reduced by 37% and the total e^- fraction was increased by 100%. We must be careful here in interpreting the results from the fit. The fit cannot distinguish between the different sources of muons in the beam, but instead is only sensitive to the total $\pi^-/\mu^-/e^-$ fraction.

5.1.3 Mitigation of electron background events

We leverage the topological difference between charged pions and electrons in the LArTPC to mitigate the electron background events in our analysis. Electrons in the tertiary beam that make it into the LArTPC can produce electromagnetic showers. When we apply the track reconstruction to an electron event, the primary electron and its numerous descendant electrons are reconstructed as multiple relatively short tracks.

Let us define the Molière region of an event as a cylinder of radius 10 cm (Molière radius in liquid argon) around the projected WC track inside the TPC, as illustrated in Fig. 5.13. Fig. 5.14 shows the distribution of the number of reconstructed tracks that lie entirely within the Molière region (primary tracks excluded). To mitigate the electron background, we reject events with more than 4 non-primary tracks that lie entirely within the Molière region. The number of events available for the cross section measurement after this rejection cut is listed in the last row of Table 5.1.

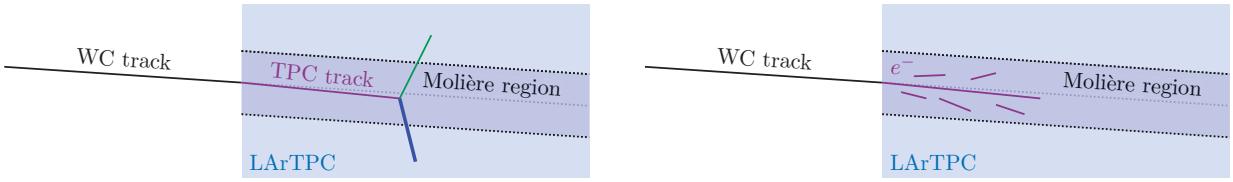

(a) Illustration of an interacting π^- event in the LArTPC

(b) Illustration of an e^- event in the LArTPC

Figure 5.13: Diagrams illustrating Molière regions of two different events.

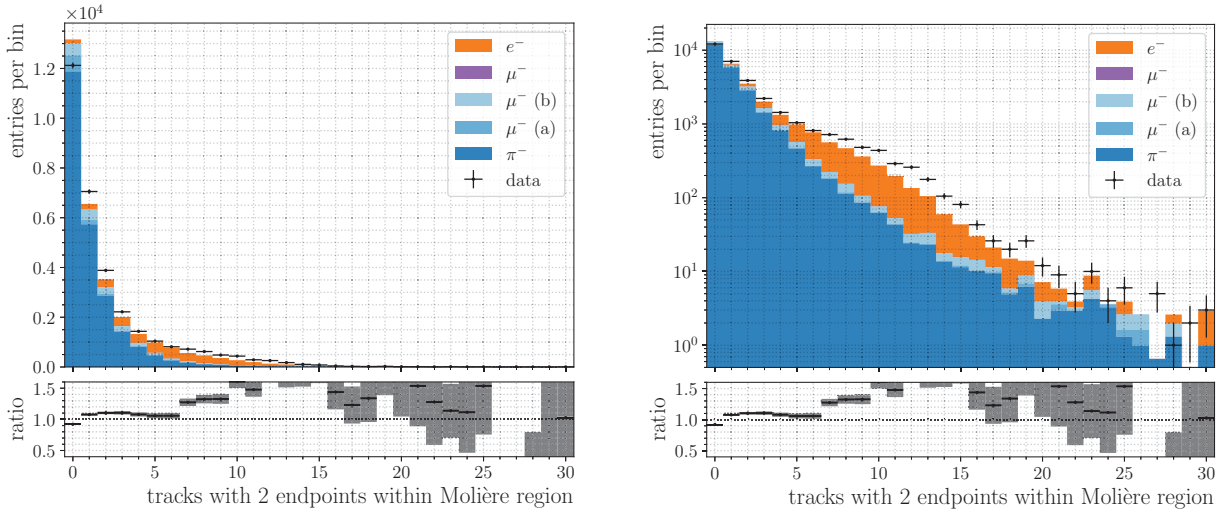

(a) Linear-linear plot

(b) Log-linear plot

Figure 5.14: Number of non-primary tracks that lie entirely within Molière region per event. To mitigate the electron background, we reject events with more than 4 non-primary tracks that lie entirely within the Molière region.

5.2 Cross Section

5.2.1 Thin-target approximation

The probability* for an interaction to occur in the target region $a \leq x \leq b$ is

$$\Pr[a \leq X \leq b] = \int_a^b \sigma n \, e^{-\sigma n x} \, \mathrm{d}x \tag{5.8}$$

where σ is the cross section per nucleon and n is the density of the target. For a target of uniform density and thickness Δx, we can choose $a = 0$ and $b = \Delta x$

$$\Pr[0 \leq X \leq \Delta x] = \int_0^{\Delta x} \sigma n \, e^{-\sigma n x} \, \mathrm{d}x = 1 - e^{-\sigma n \Delta x}. \tag{5.9}$$

Thus, the interacting and non-interacting probabilities for a target of thickness Δx are

$$\begin{aligned} P^{\Delta x}_{\text{interacting}} &= 1 - e^{-\sigma n \Delta x}, \\ P^{\Delta x}_{\text{non-interacting}} &= 1 - P^{\Delta x}_{\text{interacting}} = e^{-\sigma n \Delta x}. \end{aligned} \tag{5.10}$$

Let us suppose that in our laboratory, we have

(a) a particle gun that can fire single particles at some fixed energy, E, and

(b) a collection of N targets of various, unique thicknesses (we know the exact thickness of each target and no two targets have the same thickness).

Let us also suppose that, for whatever reason, we are only able to use each target exactly once. In our experiment, we want to determine the cross section at a fixed energy, $\sigma(E)$; we set up our experiment in such a way that our single-particle gun fires a particle of energy E

*The probability density function is $f(x) = \sigma n \, e^{-\sigma n x}$.

at a single fixed target of thickness Δx_i. After firing a single particle at the target, we must discard the i^{th} target and replace it with a new target of different thickness Δx_ℓ ($\ell \neq i$). Since we have N targets, we are able to perform N independent trials.

Suppose in the outcome of our experiment we have counted N_{int} interacting particles and $N_{\text{non-int}}$ non-interacting particles (with $N = N_{\text{int}} + N_{\text{non-int}}$). The likelihood (probability of a dataset given the model parameters) of measuring this outcome is

$$\begin{aligned}\mathcal{L}(\sigma \mid \text{data}) = P(\text{data} \mid \sigma) &= \prod_j^{N_{\text{int}}} P_{\text{interacting}}^{\Delta x_j} \prod_k^{N_{\text{non-int}}} P_{\text{non-interacting}}^{\Delta x_k} \\ &= \prod_j^{N_{\text{int}}} (1 - e^{-\sigma n \Delta x_j}) \prod_k^{N_{\text{non-int}}} e^{-\sigma n \Delta x_k}\end{aligned} \tag{5.11}$$

where Δx_j is the thickness of the j^{th} target (out of N_{int}) in which an interaction occurred, Δx_k is the thickness of the k^{th} target (out of $N_{\text{non-int}}$) in which there was no interaction, and σ is the parameter in our model; we can use maximum likelihood estimation to fit for the parameter σ. Taking the natural logarithm of the likelihood (Eq. 5.11) yields

$$\begin{aligned}\ln \mathcal{L} &= \sum_j^{N_{\text{int}}} \ln(1 - e^{-\sigma n \Delta x_j}) + \sum_k^{N_{\text{non-int}}} \ln(e^{-\sigma n \Delta x_k}) \\ &= \sum_j^{N_{\text{int}}} \ln(1 - e^{-\sigma n \Delta x_j}) + \sum_k^{N_{\text{non-int}}} (-\sigma n \Delta x_k).\end{aligned} \tag{5.12}$$

To maximize the likelihood, we take the partial derivative of Eq. 5.12 with respect to the fit

Quantity	Symbol	Value
Avogadro constant	N_{A}	$6.022\,140\,76 \times 10^{23}$ mol^{-1}
molar mass of argon	M_{Ar}	$39.948(1)$ g $\cdot$ mol^{-1}
density of liquid argon	ρ	$1396(1)$ kg $\cdot$ m^{-3}
mean track pitch	$\langle \Delta x \rangle$	4.6 mm

Table 5.5: Physical constants for computing $n\langle \Delta x \rangle$. Values taken from [29, 79–81].

parameter σ and set it to zero, $\frac{\partial}{\partial \sigma} \ln \mathcal{L} = 0$,

$$\begin{aligned} \frac{\partial}{\partial \sigma} \ln \mathcal{L} &= \sum_{j}^{N_{\text{int}}} \frac{\partial}{\partial \sigma} \ln(1 - e^{-\sigma n \Delta x_j}) + \sum_{k}^{N_{\text{non-int}}} \frac{\partial}{\partial \sigma}(-\sigma n \Delta x_k) \\ &= \sum_{j}^{N_{\text{int}}} \frac{(n\Delta x_j)\, e^{-\sigma n \Delta x_j}}{1 - e^{-\sigma n \Delta x_j}} - \sum_{k}^{N_{\text{non-int}}} n \Delta x_k \\ &= \sum_{j}^{N_{\text{int}}} \frac{n \Delta x_j}{e^{\sigma n \Delta x_j} - 1} - \sum_{k}^{N_{\text{non-int}}} n \Delta x_k = 0. \end{aligned} \tag{5.13}$$

Computationally, we can run a minimizer program (such as `MINUIT` [78] or `iminuit`*) to minimize the negative log-likelihood (which is equivalent to maximizing the likelihood), i.e., minimizing the negative of Eq. 5.12

$$-\ln \mathcal{L} = -\sum_{j}^{N_{\text{int}}} \ln(1 - e^{-\sigma n \Delta x_j}) + \sum_{k}^{N_{\text{non-int}}} \sigma n \Delta x_k \tag{5.14}$$

while varying the fit parameter σ.

In LArIAT, we make the assumption that $\sigma n \langle \Delta x \rangle$ is small enough such that higher-order

*`iminuit` is a Python interface to the `MINUIT2` C++ package: `https://github.com/scikit-hep/iminuit`

terms, $\mathcal{O}[(\sigma n\langle\Delta x\rangle)^2]$, are negligible. Let us compute $n\langle\Delta x\rangle$ using values from Table 5.5:

$$n = \frac{\rho \cdot N_{\mathrm{A}}}{M_{\mathrm{Ar}}} = \frac{\left(1396\ \frac{\mathrm{kg}}{\mathrm{m}^3}\right) \cdot \left(10^3\ \frac{\mathrm{g}}{\mathrm{kg}}\right) \cdot \left(6.022\,140\,76 \times 10^{23}\ \mathrm{mol}^{-1}\right)}{39.948\ \frac{\mathrm{g}}{\mathrm{mol}}} \tag{5.15}$$

$$= 2.104\,46 \times 10^{28}\ \mathrm{m}^{-3} = 2.104\,46 \times 10^{-2}\ \mathrm{cm}^{-1} \cdot \mathrm{b}^{-1}$$

$$n\langle\Delta x\rangle = \frac{1}{103.3 \times 10^{-28}\ \mathrm{m}^2} = \frac{1}{103.3\ \mathrm{b}} \sim 0.01\ \mathrm{b}^{-1}. \tag{5.16}$$

Since the π^-–argon cross section is on the order of $\sim$1 b (Fig. 2.10), we have $\sigma n\langle\Delta x\rangle \sim 10^{-2}$. Under this assumption, we can make an approximation in Eq. 5.13

$$\frac{\partial}{\partial\sigma}\ln\mathcal{L} = \sum_j^{N_{\text{int}}} \frac{n\Delta x_j}{e^{\sigma n\Delta x_j} - 1} - \sum_k^{N_{\text{non-int}}} n\Delta x_k = 0 \tag{5.13}$$

$$\approx \sum_j^{N_{\text{int}}} \frac{n\Delta x_j}{(1 + \sigma n\Delta x_j + \mathcal{O}[(\sigma n\Delta x_j)^2]) - 1} - \sum_k^{N_{\text{non-int}}} n\Delta x_k \tag{5.17a}$$

$$\approx \sum_j^{N_{\text{int}}} \frac{n\Delta x_j}{\sigma n\Delta x_j} - \sum_k^{N_{\text{non-int}}} n\Delta x_k \tag{5.17b}$$

$$\approx \sum_j^{N_{\text{int}}} \frac{1}{\sigma} - \sum_k^{N_{\text{non-int}}} n\Delta x_k \tag{5.17c}$$

$$\approx \frac{1}{\sigma}\sum_j^{N_{\text{int}}} - \sum_k^{N_{\text{non-int}}} n\Delta x_k \tag{5.17d}$$

$$\approx \frac{1}{\sigma}N_{\text{int}} - \sum_k^{N_{\text{non-int}}} n\Delta x_k \approx 0. \tag{5.17e}$$

This leaves us with

$$\sigma \approx \frac{N_{\text{int}}}{n\sum_k^{N_{\text{non-int}}} \Delta x_k} = \frac{N_{\text{int}}}{n\langle\Delta x\rangle \sum_k^{N_{\text{non-int}}} \frac{\Delta x_k}{\langle\Delta x\rangle}}. \tag{5.18}$$

If we make the assumption that $\Delta x_j = \Delta x_k = \langle\Delta x\rangle$ for all j, k, i.e., all targets have the

same exact thickness, Eq. 5.13 becomes

$$\frac{\partial}{\partial\sigma}\ln\mathcal{L} = \sum_{j}^{N_{\text{int}}} \frac{n\Delta x_j}{e^{\sigma n\Delta x_j}-1} - \sum_{k}^{N_{\text{non-int}}} n\Delta x_k = 0 \tag{5.13}$$

$$= \sum_{j}^{N_{\text{int}}} \frac{n\langle\Delta x\rangle}{e^{\sigma n\langle\Delta x\rangle}-1} - \sum_{k}^{N_{\text{non-int}}} n\langle\Delta x\rangle \tag{5.19a}$$

$$= n\langle\Delta x\rangle\left(\frac{1}{e^{\sigma n\langle\Delta x\rangle}-1}\sum_{j}^{N_{\text{int}}} - \sum_{k}^{N_{\text{non-int}}}\right) \tag{5.19b}$$

$$= n\langle\Delta x\rangle\left(\frac{1}{e^{\sigma n\langle\Delta x\rangle}-1}N_{\text{int}} - N_{\text{non-int}}\right) = 0. \tag{5.19c}$$

Defining $N_{\text{inc}} = N = N_{\text{int}} + N_{\text{non-int}}$ as the total number of incident particles, we can rewrite Eq. 5.19c

$$\frac{1}{e^{\sigma n\langle\Delta x\rangle}-1}N_{\text{int}} = N_{\text{non-int}} \tag{5.20a}$$

$$\frac{N_{\text{int}}}{N_{\text{non-int}}} = e^{\sigma n\langle\Delta x\rangle} - 1 \tag{5.20b}$$

$$\frac{N_{\text{int}}}{N_{\text{non-int}}} + 1 = e^{\sigma n\langle\Delta x\rangle} \tag{5.20c}$$

$$\frac{N_{\text{int}} + N_{\text{non-int}}}{N_{\text{non-int}}} = \frac{N_{\text{inc}}}{N_{\text{non-int}}} = e^{\sigma n\langle\Delta x\rangle} \tag{5.20d}$$

$$\frac{N_{\text{non-int}}}{N_{\text{inc}}} = e^{-\sigma n\langle\Delta x\rangle} = P^{\langle\Delta x\rangle}_{\text{non-interacting}}. \tag{5.20e}$$

Finally, subtracting Eq. 5.20e from 1 yields

$$\frac{N_{\text{int}}}{N_{\text{inc}}} = 1 - e^{-\sigma n\langle\Delta x\rangle} = P^{\langle\Delta x\rangle}_{\text{interacting}}. \tag{5.21}$$

Under the assumption that $\sigma n\langle\Delta x\rangle \ll 1$, Eq. 5.21 can be approximated as

$$\sigma \approx \frac{1}{n\langle\Delta x\rangle}\frac{N_{\text{int}}}{N_{\text{inc}}}. \tag{5.22}$$

5.2.2 *Thin-slab method*

The interaction length of $\pi^{\pm}$ in liquid argon is expected to be on the order of

$$\frac{1}{n\,\sigma(E_{\text{kinetic}} > 400\text{ MeV})} \simeq \frac{1}{n\,(1.0\text{ b})} \simeq 50\text{ cm} \tag{5.23a}$$

for kinetic energies above 400 MeV and

$$\frac{1}{n\,\sigma(E_{\text{kinetic}} < 400\text{ MeV})} \simeq \frac{1}{n\,(1.7\text{ b})} \simeq 30\text{ cm} \tag{5.23b}$$

for kinetic energies below 400 MeV; the length of the LArIAT TPC is 90 cm. Although the active volume of the LArIAT TPC is a big block of liquid argon rather than a thin target, the high granularity of the LArTPC enables us to treat the volume of argon as a series of adjacent thin slabs.

The induction and collection planes of the LArIAT TPC each consist of 240 wires with a wire pitch and interplanar spacing of 4 mm (Figs. 3.10 and 3.11). The wires are oriented at $\pm 60^{\circ}$ with respect to the z axis in the y–z plane, while the beam axis is oriented at -3° with respect to the z axis in the x–z plane. Thus, the trajectory of charged particles in the liquid argon volume are reconstructed with an average track pitch of

$$\langle \Delta z \rangle \approx \frac{4\text{ mm}}{\sin(60^{\circ})\cos(3^{\circ})} \approx 4.6\text{ mm} \tag{5.24}$$

as illustrated in Fig. 5.15. The charge collected on the collection plane wires is proportional to the energy deposited, so one can think of dividing the TPC into a series of thin slabs (or targets) of average thickness $\langle \Delta z \rangle \approx 4.6$ mm along the trajectory of the incident charged particle with the deposited energy measured by the wire of each slab. A simplified illustration of this method is shown in Fig. 5.18.

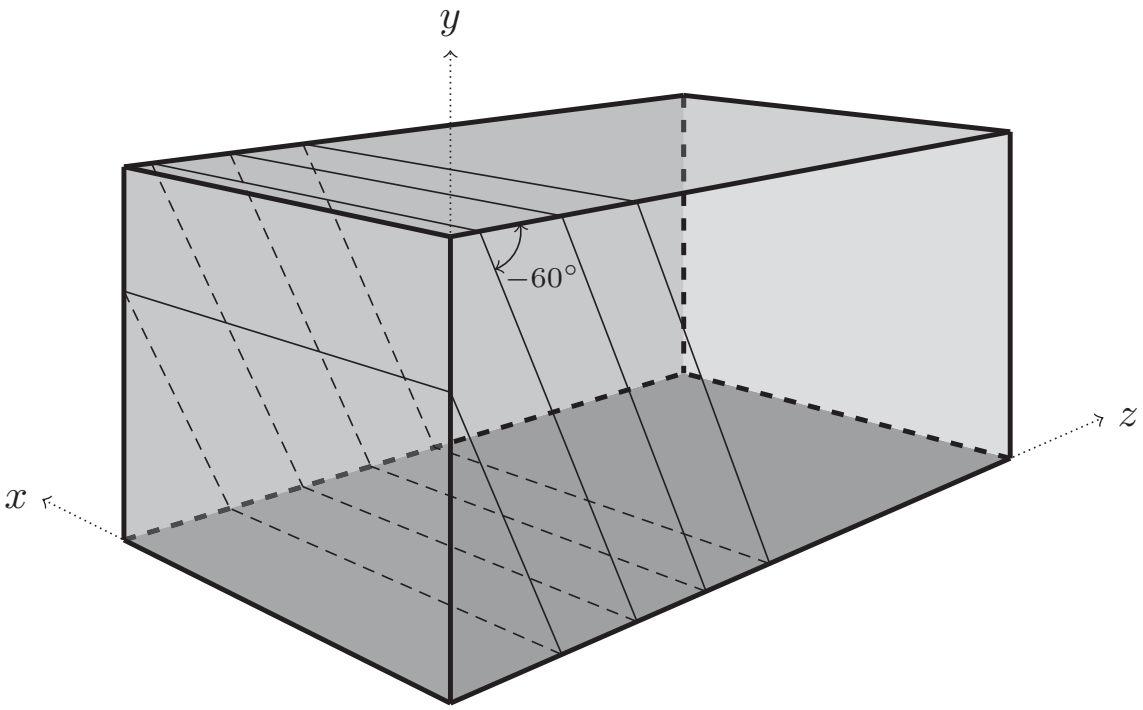

(a) 3-dimensional schematic, modified from Ref. [67]

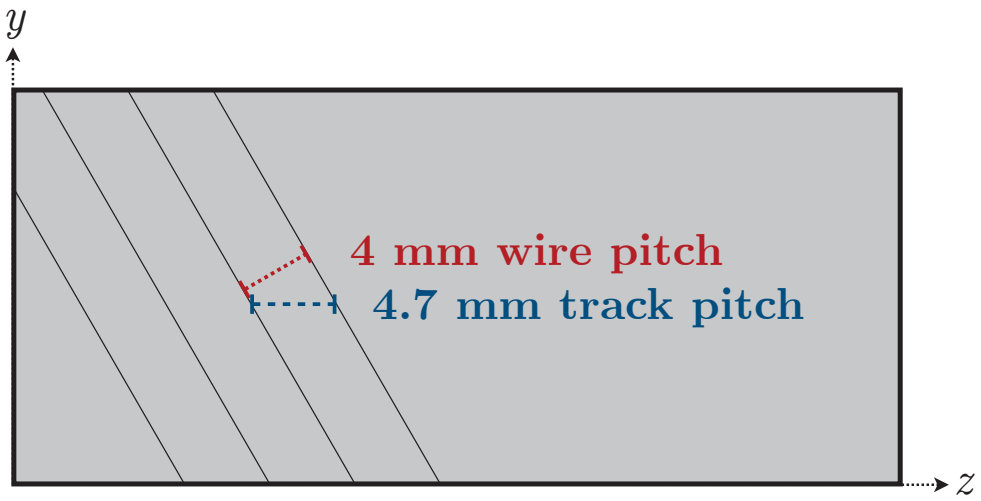

(b) 2-dimensional schematic in the y–z plane

Figure 5.15: Schematic diagram of the LArIAT TPC showing the 4 mm wire pitch and 4.6 mm track pitch in the collection plane. The beam axis is oriented at $-3°$ from the z axis in the x–z plane.

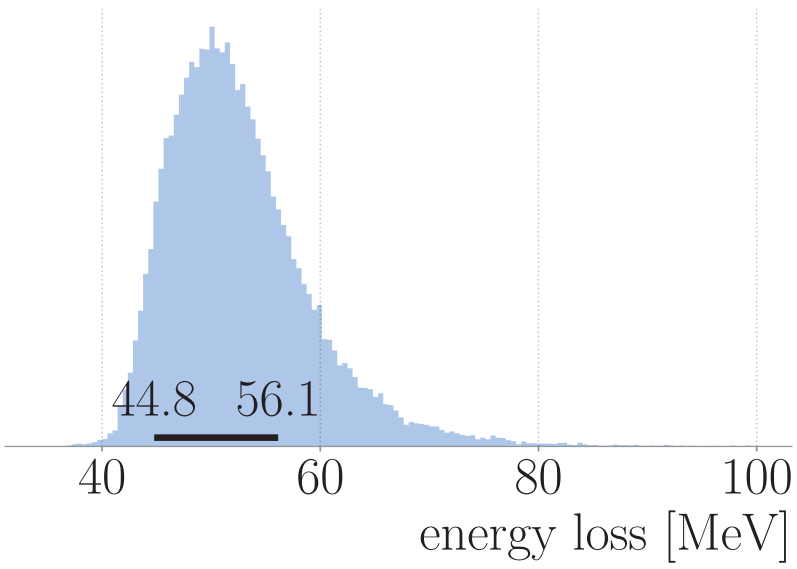

Figure 5.16: Distribution of energy loss in the uninstrumented material between WC4 and the front face of TPC as estimated from the −100 A DDMC simulation. The mode (most probable value) of the distribution is 50 MeV. The horizontal black line at the bottom of the distribution indicates the 68.3% highest density interval.

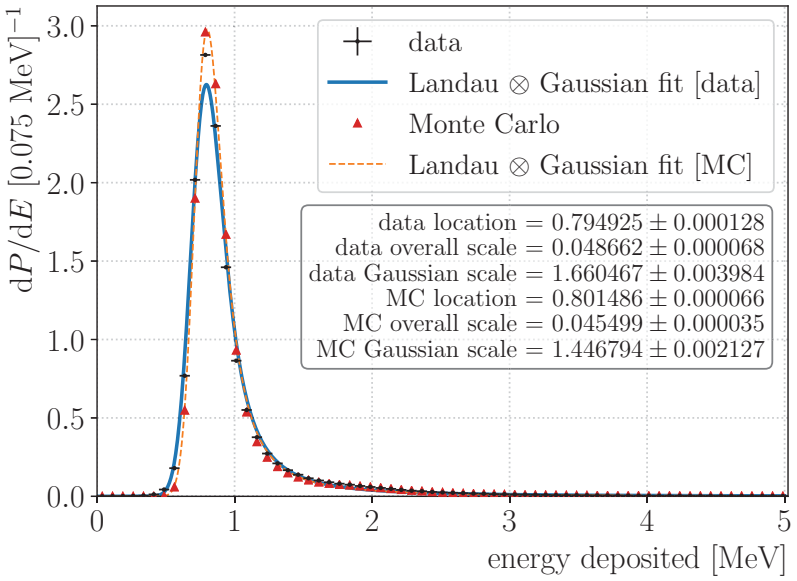

Figure 5.17: Distribution of energy deposited in a slab of argon, $E_i^{\text{deposited}}$, from the Run-II −100 A dataset and DDMC simulation. The data and Monte Carlo distributions are fit to a convolution of a Landau distribution and a Gaussian distribution. The width of the Landau ⊗ Gaussian fit is 0.0808 MeV for data and 0.0658 MeV for Monte Carlo.

Suppose we have an incident $\pi^{\pm}$ with kinetic energy of $E_{\text{beam}}^{\text{kinetic}}$ at WC4 measured by the beamline wire chambers. There is a $\sim$100 cm distance between WC4 and the front face of the TPC (start of active liquid argon volume) in which the $\pi^{\pm}$ loses some amount of energy E_{loss}; this distribution of energy loss in uninstrumented material is estimated from the -100 A DDMC simulation as shown in Fig. 5.16. Given that we know the kinetic energy of the $\pi^{\pm}$ to be $E_0^{\text{kinetic}} \equiv E_{\text{beam}}^{\text{kinetic}} - E_{\text{loss}}$ at the front face of the TPC, we can use the energy deposited by the $\pi^{\pm}$ in each slab to keep track of its kinetic energy as it propagates through the TPC. The kinetic energy of the $\pi^{\pm}$ at the j^{th} slab can be written as

$$\begin{aligned} E_j^{\text{kinetic}} &= E_0^{\text{kinetic}} - \sum_{i<j}^{j-1} E_i^{\text{deposited}} \\ &= E_{\text{beam}}^{\text{kinetic}} - E_{\text{loss}} - \sum_{i<j}^{j-1} E_i^{\text{deposited}} \\ &= \sqrt{(p_{\text{beam}}c)^2 + (mc^2)^2} - mc^2 - E_{\text{loss}} - \sum_{i<j}^{j-1} E_i^{\text{deposited}} \end{aligned} \tag{5.25}$$

where p_{beam} is the measured momentum, m is the mass, and $E_i^{\text{deposited}}$ is the energy deposited in the i^{th} slab. The distribution of energy deposited in a slab of argon from the Run-II 100 A dataset and DDMC simulation is shown in Fig. 5.17. Fig. 5.19a depicts a $\pi^{\pm}$ propagating through 9 slabs of LAr labeled A to I, before interacting in the 10^{th} slab labeled J. At slab A, the kinetic energy of the $\pi^{\pm}$ is $E_A^{\text{kinetic}} = E_0^{\text{kinetic}}$; at slab B, the kinetic energy of the $\pi^{\pm}$ is $E_B^{\text{kinetic}} = E_0^{\text{kinetic}} - E_A^{\text{deposited}}$; at slab C, the kinetic energy of the $\pi^{\pm}$ is $E_C^{\text{kinetic}} = E_0^{\text{kinetic}} - E_A^{\text{deposited}} - E_B^{\text{deposited}}$; and so forth. Let us keep track of the kinetic energy in slabs where the $\pi^{\pm}$ did not interact in a *non-interacting histogram* and the kinetic energy in slabs where it does interacts in an *interacting histogram* as illustrated in Figs. 5.19b and 5.19c, respectively, noting that this is for a single event. Doing this over an ensemble of events will yield interacting and non-interacting histograms that resemble the ones illustrated in Fig. 5.20.

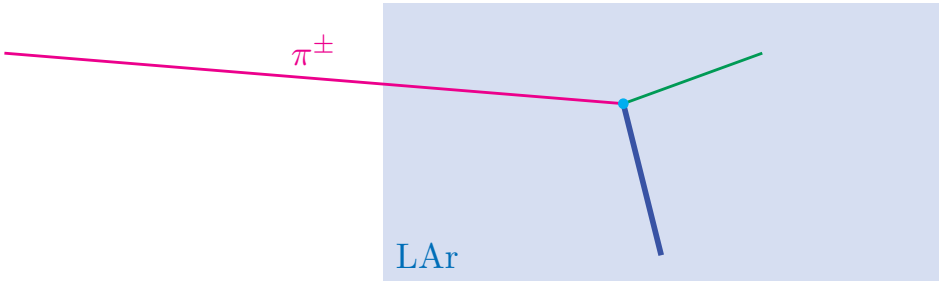

(a) Illustration of a $\pi^{\pm}$ propagating from left to right through the liquid argon volume in LArIAT TPC before interacting within the volume

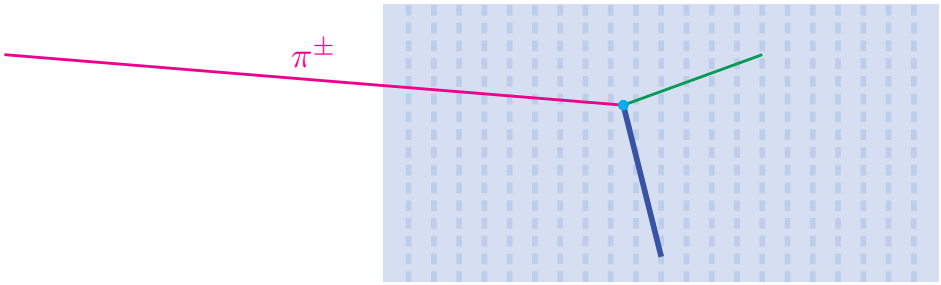

(b) TPC divided into thin slabs

Figure 5.18: LArIAT TPC divided into thin slabs with thicknesses determined by the collection plane wires and reconstructed track pitches.

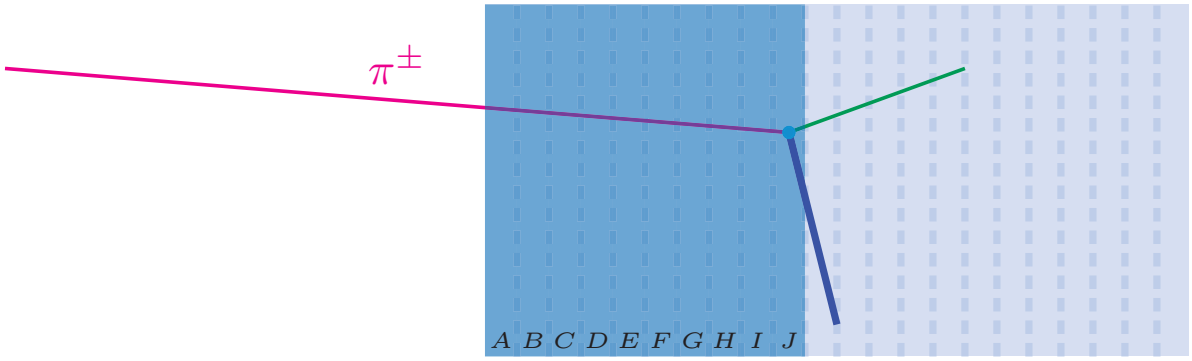

(a) Energy deposited by incident $\pi^{\pm}$ in labeled slabs

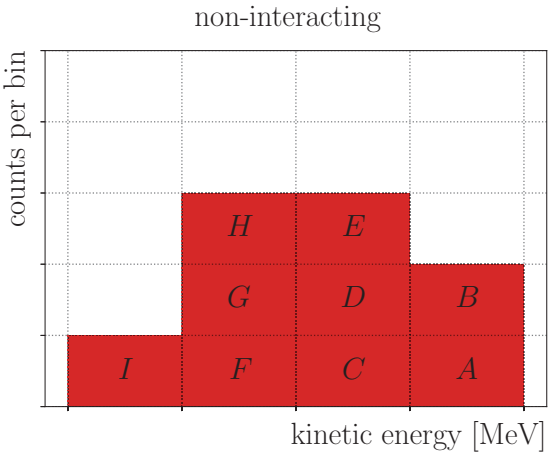

(b) Non-interacting histogram

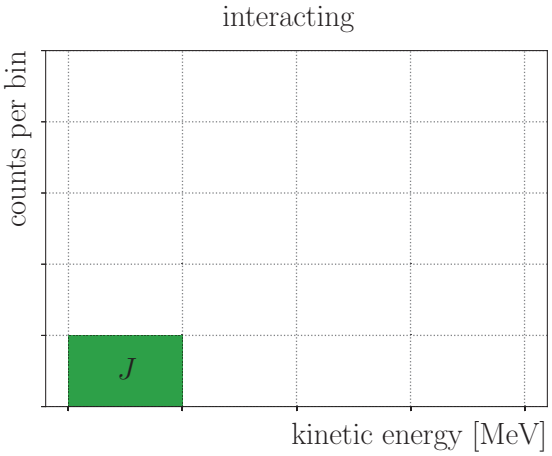

(c) Interacting histogram

Figure 5.19: Example of non-interacting and interacting histograms for the illustrated $\pi^{\pm}$ interaction event.

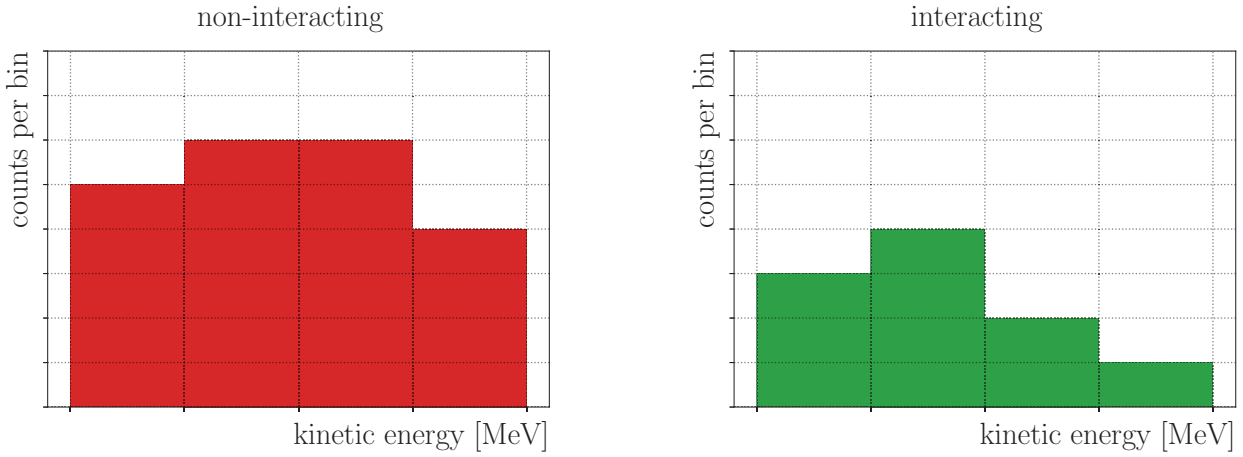

(a) Example of a non-interacting histogram

(b) Example of an interacting histogram

Figure 5.20: Example of non-interacting and interacting histograms over an ensemble of events.

The cross section can now be estimated as a function of kinetic energy on a bin-by-bin basis with the interacting and non-interacting histograms using Eq. 5.18

$$\sigma(E_{\mathrm{a}} \leq E < E_{\mathrm{b}}) \approx \left.\frac{N_{\mathrm{int}}}{n\sum_{j}^{N_{\text{non-int}}} \Delta z_j}\right|_{E_{\mathrm{a}} \leq E < E_{\mathrm{b}}} = \frac{1}{n\langle \Delta z \rangle} \left.\frac{N_{\mathrm{int}}}{\sum_{j}^{N_{\text{non-int}}} \frac{\Delta z_j}{\langle \Delta z \rangle}}\right|_{E_{\mathrm{a}} \leq E < E_{\mathrm{b}}} \tag{5.18a}$$

where E_{a} and E_{b} are lower and upper bin edges, respectively. In Eq. 5.18, the numerator corresponds to a kinetic energy bin of the interacting histogram and the denominator corresponds to a kinetic energy bin of the non-interacting histogram where each entry is *weighted* by the thickness of the slab (track pitch). In our example, the entries in the non-interacting histogram in Fig. 5.19b for slabs A to I are weighted by the thicknesses of the slabs. The cross section estimate is then simply proportional to the ratio of the unweighted interacting histogram and the weighted non-interacting histogram. In LArIAT, cross sections are estimated on a bin-by-bin basis using 50 MeV kinetic energy bins. Demonstrations of estimating the π^{-}–Ar cross section from a toy Monte Carlo simulation are shown in Fig. 5.21.

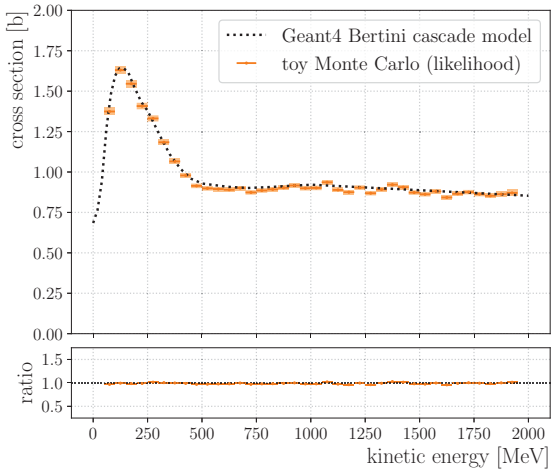

(a) Minimization of negative log-likelihood function (Eq. 5.14)

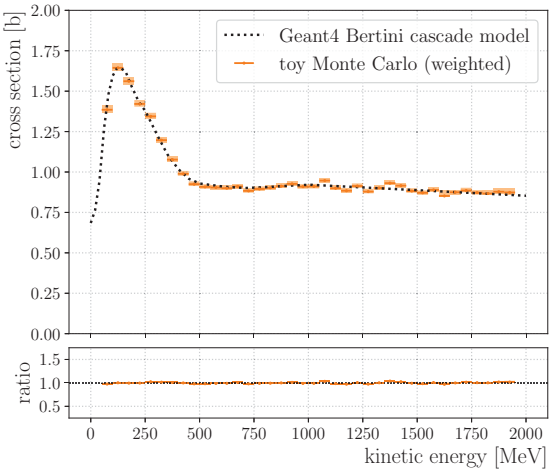

(b) Ratio of unweighted interacting and weighted non-interacting histograms (Eq. 5.18)

Figure 5.21: Demonstrations of estimating the π^-–Ar cross section with a toy Monte Carlo simulation by (a) minimizing the negative log-likelihood function and (b) by taking the ratio of the unweighted interacting and weighted non-interacting histograms.

5.2.3 Corrections to the cross section

Corrections must be made to Eq. 5.18 to account for the non-π^- background in the beam, failures in the tracking reconstruction, and smearing in the energy reconstruction. The categorization of interacting and non-interacting hits* relies heavily on whether the tracking reconstruction can properly identify a π^- interaction point. The failure to do so will result in hits being placed into the wrong histogram. Failures in the tracking reconstruction may come about from

(1) the tracking reconstruction not stopping at an interaction point, or

(2) the tracking reconstruction stopping before the interaction point.

In the case of **(1)**, hits at and after the interaction point will contaminate the non-interacting histogram; the hit at the interaction point will also be missing from the interacting histogram.

*From this point on, *hit* and *slab* will be used interchangeably.

In the case of **(2)**, what should have been hits after the track stopping point will be missing from the non-interacting histogram and the hit at the track stopping point will contaminate the interacting histogram. If there is an interaction point in case **(2)**, it will be missing from the interacting histogram. Additionally, electrons and muons from the secondary and tertiary beams that are selected in the selection process for the π^- track candidates will contaminate the interacting and non-interacting histograms. Mis-reconstruction of the deposited energy due to detector resolution effects can lead to biases and hits being placed into the wrong kinetic energy bins.

Any contamination in the histograms are to be accounted for in the form of a background subtraction, any interacting and non-interacting points missing from the histograms are to be accounted for in the form of an efficiency correction, and any hits placed into the wrong kinetic energy bin due to detector resolution effects are to be accounted for by unfolding. Let us rewrite Eq. 5.18 as

$$\sigma \approx \frac{1}{n} \frac{U_{\text{int}} \left[N_{\text{int}}^{\text{selected}} - N_{\text{int}}^{\text{background}} \right] \frac{1}{\epsilon_{\text{int}}}}{U_{\text{non-int}} \left[\sum_{j}^{N_{\text{non-int}}^{\text{selected}}} \Delta x_j - \sum_{k}^{N_{\text{non-int}}^{\text{background}}} \Delta x_k \right] \frac{1}{\epsilon_{\text{non-int}}}} \tag{5.26}$$

where $N_{\text{int}}^{\text{selected}}$ and $N_{\text{non-int}}^{\text{selected}}$ are the numbers of selected hits, $N_{\text{int}}^{\text{background}}$ and $N_{\text{non-int}}^{\text{background}}$ are the numbers of selected background hits, ϵ_{int} and $\epsilon_{\text{non-int}}$ are the efficiencies of selecting signal hits, and U_{int} and $U_{\text{non-int}}$ are the unfolding matrices. Noting that

$$N_{\text{int}}^{\text{selected}} = N_{\text{int}}^{\text{signal}} + N_{\text{int}}^{\text{background}} \tag{5.27a}$$

$$\sum_{j}^{N_{\text{non-int}}^{\text{selected}}} \Delta x_j = \sum_{k}^{N_{\text{non-int}}^{\text{signal}}} \Delta x_k + \sum_{\ell}^{N_{\text{non-int}}^{\text{background}}} \Delta x_\ell \tag{5.27b}$$

we can rewrite the terms in the numerator and denominator of Eq. 5.26 as

$$\begin{aligned} N_{\text{int}}^{\text{selected}} - N_{\text{int}}^{\text{background}} &= N_{\text{int}}^{\text{selected}} \left[1 - \frac{N_{\text{int}}^{\text{background}}}{N_{\text{int}}^{\text{selected}}} \right] \\ &= N_{\text{int}}^{\text{selected}} \left[\frac{N_{\text{int}}^{\text{signal}}}{N_{\text{int}}^{\text{selected}}} \right] \\ &= N_{\text{int}}^{\text{selected}} \, p_{\text{int}} \end{aligned} \tag{5.28a}$$

where

$$p_{\text{int}} \equiv \frac{N_{\text{int}}^{\text{signal}}}{N_{\text{int}}^{\text{selected}}} \tag{5.28b}$$

and

$$\begin{aligned} \sum_{j}^{N_{\text{non-int}}^{\text{selected}}} \Delta x_j - \sum_{k}^{N_{\text{non-int}}^{\text{background}}} \Delta x_k &= \left[\sum_{j}^{N_{\text{non-int}}^{\text{selected}}} \Delta x_j \right] \left[1 - \frac{\sum_{k}^{N_{\text{non-int}}^{\text{background}}} \Delta x_k}{\sum_{\ell}^{N_{\text{non-int}}^{\text{selected}}} \Delta x_\ell} \right] \\ &= \left[\sum_{j}^{N_{\text{non-int}}^{\text{selected}}} \Delta x_j \right] \left[\frac{\sum_{k}^{N_{\text{non-int}}^{\text{signal}}} \Delta x_k}{\sum_{\ell}^{N_{\text{non-int}}^{\text{selected}}} \Delta x_\ell} \right] \\ &= \left[\sum_{j}^{N_{\text{non-int}}^{\text{selected}}} \Delta x_j \right] p_{\text{non-int}} \end{aligned} \tag{5.28c}$$

where

$$p_{\text{non-int}} \equiv \frac{\sum_{j}^{N_{\text{non-int}}^{\text{signal}}} \Delta x_j}{\sum_{k}^{N_{\text{non-int}}^{\text{selected}}} \Delta x_k}. \tag{5.28d}$$

Putting all of this together yields

$$\sigma \approx \frac{1}{n} \frac{U_{\text{int}}^{\text{MC}} \left[p_{\text{int}}^{\text{MC}} \, N_{\text{int}}^{\text{selected}} \right] \frac{1}{\epsilon_{\text{int}}^{\text{MC}}}}{U_{\text{non-int}}^{\text{MC}} \left[p_{\text{non-int}}^{\text{MC}} \sum_{j}^{N_{\text{non-int}}^{\text{selected}}} \Delta x_j \right] \frac{1}{\epsilon_{\text{non-int}}^{\text{MC}}}}. \tag{5.26a}$$

where a *MC* superscript indicates that the term is to be estimated from Monte Carlo simulations.

Estimation of correction factors with Monte Carlo truth

For a reconstructed hit to be considered a signal interaction hit, it must satisfy certain spatial requirements along a π^- track. We require that the reconstructed hit to be

(1) within 2 cm of the true position of the π^- interaction point and

(2) within 3 hits of the hit closest to the true position of the π^- interaction point

to be considered a signal interaction hit. Plots of the 3D distance between true position of π^- interaction point and closest reconstructed hit are shown in Fig. 5.22; plots of the hit index difference between reconstructed hit categorized as an interacting hit and reconstructed hit closest to the true position of the π^- interaction point are shown in Fig. 5.23. A similar procedure is done for the signal non-interacting hits.

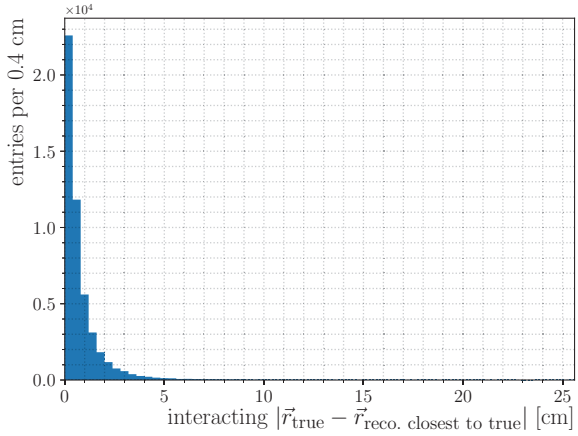

(a) 3D distance between true position of π^- interaction point and closest reconstructed hit

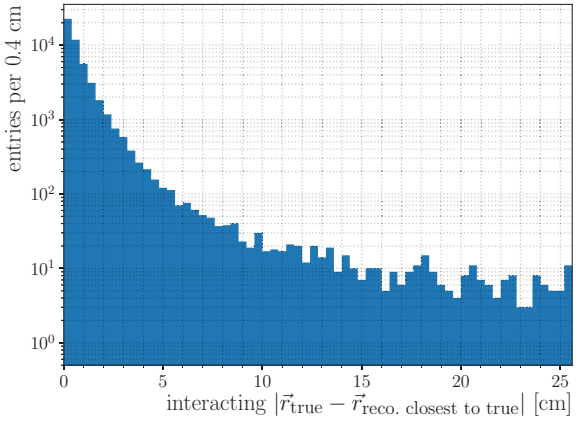

(b) Log-linear version of (a)

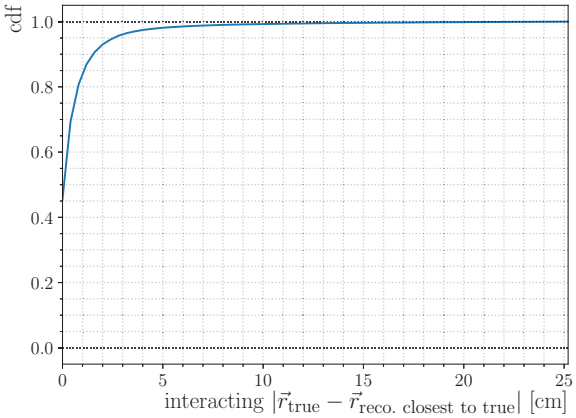

(c) Cumulative distribution function of (a), excludes overflow bin

Figure 5.22: 3D distance between true position of π^- interaction point and closest reconstructed hit. We require that the reconstructed hit be within 2 cm of the true position of the interacting point to be considered a possible "signal" hit.

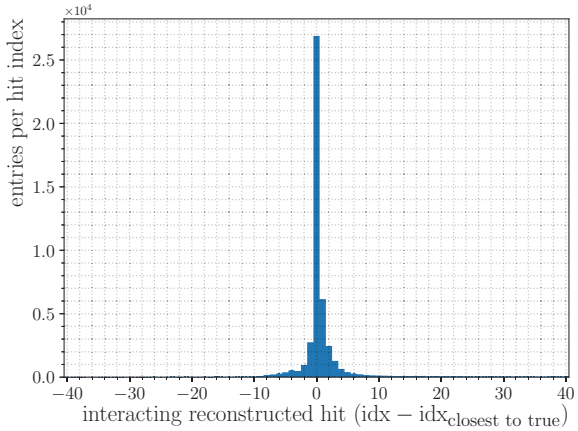

(a) Hit index difference between reconstructed hit categorized as an interacting hit and reconstructed hit closest to the true position of the π^- interaction point

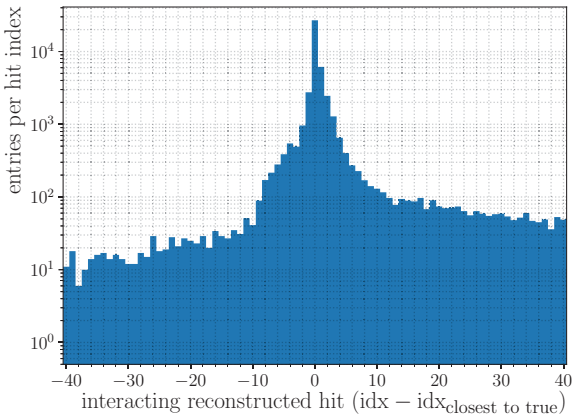

(b) Log-linear version of (a)

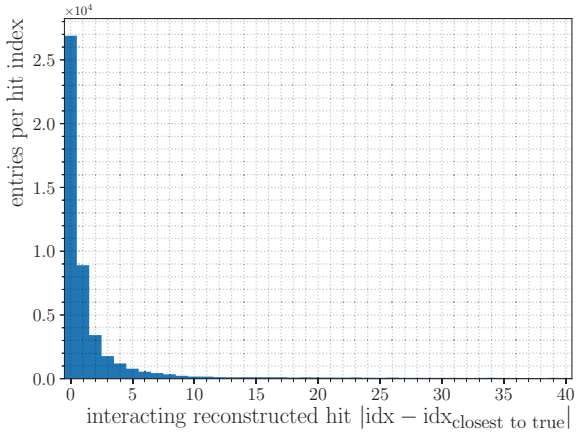

(c) Absolute value of hit index difference from (a)

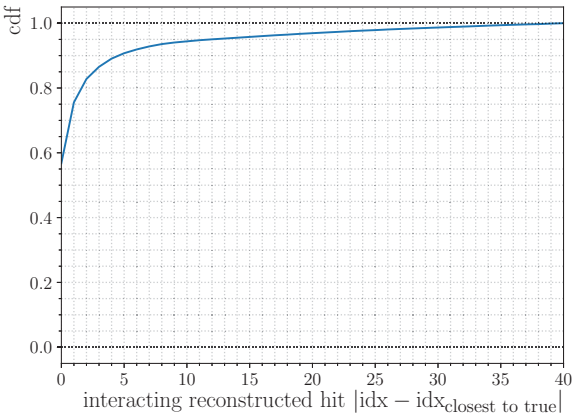

(d) Cumulative distribution function of (c), excludes overflow bin

Figure 5.23: Hit index difference between reconstructed hit selected as an interacting hit and reconstructed hit closest to the true position of the π^- interaction point. We require that the reconstructed hit be within 3 hits of the closest-to-true hit to be a reconstructed π^- to be considered a possible "signal" hit.

We can categorize the selected reconstructed hits into the following:

(1) π^- signal:

Reconstructed hits along a charged pion track that are considered signal hits.

(2) π^- background:

Reconstructed hits along a charged pion track that are not considered signal hits.

(3) μ^- background from secondary beam:

Reconstructed hits along a muon track from the secondary beam.

(4) μ^- background from tertiary beam:

Reconstructed hits along a muon track from the tertiary beam.

(5) e^- background from tertiary beam:

Reconstructed hits along an electron track from the tertiary beam.

An electron loses energy via ionization and bremsstrahlung photon production leading to a complex electron topology in the TPC. This results in short electron tracks that may be mistaken for an interacting π^- event. On the other hand, a muon with kinetic energy above $\sim$200 MeV will penetrate the full length of the TPC and be mistaken as a non-interacting, through-going π^- event. The number of selected signal hits over the total number of selected hits in Eqs. 5.28b and 5.28d can be thought of as the purity of selected reconstructed signal hits. In other words, the purity is defined to be the number of selected signal π^- hits over the number of all selected hits (signal + background). The categorized interacting and non-interacting histograms in bins of reconstructed kinetic energy from a -100 A Monte Carlo sample are shown in Fig. 5.24; the purity for each kinetic energy bin is shown below the histograms.

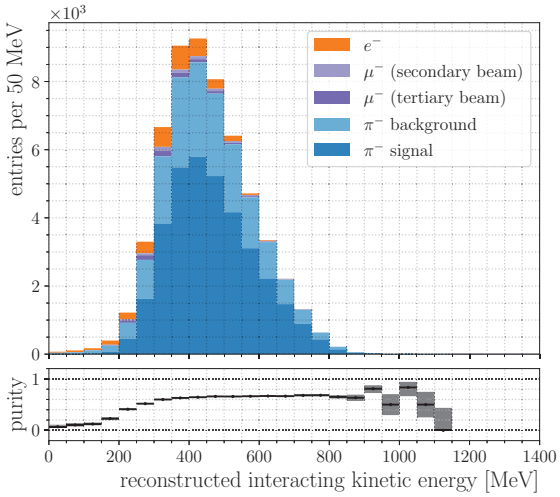

(a) Reconstructed kinetic energy of interacting hits along with selection purity $p_{\text{int}}^{\text{MC}}$

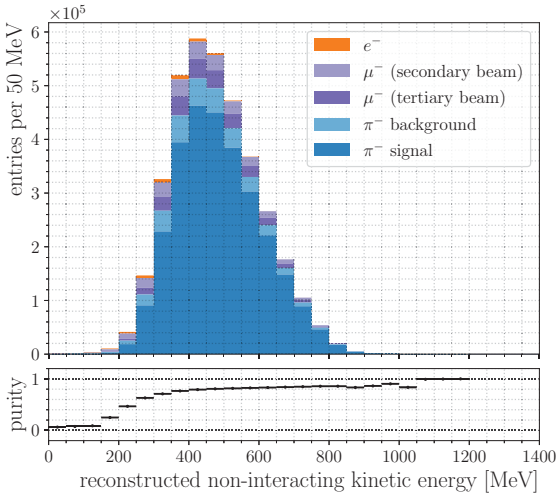

(b) Reconstructed kinetic energy of non-interacting hits along with selection purity $p_{\text{non-int}}^{\text{MC}}$

Figure 5.24: Reconstructed kinetic energy of selected interacting and non-interacting hits from a -100 A π^- Monte Carlo sample categorized into signal and background hits.

The selection efficiencies in Eq. 5.26a are defined to be

$$\epsilon_{\text{int}}^{\text{MC}} = \frac{N_{\text{true int}}^{\text{selected}}}{N_{\text{true int}}^{\text{selected}} + N_{\text{true int}}^{\text{non-selected}}} \tag{5.29a}$$

$$\epsilon_{\text{non-int}}^{\text{MC}} = \frac{\sum_{j}^{N_{\text{true non-int}}^{\text{selected}}} \Delta x_j}{\sum_{j}^{N_{\text{true non-int}}^{\text{selected}}} \Delta x_j + \sum_{k}^{N_{\text{true non-int}}^{\text{non-selected}}} \Delta x_k} \tag{5.29b}$$

where $N_{\text{true int}}^{\text{selected}}$ and $N_{\text{true non-int}}^{\text{selected}}$ are the numbers of selected true interacting and non-interacting points, and $N_{\text{true int}}^{\text{non-selected}}$ and $N_{\text{true non-int}}^{\text{non-selected}}$ are the numbers of non-selected true interacting and non-interacting points; only MC truth points within the fiducial volume are considered. The interacting and non-interacting histograms of selected and non-selected

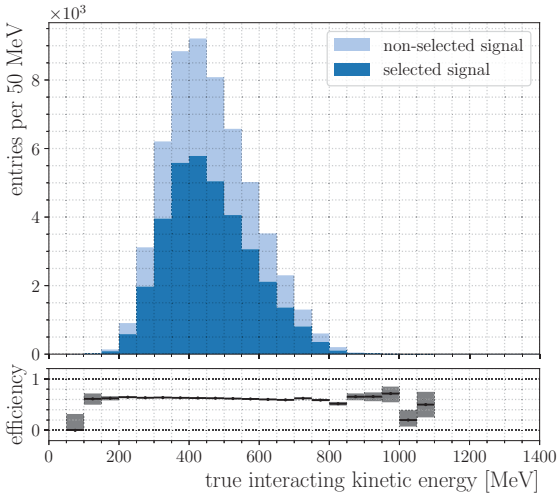

(a) True kinetic energy of interacting points along with the selection efficiency $\epsilon_{\text{int}}^{\text{MC}}$

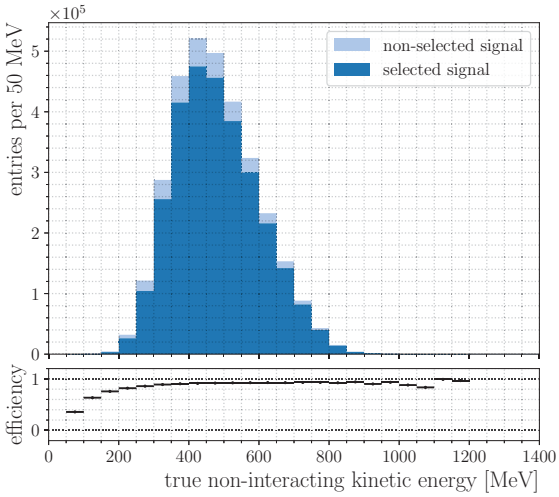

(b) True kinetic energy of non-interacting points along with the selection efficiency $\epsilon_{\text{non-int}}^{\text{MC}}$

Figure 5.25: True kinetic energy of interacting and non-interacting signal points from a -100 A π^- Monte Carlo sample categorized into selected and non-selected MC truth points.

points in bins of kinetic energy from a -100 A Monte Carlo sample are shown in Fig. 5.25; the selection efficiency for each kinetic energy bin is shown below the histograms.

Unfolding

We will now discuss unfolding by first laying out the mathematical problem as done in [82]. Let us suppose that the true probability density function of the true kinetic energy E_{true} of a particle passing through a slab of liquid argon in the TPC is $f(E_{\text{true}})$. Let us also suppose that there is a transformation or response function $R(E_{\text{reco.}} \mid E_{\text{true}})$ that maps the true distribution to the reconstructed distribution due to detector resolution effects. The probability density function of the reconstructed kinetic energy $E_{\text{reco.}}$ is then given by

$$g(E_{\text{reco.}}) = \int R(E_{\text{reco.}} \mid E_{\text{true}})\, f(E_{\text{true}})\, \mathrm{d}E_{\text{true}}. \tag{5.30}$$

In the case where the probability distribution functions of $E_{\text{reco.}}$ and E_{true} are both represented by histograms, Eq. 5.30 becomes

$$y_j^{\text{reco.}} = \sum_k^M R_{jk}\, x_k^{\text{true}} \qquad (\text{for } j = 1, \ldots, N) \tag{5.31}$$

where $y_j^{\text{reco.}}$ is the expectation value in the j^{th} bin of the histogram of $E_{\text{reco.}}$, x_k^{true} is the expectation value in the k^{th} bin of the histogram of E_{true}, and R_{jk} is the response matrix

$$R_{jk} \equiv P(\text{reconstructed in } j^{\text{th}} \text{ bin} \mid \text{true value in } k^{\text{th}} \text{ bin}) \tag{5.32}$$

(it is worth noting that $\sum_{j=1}^N R_{jk} = 1$ by construction). Generally speaking, Eq. 5.31 must be modifed to include background

$$y_j^{\text{reco.}} = \sum_k^M R_{jk}\, x_k^{\text{true}} + \beta_j^{\text{reco.}} \qquad (\text{for } j = 1, \ldots, N) \tag{5.31a}$$

where $\beta_j^{\text{reco.}}$ is the expectation value of background in the j^{th} bin of the histogram of $E_{\text{reco.}}$. If we let $\boldsymbol{n} = (n_1^{\text{data}}, n_2^{\text{data}}, \ldots, n_N^{\text{data}})$ denote the dataset, the expected values of $\boldsymbol{n}$ then is related by

$$\mathrm{E}[\boldsymbol{n}] = \boldsymbol{y} = R\,\boldsymbol{x} + \boldsymbol{\beta} \tag{5.33}$$

where $\boldsymbol{y} = (y_1^{\text{reco.}}, y_2^{\text{reco.}}, \ldots, y_N^{\text{reco.}})$, R is the response matrix, $\boldsymbol{x} = (x_1^{\text{true}}, x_2^{\text{true}}, \ldots, x_M^{\text{true}})$, and $\boldsymbol{\beta} = (\beta_1^{\text{reco.}}, \beta_2^{\text{reco.}}, \ldots, \beta_N^{\text{reco.}})$.

The goal of unfolding is to construct estimators $\hat{\boldsymbol{x}}$ for $\boldsymbol{x}$ so that the result can be directly compared to theoretical predictions. Let us now suppose that the response matrix can be

inverted

$$\boldsymbol{x} = R^{-1}(\boldsymbol{y} - \boldsymbol{\beta}). \tag{5.34}$$

If the components of $\boldsymbol{n}$ are independent and Poisson-distributed, i.e., $P(n_j; y_j) = \frac{y_j^{n_j}}{n_j!} e^{-y_j}$, then the maximum-likelihood estimators for $\boldsymbol{y}$ are $\boldsymbol{n}$, and thus the estimators for $\boldsymbol{x}$ can be taken to be

$$\hat{\boldsymbol{x}} = R^{-1}(\boldsymbol{n} - \boldsymbol{\beta}). \tag{5.35}$$

By taking the expected values of $\hat{\boldsymbol{x}}$ (Eq. 5.35), we can show that they are unbiased

$$\begin{aligned} \mathrm{E}[\hat{\boldsymbol{x}}] &= \mathrm{E}[R^{-1}(\boldsymbol{n} - \boldsymbol{\beta})] \\ &= R^{-1}(\mathrm{E}[\boldsymbol{n}] - \boldsymbol{\beta}) \\ &= \boldsymbol{x}. \end{aligned} \tag{5.36}$$

As mentioned before, mis-reconstruction of the deposited energy due to detector resolution effects can lead to biases and hits being placed into the wrong kinetic energy bins. This is accounted for by unfolding via inversion of the detector response matrix. The response matrices and inverted response matrices for the interacting and non-interacting hits are shown in Figs. 5.26 and 5.27, respectively. A high-statistics Monte Carlo sample of π^- with a uniform beam momentum spectrum from 200 MeV/c to 1750 MeV/c (rather than a realistic, data-driven beam momentum spectrum) is used to generate the response matrices; in other words, a different model—one with a flat prior—is used to generate the detector response matrices.

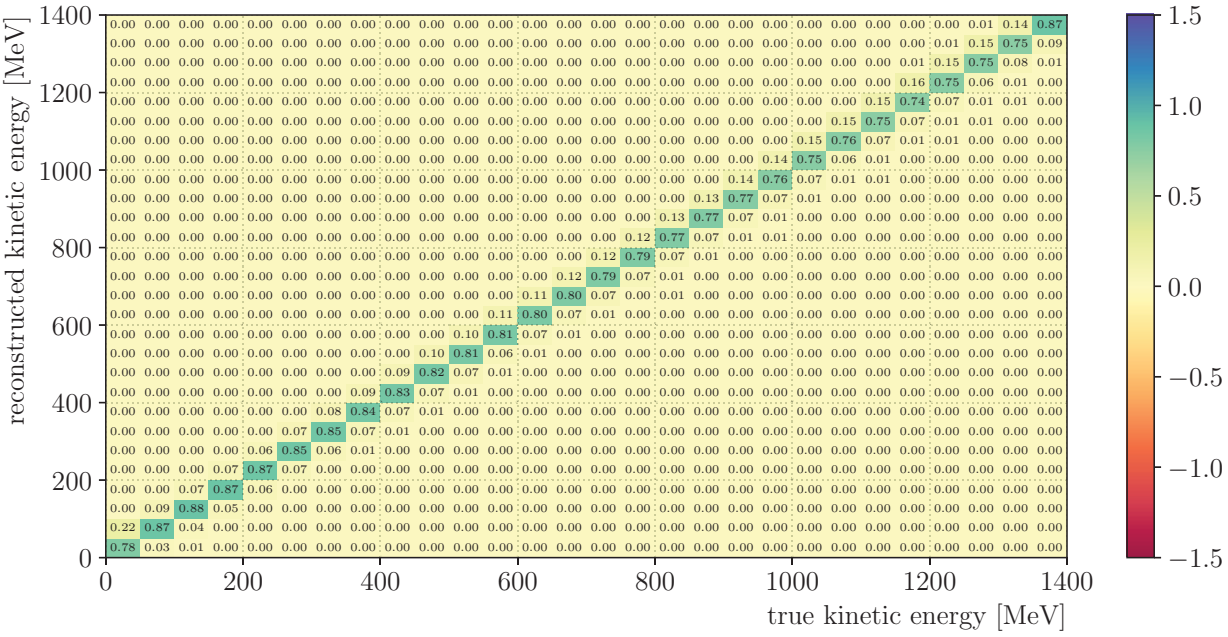

(a) Response matrix, R_{int}

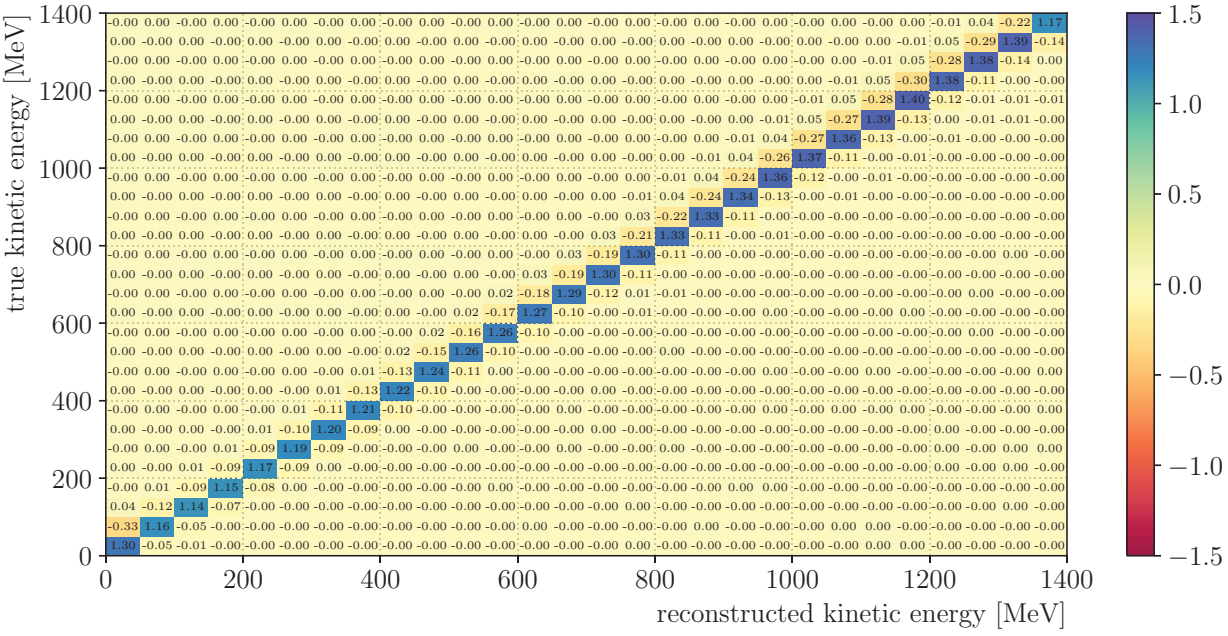

(b) Inverted response matrix, $R_{\text{int}}^{-1} = U_{\text{int}}^{\text{MC}}$

Figure 5.26: Response matrix and inverted response matrix for interacting hits.

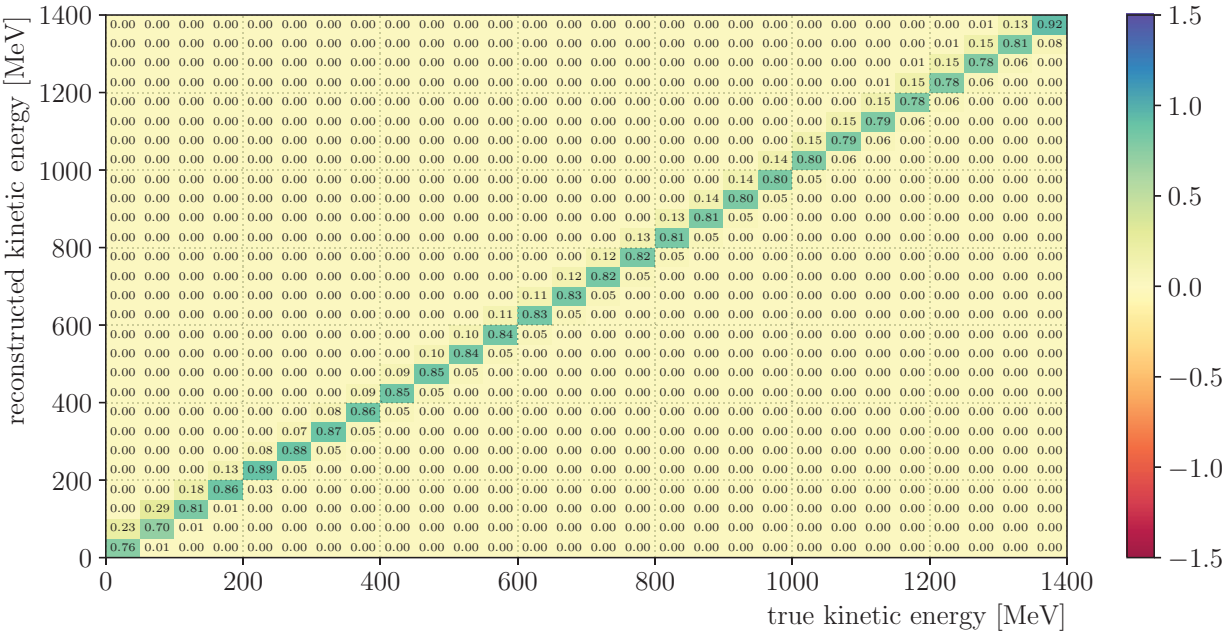

(a) Response matrix, $R_{\text{non-int}}$

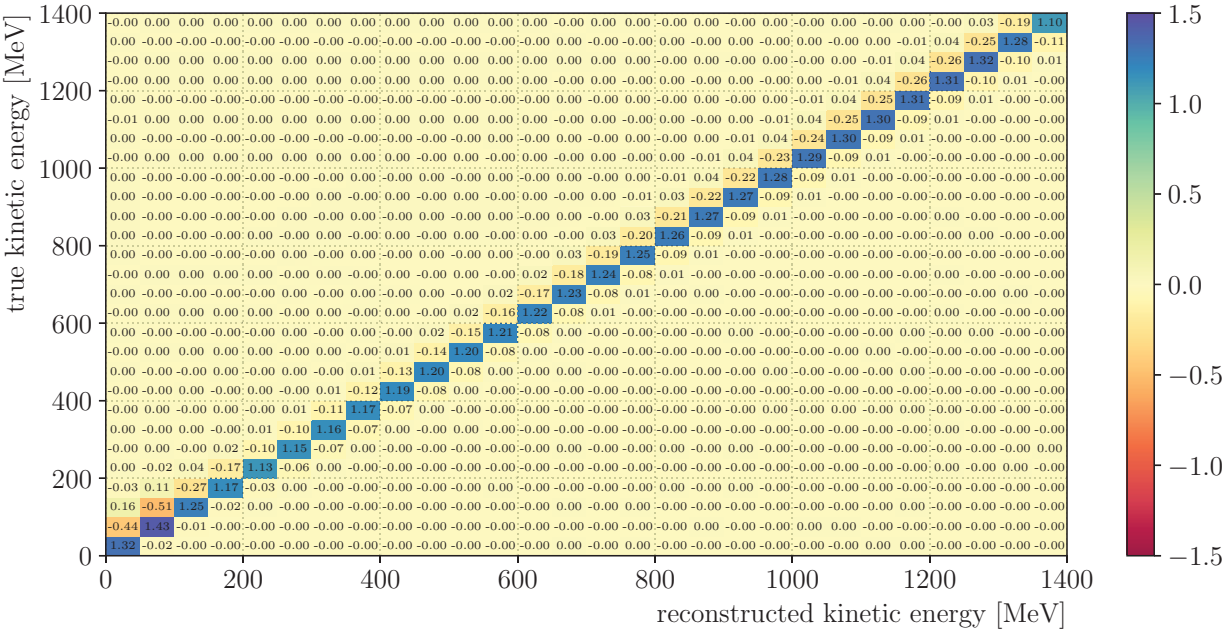

(b) Inverted response matrix, $R^{-1}_{\text{non-int}} = U^{\text{MC}}_{\text{non-int}}$

Figure 5.27: Response matrix and inverted response matrix for non-interacting hits.

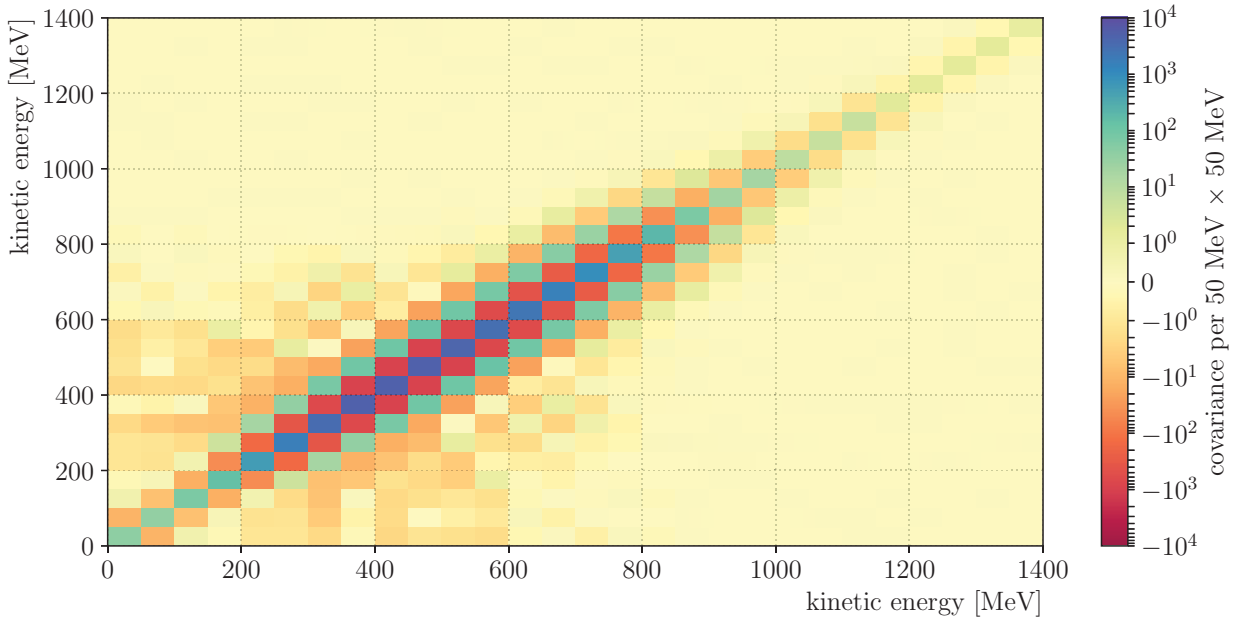

(a) Covariance matrix for interacting hits

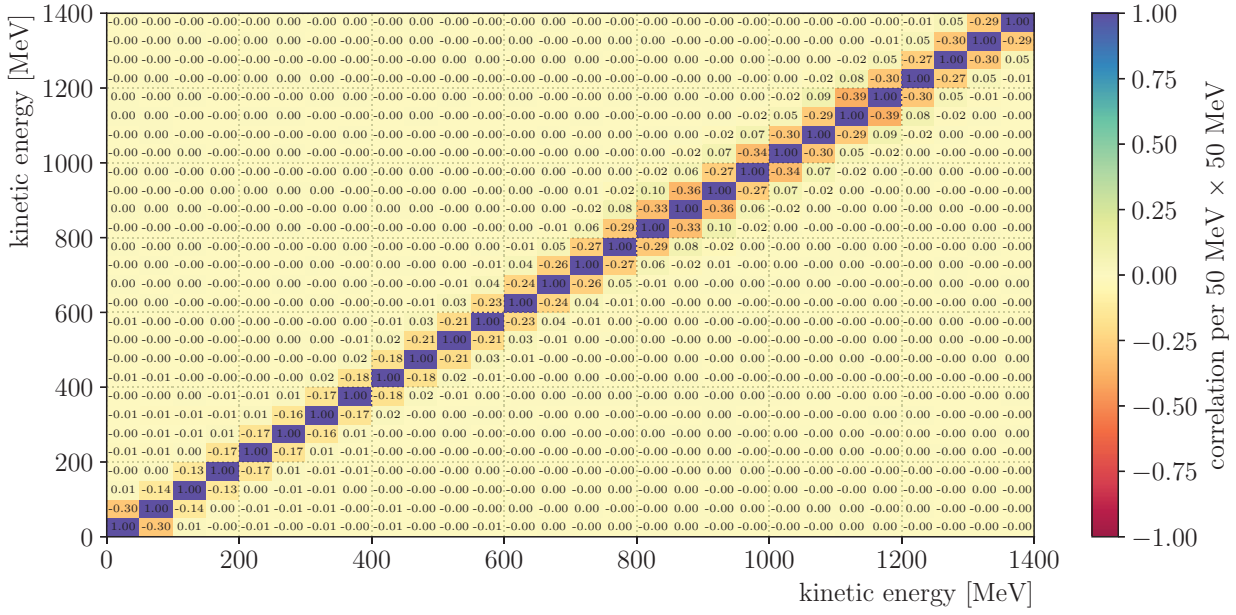

(b) Correlation matrix for interacting hits

Figure 5.28: Covariance and correlation matrices for interacting hits from the Run-II −100 A dataset.

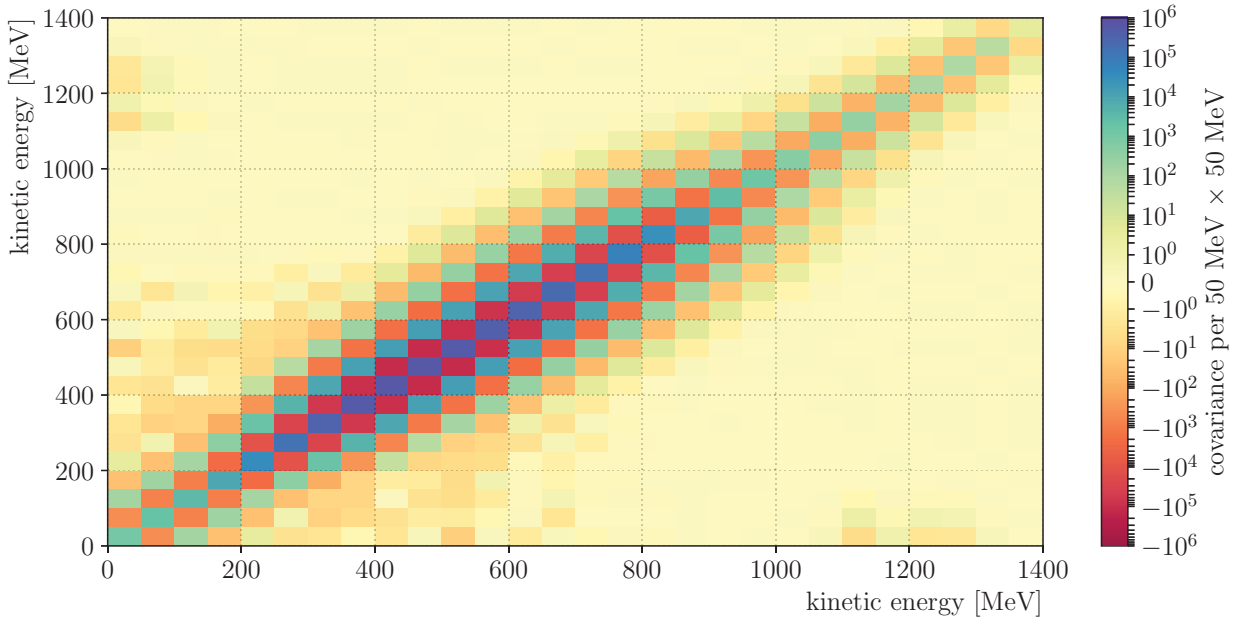

(a) Covariance matrix for non-interacting hits

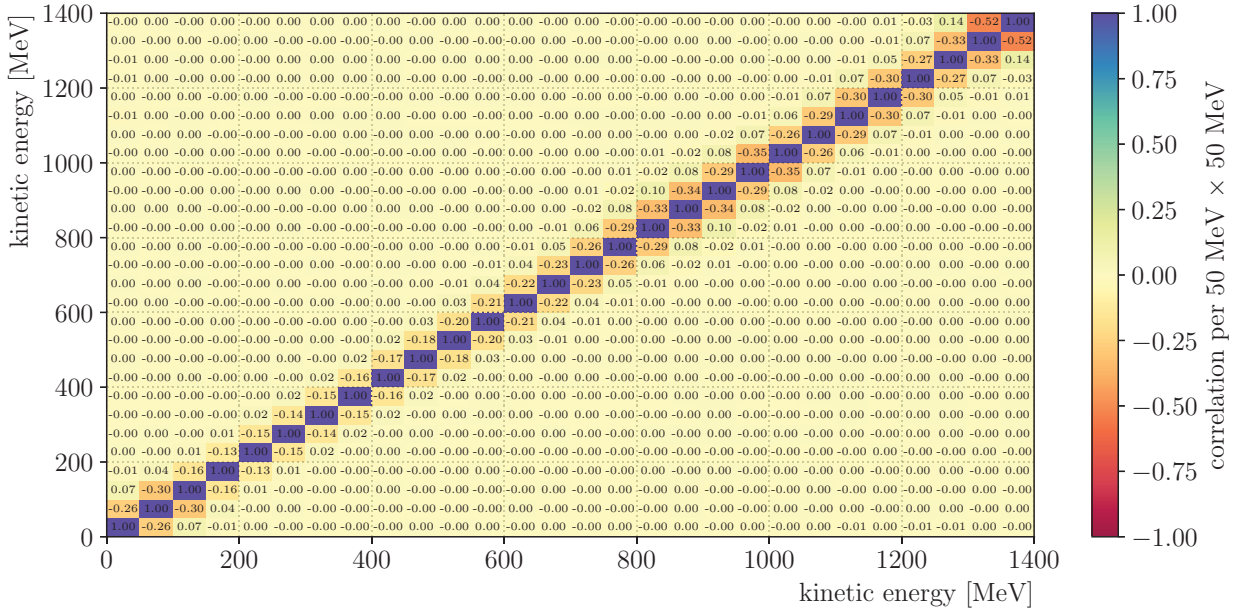

(b) Correlation matrix for non-interacting hits

Figure 5.29: Covariance and correlation matrices for non-interacting hits from the Run-II −100 A dataset.

Application to data

The background subtraction is first applied to the Run-II -100 A dataset as shown in Fig. 5.30 (the background subtraction factors $p_{\text{int}}^{\text{MC}}$ and $p_{\text{non-int}}^{\text{MC}}$ are plotted in Fig. 5.24). The unfolding procedure is then performed using the inverted response matrices $U_{\text{int}}^{\text{MC}}$ (Fig. 5.26b) and $U_{\text{non-int}}^{\text{MC}}$ (Fig. 5.27b). The matrices are multiplied by the background-subtracted number of hits in the numerator and denominator of Eq. 5.26a

$$p_{\text{int}}^{\text{MC}}\, N_{\text{int}}^{\text{selected}} \quad \rightarrow \quad U_{\text{int}}^{\text{MC}} \left[p_{\text{int}}^{\text{MC}}\, N_{\text{int}}^{\text{selected}} \right], \tag{5.37a}$$

$$p_{\text{non-int}}^{\text{MC}} \sum_{j}^{N_{\text{non-int}}^{\text{selected}}} \Delta x_j \quad \rightarrow \quad U_{\text{non-int}}^{\text{MC}} \left[p_{\text{non-int}}^{\text{MC}} \sum_{j}^{N_{\text{non-int}}^{\text{selected}}} \Delta x_j \right], \tag{5.37b}$$

The background-subtracted and unfolded distributions of kinetic energy of hits are plotted on top of the Monte Carlo truth (selected) distributions in Fig. 5.31. The covariance and correlation matrices for interacting hits are shown in Fig. 5.28; the covariance and correlation matrices for non-interacting hits are shown in Fig. 5.29. Uncertainties of matrix elements are propagated through using methods described in [83]. The unfolded distributions are then efficiency-corrected using the efficiency correction factors plotted in Fig. 5.25

$$U_{\text{int}}^{\text{MC}} \left[p_{\text{int}}^{\text{MC}}\, N_{\text{int}}^{\text{selected}} \right] \quad \rightarrow \quad U_{\text{int}}^{\text{MC}} \left[p_{\text{int}}^{\text{MC}}\, N_{\text{int}}^{\text{selected}} \right] \frac{1}{\epsilon_{\text{int}}^{\text{MC}}}, \tag{5.38a}$$

$$U_{\text{non-int}}^{\text{MC}} \left[p_{\text{non-int}}^{\text{MC}} \sum_{j}^{N_{\text{non-int}}^{\text{selected}}} \Delta x_j \right] \quad \rightarrow \quad U_{\text{non-int}}^{\text{MC}} \left[p_{\text{non-int}}^{\text{MC}} \sum_{j}^{N_{\text{non-int}}^{\text{selected}}} \Delta x_j \right] \frac{1}{\epsilon_{\text{non-int}}^{\text{MC}}}. \tag{5.38b}$$

The efficiency-corrected distributions of kinetic energy of hits are plotted on top of the Monte Carlo truth distributions in Fig. 5.32. Finally, the Monte Carlo π^-–Ar cross section

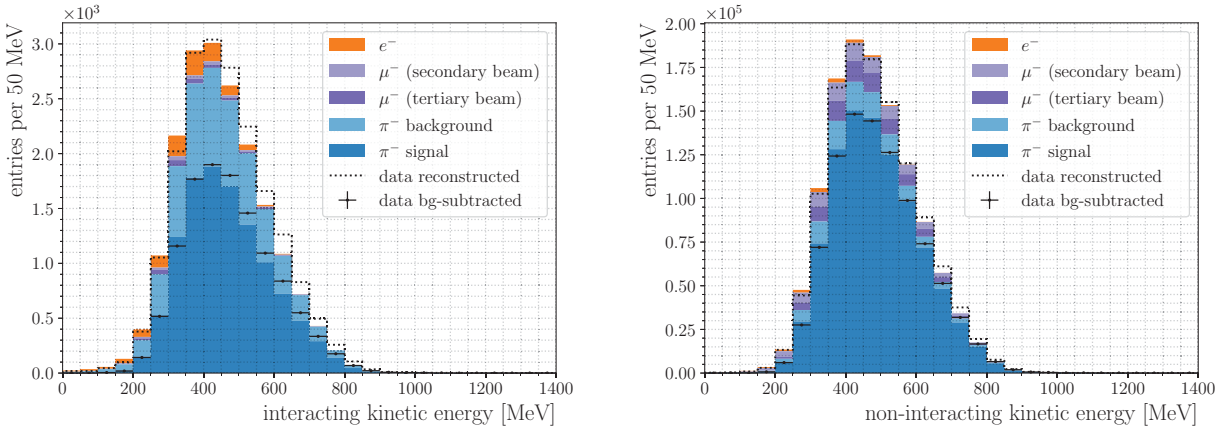

(a) Kinetic energy of interacting hits

(b) Kinetic energy of non-interacting hits

Figure 5.30: Background-subtracted of distributions of kinetic energy of hits in the Run-II −100 A dataset. The reconstructed distributions are plotted with dotted lines, and the background-subtracted distributions are plotted with markers accompanied with statistical error bars.

is estimated by taking the ratio of the efficiency-corrected distributions

$$\sigma \approx \frac{1}{n} \frac{U_{\text{int}}^{\text{MC}} \left[p_{\text{int}}^{\text{MC}} \, N_{\text{int}}^{\text{selected}} \right] \dfrac{1}{\epsilon_{\text{int}}^{\text{MC}}}}{U_{\text{non-int}}^{\text{MC}} \left[p_{\text{non-int}}^{\text{MC}} \displaystyle\sum_{j}^{N_{\text{non-int}}^{\text{selected}}} \Delta x_j \right] \dfrac{1}{\epsilon_{\text{non-int}}^{\text{MC}}}} \tag{5.26a}$$

as plotted in Fig. 5.33 with statistical uncertainties. The same procedure is performed on the Run-II −60 A dataset for validation and there is good agreement with the Run-II −100 A dataset as shown in Fig. 5.34. A Monte Carlo closure test is also performed on a −100 A Monte Carlo sample as shown in Fig. 5.35.

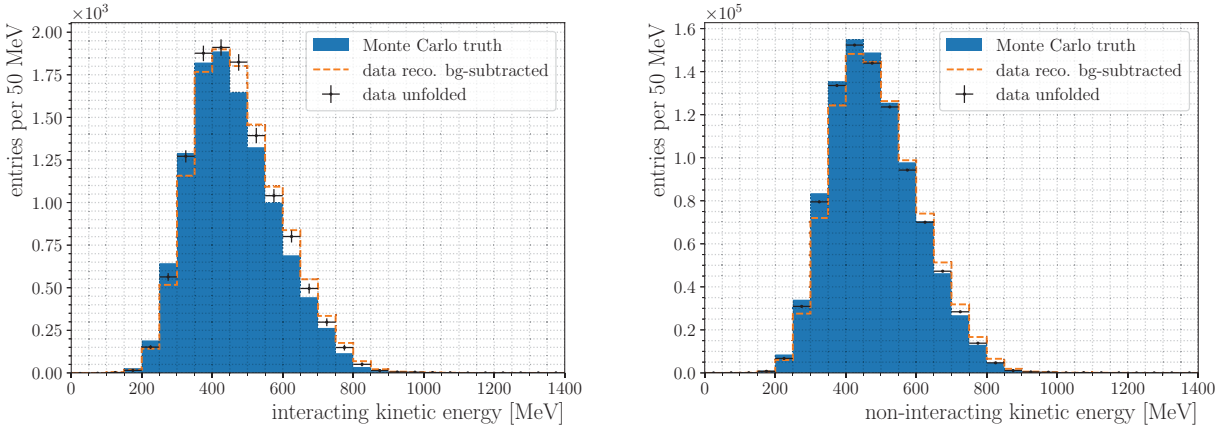

(a) Kinetic energy of interacting hits

(b) Kinetic energy of non-interacting hits

Figure 5.31: Unfolding of distributions of kinetic energy of hits using matrix inversion on the Run-II −100 A dataset. The background-subtracted distributions are plotted with dashed lines, and the unfolded distributions are plotted with markers accompanied with statistical error bars. Non-selected MC truth points are excluded from the Monte Carlo distribution.

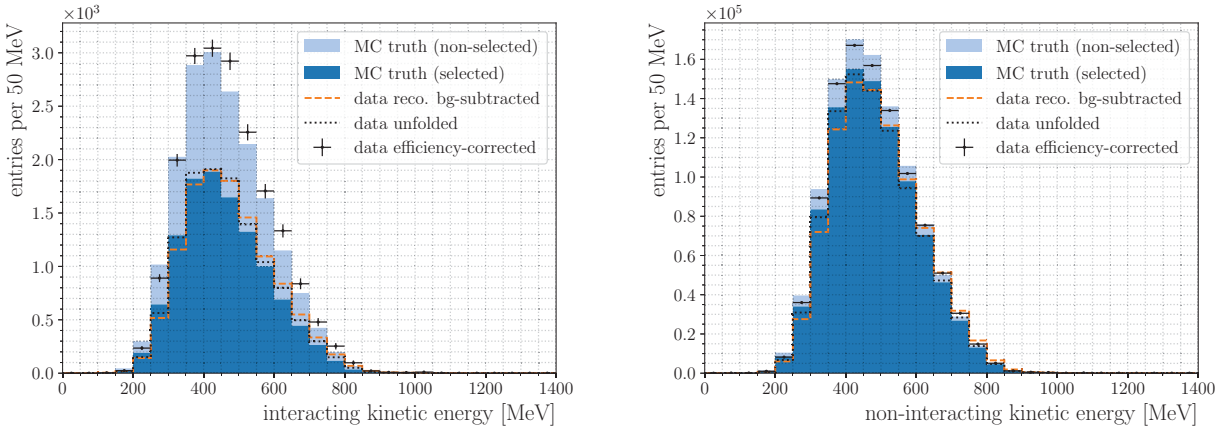

(a) Kinetic energy of interacting hits

(b) Kinetic energy of non-interacting hits

Figure 5.32: Efficiency-corrected distributions of kinetic energy of hits in the Run-II −100 A dataset. The background-subtracted distributions are plotted with dashed lines, and the unfolded distributions are plotted with dotted lines, and the efficiency-corrected distributions are plotted with markers accompanied with statistical error bars.

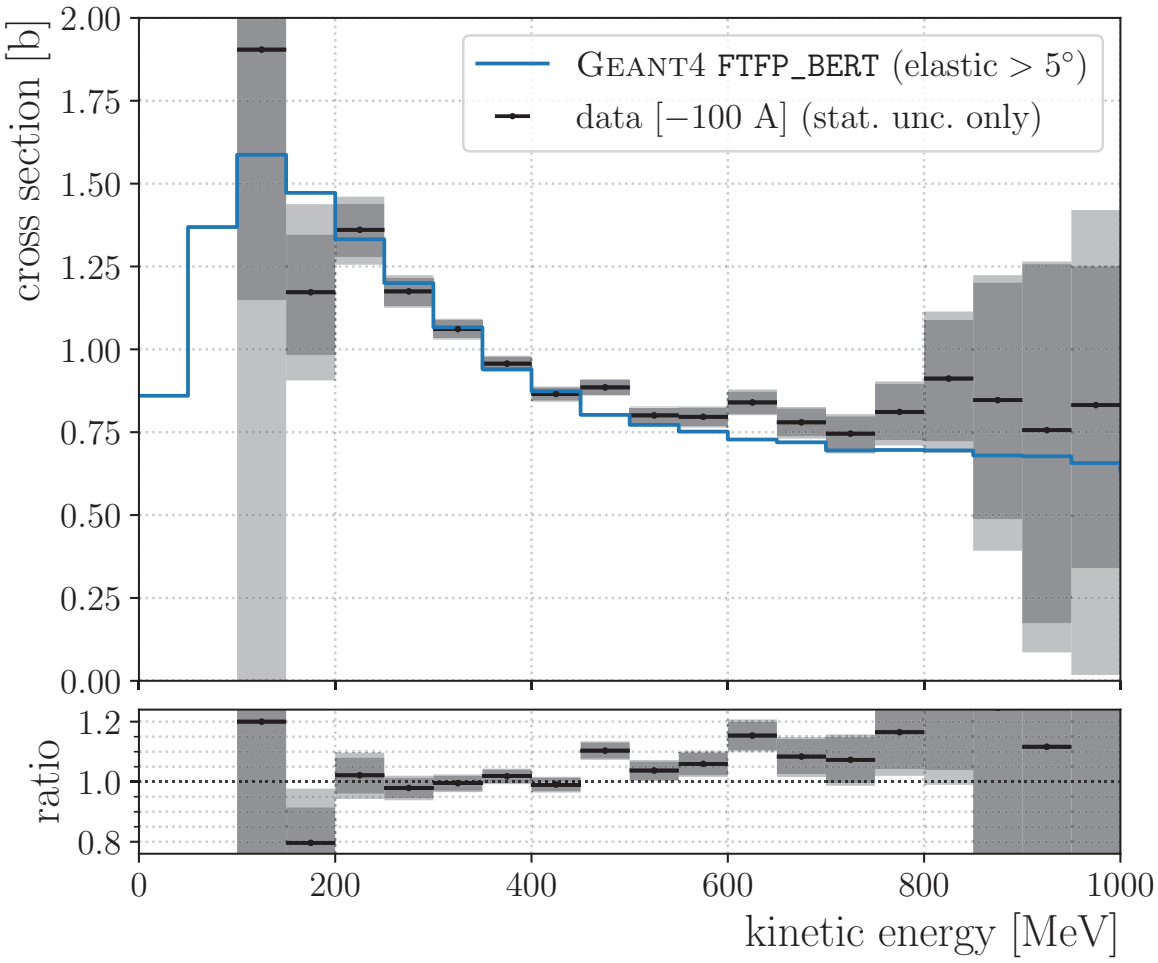

Figure 5.33: Total hadronic π^-–Ar cross section estimate using the Run-II −100 A dataset. The darker error bars indicate statistical errors on the number of selected hits; the lighter error bars indicate statistical errors on the Monte Carlo correction factors in addition to the statistical errors on the number of selected hits.

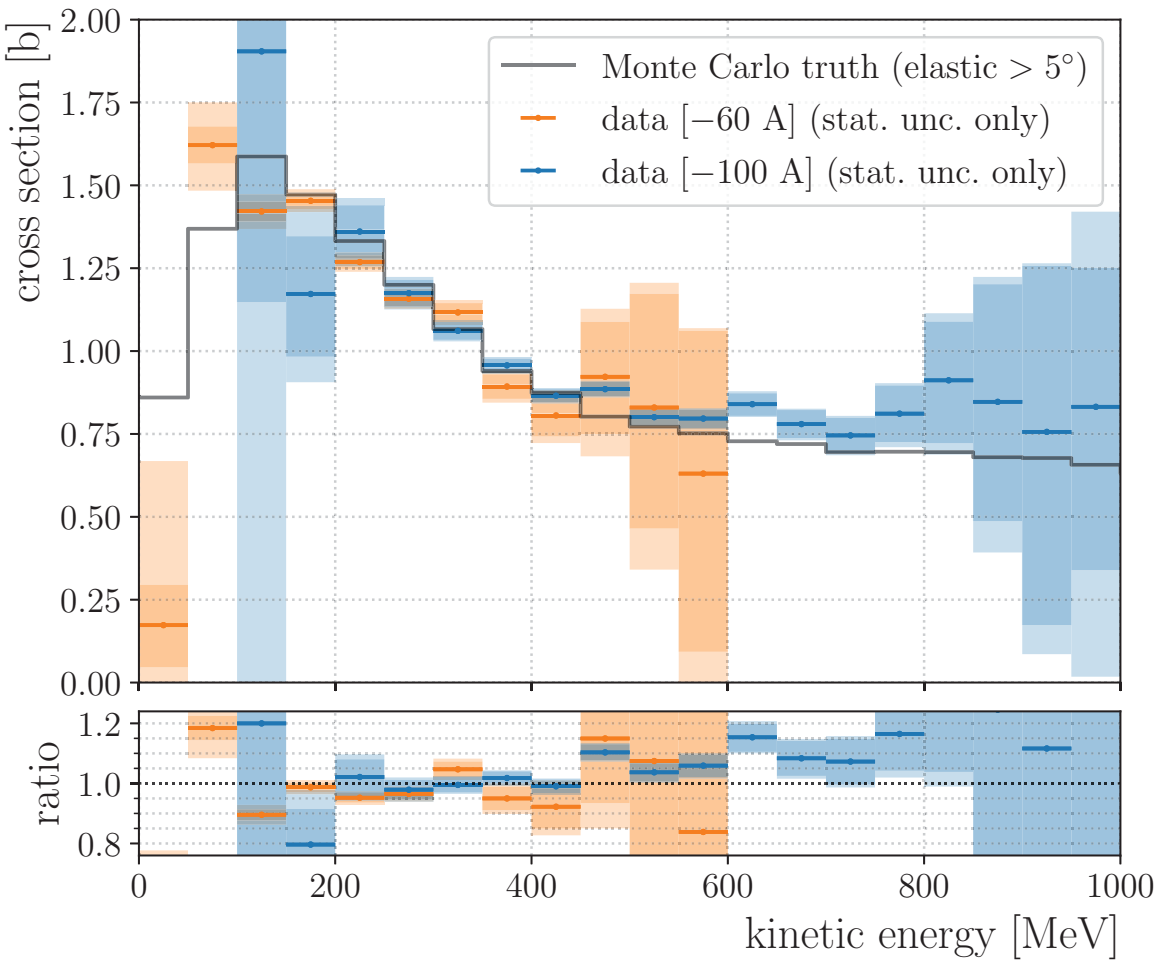

Figure 5.34: Total hadronic π^-–Ar cross section estimate using the Run-II −60 A and −100 A datasets. The darker error bars indicate statistical errors on the number of selected hits; the lighter error bars indicate statistical errors on the Monte Carlo correction factors in addition to the statistical errors on the number of selected hits.

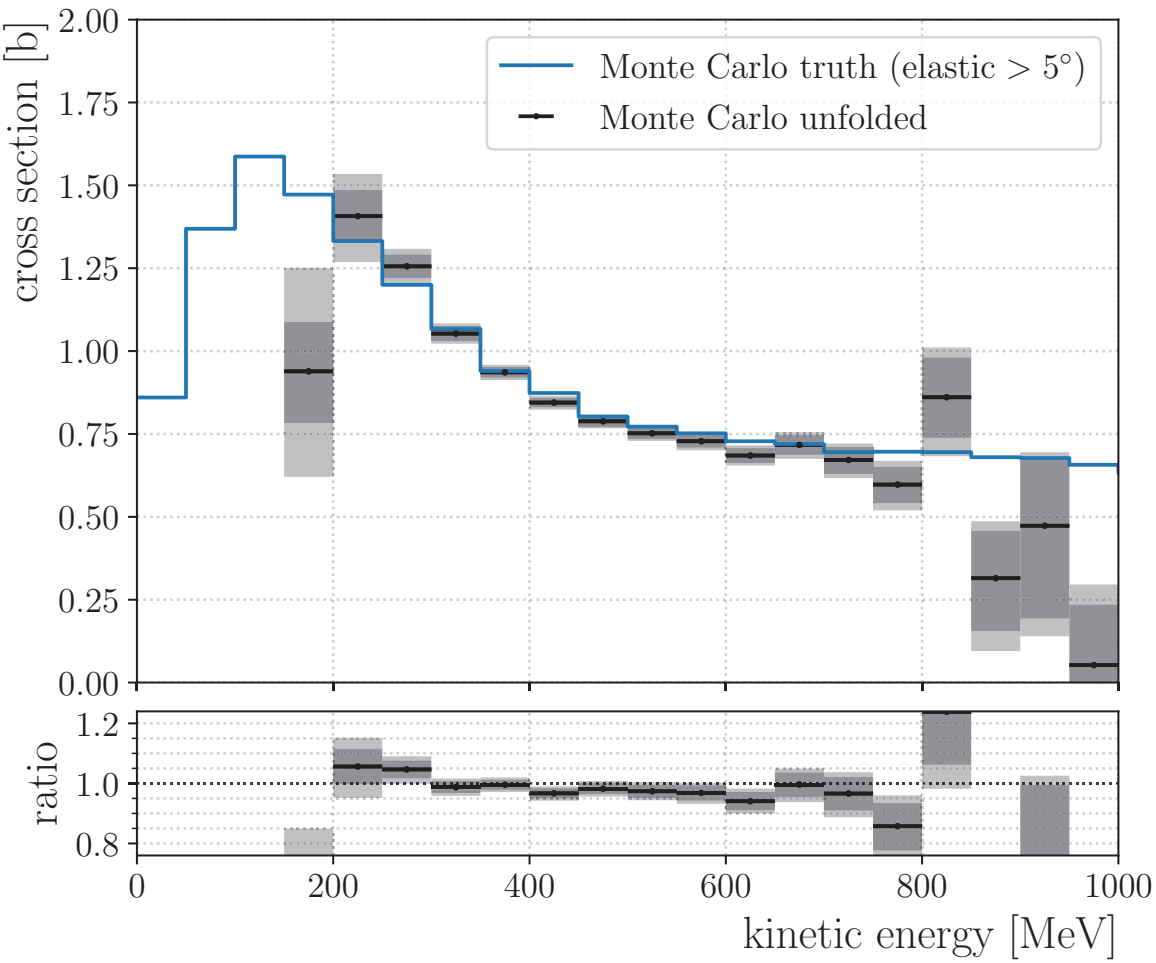

Figure 5.35: Monte Carlo closure test. Total hadronic π^-–Ar cross section estimate using a −100 A Monte Carlo sample. The darker error bars indicate statistical errors on the number of selected hits; the lighter error bars indicate statistical errors on the Monte Carlo correction factors in addition to the statistical errors on the number of selected hits.

5.3 Uncertainties

5.3.1 Statistical uncertainties

Statistical uncertainties are propagated through using 500,000 Monte Carlo simulations. The purity and efficiency values are generated using a binomial posterior distribution [84–86]

$$\begin{aligned} P(\epsilon \mid k, N) &= \frac{\Gamma(N+2)}{\Gamma(k+1)\,\Gamma(N-k+1)}\,\epsilon^{k}\,(1-\epsilon)^{N-k} \\ &= \frac{(N+1)!}{k!\,(N-k)!}\,\epsilon^{k}\,(1-\epsilon)^{N-k} \end{aligned} \tag{5.39}$$

where $k = 1, 2, \ldots, N$. The mode of Eq. 5.39 is $\epsilon_{\text{mode}} = \frac{k}{N}$, the mean is $\epsilon_{\text{mean}} = \text{E}[\epsilon] = \frac{k+1}{N+2}$, and the variance is $\text{Var}(\epsilon) = \frac{(k+1)(k+2)}{(N+2)(N+3)} - \frac{(k+1)^2}{(N+2)^2}$. The histogram bin count values are randomly drawn from Poisson distributions. The cross section as a function of kinetic energy is computed using Eq. 5.26a for each simulation. In the final ensemble of cross sections for each kinetic energy bin, we take the 68.3% highest density interval (HDI) as the estimate on the uncertainty. Distributions from the propagation of statistical uncertainties are plotted in Appendix B (Figs. **??** and **??**).

5.3.2 Systematic uncertainties

The following systematic uncertainties are propagated through using Monte Carlo simulations.

i. **Beamline momentum scale systematic uncertainty:**

   A data-driven calibration of the TOF system and the absolute scale of the beamline momentum reconstruction was performed, and provided the momentum scale systematic uncertainty of 0.5% [51]. To assess the impact of this on the total hadronic cross

section measurement, the reconstructed WC track momentum for every event in a single simulation is scaled by the same amount, $p_{\text{beam}} \to a\, p_{\text{beam}}$, where a is randomly drawn from a normal distribution with a location parameter of 1 and a scale parameter of 0.005.

ii. **Beamline momentum resolution systematic uncertainty:**

The beamline momentum resolution is determined by: (1) the uncertainties in the location of the wire chambers, and the position and pitch of the wires within the chambers; and (2) the energy loss and multiple scattering of beam particles in the air through the spectrometer. The contributions to the momentum resolution from (1) and (2), estimated with Monte Carlo simulations, are 0.8% and 1.3%, respectively; the overall momentum resolution is 1.5% [51]. To assess the impact of this on the total hadronic cross section measurement, the reconstructed WC track momentum for each event is smeared; the smeared momentum value is randomly drawn from a normal distribution with a location parameter of p_{beam} and a scale parameter of $0.015 \times p_{\text{beam}}$.

iii. **Beam content systematic uncertainty:**

The fit parameters from the data-constrained re-weighting of fractional particle content in the DDMC simulation (Table 5.2) are varied in order to access their impact on the total hadronic cross section measurement. The distributions generated for assessing this systematic uncertainty are shown in Appendix C.

Due to time constraints, the following systematic uncertainties have not been included in the result of this thesis, but will be included in the published result. The first two require generating several unfolding matrices which is computationally expensive, and the last one requires generating several DDMC samples with varying pile-up rates.

iv. **Energy loss in uninstrumented material:**

The distibution of energy loss in the uninstrumented material between the last beamline

wire chamber and the front face of the LArIAT TPC was estimated with Monte Carlo simulations as shown in Fig. 5.16. To assess the impact of this on the total hadronic cross section measurement, several unfolding matrices are required to be generated.

v. **Reconstructed hit energy resolution systematic uncertainty:**

The reconstructed hit energy resolution is taken into account by the detector simulation in LArSoft, however, as shown in Fig. 5.17, the resolution in the simulation is smaller than in the data by about 0.015 MeV. To assess the impact of this on the total hadronic cross section measurement, several unfolding matrices are required to be generated. The impact of this on the total hadronic cross section measurement is expected to be negligible.

vi. **Halo pile-up systematic uncertainty:**

Preliminary studies have been performed by shifting the MC-estimated tracking efficiencies of halo-pile up particles (Fig. A.2) by $\pm 10\%$. The impact of this on the total hadronic cross section measurement is small, however, it is expected to be significant for the pion single-charge exchange channel*.

5.4 Result

The total hadronic π^-–Ar cross section measurement using the Run-II -100 A dataset is shown in Fig. 5.36 with combined statistical and systematic uncertainties. Table 5.6 shows a summary of the estimated cross section values with a breakdown of the uncertainties for each kinetic energy bin.

*A discussion of the ongoing work on the pion single-charge exchange channel is presented in Appendix D.

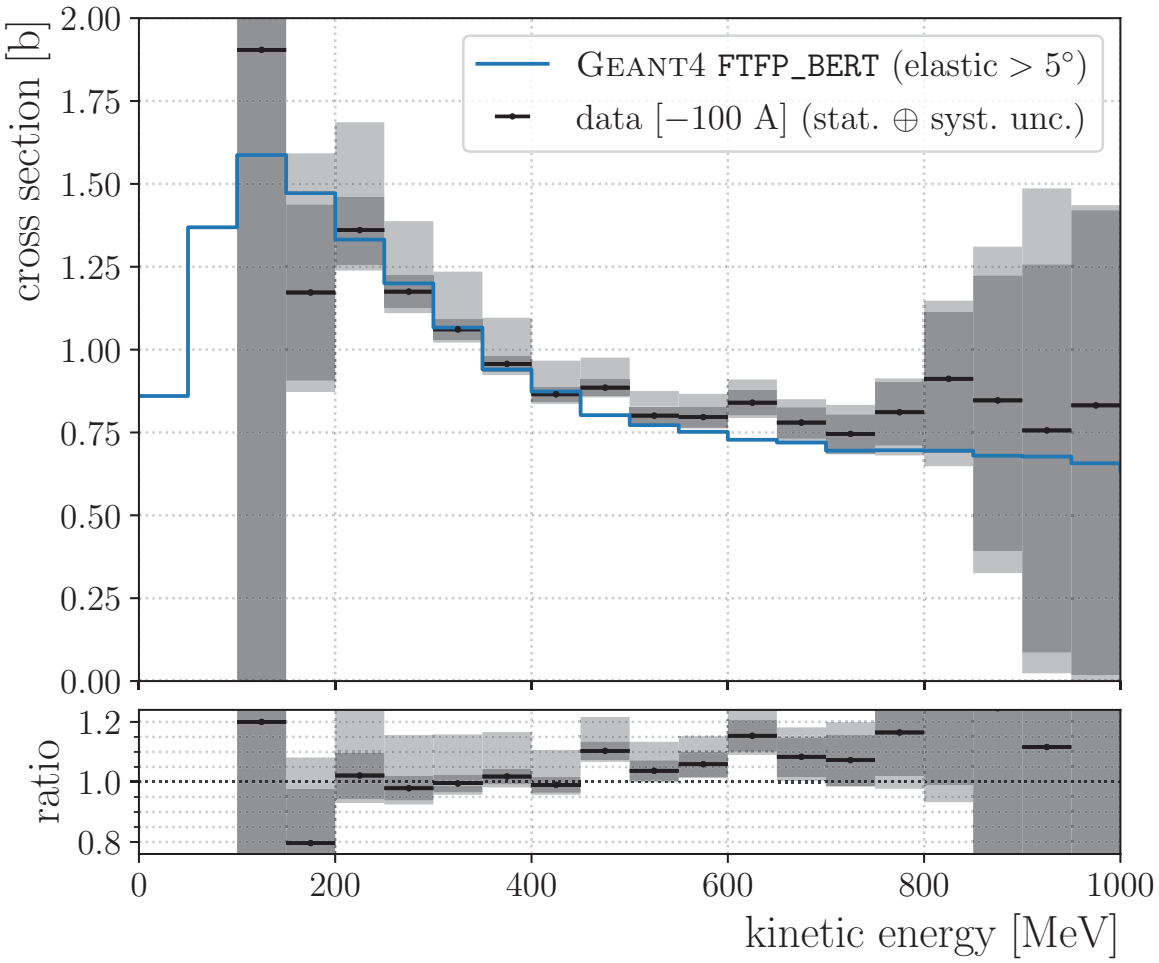

Figure 5.36: Total hadronic π^-–Ar cross section estimate using the Run-II −100 A dataset. The darker error bars indicate statistical uncertainties; the lighter error bars indicate the combined statistical and systematic uncertainties.

Kinetic energy bin [MeV]	σ_{total} [b]	Stat. unc. [b] (data+MC)	Syst. unc. [b] (energy)	Syst. unc. [b] (C_μ, C_e)	Syst. unc. [b] (C_π, C_e)	Total unc. [b]
$[100, 150)$	1.904	$^{+0.545}_{-1.986}$	$^{+0.293}_{-0.401}$	$^{+0.325}_{-0.000}$	$^{+0.315}_{-0.183}$	$^{+0.767}_{-2.034}$
$[150, 200)$	1.172	$^{+0.266}_{-0.266}$	$^{+0.089}_{-0.088}$	$^{+0.269}_{-0.000}$	$^{+0.159}_{-0.107}$	$^{+0.420}_{-0.300}$
$[200, 250)$	1.361	$^{+0.100}_{-0.105}$	$^{+0.032}_{-0.040}$	$^{+0.297}_{-0.000}$	$^{+0.080}_{-0.047}$	$^{+0.325}_{-0.122}$
$[250, 300)$	1.175	$^{+0.049}_{-0.049}$	$^{+0.010}_{-0.033}$	$^{+0.202}_{-0.000}$	$^{+0.046}_{-0.026}$	$^{+0.213}_{-0.065}$
$[300, 350)$	1.061	$^{+0.031}_{-0.032}$	$^{+0.023}_{-0.009}$	$^{+0.165}_{-0.000}$	$^{+0.039}_{-0.022}$	$^{+0.174}_{-0.040}$
$[350, 400)$	0.957	$^{+0.024}_{-0.025}$	$^{+0.011}_{-0.014}$	$^{+0.132}_{-0.000}$	$^{+0.035}_{-0.019}$	$^{+0.139}_{-0.034}$
$[400, 450)$	0.865	$^{+0.023}_{-0.023}$	$^{+0.009}_{-0.013}$	$^{+0.096}_{-0.000}$	$^{+0.021}_{-0.011}$	$^{+0.101}_{-0.029}$
$[450, 500)$	0.885	$^{+0.025}_{-0.025}$	$^{+0.011}_{-0.014}$	$^{+0.085}_{-0.000}$	$^{+0.013}_{-0.007}$	$^{+0.091}_{-0.029}$
$[500, 550)$	0.801	$^{+0.027}_{-0.027}$	$^{+0.019}_{-0.011}$	$^{+0.066}_{-0.000}$	$^{+0.009}_{-0.005}$	$^{+0.075}_{-0.029}$
$[550, 600)$	0.796	$^{+0.031}_{-0.032}$	$^{+0.021}_{-0.013}$	$^{+0.059}_{-0.000}$	$^{+0.002}_{-0.001}$	$^{+0.070}_{-0.035}$
$[600, 650)$	0.840	$^{+0.039}_{-0.039}$	$^{+0.017}_{-0.026}$	$^{+0.056}_{-0.000}$	$^{+0.003}_{-0.002}$	$^{+0.070}_{-0.046}$
$[650, 700)$	0.780	$^{+0.046}_{-0.049}$	$^{+0.022}_{-0.031}$	$^{+0.048}_{-0.000}$	$^{+0.000}_{-0.000}$	$^{+0.071}_{-0.058}$
$[700, 750)$	0.746	$^{+0.059}_{-0.060}$	$^{+0.054}_{-0.015}$	$^{+0.036}_{-0.000}$	$^{+0.003}_{-0.001}$	$^{+0.088}_{-0.062}$
$[750, 800)$	0.811	$^{+0.092}_{-0.101}$	$^{+0.031}_{-0.083}$	$^{+0.031}_{-0.000}$	$^{+0.001}_{-0.002}$	$^{+0.102}_{-0.131}$
$[800, 850)$	0.912	$^{+0.202}_{-0.224}$	$^{+0.118}_{-0.139}$	$^{+0.029}_{-0.000}$	$^{+0.002}_{-0.001}$	$^{+0.236}_{-0.264}$
$[850, 900)$	0.847	$^{+0.377}_{-0.454}$	$^{+0.270}_{-0.255}$	$^{+0.015}_{-0.000}$	$^{+0.001}_{-0.002}$	$^{+0.464}_{-0.521}$
$[900, 950)$	0.756	$^{+0.501}_{-0.671}$	$^{+0.531}_{-0.296}$	$^{+0.002}_{-0.000}$	$^{+0.001}_{-0.001}$	$^{+0.730}_{-0.733}$
$[950, 1000)$	0.832	$^{+0.589}_{-0.814}$	$^{+0.135}_{-0.598}$	$^{+0.000}_{-0.001}$	$^{+0.000}_{-0.000}$	$^{+0.604}_{-1.010}$

Table 5.6: Value of σ_{total} for each kinetic energy bin.

Chapter 6

Conclusion

The LArTPC has become the technology of choice for studying neutrino oscillations over short (< 1 km) and long (> 1000 km) baselines by experiments such as MicroBooNE, SBND, ICARUS, and DUNE. Given that it is a relatively new detector technology, it can benefit from studies and calibration that would reduce systematic uncertainties in the measurements of neutrino oscillations. Neutrino–argon interactions in the few-GeV energy domain produce large numbers of hadronic particles, and two significant sources of uncertainty come from: (1) the largely unknown dynamics of hadron–nucleon interactions within the target argon nuclei, and (2) the hadron–argon interactions outside the target argon nuclei as the outgoing hadrons propagate through the liquid argon detection medium. Hadron–argon scattering data is required for the tuning of nuclear models used in GENIE and GEANT4 in order to help constrain systematic uncertainties in measurements of neutrino oscillations in LArTPC-based neutrino experiments.

Using data from the LArIAT experiment, we have performed the first total hadronic π^-–Ar cross section measurement, which can be used to constrain Monte Carlo simulations and especially systematic uncertainties on hadronic cross sections. This measurement is also the first step towards measuring the exclusive π^-–Ar cross sections. It is critical that the relative reaction rates of the exclusive $\pi^\pm$–Ar interaction channels are properly measured, so that Monte Carlo simulations may accurately predict how often the various reactions occur since these can lead to different backgrounds and biases in analyses of neutrino data. The agreement of the total hadronic π^-–Ar cross section measurement between the two different Run-II -60 A and -100 A data sets gives us confidence that our methodology is valid,

thus laying the groundwork for the important cross section measurements of the exclusive channels, such as pion single-charge exchange* and pion absorption.

*A discussion of the ongoing work on the pion single-charge exchange channel is presented in Appendix D.

Appendix A

Estimation of Halo Pile-Up Rate

Who ordered that?

Isidor Isaac Rabi

Suppose that the probability of n pile-up particles in an event is $P(n$ particles) and the probability of reconstructing k tracks given that there are n pile-up particles is $P(k$ tracks $\mid n$ particles). The probability that k tracks are reconstructed would then be written as a convolution of two probability mass functions

$$P(k \text{ tracks}) = \sum_{n} P(k \text{ tracks} \mid n \text{ particles}) \times P(n \text{ particles}). \tag{A.1}$$

The probability $P(k$ tracks $\mid n$ particles) is described by the binomial probability mass function

$$\begin{aligned} P(k \text{ tracks} \mid n \text{ particles}) &= \binom{n}{k} (\mu_n)^k (1-\mu_n)^{n-k} \\ &= \frac{n!}{(n-k)!\, k!} (\mu_n)^k (1-\mu_n)^{n-k} \end{aligned} \tag{A.2}$$

where μ_n is defined to be the tracking efficiency given that there are n pile-up particles in the event. The probability $P(k$ tracks) can be estimated from data (Fig. A.1) while the tracking efficiencies μ_n can be estimated from Monte Carlo (Fig. A.2). In order to estimate

$P(n$ particles), we must perform a deconvolution. Defining

$$\begin{aligned} f(k) &\equiv P(k \text{ tracks}) \\ g(n) &\equiv P(n \text{ particles}) \\ A_n^k(\mu_n) &\equiv \frac{n!}{(n-k)!\ k!}\ (\mu_n)^k (1-\mu_n)^{n-k} \end{aligned} \tag{A.3}$$

we can rewrite Eq. A.1 as

$$\begin{aligned} f(k) &= \sum_{n=k}^{\infty} \frac{n!}{(n-k)!\ k!}\ (\mu_n)^k (1-\mu_n)^{n-k}\ g(n) \\ &= \sum_{n=k}^{\infty} A_n^k(\mu_n)\ g(n) \end{aligned} \tag{A.4}$$

noting that $A_n^k(\mu_n) = 0$ for $n < k$. We can also rewrite Eq. A.4 in matrix form as

$$\begin{bmatrix} A_0^0(\mu_0) & A_1^0(\mu_1) & \cdots & A_n^0(\mu_n) \\ A_0^1(\mu_0) & A_1^1(\mu_1) & \cdots & A_n^1(\mu_n) \\ \vdots & \vdots & \ddots & \vdots \\ A_0^k(\mu_0) & A_1^k(\mu_1) & \cdots & A_n^k(\mu_n) \end{bmatrix} \begin{bmatrix} g(0) \\ g(1) \\ \vdots \\ g(n) \end{bmatrix} = \begin{bmatrix} f(0) \\ f(1) \\ \vdots \\ f(k) \end{bmatrix}. \tag{A.5}$$

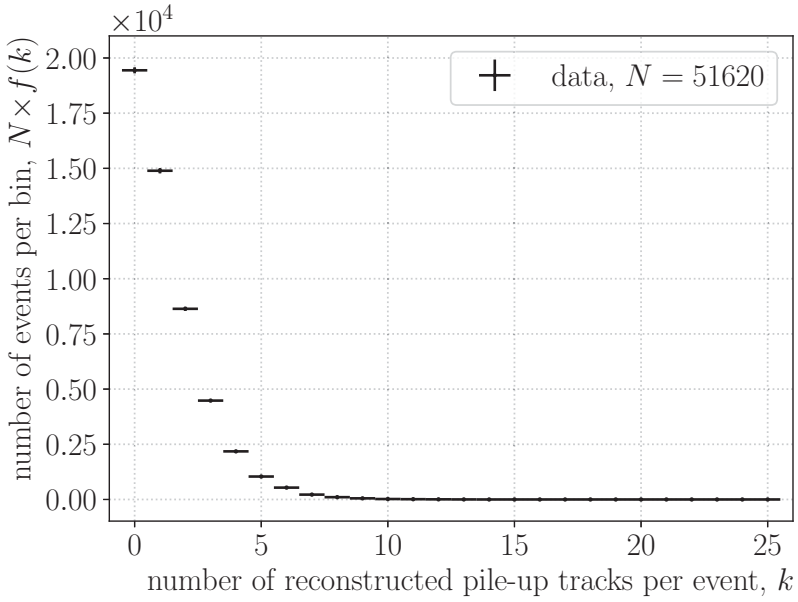

Figure A.1: Number of reconstructed halo pile-up tracks per event measured from the −100 A dataset.

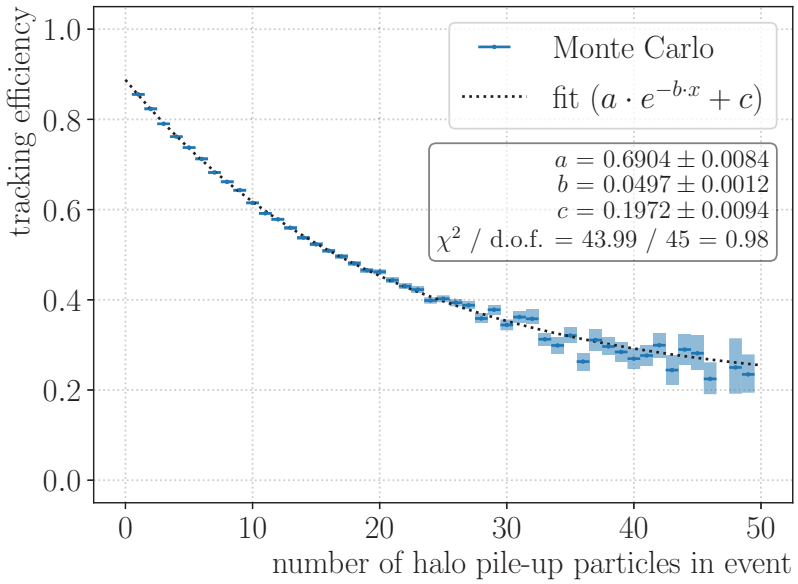

Figure A.2: Tracking efficiencies of halo pile-up particles estimated from Monte Carlo.

Deconvolution

Deconvolution of $g(n)$ can be performed using maximum likelihood estimation. Suppose that we have counted a total of N reconstructed pile-up tracks in our experiment such that the number of events with k reconstructed pile-up tracks is $x_k \equiv Nf(k)$ (with $\sum_k x_k = 1$). Since this is a counting measurement, the probability of measuring a particular value of x_k is given by the Poisson probability mass function

$$P(x_k \mid \lambda_k) = \frac{(\lambda_k)^{x_k} \exp(-\lambda_k)}{x_k!} \tag{5.4}$$

where $x_k \equiv Nf(k)$ are our measurements and $\lambda_k \equiv N \sum_n A_n^k(\mu_n)\ g(n)$ are parameters from our model. The likelihood (probability of the data given the model) of measuring the outcome in our experiment is

$$\mathcal{L}(\lambda \mid \text{data}) = P(\text{data} \mid \lambda) = \prod_k P(x_k \mid \lambda_k) = \prod_k \frac{(\lambda_k)^{x_k} \exp(-\lambda_k)}{x_k!}. \tag{5.5}$$

Taking the natural logarithm of the likelihood (Eq. 5.5) yields

$$\ln \mathcal{L} = \sum_k [x_k \ln(\lambda_k) - \lambda_k - \ln(x_k!)] \tag{5.6}$$

$$= \sum_k \left\{ Nf(k)\ \ln\left[N \sum_n A_n^k(\mu_n)\ g(n)\right] - \left[N \sum_n A_n^k(\mu_n)\ g(n)\right] - \ln[Nf(k)]! \right\}. \tag{A.6}$$

We can fit for the parameters $g(n)$ by maximizing the log-likelihood (Eq. A.6). Fig. A.3 shows the deconvolution done with the -100 A dataset (using $f(k)$ from Fig. A.1 and μ_n from Fig. A.2).

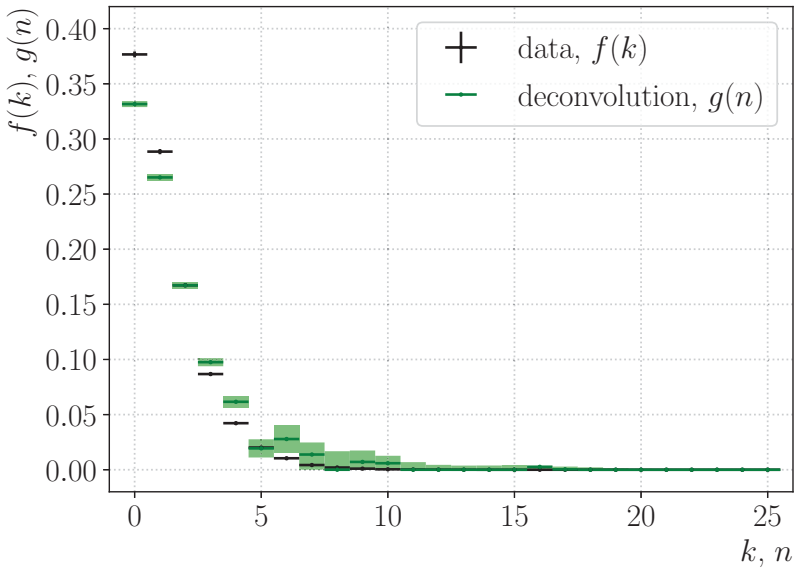

Figure A.3: Estimated probability mass of reconstructing k pile-up tracks in an event, $f(k)$, taken from data, and estimated probability of n pile-up particles in an event, $g(n)$, from deconvolution.

Appendix B

Monte Carlo Simulations for Propagation of Statistical Uncertainties

This section contains select distributions from the 500,000 Monte Carlo simulations done to propagate statistical uncertainties:

(1) Distributions of $p_{\text{int}}^{\text{MC}}$ are shown in Figs. B.1 and B.2

(2) Distributions of $p_{\text{non-int}}^{\text{MC}}$ are shown in Fig. B.3 and B.4

(3) Distributions of $\epsilon_{\text{int}}^{\text{MC}}$ are shown in Fig. B.5 and B.6

(4) Distributions of $\epsilon_{\text{non-int}}^{\text{MC}}$ are shown in Fig. B.7 and B.8

(5) Distributions of $\sigma_{\text{total}}^{\text{data}}$ (statistical uncertainty on data only) are shown in Fig. B.9 and B.10

(6) Distributions of $\sigma_{\text{total}}^{\text{data+MC}}$ (statistical uncertainty on both data and MC correction factors) are shown in Fig. B.11 and B.12

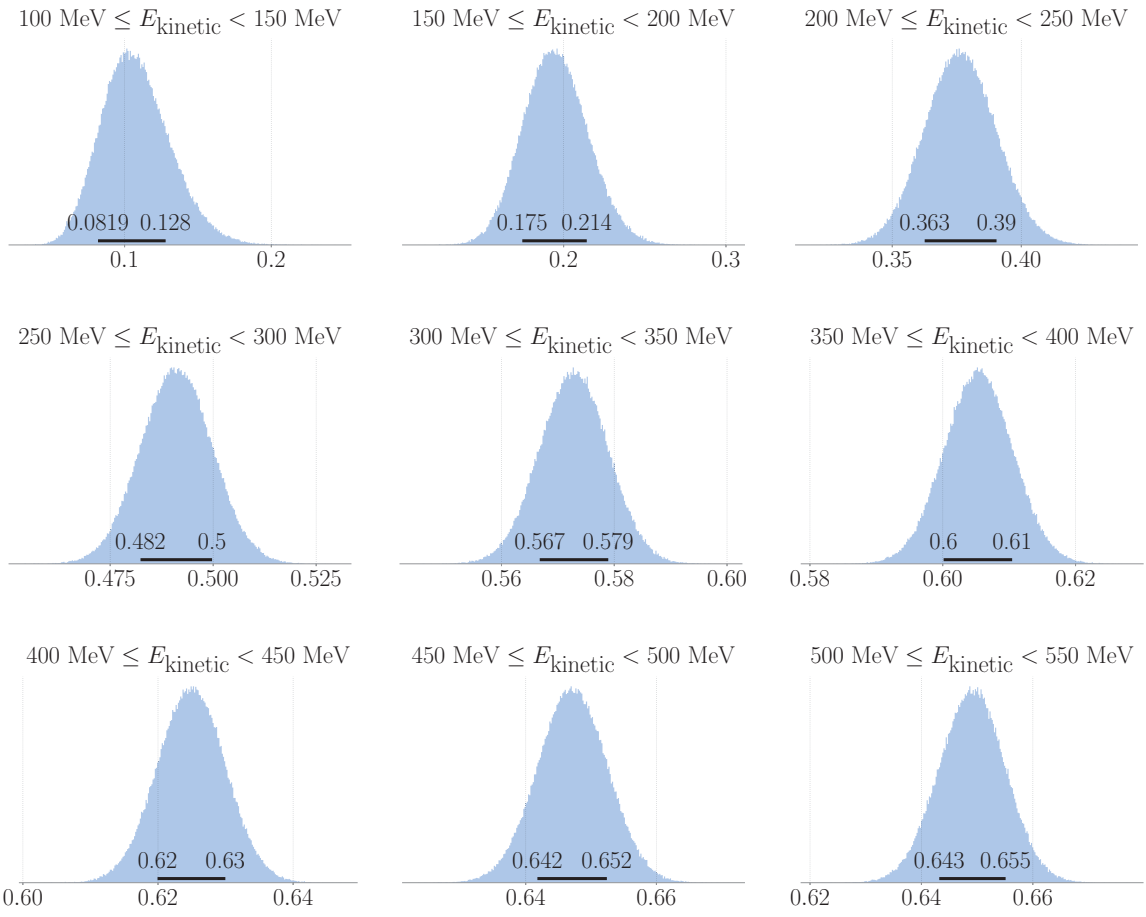

Figure B.1: Distributions of $p_{\text{int}}^{\text{MC}}$ generated from Monte Carlo simulations for kinetic energy bins between 100 MeV and 550 MeV. The horizontal black line at the bottom of each distribution indicates the 68.3% highest density interval (numerical labels are rounded to 3 significant figures). The nominal value of $p_{\text{int}}^{\text{MC}}$ is the mode (most probable value) of the distribution.

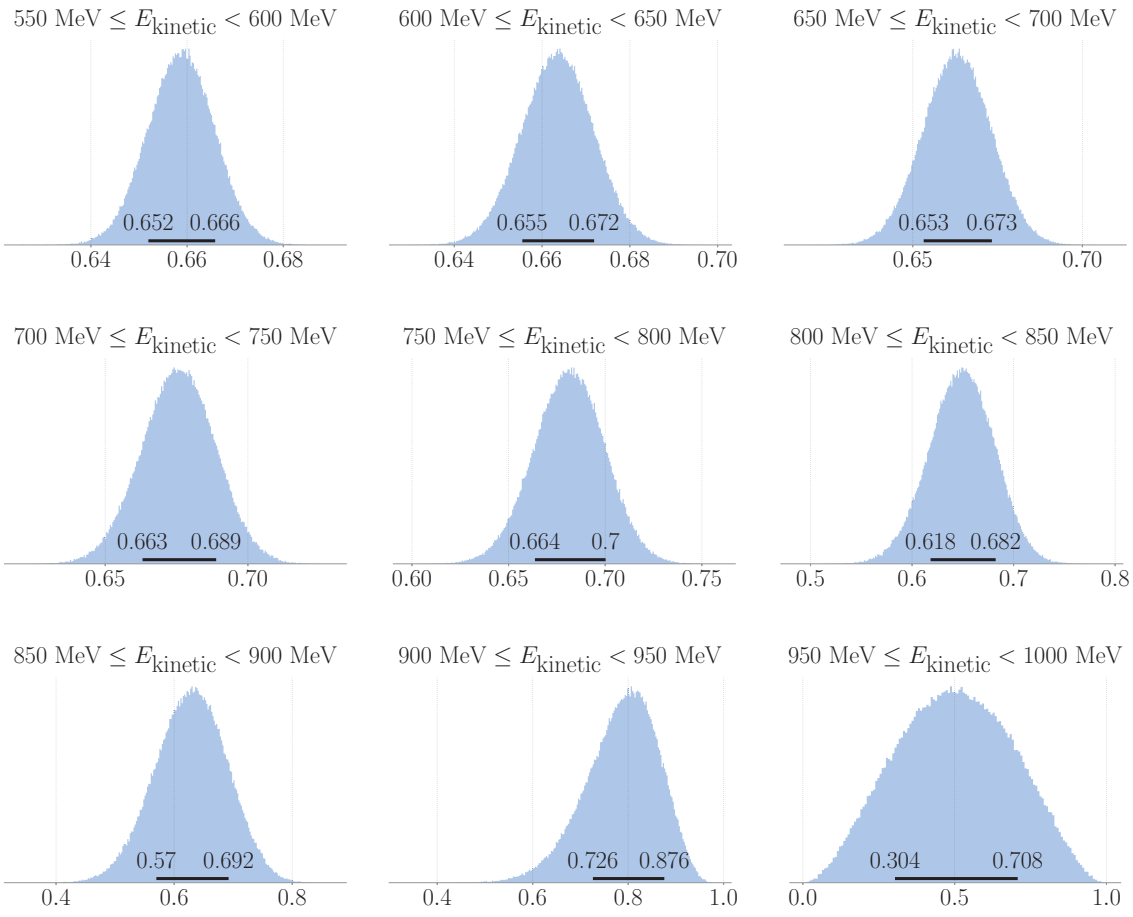

Figure B.2: Distributions of $p_{\text{int}}^{\text{MC}}$ generated from Monte Carlo simulations for kinetic energy bins between 550 MeV and 1000 MeV. The horizontal black line at the bottom of each distribution indicates the 68.3% highest density interval (numerical labels are rounded to 3 significant figures). The nominal value of $p_{\text{int}}^{\text{MC}}$ is the mode (most probable value) of the distribution.

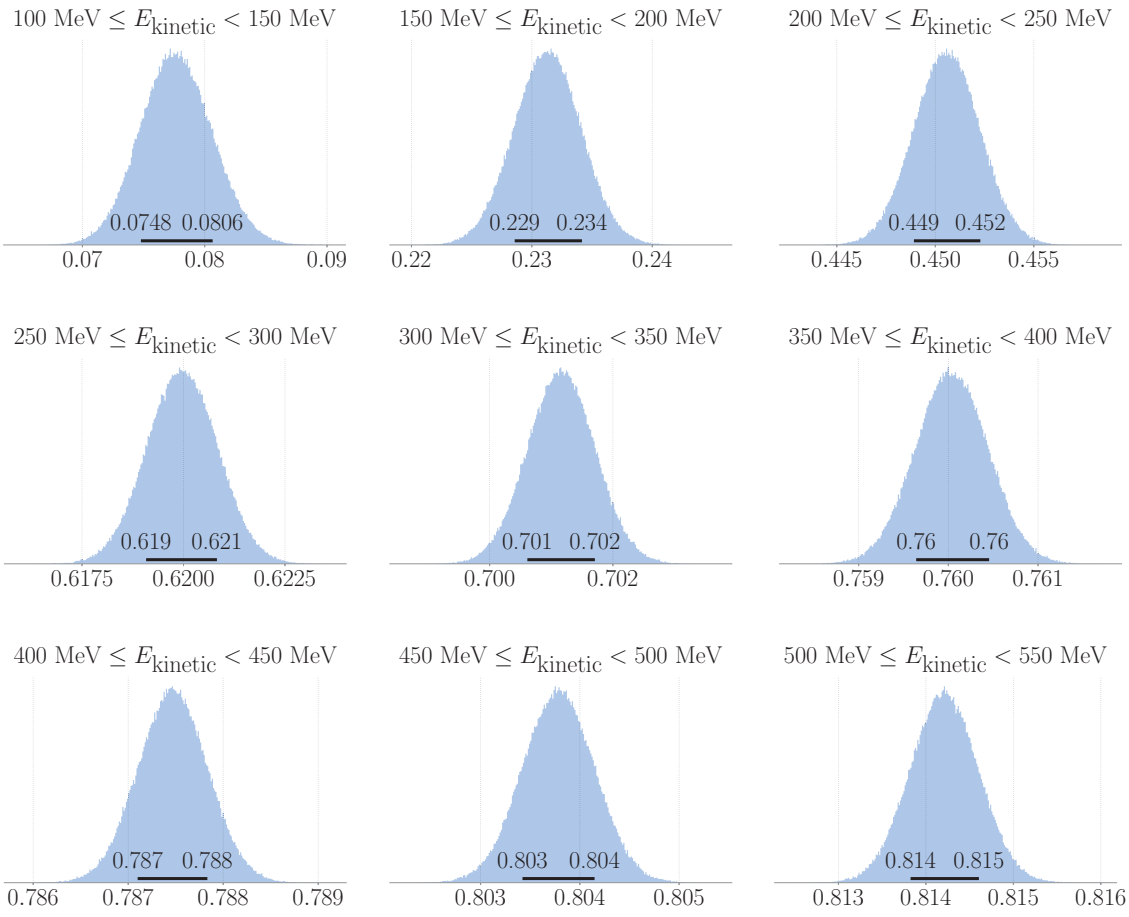

Figure B.3: Distributions of $p^{\text{MC}}_{\text{non-int}}$ generated from Monte Carlo simulations for kinetic energy bins between 100 MeV and 550 MeV. The horizontal black line at the bottom of each distribution indicates the 68.3% highest density interval (numerical labels are rounded to 3 significant figures). The nominal value of $p^{\text{MC}}_{\text{non-int}}$ is the mode (most probable value) of the distribution.

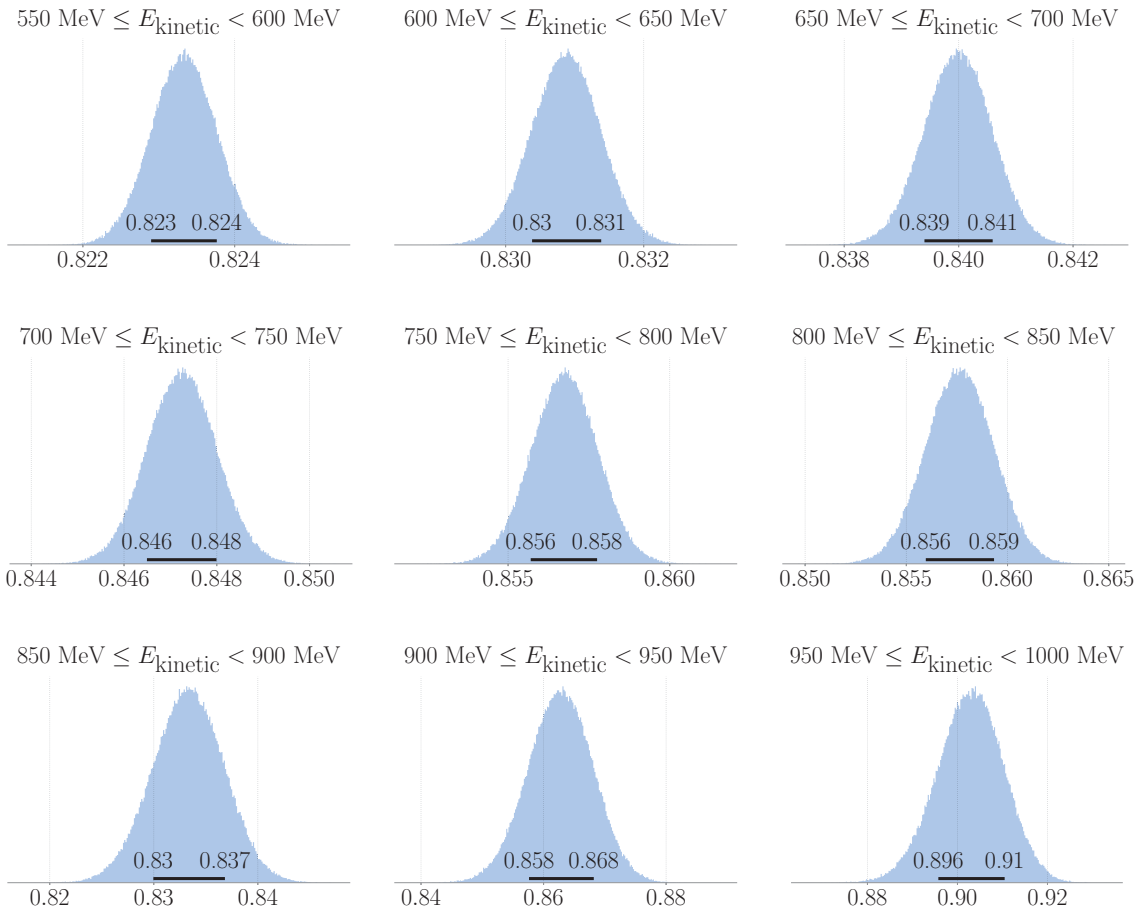

Figure B.4: Distributions of $p^{\text{MC}}_{\text{non-int}}$ generated from Monte Carlo simulations for kinetic energy bins between 550 MeV and 1000 MeV. The horizontal black line at the bottom of each distribution indicates the 68.3% highest density interval (numerical labels are rounded to 3 significant figures). The nominal value of $p^{\text{MC}}_{\text{non-int}}$ is the mode (most probable value) of the distribution.

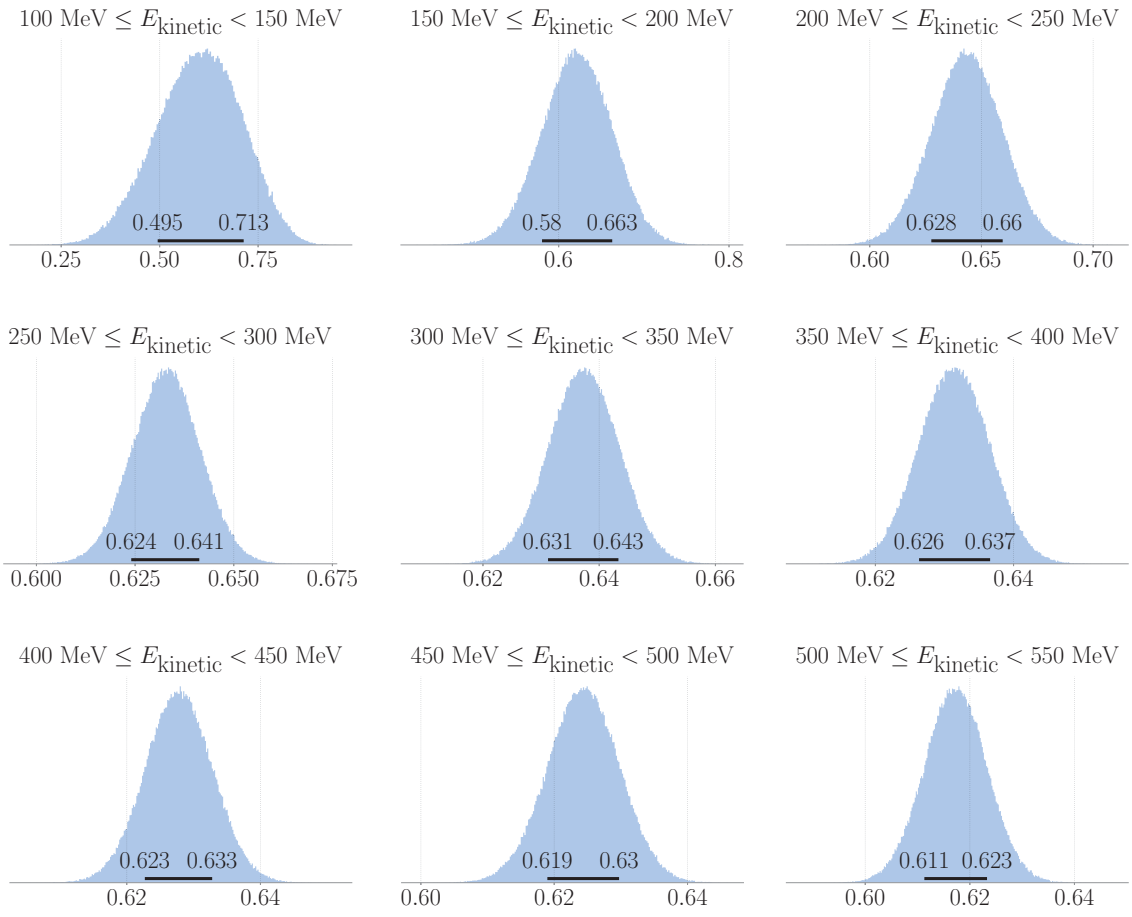

Figure B.5: Distributions of $\epsilon_{\text{int}}^{\text{MC}}$ generated from Monte Carlo simulations for kinetic energy bins between 100 MeV and 550 MeV. The horizontal black line at the bottom of each distribution indicates the 68.3% highest density interval (numerical labels are rounded to 3 significant figures). The nominal value of $\epsilon_{\text{int}}^{\text{MC}}$ is the mode (most probable value) of the distribution.

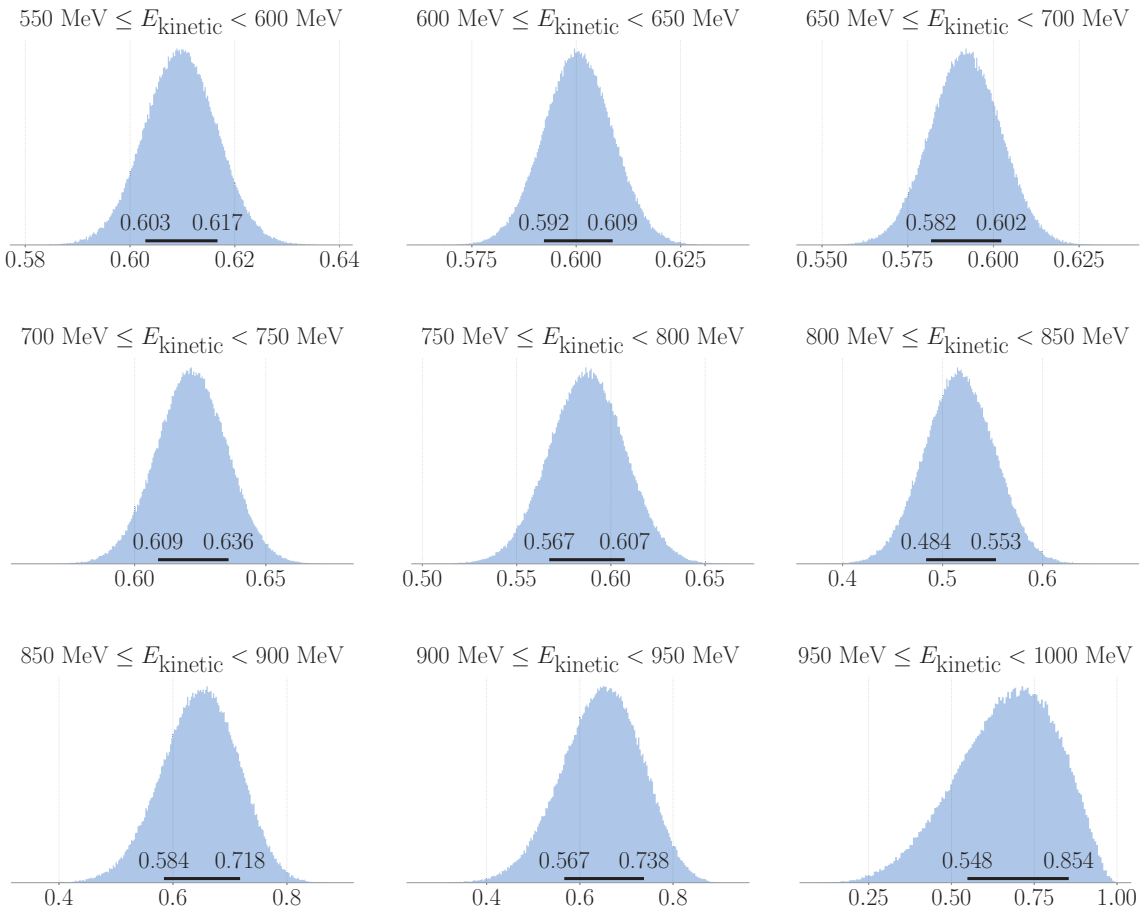

Figure B.6: Distributions of $\epsilon_{\text{int}}^{\text{MC}}$ generated from Monte Carlo simulations for kinetic energy bins between 550 MeV and 1000 MeV. The horizontal black line at the bottom of each distribution indicates the 68.3% highest density interval (numerical labels are rounded to 3 significant figures). The nominal value of $\epsilon_{\text{int}}^{\text{MC}}$ is the mode (most probable value) of the distribution.

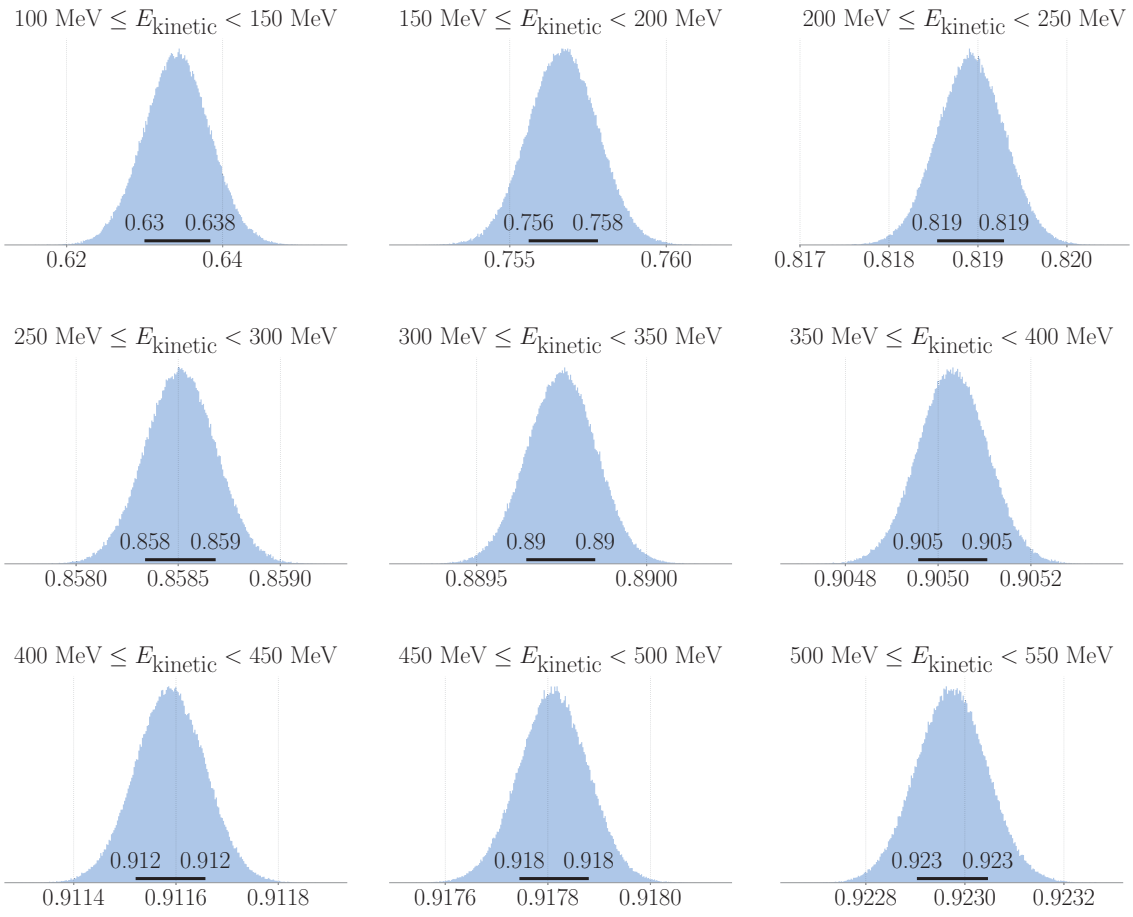

Figure B.7: Distributions of $\epsilon^{\text{MC}}_{\text{non-int}}$ generated from Monte Carlo simulations for kinetic energy bins between 100 MeV and 550 MeV. The horizontal black line at the bottom of each distribution indicates the 68.3% highest density interval (numerical labels are rounded to 3 significant figures). The nominal value of $\epsilon^{\text{MC}}_{\text{non-int}}$ is the mode (most probable value) of the distribution.

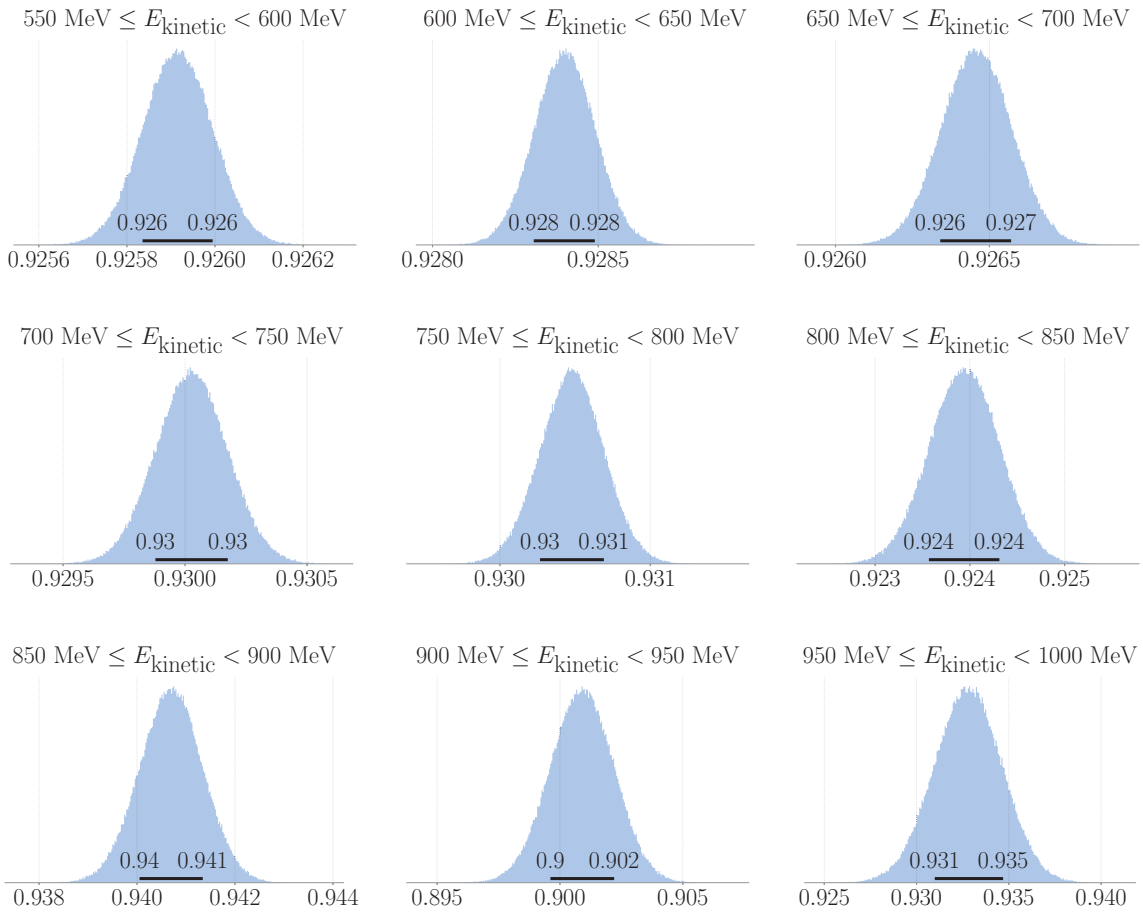

Figure B.8: Distributions of $\epsilon^{\text{MC}}_{\text{non-int}}$ generated from Monte Carlo simulations for kinetic energy bins between 550 MeV and 1000 MeV. The horizontal black line at the bottom of each distribution indicates the 68.3% highest density interval (numerical labels are rounded to 3 significant figures). The nominal value of $\epsilon^{\text{MC}}_{\text{non-int}}$ is the mode (most probable value) of the distribution.

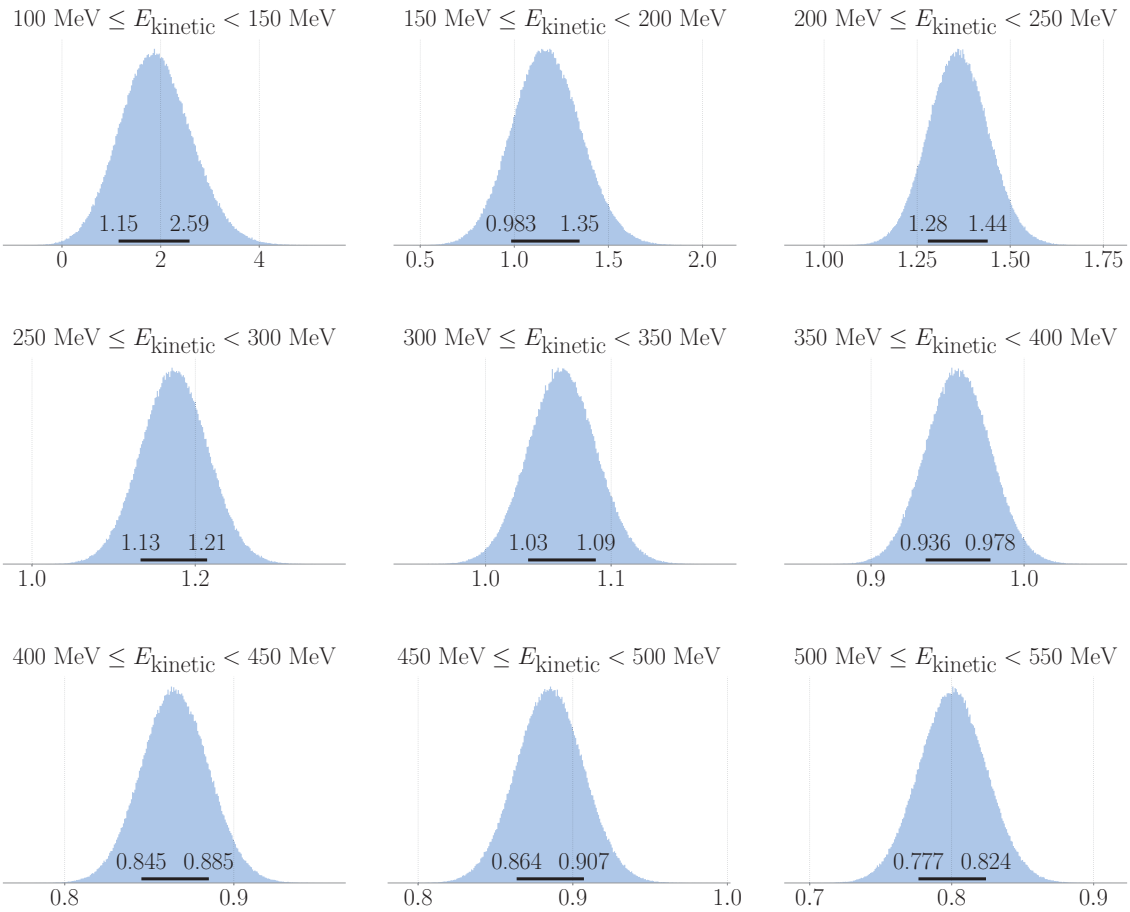

Figure B.9: Distributions of $\sigma_{\text{total}}^{\text{data}}$ generated from Monte Carlo simulations for kinetic energy bins between 100 MeV and 550 MeV. The horizontal black line at the bottom of each distribution indicates the 68.3% highest density interval (numerical labels are rounded to 3 significant figures).

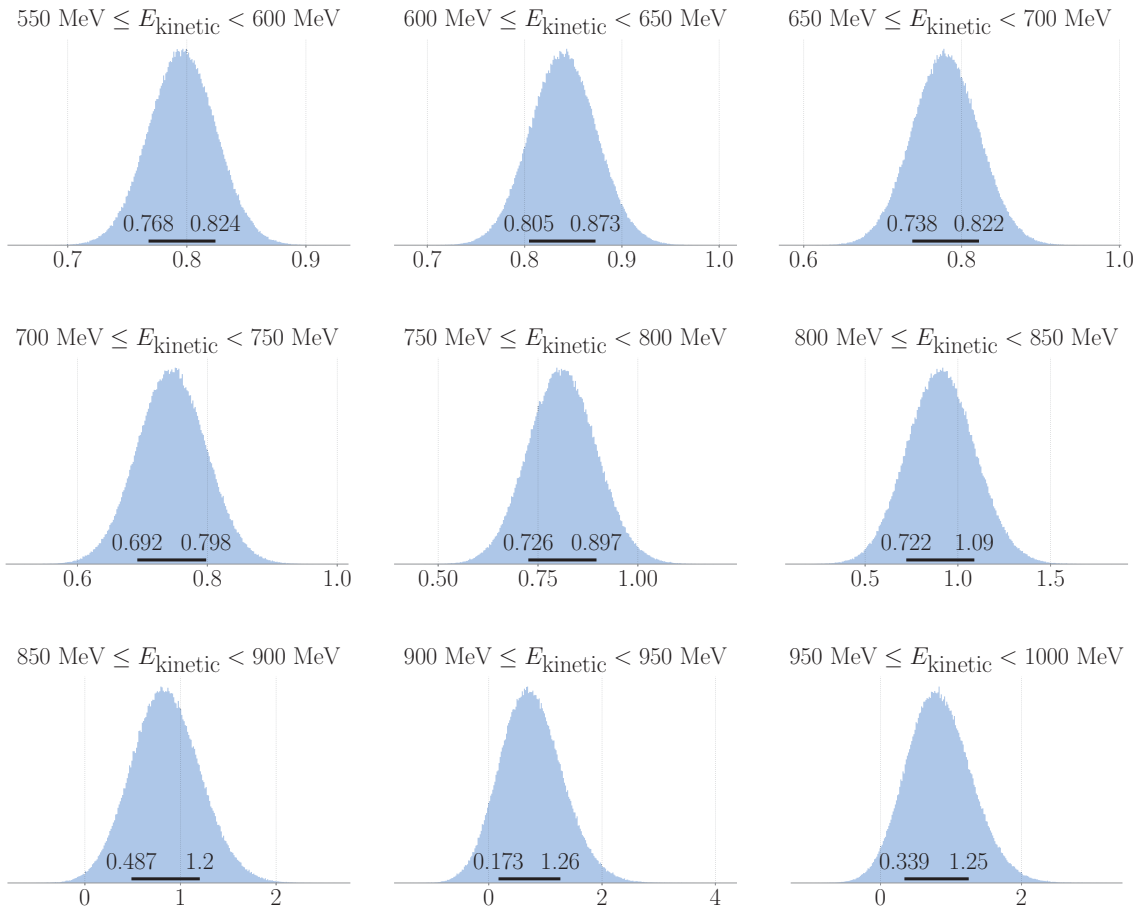

Figure B.10: Distributions of $\sigma_{\text{total}}^{\text{data}}$ generated from Monte Carlo simulations for kinetic energy bins between 550 MeV and 1000 MeV. The horizontal black line at the bottom of each distribution indicates the 68.3% highest density interval (numerical labels are rounded to 3 significant figures).

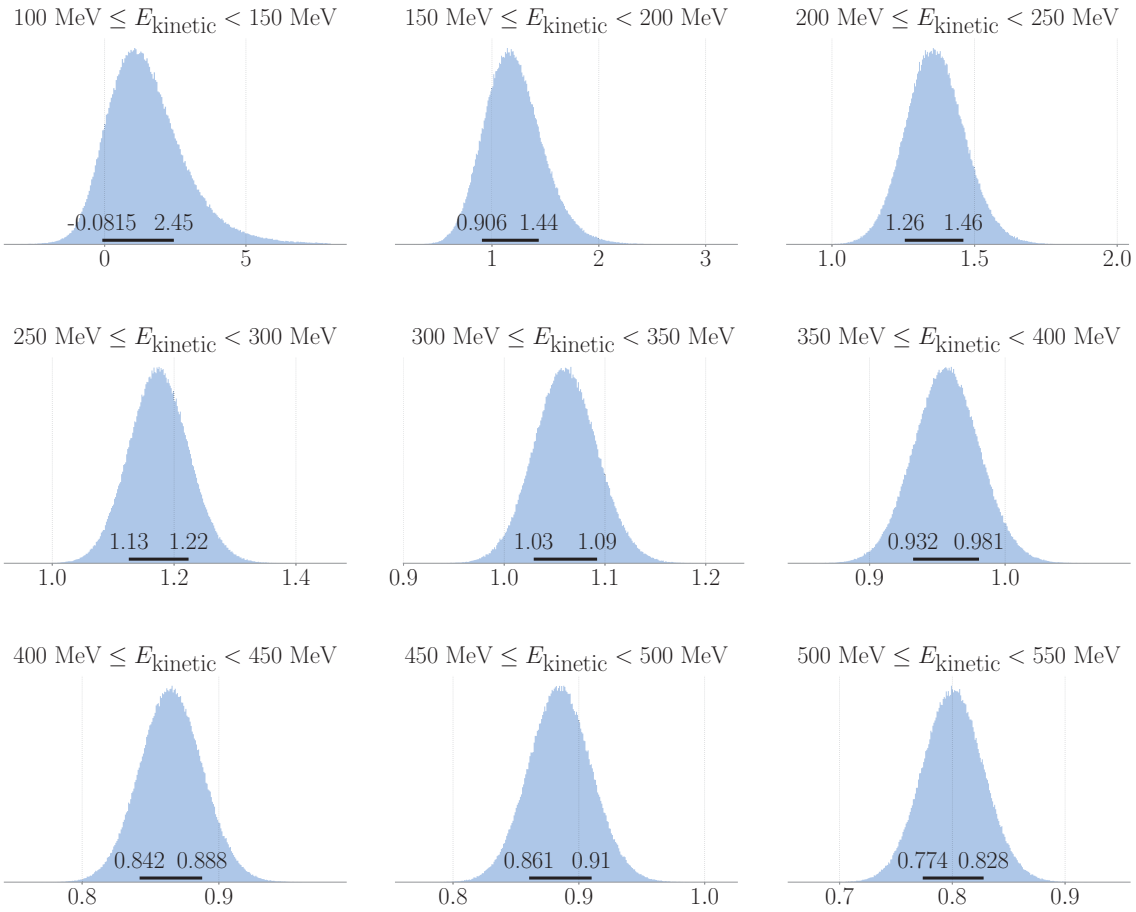

Figure B.11: Distributions of $\sigma_{\text{total}}^{\text{data+MC}}$ generated from Monte Carlo simulations for kinetic energy bins between 100 MeV and 550 MeV. The horizontal black line at the bottom of each distribution indicates the 68.3% highest density interval (numerical labels are rounded to 3 significant figures).

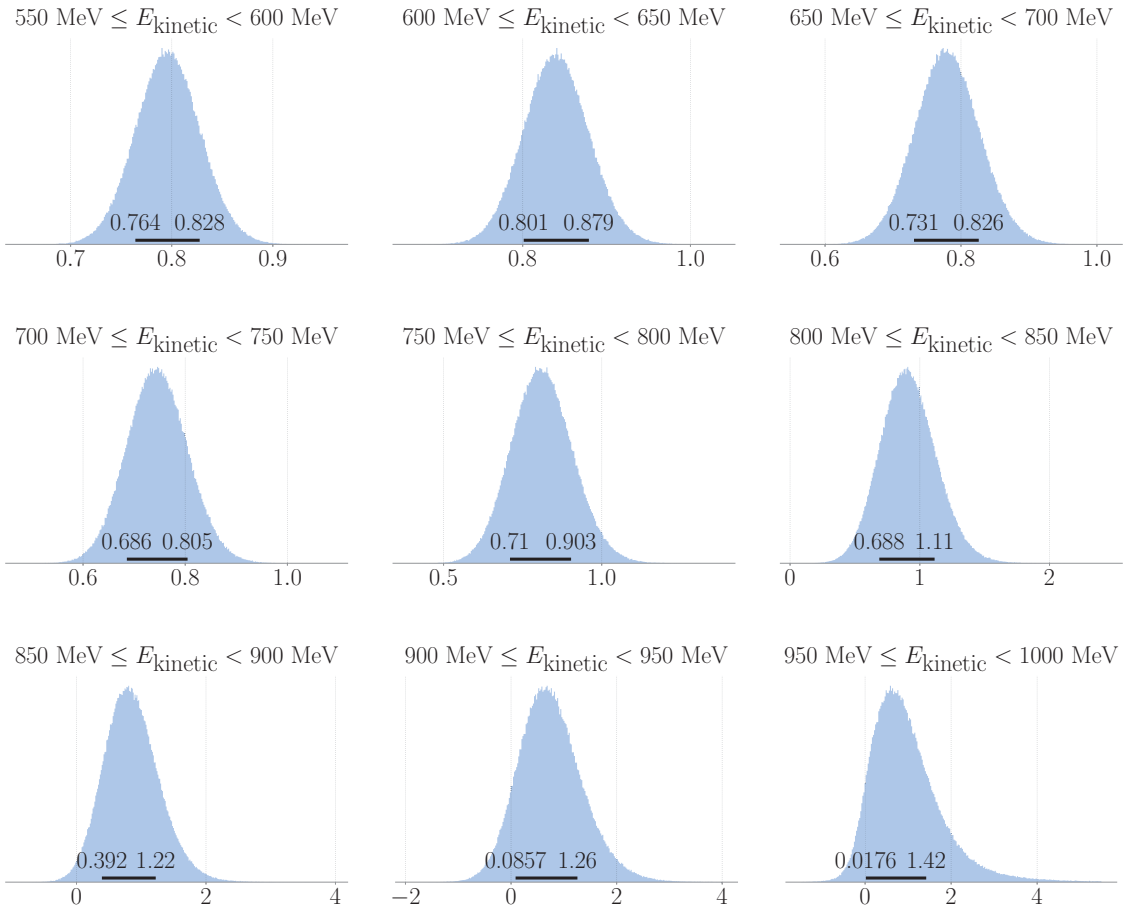

Figure B.12: Distributions of $\sigma_{\text{total}}^{\text{data+MC}}$ generated from Monte Carlo simulations for kinetic energy bins between 550 MeV and 1000 MeV. The horizontal black line at the bottom of each distribution indicates the 68.3% highest density interval (numerical labels are rounded to 3 significant figures).

Appendix C

Monte Carlo Simulations for Propagation of Systematic Uncertainties

This section contains select distributions from the Monte Carlo simulations done to propagate systematic uncertainties:

(1) Distributions of C_π, C_μ, and C_e for the beam content systematic uncertainty, where C_μ and C_e are varied, are shown in Fig. C.1

(2) Distributions of $\sigma^{\mu/e}_{\text{total}}$ for the beam content systematic uncertainty, where C_μ and C_e are varied, are shown in Fig. C.3 and C.4

(3) Distributions of C_π, C_μ, and C_e for the beam content systematic uncertainty, where C_π and C_e are varied, are shown in Fig. C.2

(4) Distributions of $\sigma^{\pi/e}_{\text{total}}$ for the beam content systematic uncertainty, where C_π and C_e are varied, are shown in Fig. C.5 and C.6

(5) Distributions of $\sigma^{\text{energy}}_{\text{total}}$ for the energy systematic uncertainties are shown in Fig. C.7 and C.8

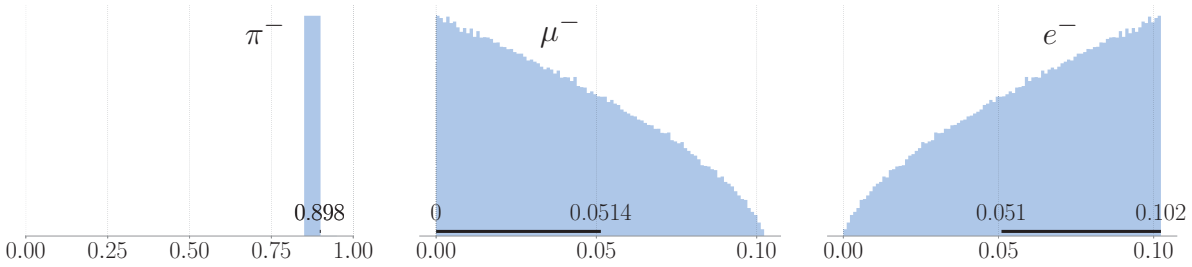

Figure C.1: Distributions of C_π, C_μ, and C_e. C_μ and C_e are simulated from a beta distribution with parameters $a = 1.65$ and $b = 1.0$.

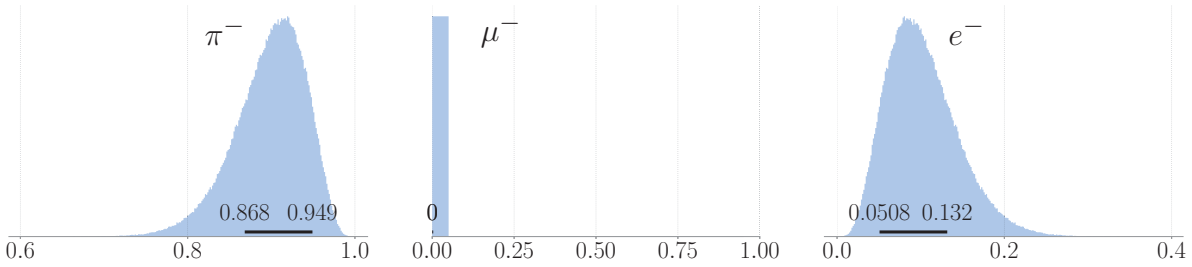

Figure C.2: Distributions of C_π, C_μ, and C_e simulated from a Dirichlet distribution.

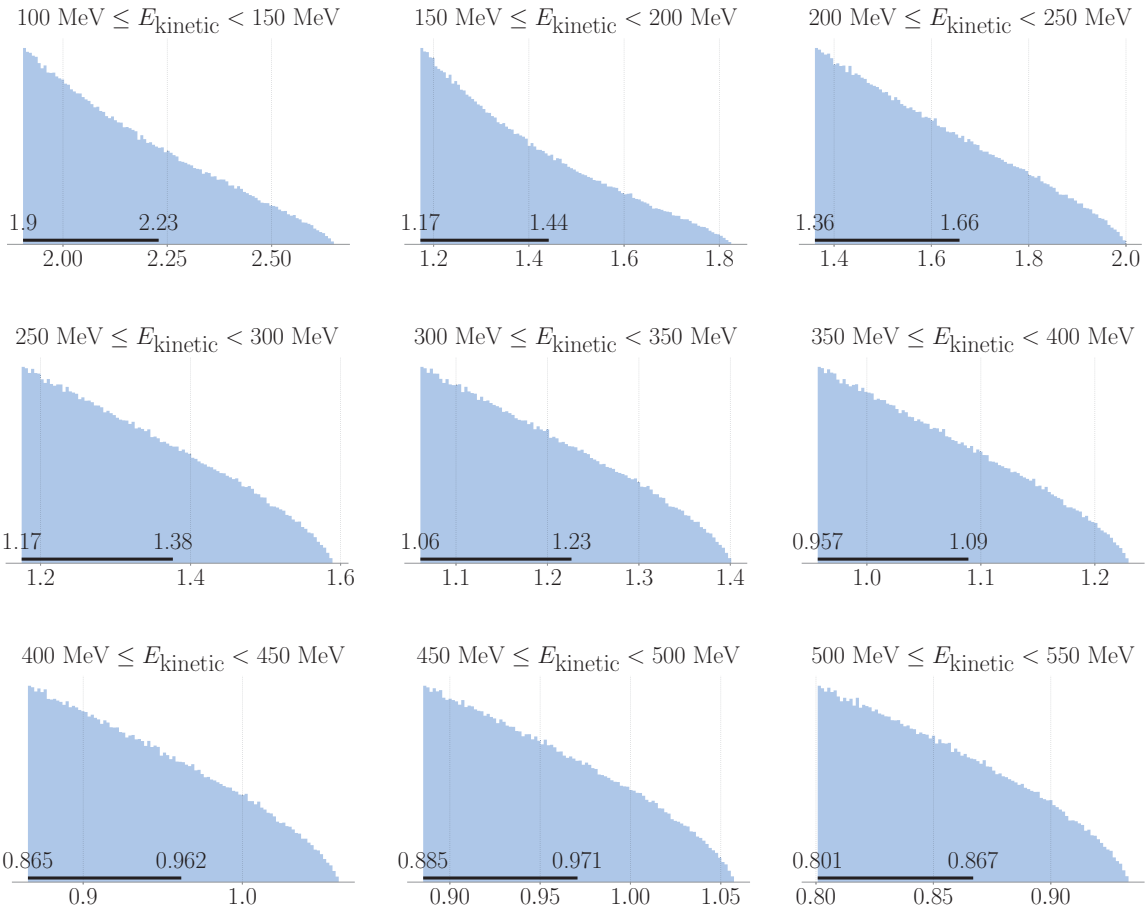

Figure C.3: Distributions of $\sigma^{\mu/e}_{\text{total}}$ generated from Monte Carlo simulations for kinetic energy bins between 100 MeV and 550 MeV. The horizontal black line at the bottom of each distribution indicates the 68.3% highest density interval (numerical labels are rounded to 3 significant figures).

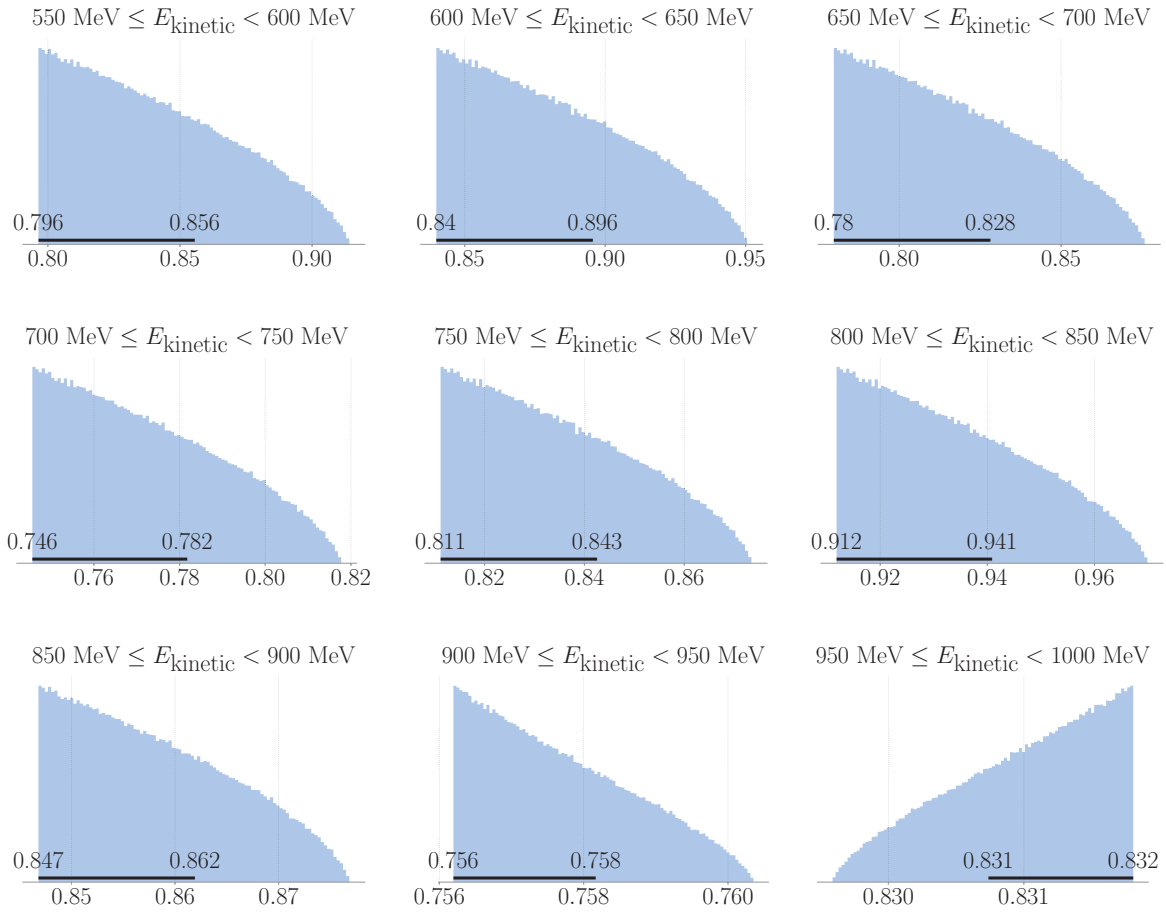

Figure C.4: Distributions of $\sigma^{\mu/e}_{\text{total}}$ generated from Monte Carlo simulations for kinetic energy bins between 550 MeV and 1000 MeV. The horizontal black line at the bottom of each distribution indicates the 68.3% highest density interval (numerical labels are rounded to 3 significant figures).

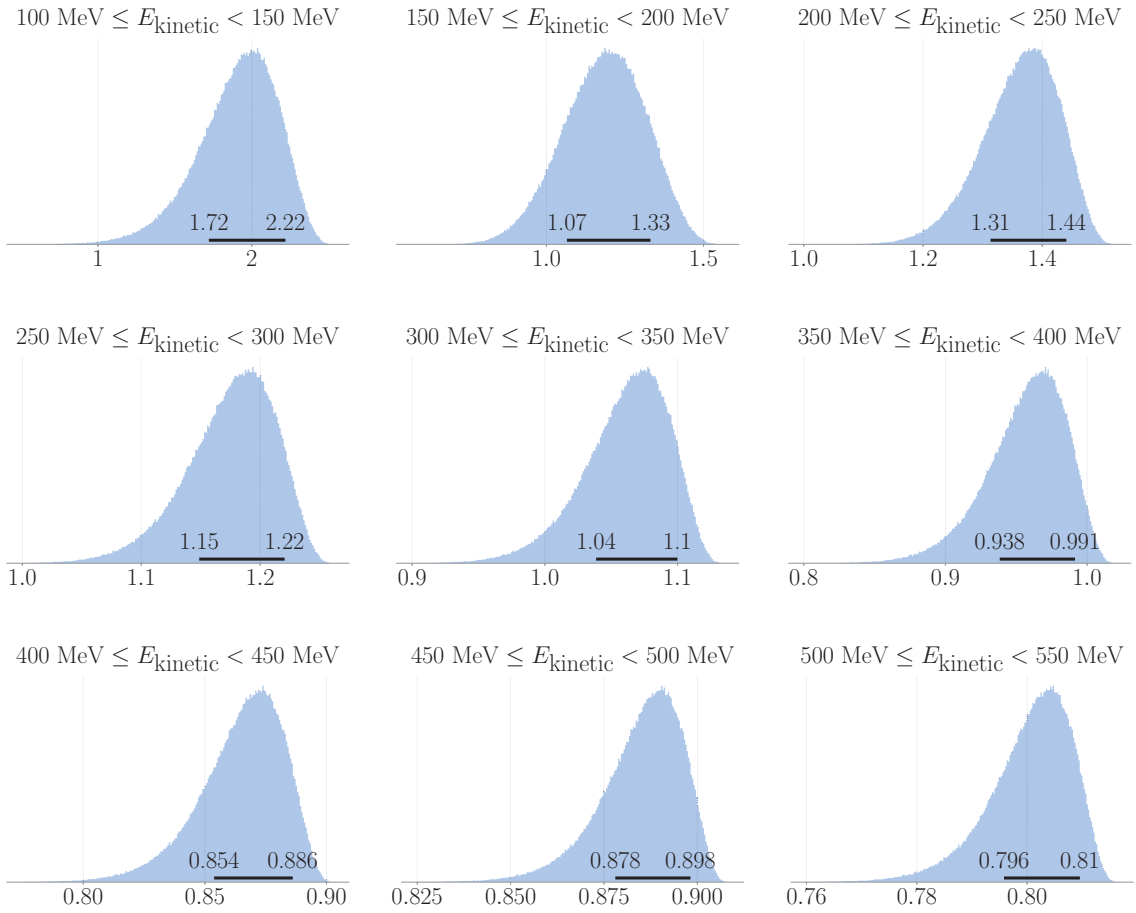

Figure C.5: Distributions of $\sigma^{\pi/e}_{\text{total}}$ generated from Monte Carlo simulations for kinetic energy bins between 100 MeV and 550 MeV. The horizontal black line at the bottom of each distribution indicates the 68.3% highest density interval (numerical labels are rounded to 3 significant figures).

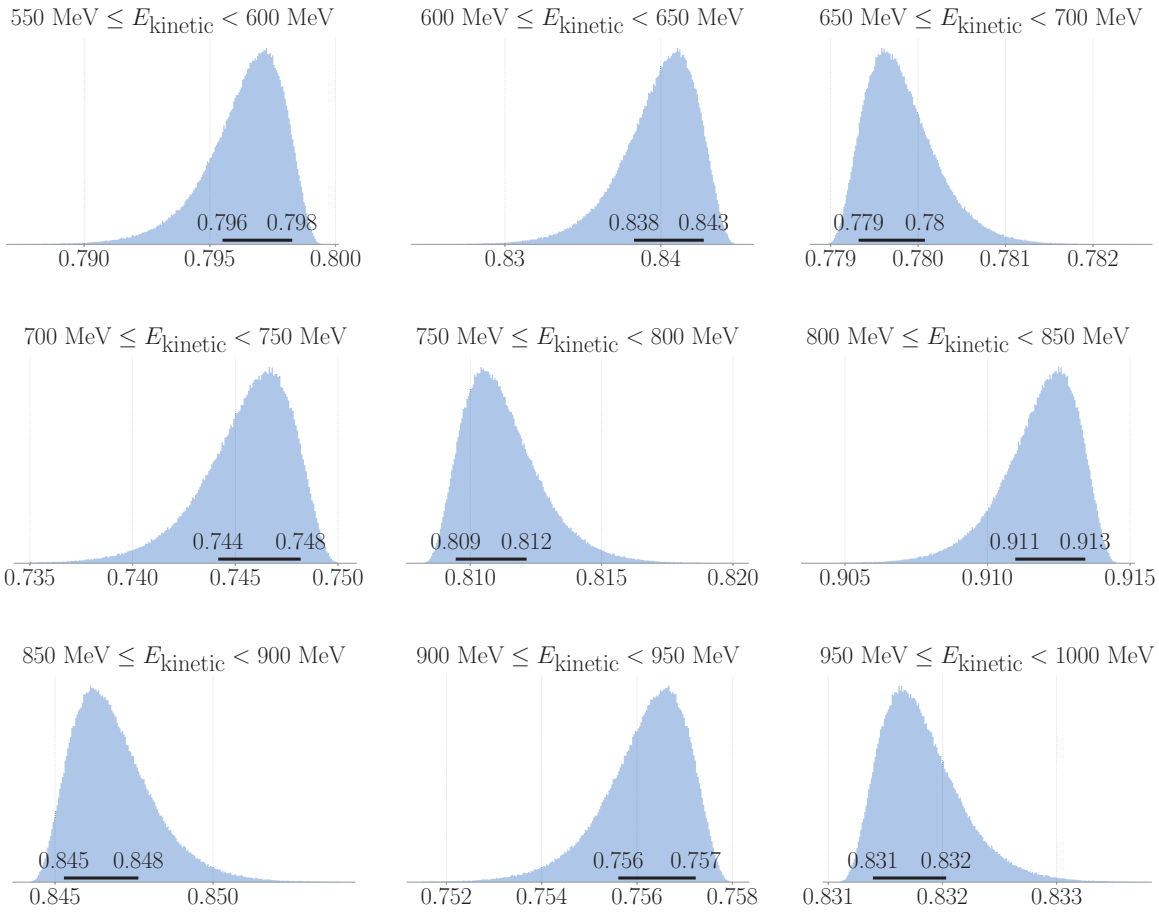

Figure C.6: Distributions of $\sigma^{\pi/e}_{\text{total}}$ generated from Monte Carlo simulations for kinetic energy bins between 550 MeV and 1000 MeV. The horizontal black line at the bottom of each distribution indicates the 68.3% highest density interval (numerical labels are rounded to 3 significant figures).

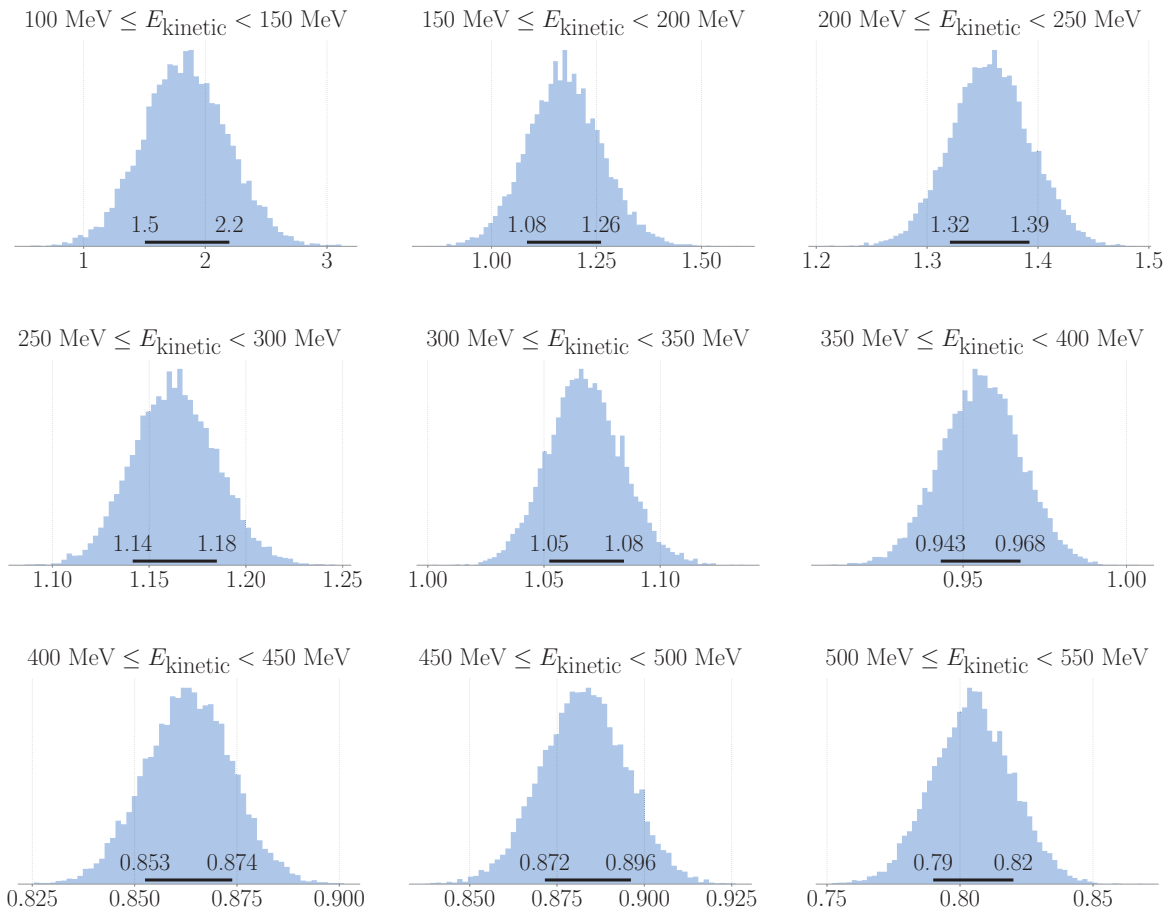

Figure C.7: Distributions of $\sigma_{\text{total}}^{\text{energy}}$ generated from Monte Carlo simulations for kinetic energy bins between 100 MeV and 550 MeV. The horizontal black line at the bottom of each distribution indicates the 68.3% highest density interval (numerical labels are rounded to 3 significant figures).

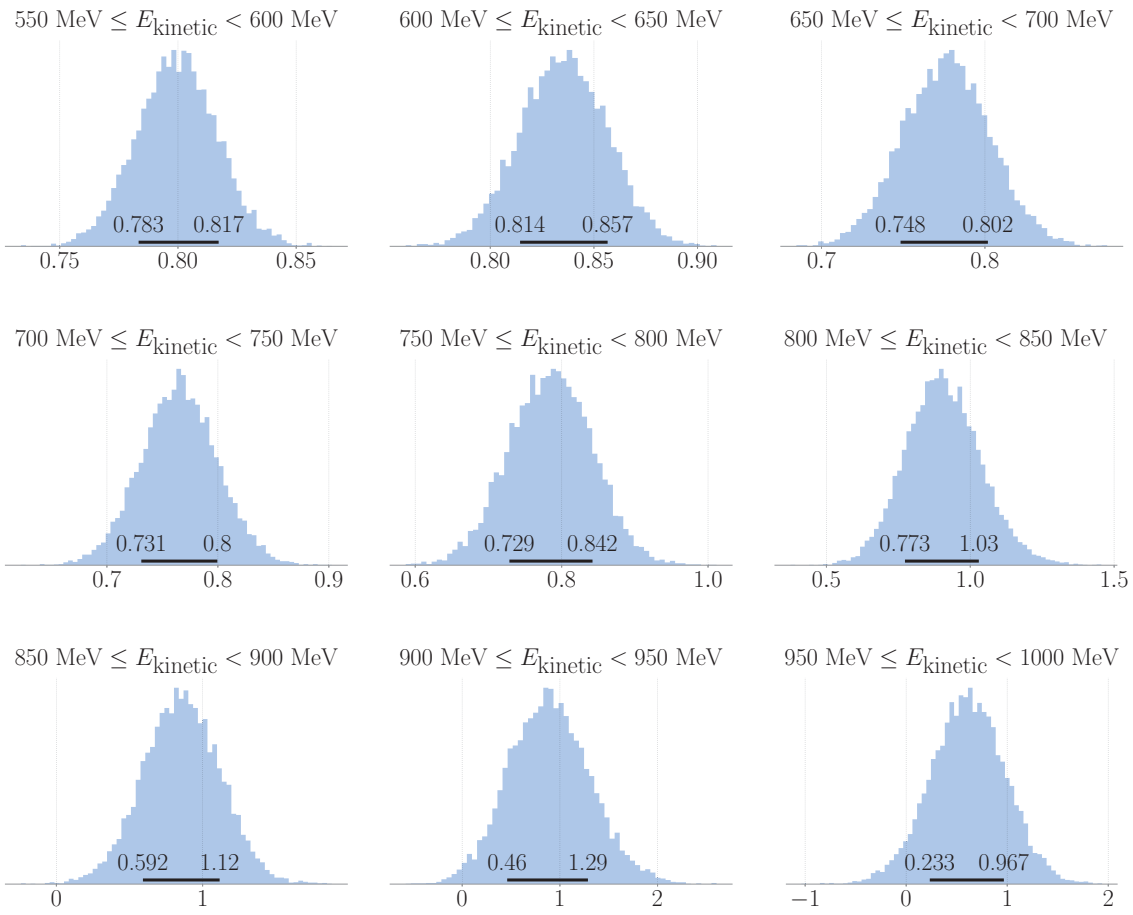

Figure C.8: Distributions of $\sigma_{\text{total}}^{\text{energy}}$ generated from Monte Carlo simulations for kinetic energy bins between 550 MeV and 1000 MeV. The horizontal black line at the bottom of each distribution indicates the 68.3% highest density interval (numerical labels are rounded to 3 significant figures).

Appendix D

Pion Single-Charge Exchange

The pion single-charge exchange (SCX) reactions for π^- and π^+ are

$$\begin{aligned} \pi^- + p &\rightarrow \Delta^0 \\ \Delta^0 &\rightarrow \pi^0 + n, \end{aligned} \tag{D.1}$$

$$\begin{aligned} \pi^+ + n &\rightarrow \Delta^+ \\ \Delta^+ &\rightarrow \pi^0 + p. \end{aligned} \tag{D.2}$$

Since the mean lifetime of the π^0 is $8.52(18) \times 10^{-17}$ s [30], the π^0 immediately decays into two gamma rays. A pion SCX on argon event in LArIAT is illustrated in Fig. D.1, where the gamma rays from the π^0 decay may induce electromagnetic showers within the TPC. Given the relatively small dimensions of the LArIAT TPC (47 cm $\times$ 40 cm $\times$ 90 cm) and the 14 cm radiation length in liquid argon (LAr), a significant fraction of gamma rays in pion SCX events may escape the TPC or induce electromagnetic (EM) showers that are partially contained. Pion single-charge exchange events from the LArIAT dataset are shown in Figs. 2.7c and 3.1c.

An EM shower reconstruction algorithm was developed to identify gamma-induced EM showers in pion SCX interactions. Starting from a π^- candidate identified in the total hadronic π^-–Ar cross section analysis:

(1) check if reconstructed interaction vertex exists in 3D and 2D (on a 2D wire plane),

(2) tag outgoing reconstructed secondary tracks connected at the reconstructed interaction vertex,

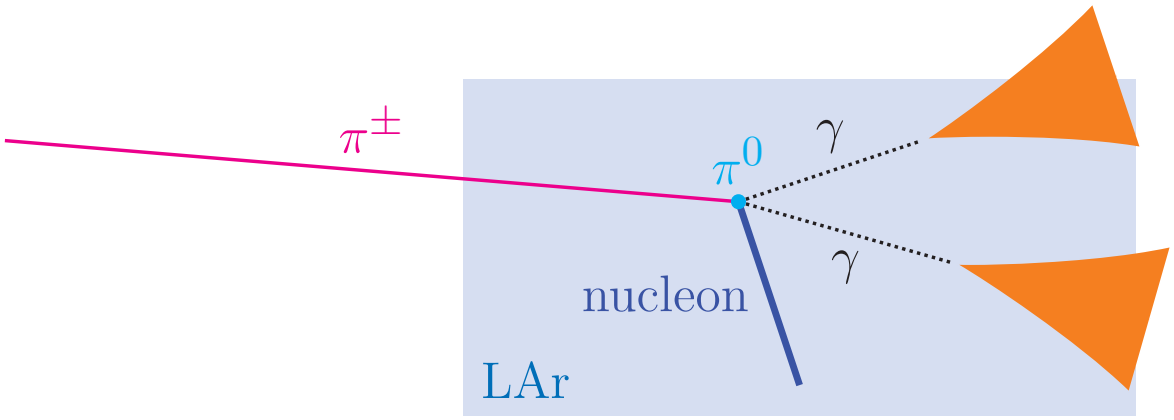

Figure D.1: Illustration of a pion single-charge-exchange event within the LArIAT TPC. The nucleon from the pion charge-exchange reaction can knock other nucleons out of the target nucleus via final-state interactions.

(3) using the 2D interaction vertex as an anchor point, perform a conical scan for 2D hits from EM activity,

(4) form an EM shower cluster and a principle 2D axis if enough hits are found,

(5) iteratively add unclustered hits into the EM shower cluster based on their proximity to the EM shower cluster,

(6) repeat until no additional EM shower clusters can be formed.

This is done on both the induction plane and collection plane for each event. We define the 2D start point of an EM shower cluster to be the position of the clustered hit that is closest to the 2D interaction vertex. Fig. D.2 shows a pion SCX candidate event with EM shower clusters. Reconstructed hits with the same color belong in the same cluster, with the exception of unclustered hits shown in black; reconstructed interaction vertices are shown with a star/circle.

We then attempt to match clusters between the wire planes based on the shapes of their charge distributions as a function of time. These distributions are compared using an overlap

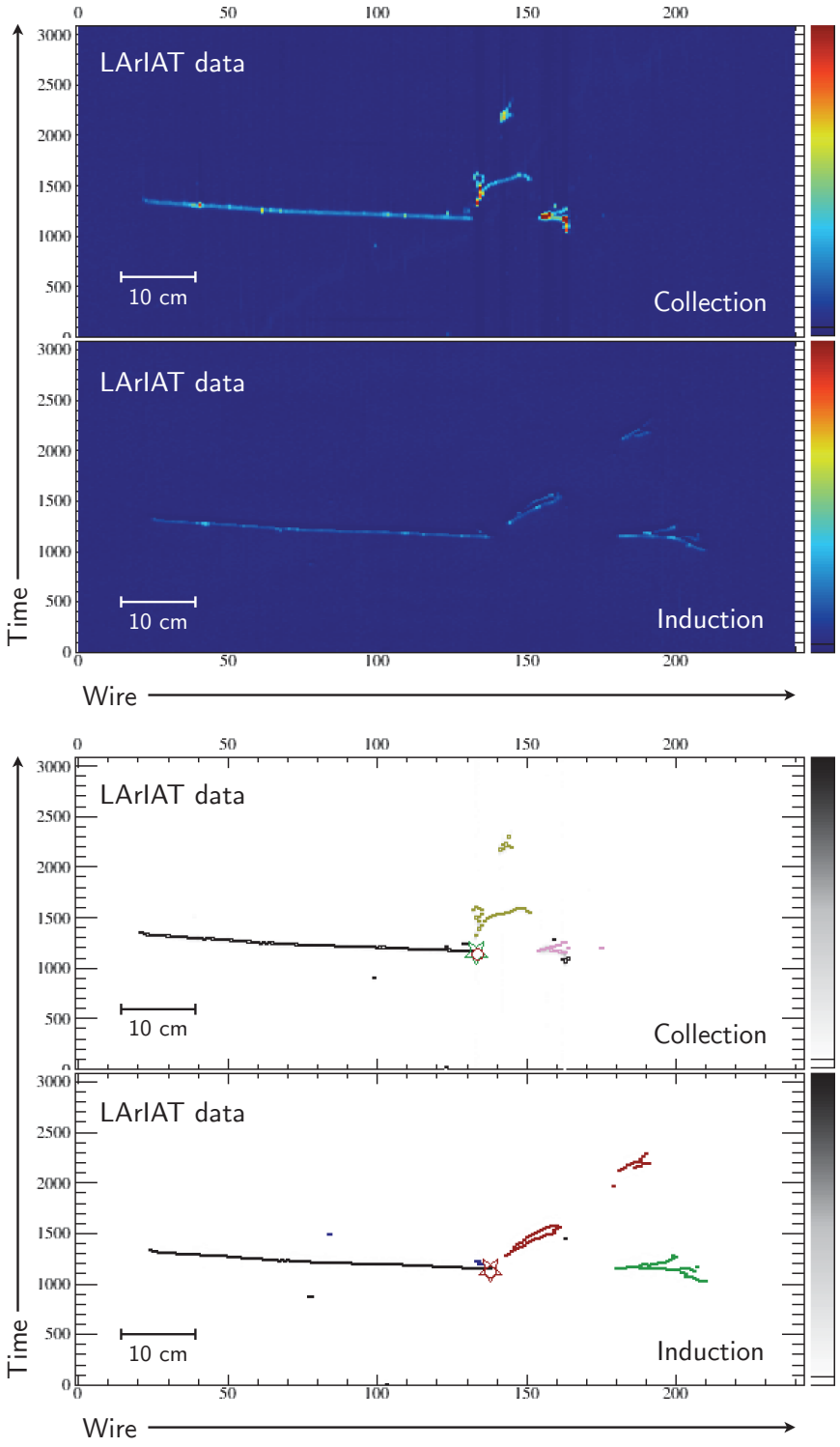

Figure D.2: Pion SCX candidate event. Raw event display is shown at the top; event display with reconstructed hits is shown at the bottom. Reconstructed hits with the same color belong in the same cluster (black excluded).

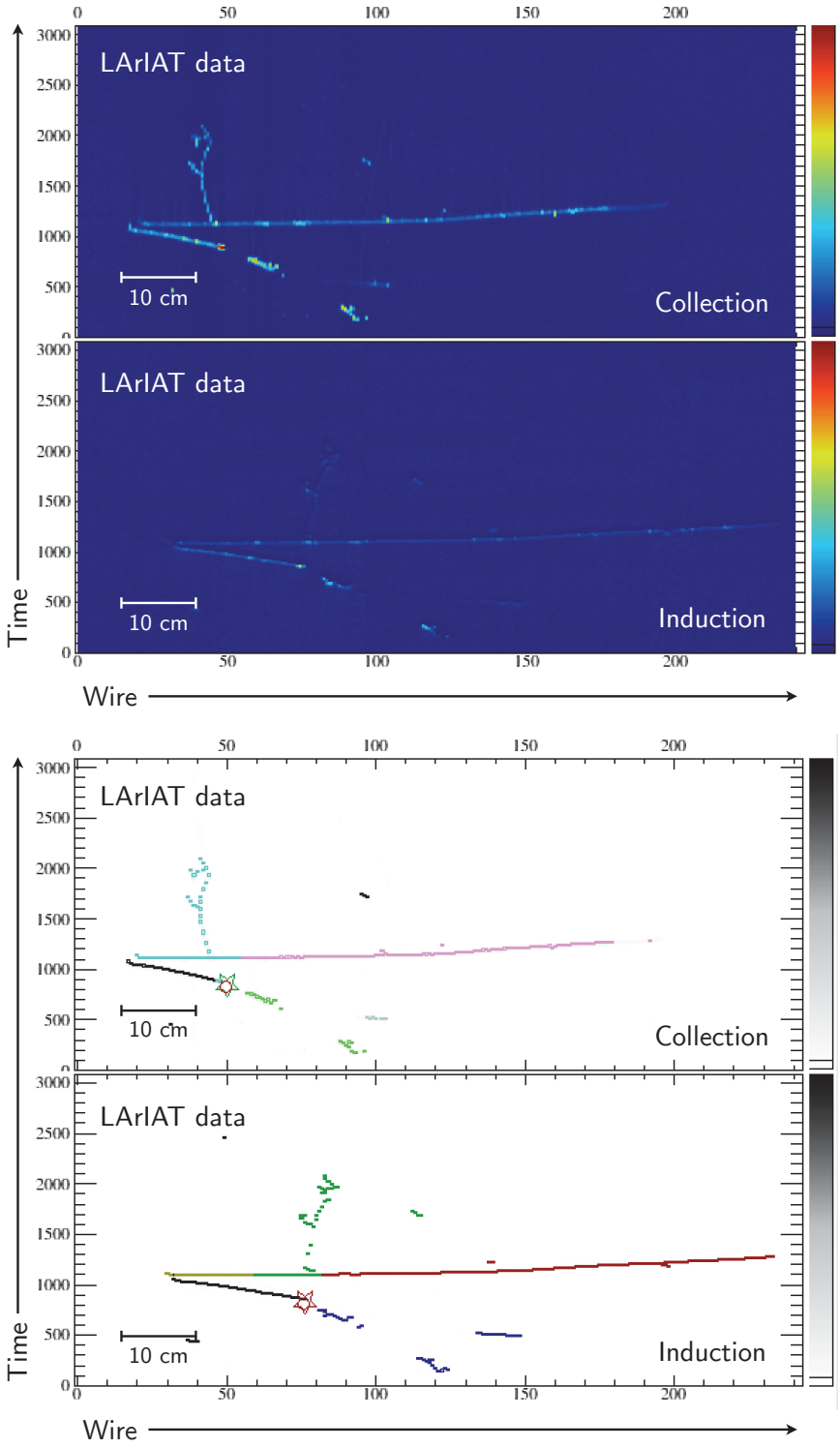

Figure D.3: Pion SCX candidate event with a pile-up particle. Raw event display is shown at the top; event display with reconstructed hits is shown at the bottom. Reconstructed hits with the same color belong in the same cluster (black excluded).

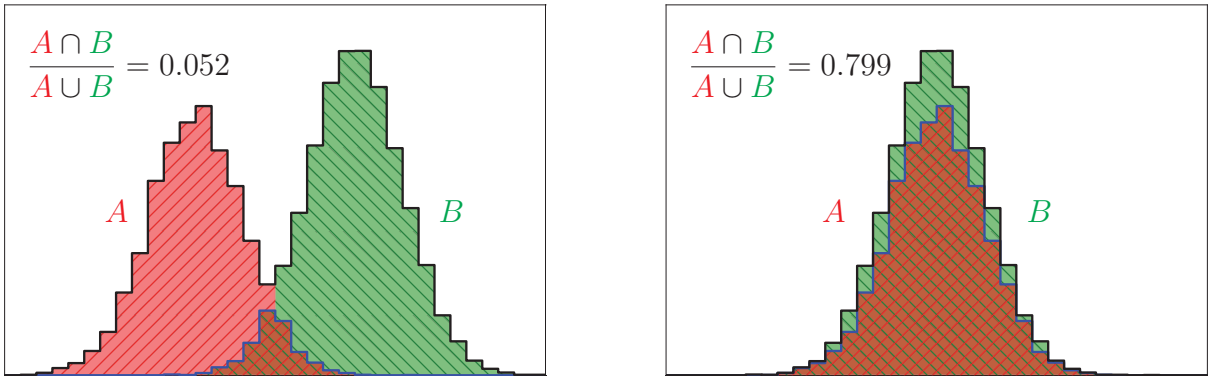

Figure D.4: Examples of the overlap coefficient. ADC is plotted along the vertical axis, and time is plotted along the horizontal axis.

coefficient*

$$\text{overlap}(A, B) \equiv \frac{A \cap B}{A \cup B} \tag{D.3}$$

where A is the integral of the distribution in one wire plane and B is the integral of the distribution in a different wire plane. Examples of the overlap coefficient are shown in Fig. D.4. The primary 2D axis of an EM shower cluster is determined by running a RANSAC (Random Sample Consensus) [87] algorithm. Clustered hits near the primary 2D axis are fed into the projection-matching algorithm [76], mentioned in Chapter 3, to reconstruct 3D hits. Principal component analysis (PCA) [88] is then performed on the 3D hits in order to determine the primary 3D axis of the EM shower.

As shown in Fig. D.3, a pile-up particle passing through the TPC can negatively impact the EM shower reconstruction in a pion SCX event. Quality cuts can be made in order to reject poorly reconstructed EM showers or hadronic particles that are mis-reconstructed as EM showers. As illustrated in Fig. D.5, we can project the primary 3D axis of the EM shower

*This should really be called the *modified* overlap coefficient since the overlap coefficient is usually defined as: $\text{overlap}(A, B) \equiv \frac{|A \cap B|}{\min(|A|, |B|)}$.

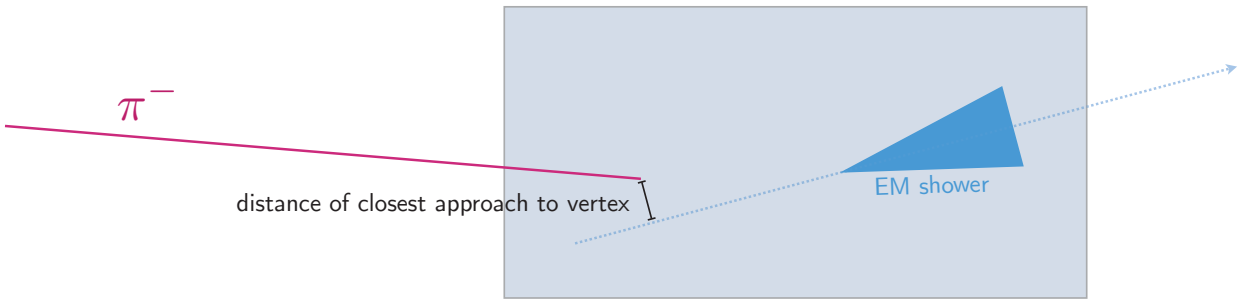

Figure D.5: Illustration of the distance of closest approach to vertex.

backwards towards the interaction vertex, and compute the distance of closest approach (DCA) to the vertex. Other reconstructed quantities to consider are the EM shower angle with respect to the z axis, as seen from the vertex, and the $\mathrm{d}E/\mathrm{d}x$ within the first 4 cm of the EM shower. These distributions are all shown in Fig. D.6. There is background that is not yet simulated in the data-driven Monte Carlo simulations, however, a cut can be applied to reject EM showers with DCA > 5 cm and reduced the unsimulated background, as shown in Fig. D.7. Ongoing work is being done to further clean up the sample and select pion SCX events.

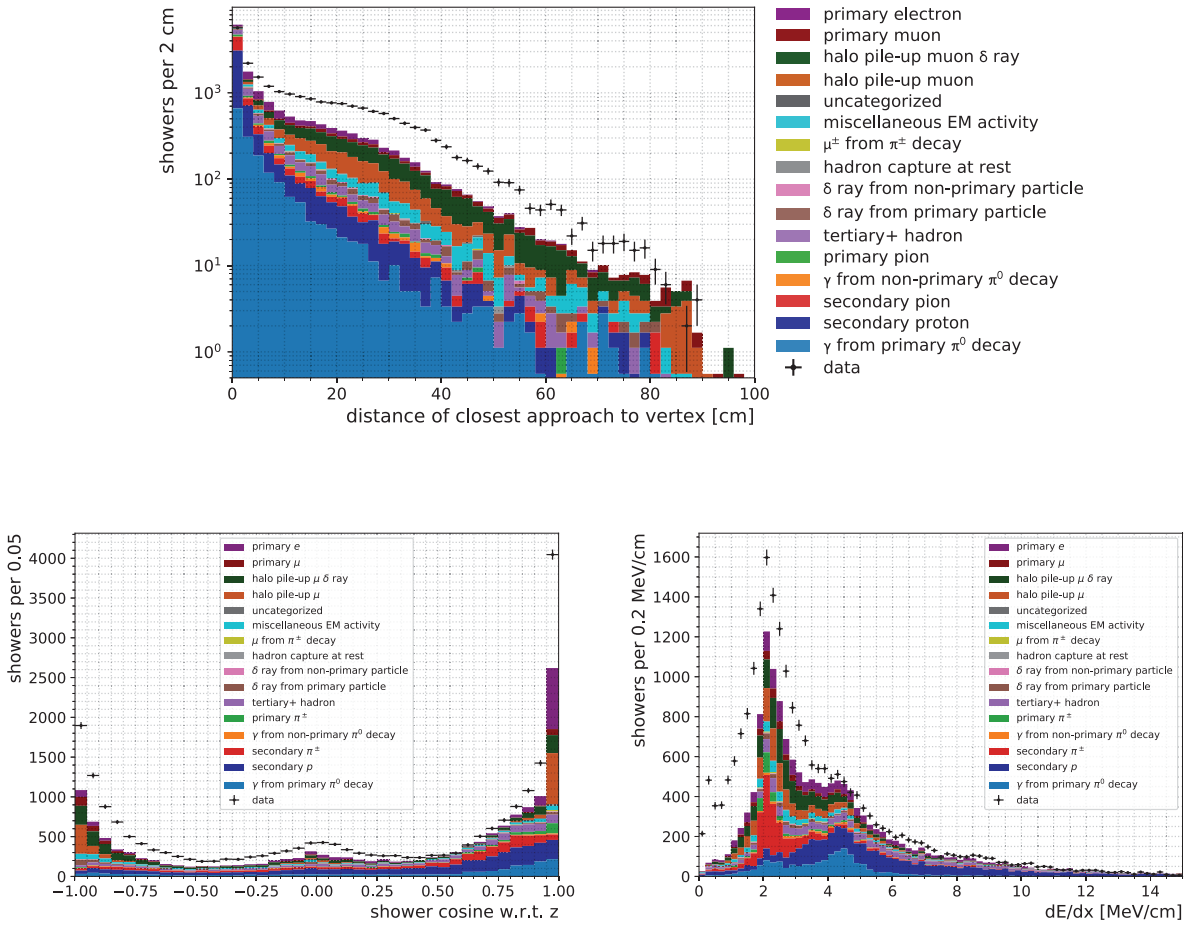

Figure D.6: Distributions of the distance of closest approach to vertex (top), cosine w.r.t. the z axis (bottom left), and $\mathrm{d}E/\mathrm{d}x$ (bottom right).

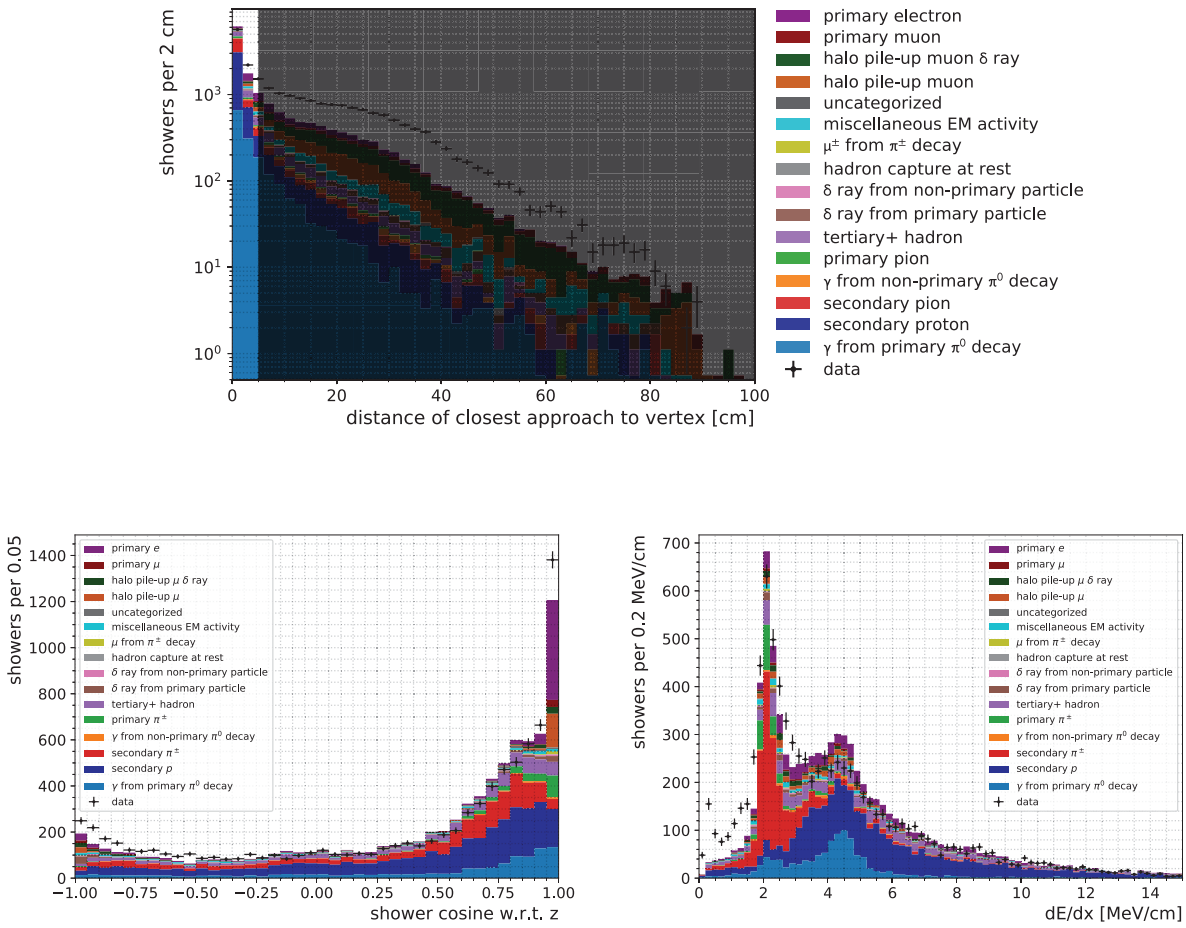

Figure D.7: Distributions of EM shower cosine w.r.t. the z axis (bottom left) and $\mathrm{d}E/\mathrm{d}x$ (bottom right) after a cut is applied to reject EM showers with DCA > 5 cm (top).

References

[1] J. Davis, Raymond, D. S. Harmer, and K. C. Hoffman, "Search for Neutrinos from the Sun," Phys. Rev. Lett. **20**, 1205 (1968).

[2] Y. Fukuda *et al.* (Super-Kamiokande), "Evidence for Oscillation of Atmospheric Neutrinos," Phys. Rev. Lett. **81**, 1562 (1998), arXiv:hep-ex/9807003.

[3] Q. R. Ahmad *et al.* (SNO), "Measurement of the Rate of $\nu_e + d \to p + p + e^-$ Interactions Produced by ^{8}B Solar Neutrinos at the Sudbury Neutrino Observatory," Phys. Rev. Lett. **87**, 071301 (2001), arXiv:nucl-ex/0106015.

[4] D. G. Michael *et al.* (MINOS), "Observation of Muon Neutrino Disappearance with the MINOS Detectors and the NuMI Neutrino Beam," Phys. Rev. Lett. **97**, 191801 (2006), arXiv:hep-ex/0607088.

[5] K. Abe *et al.* (T2K), "Indication of Electron Neutrino Appearance from an Accelerator-produced Off-Axis Muon Neutrino Beam," Phys. Rev. Lett. **107**, 041801 (2011), arXiv:1106.2822 [hep-ex].

[6] Y. Abe *et al.* (Double Chooz), "Indication of Reactor $\bar{\nu}_e$ Disappearance in the Double Chooz Experiment," Phys. Rev. Lett. **108**, 131801 (2012), arXiv:1112.6353 [hep-ex].

[7] F. P. An *et al.* (Daya Bay), "Observation of Electron-Antineutrino Disappearance at Daya Bay," Phys. Rev. Lett. **108**, 171803 (2012), arXiv:1203.1669 [hep-ex].

[8] J. K. Ahn *et al.* (RENO), "Observation of Reactor Electron Antineutrinos Disappearance in the RENO Experiment," Phys. Rev. Lett. **108**, 191802 (2012), arXiv:1204.0626 [hep-ex].

[9] K. Hirata *et al.* (Kamiokande-II), "Observation of a Neutrino Burst from the Supernova SN1987A," Phys. Rev. Lett. **58**, 1490 (1987).

[10] R. M. Bionta *et al.*, "Observation of a Neutrino Burst in Coincidence with Supernova 1987A in the Large Magellanic Cloud," Phys. Rev. Lett. **58**, 1494 (1987).

[11] M. G. Aartsen *et al.* (IceCube), "Neutrino emission from the direction of the blazar TXS 0506+056 prior to the IceCube-170922A alert," Science **361**, 147 (2018), arXiv:1807.08794 [astro-ph.HE].

[12] M. G. Aartsen *et al.* (IceCube, Fermi-LAT, MAGIC, AGILE, ASAS-SN, HAWC, H.E.S.S., INTEGRAL, Kanata, Kiso, Kapteyn, Liverpool Telescope, Subaru, Swift NuSTAR, VERITAS, VLA/17B-403), "Multimessenger observations of a flaring blazar coincident with high-energy neutrino IceCube-170922A," Science **361**, eaat1378 (2018), arXiv:1807.08816 [astro-ph.HE].

[13] M. Antonello *et al.* (MicroBooNE, LAr1-ND, ICARUS-WA104), "A Proposal for a Three Detector Short-Baseline Neutrino Oscillation Program in the Fermilab Booster Neutrino Beam," (2015), arXiv:1503.01520 [physics.ins-det].

[14] R. Acciarri *et al.* (MicroBooNE), "Design and Construction of the MicroBooNE Detector," JINST **12**, P02017 (2017), arXiv:1612.05824 [physics.ins-det].

[15] S. Amerio *et al.* (ICARUS), "Design, construction and tests of the ICARUS T600 detector," Nucl. Instrum. Meth. A **527**, 329 (2004).

[16] R. Acciarri *et al.* (DUNE), *Long-Baseline Neutrino Facility (LBNF) and Deep Underground Neutrino Experiment (DUNE): Conceptual Design Report, Volume 1: The LBNF and DUNE Projects*, Tech. Rep. (2016) arXiv:1601.05471 [physics.ins-det].

[17] R. Acciarri *et al.* (DUNE), *Long-Baseline Neutrino Facility (LBNF) and Deep Underground Neutrino Experiment (DUNE): Conceptual Design Report, Volume 2: The Physics Program for DUNE at LBNF*, Tech. Rep. (2015) arXiv:1512.06148 [physics.ins-det].

[18] J. Strait *et al.* (DUNE), *Long-Baseline Neutrino Facility (LBNF) and Deep Underground Neutrino Experiment (DUNE): Conceptual Design Report, Volume 3: Long-Baseline Neutrino Facility for DUNE June 24, 2015*, Tech. Rep. (2016) arXiv:1601.05823 [physics.ins-det].

[19] R. Acciarri *et al.* (DUNE), *Long-Baseline Neutrino Facility (LBNF) and Deep Underground Neutrino Experiment (DUNE): Conceptual Design Report, Volume 4 The DUNE Detectors at LBNF*, Tech. Rep. (2016) arXiv:1601.02984 [physics.ins-det].

[20] B. Abi *et al.* (DUNE), "The DUNE Far Detector Interim Design Report Volume 1: Physics, Technology and Strategies," (2018), arXiv:1807.10334 [physics.ins-det].

[21] B. Abi *et al.* (DUNE), "Deep Underground Neutrino Experiment (DUNE), Far Detector Technical Design Report, Volume II DUNE Physics," (2020), arXiv:2002.03005 [hep-ex].

[22] D. R. Nygren, "The Time-Projection Chamber: A New 4π Detector for Charged Particles," eConf **C740805**, 58 (1974).

[23] J. N. Marx and D. R. Nygren, "The Time Projection Chamber," Phys. Today **31N10**, 46 (1978).

[24] A. R. Clark *et al.*, "Proposal for a PEP Facility Based on the Time Projection Chamber," (1976).

[25] H. J. Hilke, "Time projection chambers," Rept. Prog. Phys. **73**, 116201 (2010).

[26] W. J. Willis and V. Radeka, "Liquid-Argon Ionization Chambers as Total-Absorption Detectors," Nucl. Instrum. Meth. **120**, 221 (1974).

[27] C. Rubbia, "The Liquid-Argon Time Projection Chamber: A New Concept for Neutrino Detectors," (1977).

[28] M. Schenk, *Studies with a liquid argon time projection chamber : addressing technological challenges of large-scale detectors*, Master's thesis, Bern U., Wiesbaden (2014).

[29] W. M. Haynes, ed., *CRC Handbook of Chemistry and Physics*, 97th ed. (CRC Press, 2016).

[30] M. Tanabashi *et al.* (Particle Data Group), "Review of Particle Physics," Phys. Rev. D **98**, 030001 (2018).

[31] D. Groom, "Atomic and Nuclear Properties of Materials," `http://pdg.lbl.gov/2019/AtomicNuclearProperties` (2018), accessed: 2020-03-16.

[32] E. Aprile and T. Doke, "Liquid Xenon Detectors for Particle Physics and Astrophysics," Rev. Mod. Phys. **82**, 2053 (2010), arXiv:0910.4956 [physics.ins-det].

[33] J. A. Nikkel, T. Gozani, C. Brown, J. Kwong, D. N. McKinsey, Y. Shin, S. Kane, C. Gary, and M. Firestone, "Liquefied Noble Gas (LNG) detectors for detection of nuclear materials," JINST **7**, C03007 (2012).

[34] V. Chepel and H. Araujo, "Liquid noble gas detectors for low energy particle physics," JINST **8**, R04001 (2013), arXiv:1207.2292 [physics.ins-det].

[35] K. Kleinknecht, *Detectors for Particle Radiation* (1998).

[36] J. A. Formaggio and G. P. Zeller, "From eV to EeV: Neutrino Cross Sections Across Energy Scales," Rev. Mod. Phys. **84**, 1307 (2012), arXiv:1305.7513 [hep-ex].

[37] C. Andreopoulos, C. Barry, S. Dytman, H. Gallagher, T. Golan, R. Hatcher, G. Perdue, and J. Yarba, "The GENIE Neutrino Monte Carlo Generator: Physics and User Manual," (2015), arXiv:1510.05494 [hep-ph].

[38] F. G. Binon, P. Duteil, J. P. Garron, J. Gorres, L. Hugon, J. P. Peigneux, C. Schmit, M. Spighel, and J. P. Stroot (CERN-IPN (Orsay)), "Scattering of negative pions on carbon," Nucl. Phys. B **17**, 168 (1970).

[39] B. W. Allardyce *et al.*, "Pion Reaction Cross Sections and Nuclear Sizes," Nucl. Phys. A **209**, 1 (1973).

[40] C. Wilkin, C. R. Cox, J. J. Domingo, K. Gabathuler, E. Pedroni, J. Rohlin, P. Schwaller, and N. W. Tanner, "A Comparison of π^+ and π^- Total Cross Sections of Light Nuclei Near the 3–3 Resonance," Nucl. Phys. B **62**, 61 (1973).

[41] A. S. Clough *et al.*, "Pion-Nucleus Total Cross Sections from 88 to 860 MeV," Nucl. Phys. B **76**, 15 (1974).

[42] A. S. Carroll, I.-H. Chiang, C. B. Dover, T. F. Kycia, K. K. Li, P. O. Mazur, D. N. Michael, P. M. Mockett, D. C. Rahm, and R. Rubinstein, "Pion-nucleus total cross sections in the (3, 3) resonance region," Phys. Rev. C **14**, 635 (1976).

[43] D. Ashery, I. Navon, G. Azuelos, H. K. Walter, H. J. Pfeiffer, and F. W. Schleputz, "True absorption and scattering of pions on nuclei," Phys. Rev. C **23**, 2173 (1981).

[44] V. Flaminio, W. G. Moorhead, D. R. O. Morrison, and N. Rivoire, *Compilation of Cross-Sections I: π^+ and π^- Induced Reactions* (CERN, Geneva, 1983).

[45] V. Flaminio, W. G. Moorhead, D. R. O. Morrison, and N. Rivoire, *Compilation of Cross-Sections II. K^+ and K^- Induced Reactions* (CERN, Geneva, 1983).

[46] S. Agostinelli *et al.* (GEANT4), "GEANT4—A simulation toolkit," Nucl. Instrum. Meth. A **506**, 250 (2003).

[47] J. Allison *et al.*, "Geant4 Developments and Applications," IEEE Trans. Nucl. Sci. **53**, 270 (2006).

[48] J. Allison *et al.*, "Recent developments in GEANT4," Nucl. Instrum. Meth. A **835**, 186 (2016).

[49] D. H. Wright and M. H. Kelsey, "The Geant4 Bertini Cascade," Nucl. Instrum. Meth. A **804**, 175 (2015).

[50] F. Cavanna, M. Kordosky, J. Raaf, and B. Rebel (LArIAT), "LArIAT: Liquid Argon In A Testbeam," (2014), arXiv:1406.5560 [physics.ins-det].

[51] R. Acciarri *et al.* (LArIAT), "The Liquid Argon In A Testbeam (LArIAT) Experiment," (2019), arXiv:1911.10379 [physics.ins-det].

[52] M. G. Albrow *et al.*, "Fermilab Testbeam Facility Annual Report – FY 2015," (2015), 10.2172/1251186.

[53] M. G. Albrow *et al.*, "Fermilab Testbeam Facility Annual Report – FY 2016," (2016), 10.2172/1335646.

[54] M. Rominsky *et al.*, "Fermilab Test Beam Facility Annual Report: FY17," (2018), 10.2172/1418446.

[55] A. Brandt *et al.*, "Fermilab Testbeam Facility Annual Report – FY 2014," (2015), 10.2172/1182553.

[56] S. Dimopoulos, S. Raby, and F. Wilczek, "Proton Decay in Supersymmetric Models," Phys. Lett. B **112**, 133 (1982).

[57] B. Bajc, J. Hisano, T. Kuwahara, and Y. Omura, "Threshold corrections to dimension-six proton decay operators in non-minimal SUSY $SU(5)$ GUTs," Nucl. Phys. B **910**, 1 (2016), arXiv:1603.03568 [hep-ph].

[58] R. Acciarri *et al.* (ArgoNeuT), "First observation of low energy electron neutrinos in a liquid argon time projection chamber," Phys. Rev. D **95**, 072005 (2017), arXiv:1610.04102 [hep-ex].

[59] R. Acciarri *et al.* (WArP), "Effects of Nitrogen contamination in liquid Argon," JINST **5**, P06003 (2010), arXiv:0804.1217 [nucl-ex].

[60] P. Agnes *et al.* (DarkSide), "First Results from the DarkSide-50 Dark Matter Experiment at Laboratori Nazionali del Gran Sasso," Phys. Lett. B **743**, 456 (2015), arXiv:1410.0653 [astro-ph.CO].

[61] J. Calvo *et al.* (ArDM), "Commissioning of the ArDM experiment at the Canfranc underground laboratory: first steps towards a tonne-scale liquid argon time projection chamber for Dark Matter searches," JCAP **03**, 003 (2017), arXiv:1612.06375 [physics.ins-det].

[62] W. Foreman *et al.* (LArIAT), "Calorimetry for low-energy electrons using charge and light in liquid argon," Phys. Rev. D **101**, 012010 (2020), arXiv:1909.07920 [physics.ins-det].

[63] T. J. Roberts, K. B. Beard, D. Huang, S. Ahmed, D. M. Kaplan, and L. K. Spentzouris, "G4Beamline Particle Tracking in Matter-dominated Beam Lines," Conf. Proc. C **0806233**, WEPP120 (2008).

[64] H. C. Fenker, "A Standard Beam PWC for Fermilab," (1983).

[65] C. Anderson *et al.*, "The ArgoNeuT Detector in the NuMI Low-Energy beam line at Fermilab," JINST **7**, P10019 (2012), arXiv:1205.6747 [physics.ins-det].

[66] M. Adamowski *et al.*, "The Liquid Argon Purity Demonstrator," JINST **9**, P07005 (2014), arXiv:1403.7236 [physics.ins-det].

[67] F. Lesaint, "Example: Cuboid in a 2 vanishing points perspective," URL: `http://www.texample.net/tikz/examples/cuboid/`, License: Creative Commons Attribution 3.0 Unported License (CC BY 3.0), (2012).

[68] G. De Geronimo *et al.*, "Front-End ASIC for a Liquid Argon TPC," IEEE Trans. Nucl. Sci. **58**, 1376 (2011).

[69] K. Biery, E. Flumerfelt, J. Freeman, W. Ketchum, G. Lukhanin, and R. Rechenmacher, "*artdaq*: DAQ software development made simple," J. Phys. Conf. Ser. **898**, 032013 (2017).

[70] C. Green, J. Kowalkowski, M. Paterno, M. Fischler, L. Garren, and Q. Lu, "The art framework," J. Phys. Conf. Ser. **396**, 022020 (2012).

[71] R. Brun and F. Rademakers, "ROOT – An object oriented data analysis framework," Nucl. Instrum. Meth. A **389**, 81 (1997).

[72] E. D. Church, "LArSoft: A Software Package for Liquid Argon Time Projection Drift Chambers," (2013), arXiv:1311.6774 [physics.ins-det].

[73] E. L. Snider and G. Petrillo, "LArSoft: toolkit for simulation, reconstruction and analysis of liquid argon TPC neutrino detectors," J. Phys. Conf. Ser. **898**, 042057 (2017).

[74] B. Baller, "Liquid argon TPC signal formation, signal processing and reconstruction techniques," JINST **12**, P07010 (2017), arXiv:1703.04024 [physics.ins-det].

[75] B. Baller, *TrajCluster Users Guide*, Tech. Rep. (Fermi National Accelerator Laboratory, 2018) `https://cdcvs.fnal.gov/redmine/documents/1026`.

[76] M. Antonello *et al.*, "Precise 3D Track Reconstruction Algorithm for the ICARUS T600 Liquid Argon Time Projection Chamber Detector," Adv. High Energy Phys. **2013**, 260820 (2013), arXiv:1210.5089 [physics.ins-det].

[77] S. E. Kopp, "Accelerator neutrino beams," Phys. Rept. **439**, 101 (2007), arXiv:physics/0609129.

[78] F. James and M. Roos, "MINUIT – A System for Function Minimization and Analysis of the Parameter Errors and Correlations," Comput. Phys. Commun. **10**, 343 (1975).

[79] P. J. Mohr, D. B. Newell, and B. N. Taylor, "CODATA Recommended Values of the Fundamental Physical Constants: 2014," Rev. Mod. Phys. **88**, 035009 (2016), arXiv:1507.07956 [physics.atom-ph].

[80] E. Tiesinga, P. J. Mohr, D. B. Newell, and B. N. Taylor, "The 2018 CODATA Recommended Values of the Fundamental Physical Constants," (National Institute of Standards and Technology, Gaithersburg, MD 20899, 2019) `http://physics.nist.gov/constants`.

[81] E. W. Lemmon, M. O. McLinden, and D. G. Friend, "Thermophysical properties of fluid systems," in *NIST Chemistry WebBook*, NIST Standard Reference Database Number No. 69, edited by P. J. Linstrom and W. G. Mallard (National Institute of Standards and Technology, Gaithersburg, MD 20899, 2018) `http://webbook.nist.gov/chemistry/fluid/`.

[82] G. Cowan, "A Survey of Unfolding Methods for Particle Physics," Conf. Proc. C **0203181**, 248 (2002).

[83] M. Lefebvre, R. K. Keeler, R. Sobie, and J. White, "Propagation of errors for matrix inversion," Nucl. Instrum. Meth. A **451**, 520 (2000), arXiv:hep-ex/9909031.

[84] M. Paterno, "Calculating Efficiencies and Their Uncertainties," (2004), 10.2172/15017262, [FERMILAB-TM-2286-CD].

[85] T. Ullrich and Z. Xu, "Treatment of Errors in Efficiency Calculations," (2007), arXiv:physics/0701199 [physics.data-an].

[86] D. Casadei, "Estimating the selection efficiency," JINST **7**, P08021 (2012), arXiv:0908.0130 [physics.data-an].

[87] M. A. Fischler and R. C. Bolles, "Random Sample Consensus: A Paradigm for Model Fitting with Applications to Image Analysis and Automated Cartography," Commun. ACM **24**, 381 (1981).

[88] K. Pearson, "On Lines and Planes of Closest Fit to Systems of Points in Space," Philosophical Magazine **2**, 559 (1901).